Czech Technical University in Prague
Faculty of Electrical Engineering
Department of Physics

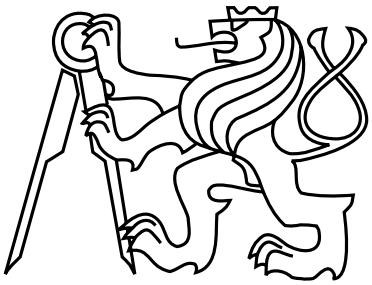

High Energy Density Plasma Diagnostics Using Neutron and Gamma Detectors

Doctoral Thesis

Ing. Jakub Cikhardt

Prague, November 2017

Study Programme: Electrical Engineering and Information Technology (P 2612)

Branch of Study: Plasma Physics (1701V011)

Supervisor: doc. Ing. Daniel Klír, Ph.D.

Acknowledgements

The author of this thesis would like to thank very much his supervisor doc. Ing. Daniel Klír, Ph.D. and to all members of the hot plasma physics experimental group at the Department of Physics at the Faculty of Electrical Engineering CTU in Prague, especially the head of this group prof. RNDr. Pavel Kubeš, CSc, doc. Ing. Josef Kravárik, Csc, and Ing. Karel Řezáč, Ph.D. for providing the opportunity to participate in experiments and extensive help with all aspects of the research including theory, experiments, data processing, and writing of publications. Great thanks also to Ing. Ondřej Šíla for performing of the simulations in the MCNP code.

At the same time, the great thanks to the colleagues from the Institute of High Current Electronics in Tomsk and Tomsk Polytechnic University, namely to Dr. Alexander Shishlov, Dr. Vladimir Kokshenev, Dr. Vladimir Padalko, Dr. Gennady Dudkin, Rustam Cheridzov, Alexey Labetsky, Nikolai Kurmaev, and Fedor Fursov for the wonderful scientific collaboration and experimental support.

Last but not least, the author of this thesis is very grateful to RNDr. Jozef Krása, CSc, and Ing. Miroslav Pfeifer, CSc, for the excellent experimental collaboration and for the help with publishing. Special thanks also to Ing. Jan Dostál, Ph.D. and RNDr. Roman Dudžak, Ph.D. for allowing the realization of experiments on the PALS laser system.

Thanks to all the above-mentioned colleagues and friends for the wonderful and pleasant collaboration and help. Without their help, this thesis could not be completed.

The research connected with this thesis was supported by the Grant Agency of the Czech Republic (Grant No. P205/12/0454 and 16-07036S), Ministry of Education, Youth, and Sports of the Czech Republic (Project No. LA08024, ME09087, LM2010014, LG13029, LH13283, LD14089, LG1513, LG13015, LA08024), the LASERLAB – EUROPE (Grant Agreement No 284464, EC's Seventh Framework Program), Student Grant Competition CTU (Grant No. 10/ 266/ OHK3/ 3T/ 13, OHK3-053-13, and 16/ 223/ OHK3/ 3T/ 13), International Atomic Energy Agency in Vienna (Project No. RC 14817, RC-16115, RC-16954, RC-16956, RC-17088, and RC-19253), and from the European Social Fund and the national budget of the Czech Republic (Project No. CZ.1.07/ 2.3.00/ 20.0279).

Declaration

I hereby declare that I have completed this thesis independently and that I have listed all the literature and publications used.
I have no objection to usage of this work in compliance with the act §60 Zákon č. 121/2000Sb. (copyright law), and with the rights connected with the copyright act including the changes in the act.

In Prague on November 27, 2017 .....

Abstract

Deuterium Z-pinches are efficient sources of pulsed soft and hard x-rays, fast ions, and neutrons. Many phenomena related to an acceleration of ions and neutron production on the Z-pinches have not yet been explained. Detailed understanding of these phenomena could be multidisciplinary important. Therefore, these phenomena are investigated in joint Czech-Russian experiments on the terawatt class GIT-12 device with the generator output voltage of 600 kV and current at stagnation of about 3 MA. These experiments are interesting since by using the novel experimental load composed of the deuterium gas-puff with outer plasma shell, the neutron yields were significantly increased from the order of 10^{11} to the order of 10^{12}. Such relatively high neutron yields were earlier observed on the devices with significantly higher current as the Saturn generator with the pulsed current of about 10 MA. At the same time, in our experiments, hydrogen ions with an energy above 38 MeV were detected. Such results are unique in experiments on the generator with the above-mentioned maximum current and voltage.

The work reported in this thesis is focused on the diagnostics of Z-pinch plasma by neutron detectors and interpretation of the experimental results. The precise neutron diagnostics is in our experiments necessary because the produced neutron pulses carry the information about the deuterons which produced them. In this thesis, the extensive neutron detection system is presented. This system is based on several principally independent methods: neutron bubble detectors, scintillation neutron time-of-flight diagnostics, neutron activation diagnostics with the moderator (silver activation counter), and fast neutron activation diagnostics with various energy threshold. This diagnostic system was used to evaluate neutron yields, energy spectrum, and neutron fluences at different distances and directions. The influence of non-dd neutrons on the experimental results is discussed.

Abstrakt

Deuteriové Z-pinče jsou účinnými zdroji měkkého a tvrdého rentgenového záření, rychlých iontů a neutronů. Mnoho jevů spojených s urychlováním iontů a produkcí neutronů na Z-pinčích není stále objasněno. Detailní porozumění těmto jevům může být důležité i v řadě jiných oborů. Proto jsou tyto jevy zkoumány ve společných česko-ruských experimentech na terawattovém zařízení GIT-12 s výstupním napětím generátoru 600 kV a proudem v době stagnace 3 MA. Tyto experimenty jsou zajímavé, neboť použitím nové experimentální zátěže tvořené deuteriovým "gas-puffem" obklopeným vnější vrstvou plazmatu bylo dosaženo významného zvýšení neutronového zisku z řádu 10^{11} na řád 10^{12}. Takto poměrně vysoké neutronové zisky byly dříve pozorovány jen na zařízeních s mnohem vyšším maximem proudu, jako je například zařízení Saturn s maximem proudu okolo 10 MA. Současně byly v našich experimentech pozorovány vodíkové ionty s energií převyšující 38 MeV. Uvedené experimentální výsledky jsou na zařízení s výše zmíněným maximálním proudem a napětím unikátní.

Tato doktorská práce je zaměřena na diagnostiku z-pinčového plazmatu pomocí neutronových detektorů a interpretaci experimentálních výsledků. V těchto experimentech je nezbytná precizní neutronová diagnostika, neboť vzniklé neutronové impulzy v sobě nesou informaci o deuteronech jejichž reakcí neutrony vznikly. V této doktorské práci je důkladně popsána rozsáhlá soustava neutronové diagnostiky, která je tvořena detektory založenými na nezávislých principech detekce: neutronové bublinkové detektory, scintilační neutronové detektory doby letu, aktivační diagnostika s moderací neutronů (detektor založený na aktivaci stříbra) a rychlá neutronová aktivační diagnostika s energetickým prahem. Tato soustava neutronové diagnostiky byla použita k určení neutronových zisků, energetického spektra a neutronových toků v různých vzdálenostech a směrech. V práci je rovněž diskutován vliv neutronů jiného původu než z dd reakce.

Contents

List of Figures

List of Tables

Chapter 1

Introduction

This thesis is devoted to the experimental research of the high energy density (HED) plasma. This is a plasma with an energy density above 10^5 J/cm^3 [1]. It is possible to reach such extreme energy density only at pulsed devices. A lifetime of the HED plasma varies from a few picoseconds to several tens of nanoseconds. A density of the HED plasma experiments ranges typically from 10^{17} to 10^{23} particles per cm^3 and the energy of the plasma particles can reach up to tens of MeV [2, 3]. However, in some individual cases, we can meat even higher values. Typical representatives of the HED plasma are Z-pinch plasma, laser-produced plasmas, and plasma produced by particle beams. Nevertheless, this thesis deals with Z-pinch experiments only.

The Z-pinch experiments reported in this thesis are performed on the terawatt-class GIT-12 generator with an output voltage of 600 kV and a current pulse maximum of 5 MA. In comparison with other Z-pinch experiments, our experiments are different in the novel Z-pinch load composed of a deuterium gas-puff with the outer plasma shell generated by coaxial plasma guns. The neutron yields on the order of 10^{12} and very broad neutron energy spectra from 0 to 20 MeV in the radial direction are unique at the device with the mentioned output voltage and current. Because of high neutron yields and unprecedented neutron spectra, it seems natural to put emphasis on the neutron diagnostics.

1.1 Aim of Thesis

The main aim of this thesis is to use neutron and gamma-ray detectors for diagnostics of HED plasmas produced by the GIT-12 device. It is well known that the produced neutron pulses carry important information about deuterons accelerated in Z-pinch plasmas. For instance, an energy distribution of deuterons in HED plasma could be derived from an energy spectrum of neutrons produced by dd reactions. For this purpose, the neutron spectra are evaluated by time-resolved signals of a neutron time-of-flight (nToF) detector at the distance of 25.8 m from the pinch. However, the neutron spectra in our experiments are very broad and therefore the energy-dependent pulse response on neutrons has to be taken into account. For this reason, the nToF detectors have to be calibrated. The calibration of the nToF detector is achieved with a help of several material samples with different energy thresholds of a neutron induced activation. The induced activities of the activation samples are measured post-shot by gamma-ray spectrometers with NaI(Tl) and HPGe gamma-ray detectors. The samples can be activated not only by fast neutrons but also by photons produced by our Z-pinch. It is the reason why the influence of the strong bremsstrahlung on the activation samples is experimentally examined.

Finally, in order to calculate deuteron spectra from neutrons, we have to know that the observed neutrons are really produced by the dd reaction. Therefore, another goal of our experiment is to measure the contribution and influence of neutrons produced by non-dd reactions. If and when all these effects are taken into account, we will be able to derive the deuteron energy distribution functions and to make conclusions on energetic processes in Z-pinch plasmas.

1.2 Layout of Thesis

This thesis is divided into 10 chapters. Chapters 2 – 5 are devoted to the introduction to the Z-pinch research and theoretical background. Basic principles of Z-pinches, various types of Z-pinches, history, and state of the art are introduced in chapter 2. The basic Z-pinch models are described in chapter 3. The dd reactions and energy and angular distribution of dd neutrons are presented in chapter 4. Interactions of photons and neutrons which are crucial for our diagnostics methods are described in chapter 5.

The following chapters 6 and 7 are focused on the description of our experiments. The GIT-12 generator and the experimental load are described in chapter 6. In section 7, the principles of our neutron and gamma-ray diagnostics are explained and diagnostics setup, arrangement, and calibration are reported.

Results of the neutron diagnostics and gamma-ray analysis of the neutron activation samples including the total neutron yields, yields of the neutrons with an energy above 12 MeV, radial neutron spectra, neutron fluences in different directions and distances, and an influence of non-dd neutrons and strong bremsstrahlung on the neutron diagnostics are presented in section 8. The overall experimental results, comparison with other experiments and hypothetically possible applications are discussed in chapter 9. Chapter 10 is the conclusion of this thesis.

A personal contribution of the author of this thesis to the experiments on the GIT-12 device is summarized in appendix A. Appendix B contains a list of publications where the author of this thesis is a main author or coauthor. In appendix C, a list of author's conference contributions is presented. Appendix D is a list of internships in which the author of this thesis actively participated. The last part of this thesis is a bibliography.

Chapter 2

Z-Pinches

2.1 Basic Principles of Z-Pinches

At the beginning, we briefly introduce Z-pinches. The Z-pinches are pulsed power electric discharge devices. The high pulsed current is achieved using a generator with capacitor energy storage. The discharge is of a cylindrical form with the current in the direction of the z-axis (prefix "Z" means the current direction). During such discharge, the plasma is compressed by the pinch effect. This phenomenon is caused by the Lorentz force

$$\mathrm{d}\mathbf{F} = I\,\mathbf{B} \times \mathrm{d}\mathbf{l}, \tag{2.1}$$

where $\mathrm{d}\mathbf{F}$ is the element of the force which compresses the element of the discharge length $\mathrm{d}\mathbf{l}$, I is the discharge current and $\mathbf{B}$ is the self-magnetic field generated by the discharge. The pinch effect is illustrated in fig. 2.1. This kind of pinch is the most common and it is the focal point of this thesis. Maximum of the current pulse of the Z-pinches can reach from several tens of kA at small devices to several tens of MA as at the Atlas device at LANL[1] [5]. It should be noted that we can also meet different pinch configurations as θ-pinch or toroidal pinch.

2.2 Various Types of Z-pinch Loads

The basic various types of Z-pinch loads are illustrated in fig. 2.2. Most of the earliest experiments were performed with compressional Z-pinch loads (see fig. 2.2(a)).

[1] Los Alamos National Laboratories, USA

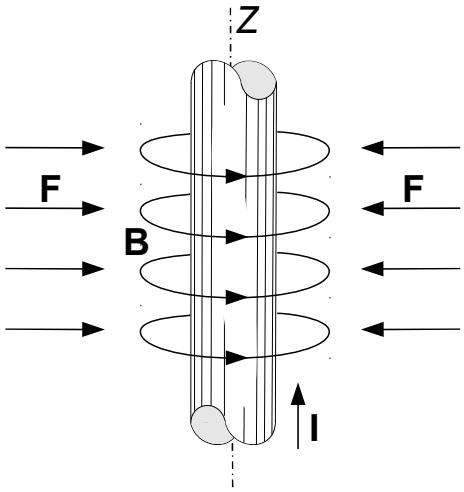

Figure 2.1: The pinch effect principle

This load is created by two electrodes surrounded by a cylindrical vessel. The space between the electrodes is filled with a gas. The pressure of the gas varies usually from a thousandth of atm to tenths of atm [9, 10]. Applying a high voltage in the range from tens of kV to hundreds of kV, a breakdown occurs near the insulating wall and a current shell is formed [20]. The pinch effect compresses the current shell towards the Z-axis. If the diameter of the vessel is reduced from the order of centimeters to the order of millimeters or less, we talk about the capillary Z-pinch (see fig 2.2(b)). The capillary discharge has been very successful in producing a plasma uniform enough to form a lasing medium [20].

The load shown in fig. 2.2(c) is an exploding wire Z-pinch. A wire of the diameter of tens or hundreds of micrometers connects the anode with the cathode. The distance between the electrodes is typically 1-2 cm. Applying a high voltage pulse to the electrodes the wire explodes. The exploded material is ionized and implodes onto the axis by the pinch effect. The material of the wire may be of various nature. Typically it is carbon, tungsten, aluminum, and for the nuclear fusion research, the wire can be made of deuterated polyethylene or cryogenic deuterium [7]. Single-wire experiments have been almost abandoned, but multi-wire pinches are still in use.

A special configuration arises when we create an X-shape crossing of two wires. This configuration is shown in fig. 2.2(d) and it is called an X-pinch. The X-pinches are very efficient sources of x-rays. Due to the fact that the x-rays are produced

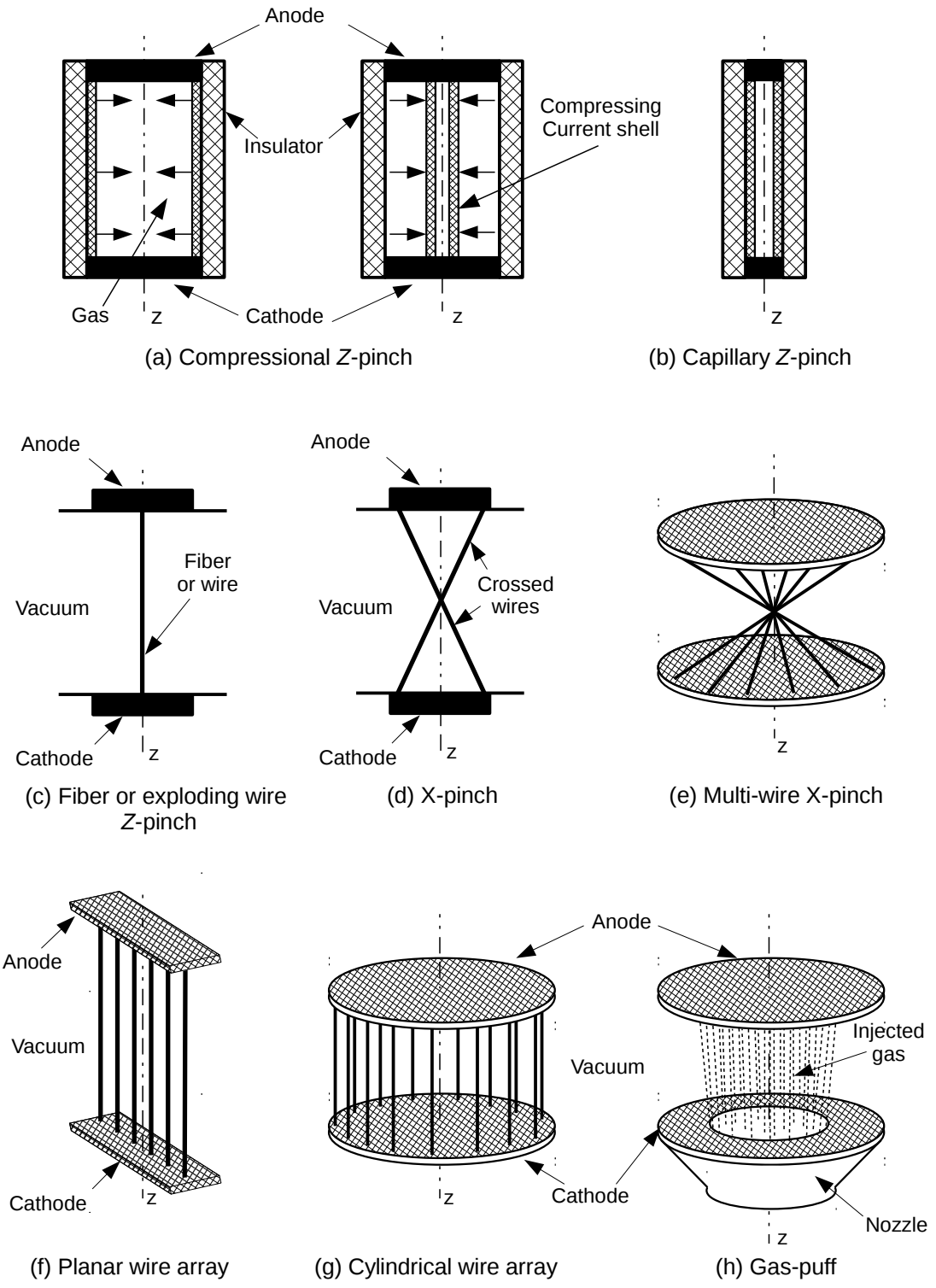

Figure 2.2: The basic configurations of Z-pinch loads

in a small spot where the wires are crossed, the X-pinches are used for soft x-ray imaging as a point source of radiation [11, 12]. At this point, it should be noted that the X-pinches can be formed not only with two wires, but it can be created by crossing a lot of wires as is shown in fig. 2.2(e).

Another multi-wire configuration, which is presented in the fig. 2.2(f) is called a planar wire-array. The number of wires in the wire array can range from a few units to a few hundred. Some experiments, show that the planar wire-arrays could be more efficient for K-shell x-ray production than more common and historically older cylindrical wire-arrays (see fig. 2.2(g)). For example, in the experiments described in [13], the maximum K-shell yield from an Al planar wire array at the current of 2.2 – 3.7 MA on the microsecond generator GIT-12 achieved of 6 kJ/cm. This radiation yield was about 1.5 times higher than in the comparable experiments with the cylindrical wire array implosions on the GIT-12. The experiments with cylindrical wire-arrays were popular especially in the 1990s and 2000s for their K-shell and black body radiation efficiency and great reproducibility. The cylindrical wire-array can contain more than one wire-array cylinder [34] or can be combined with another load. In principle, the cylindrical wire-array could be replaced by a thin metal shell liner, but to keep the mass per unit length the same as is typical for wire-array, e.g. 240 wires of 4 μm diameter on an array radius of 12 mm, would mean a shell thickness of only 40 nm [20].

A very important kind of the Z-pinch load is so-called gas-puff (see fig. 2.2(h)). Currently, the gas-puff load appears to be the most efficient for Z-pinch nuclear fusion experiments [39, 2]. The principle of the gas-puff is based on a supersonic jet of the gas injected into a vacuum chamber. The gas is injected by a nozzle through one electrode in the direction of the z-axis. The high voltage pulse is applied at the time when the gas still stays in a cylindrical or a conical shape. The geometry of the nozzle is often optimized for a multi-shell gas-puff creation [45, 47]. The shells can be created from different gases.

A special configuration of Z-pinch is a plasma focus. It was invented by Nikolai Vasilievich Filippov and Tatiana I. Filippova [14] and independently by Joseph W. Mather [15] in the 1960s. These two first devices differ in geometry. Therefore, today we distinguish between so-called Mather-type (fig. 2.3(a)) and Filippov-type (fig. 2.3(b)). However, most of the plasma focus devices are of the Mather-type.

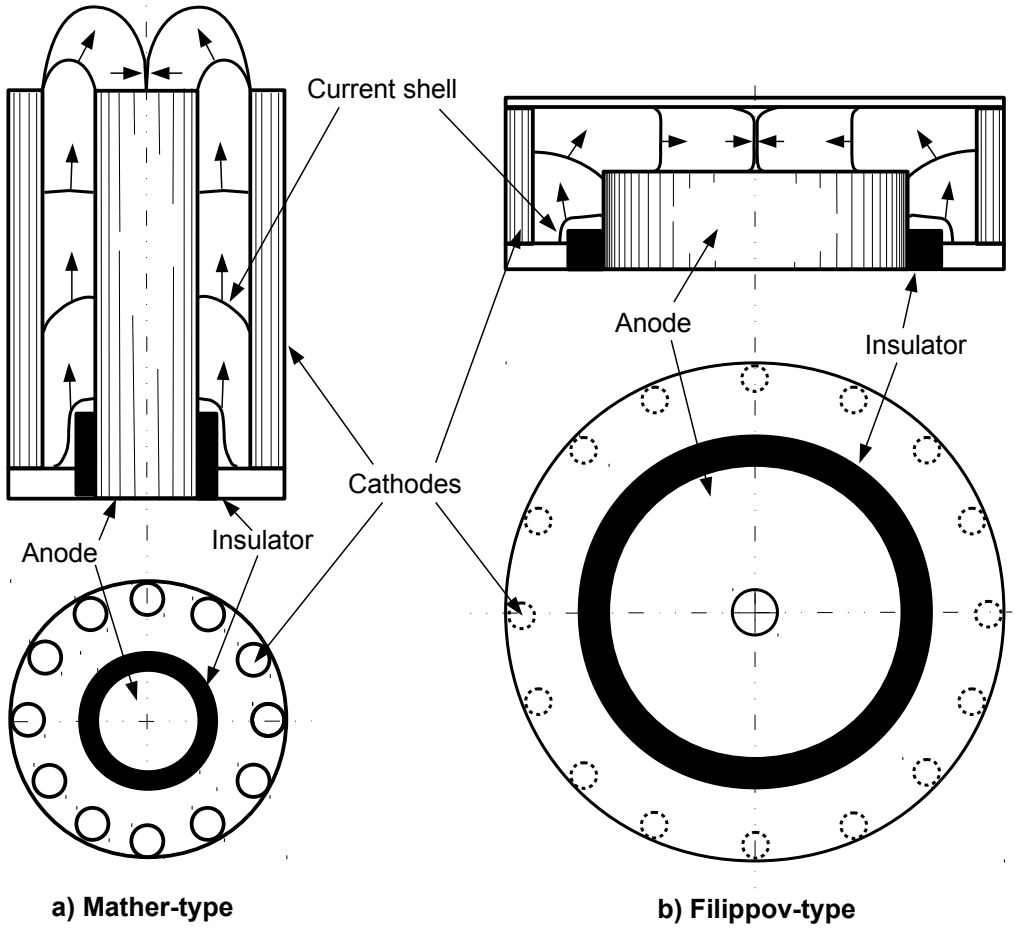

Figure 2.3: Plasma focus device

Inside a chamber, there is a coaxial electrode system with a cylindrical anode[2] in the center and several coaxial cathodes around. The chamber contains a gas with a pressure of tens or hundreds of Pascals. After applying a high voltage, a breakdown is formed near the insulator. The current shell formed is accelerated in the coaxial system by the Lorentz force. This part is called the coaxial accelerator. At the end of the coaxial accelerator, the current shell is pushed above the electrodes. Near the center of the anode the current shell pinches in the radial direction.

The plasma foci are very popular because of their neutron yield efficiency at currents up to 2 MA. They usually allow higher shot repetition rate than the classical

[2]We note that, the cathode may be in center and the anodes around. Such device is called the "inverse plasma focus".

Z-pinches. In addition to that, plasma foci do not impose such strict requirements on the rise time of the pulse generator, because the shape of the pulse is formed during the accelerating in the coaxial part. However, they have a few disadvantages as well. Namely, neutron yield stops growing at the discharge current of about 2 MA because a fraction of the current is not flowing through the pinch, but on a periphery [16, 17]. The pinch current limitation is caused by a high inductance of the pinch in comparison with an inductance of the plasma focus pulsed generators which operate usually with the voltage on the order of tens of kV [18, 19].

A lot of other loads and their combinations are used at the present. For example, the magnetized liner inertial fusion (MagLIF) which is described in subsection 2.4.

2.3 Brief History of Z-pinches

Probably the first Z-pinch device was constructed in Amsterdam by the British engineer John Cuthbertson for Martinus van Marum in 1790. This device stored the energy in 100 Leyden jars of 0.5 μF of total capacitance. These capacitors could be charged up to the voltage of 60 kV (1.8 kJ of maximal capacitive energy). Discharges were performed with an exploding wire up to 1 m length. The maximum of the current pulse reached about 60 kA [7, 8, 20]. The device is illustrated in fig. 2.4. However, this device was not called Z-pinch in those days.

The following significant milestone is the later discovery of James Arthur Pollock and Samuel Henry Egerton Barraclough in 1905 in Australia. They explained the distorted compression of a copper tube used as a lightning conductor by the effect of $\mathbf{J} \times \mathbf{B}$ magnetic force generated by the lightning current [8, 21]. Soon, in 1907 in the USA, Edwin Fitch Northrup proposed a continuous flow liquid metal Z-pinch exploiting the $\mathbf{J} \times \mathbf{B}$ force [8, 22]. In Northrup's paper "Some Newly Observed Manifestations of Forces in The Interior of an Electric Conductor" the term "pinch" is first mentioned. It was used for the symmetrical instability of a liquid-metal conductor in induction furnaces [22, 24].

In 1934 when Willard Harrison Bennett derived his theoretical model of the pressure equilibrium of charged particle streams and published the paper "Magnetically Self-Focussing Streams" [24, 23]. This model is described in subsection 3.1.1. Three years later, in 1937 Lewi Tonks used term "pinch effect" to describe self-constricted plasma [24, 7].

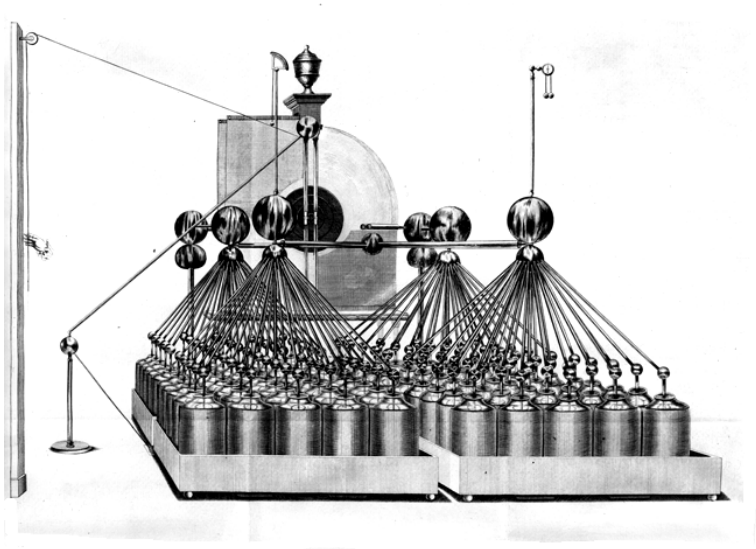

Figure 2.4: The first Z-pinch-like device built in Amsterdam in 1790 [20].

The first systematic research of Z-pinch discharge configurations began in the second half of the 1940s when the interest was driven by the vision of easily achievable thermonuclear fusion. It turned out that during the discharges in deuterium a lot of dd reactions were observed. In 1946 George Paget Thomson and Moses Blackman from Imperial College patented a toroidal pinch as the nuclear fusion reactor [25]. During the 1950s, several USA, UK and USSR laboratories simultaneously investigated Z-pinches which operated with currents on the order of hundreds of kA [26]. At the 1958 Geneva Conference on Peaceful Uses of Atomic Energy, many papers concluded that the measured neutrons were not of the thermal origin but were rather generated by the beam-target mechanism driven by instabilities [26]. It led to a significant reduction of Z-pinch experiments in the frame of the thermonuclear fusion research programs of most of the laboratories in the 1960s [24, 20].

In the 1960s, Z-pinches were used as efficient UV, XUV and soft x-ray sources [7]. Such Z-pinch experiments were performed with exploding wires with a diameter of 10-100 μm [7].

In the mid-1970s the interest in Z-pinches revived since the modern pulsed-power technologies made it possible to achieve higher currents on the order of mega amperes and shorter rise times on the order of hundreds or tens of nanoseconds. The experiments were performed with various configurations of the load. The research

was focused especially on wire array [27] or thin-foil [28] implosions for the lower initial impedance which allows better coupling with a generator than the single wires [6]. In the late 1970s, the experiments with gas-puff were prepared (see Shiloh's, Fisher's or Stallings's papers [29, 30, 31]).

The interest in gas-puff Z-pinches increased during the 1980s and 1990s. The gas-puff experiments were performed with the heavier gases e.g. Ne, Ar, Kr, Xe, etc. in order to achieve efficient x-ray source. For example, such experiments were performed on the Proto-II and the Z machine in SNL, [32, 34] and in Czechoslovak Academy of Sciences [33]. In order to produce neutrons, the deuterium gas-puff was used in the Irvine experiment [35], on the Angara device [37], and on the Saturn device [38]. These experiments show that the deuterium gas-puff is very efficient and cheap source of the intensive neutron pulses in comparison with laser systems. It led to numerous experiments with deuterium gas-puffs in the two following decades the 2000s and 2010s [39, 40, 44, 45, 46, 42, 43, 41].

Very successful experiments were performed on the Z machine in SNL where the record dd neutron yield of 3.9×10^{13} from a single Z-pinch shot was achieved at the current of 20 MA in 2007 [39]. This research was followed by experiments in Kurchatov Institute at the S-300 device [40] and at IHCE[3] on the GIT-12 generator in Tomsk [44].

Currently, various Z-pinch configurations are used. The applications and the current state of the Z-pinch research are presented in the following section.

2.4 State of the Art and Applications

This section is focused on the present Z-pinch research in the world-class laboratories. Generally, the main goal of the Z-pinch research is not to develop some industrially applicable device or even commercial product. The main goal is to study the fundamental physics such as physics of the hot dense plasma, mechanisms of particle acceleration in high energy density conditions, interactions of high-energy particle and radiation fluxes with the matter, neutron physics, laboratory astrophysics, material research and so on. In order to show an importance of the Z-pinch research, we will outline some scientific applications.

[3]Institute of High Current Electronic of the Siberian Branch of Russian Academy of Sciences in Tomsk.

2.4.1 Magnetized Liner Inertial Fusion

At the time of writing this thesis, the magnetized liner inertial fusion (MagLIF) is the most important Z-pinch project in the world. The aim of this project is to inhibit the heat losses by the escape of charged particles in the radial direction by the strong magnetic field during the magnetically driven implosion of the cylindrical liner and achieve thermonuclear fusion [49]. The MagLIF concept is illustrated in fig. 2.5. The liner is composed of a thin metal foil which encapsulates the gaseous D_2

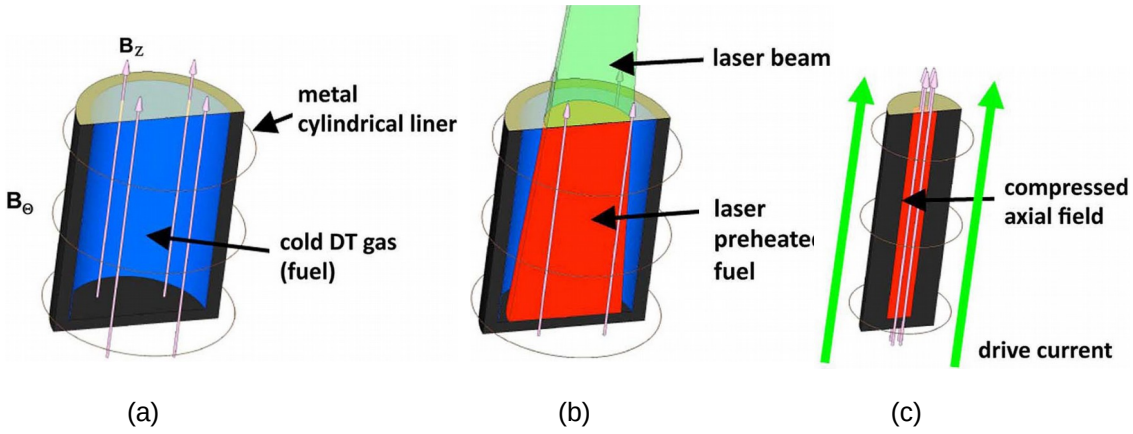

Figure 2.5: The MagLIF concept: (a) axial pre-magnetization phase, (b) laser pre-heat phase, and (c) magnetically driven liner implosion phase [50].

or D_2-T_2 mixture fuel. Such liner is placed in the initial axial magnetic field with a strength of 10 T generated by the Helmholtz coils. When the liner driven by the magnetic field starts to move, the gaseous fuel is preheated by the Z-Beamlet laser (Nd:YAG, second harmonic, 2.5 kJ, 1 TW) to the temperature of 100-200 eV. Consequently, the gaseous fuel is ionized, becomes very conductive and the magnetic field is effectively frozen there [49, 51]. The magnetic field is compressed by the liner implosion and achieved a few kT at the stagnation [49]. In accordance with the theoretical predictions and simulations, during the experiments the ion and electron temperature achieves approximately 3 keV and up to 2×10^{12} thermonuclear dd neutrons is produced at the current of 19 MA and 100 ns rise time [51]. Such neutron yield is equivalent to approximately 2 J of the fusion energy yield. Higher fusion yield could be achieved when the D-T mixture is used, the initial magnetic field achieves 30 T, and the peak current achieves to the Z machine maximum

of 25 MA. Then the predicted neutron yield should exceed 3.5×10^{16}, which is equivalent to the nuclear fusion yield of 100 kJ [50, 52]. The maximum peak current of 25 MA was not achieved at the MagLIF experiments due to the Helmholtz coils which require an extension of the power feeds and it leads to increase of the load inductance. The enhancement of the experimental parameters could be achieved by the auto-magnetized MagLIF liner [53]. The auto-magnetization is achieved using a composite liner with helical conduction paths separated by an insulating material to provide fuel magnetization from the early part of the drive current (see fig. 2.6). Breakdown of the insulators at the end of the magnetization phase allows the drive

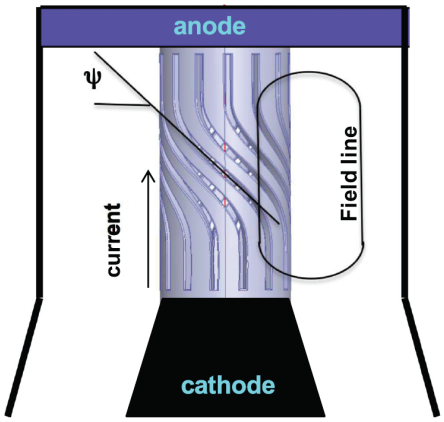

Figure 2.6: The auto-magnetized MagLIF concept [53].

current to flow in the axial direction and implode the liner by the conventional Z-pinch mechanism [53]. In this approach the Helmholtz coils are not used, thus the Z-pinch is more compact, power feeds significantly shorter and the initial load inductance reduced from 6.3 nH to 3.7 nH in comparison with the MagLIF with the Helmholtz coils. By the numerical simulations, it will increase the peak current from 18 MA to 22 MA [53].

Much higher fusion yields of 18 MJ and 440 MJ are predicted for the MagLIF liner driven by peak currents of 48 MA and 65 MA generated by the Z 300 and Z 800 conceptual petawatt-class pulsed power generators, respectively [54]. The Z 300 concept stores 48 MJ of the electrical energy in its LTD capacitors and by the 2D magnetohydrodynamic (MHD) simulations delivers the energy of 4.3 MJ to the MagLIF liner. The greater concept Z 800 stores 130 MJ of electric energy in

the capacitors and delivers the energy of 8.0 MJ to the MagLIF liner [54]. Thus, in both conceptual generators, the fusion energy theoretically exceeds the energy delivered to the liner and the thermonuclear fusion will be ignited. In the case of the Z 800 concept, the fusion energy should exceed the energy stored in the capacitors [49, 52, 54]. If such experiments will be successfully performed, it will be the first ignition of the controlled nuclear fusion on Earth. In [49] Slutz noted: "Even without commercial application, fusion yields with gain greater than unity would be interesting for the study of fusion physics in laboratory".

2.4.2 Sources of Intensive X-Ray Pulses

The Z-pinches are the most intense and efficient laboratory sources of the keV x-ray radiation [48, 50]. At the same time, the Z-pinches are cheaper in comparison with the concurrent high-power pulsed x-ray sources – lasers. These x-ray sources are important for the radiation-matter interaction studies, radiation absorption and transmission measurements, astrophysical research, shock physics experiments, etc [48].

The highest x-ray yield was reached at the Z machine in SNL. Using the cylindrical tungsten wire array, almost 2 MJ (200 TW) of x-ray pulse with Planckian-like spectrum with a temperature below 1 keV was achieved [50, 55]. Since the total stored electrical energy at Z machine was 11.4 MJ, the efficiency of conversion of electrical energy into x-rays was about 17%. Nowadays, such research continues at several laboratories with various wire-array modifications. For example, in Russia, the wire array implosions and x-ray emission are studied at the peak current up to 4 MA on the Angara-5-1 generator [56, 57, 58]. In France, the wire-array experiments are performed on the SPHINX generator with the peak current up to 5 MA [59, 60]. We should mention also the tungsten wire-array experiments in China on the JULONG-I device at the maximum current peak up to 8 MA [61]. As far as the planar wire-array implosion is concerned, it is studied for example at the ZEBRA generator with the peak current up to 2 MA [62].

Simultaneously with the study of x-ray production by wire-array implosions, the gas-puff x-ray sources are studied. The advantages of gas-puff in comparison with the wire-array are following. First, there is no need for the complicated and expensive wire array assembly. Second, the initial density distribution is axially

symmetric, whereas at the wire arrays the azimuthal variation is given by the finite number of the wires [63]. Third, at the small generators with a current of about 1 MA, the gas-puff load allows much higher shot rate, often without any need to open the vacuum chamber. On the other hand, it is complicated to evaluate the initial density distribution of the gas-puff, whereas at the case of the wire-array it is determined very precisely. As far as the chemical content is concerned, for x-ray generation usually the N_2, Ne, Ar, Kr, and Xe or their mixtures are used. At the recent experiments at the Z machine, using the Ar gas-puff doped by Xe, the x-ray yield of 1.14 MJ was achieved [64]. Thus, the x-ray yield is lower than at the case of the wire-array. On the other hand, the gas-puff is more promising for the applications. The gas-puff x-ray production is studied also at the SPHINX device [65] and on the Weizmann Institute of Science at the small 0.5 MA Z-pinch [66].

2.4.3 Sources of Intensive Neutron Pulses

The neutron radiation is necessary for many research activities or technological tasks. Obviously, the neutrons are generated in nuclear reactors, but usually it is inconvenient or impossible to use the nuclear reactor. Therefore, the neutrons are also produced by the laboratory sources. The neutron sources could be based on the spontaneous fission. The common such source is ^{252}Cf, however, it is very expensive (hundreds of thousands €[117]) and its half-life is 2.65 years only. The widespread sources are also the sources based on (α,n) reactions, typically ^{241}Am-Be, or ^{239}Pu-Be. Their half-lives of 433 years and 24 000 years, respectively are significantly longer than the half-life of the ^{252}Cf, but their costs are also higher. Moreover, it is not possible to simply "switch-off" these radioisotopic sources and a safe storage and ecological liquidation are complicated. Another possibility is to use sources which produce neutrons by the nuclear reactions of an accelerated particle beam with an appropriate target. For example, often used reactions are D(d,n)^{3}He, ^{9}Be(d,n), ^{7}Li(p,n), etc. Such an approach is close to the mechanism of neutron production in Z-pinches with deuterium or deuterated liners. The significant difference between the neutron radiation produced by the accelerator neutron source and Z-pinch is that the accelerator source usually produces the neutrons continuously whereas the Z-pinch is inherently a pulsed device. However, in such relatively short neutron pulse, the Z-pinch is able to generate tremendous amount of the D(d,n)^{3}He

neutrons (3.9×10^{13} during tens of nanoseconds [39]). The short and very intensive neutron fluxes are required for many laboratory purposes. For example, it could be used for the study of the multiple neutron capture reactions which are known as the r-processes. Another laboratory application which requires the intensive neutron pulse is the production of isotopes with a high radioactivity and a short half-life. In such a case, the irradiation of a material sample should not be longer than the half-life of the produced isotope, since the decay during the irradiation limits the maximum radioactivity of the sample. The short and intensive neutron pulses generated by Z-pinches allow obtaining the radioisotopes with a practically unlimited half-life (assuming that the neutron pulse duration is on the order of nanoseconds)[4]. In practice, it could be used for example in the neutron activation analysis[5]. As far as the long-duration neutron production is concerned, we note that some Z-pinch modifications, namely small plasma foci with a peak current up to 100 kA could operate in a repetition regime with a frequency up to 10 Hz and produce the neutron bursts continuously [67].

As far as the single shot Z-pinch is concerned, the extensive experimental research of the Z-pinch neutron production is being carried out on the GIT-12 generator (see [68]) at the Institute of High Current Electronic (IHCE) of Siberian Branch of Russian Academy of Sciences in Tomsk in collaboration with the Department of Physics of Faculty of Electrical Engineering of Czech Technical University in Prague (CTU). This doctoral thesis is based on these experiments. The first deuterium gas-puff shots on the GIT-12 device were performed in 2011 (see [44]). During this experimental campaign, the GIT-12 generator was operated in the fast regime with a rise time of 200 ns and also in the slow regime with the rise time of 1700 ns. Both in the fast and slow regime, the maximum load current varied between 2 and 3 MA. This experimental campaign was unique since the previous deuterium gas-puff experiments at MA current were performed at the 100-ns generators only. Any significant difference between the neutron yields at the fast and slow regime was not

[4]The production of radioisotopes with a very short half-life on Z-pinches could be achieved also by the interaction of the pulsed ion beams with a material sample.

[5]The neutron activation analysis lies in the activation of a sample and subsequently the radioisotopic content is determined by the gamma-ray analysis. The original chemical content is evaluated by the known nuclear reactions, their cross-sections and natural isotopic content of the chemical elements. The advantage of this method is that it is nondestructive, thus it is often used for analysis of works of art and historical artifacts.

observed, in both cases, the average neutron yield was of about 2×10^{11}. The significant increase of neutron yield occurred at the campaign in 2013, when the outer plasma shell surrounding the deuterium gas-puff was used. The dd neutron yield of the shots with such "hybrid" gas-puff achieved up to 3×10^{12} [2, 4]. By the optimization of the "hybrid" gas-puff, the maximum dd neutron yield achieved a value of 6×10^{12} in the experimental campaign in 2016. Moreover, the neutron energy spectrum was very broad. The energy of a significant number of neutrons exceeded 20 MeV. Considering the neutron energy distribution and substantial anisotropy it is apparent that practically all neutrons are of the beam-target origin. Notwithstanding, the neutron production is uncommonly efficient. It could be caused by relatively high energies of the deuterons. The D(d,n)^{3}He reaction cross-section is much higher at deuteron energies on the order of hundreds of keV. Using the comprehensive set of the ion diagnostics on the GIT-12, a significant number of such hydrogen ions was observed, even the hydrogen ions with energy above 38 MeV were detected [2, 123]. This hypothesis particularly explains the broad neutron energy spectrum and strong anisotropy. Nevertheless, the mechanism of deuteron acceleration is not entirely clear. The GIT-12 generator delivers the electric pulse with a maximum voltage of 600 kV only (considering 50 kV capacitor charging). On the other hand, the multi-MeV deuterons[6] should be accelerated by the corresponding voltage. Thus, such voltage must have been related to some effects of the Z-pinch plasma. The explanation of this phenomena is important not only for the Z-pinch neutron sources research but it could be important for high-energy density physics generally. Therefore, this thesis is devoted to the precise neutron diagnostics which allows the evaluation of neutron yields, spectra, anisotropy, etc., and interpretation of the obtained experimental data in order to contribute to the explanation of the phenomena of the ion acceleration and neutron production.

[6] At the shots with natural hydrogen gas-puff the multi-MeV protons were observed too.

Chapter 3

Basic Z-Pinch Models

This chapter is devoted to the theoretical background. This background includes the basic models and physics of the Z-pinches.

3.1 Equilibrium Z-Pinch

3.1.1 Bennett Equilibrium

The Bennett equilibrium is one of the basic theories of Z-pinches. It describes the situation when a current flows axially through the steady-state plasma cylinder (Z-pinch) which is in the pressure equilibrium. At the real Z-pinch, such a situation usually occurs only for a very short time.

The following derivation is based on paper [20]. If the plasma is in the pressure balance, the forces induced by the thermodynamic and magnetic pressure are equal, thus

$$\nabla P = \mathbf{j} \times \mathbf{B}. \tag{3.1}$$

The relation between magnetic field $\mathbf{B}$ and current density $\mathbf{j}$ is given by the Ampere's law. Assuming a constant current we neglected the displacement current:

$$\nabla \times \mathbf{B} = \mu_0 \mathbf{j}, \tag{3.2}$$

where μ_0 is the permeability of vacuum. Using the cylindrical coordinates and assuming only j_z the axial component of the $\mathbf{j}$ we obtain

$$\frac{1}{r}\frac{\partial}{\partial r}\left(rB_\theta\right) = \mu_0 j_z. \tag{3.3}$$

Obviously, the azimuthal component of the magnetic field B_θ is given by integration of (3.3)

$$B_\theta(r) = \frac{\mu_0}{r}\int_0^r j_z r' \,\mathrm{d}r'. \tag{3.4}$$

Combining (3.1) and (3.4) we obtain

$$\frac{\partial P}{\partial r} = -\frac{\mu_0 j_z}{r}\int_0^r j_z r' \,\mathrm{d}r'. \tag{3.5}$$

The ion linear density[1] N_i of the plasma cylinder is defined by

$$N_i = \int_0^R 2\pi n_i r \,\mathrm{d}r, \tag{3.6}$$

where R is the radius of the plasma cylinder and an n_i ion density. Then, the equation of state is following

$$N_i k_B \left(ZT_e + T_i\right) = \int_0^R 2\pi P r \,\mathrm{d}r, \tag{3.7}$$

where k_B is the Boltzmann's constant, Z is the atomic number, and T_e and T_i are the electron and ion average temperatures, respectively. Integration by parts of equation (3.7) gives

$$N_i k_B \left(ZT_e + T_i\right) = \left[2\pi P\frac{r^2}{2}\right]_0^R - \pi\int_0^R r^2\frac{\partial P}{\partial r}\,\mathrm{d}r. \tag{3.8}$$

Assuming that the magnetic pressure on the surface and axis of the plasma cylinder (pinch) is equal to zero ($P(R) = 0$ and $P(0) = 0$) equation (3.8) becomes

$$N_i k_B \left(ZT_e + T_i\right) = -\pi\int_0^R r^2\frac{\partial P}{\partial r}\,\mathrm{d}r. \tag{3.9}$$

Employing equation (3.5) in equation (3.9) we obtain

$$N_i k_B \left(ZT_e + T_i\right) = \pi\mu_0\int_0^R \left(j_z r\int_0^r j_z r' \mathrm{d}r'\right)\mathrm{d}r. \tag{3.10}$$

Equation (3.10) can be modified, as follows:

$$N_i k_B \left(ZT_e + T_i\right) = \frac{\mu_0}{4\pi}\int_0^R \left(2\pi r j_z\int_0^r 2\pi r' j_z \mathrm{d}r'\right)\mathrm{d}r. \tag{3.11}$$

[1] In this case, the linear density is in number of particles per length unit and density in number of particles per volume unit. Perhaps a more exact word is concentration, but in this case the density and linear density are the established terms.

Consequently, we obtain

$$N_i k_B \left(ZT_e + T_i\right) = \frac{\mu_0}{4\pi} \int_0^R 2\pi r j_z \left[\pi r'^2 j_z\right]_0^r \mathrm{d}r, \tag{3.12}$$

$$N_i k_B \left(ZT_e + T_i\right) = \frac{\mu_0}{4\pi} \int_0^R 2\pi^2 j_z^2 r^3 \mathrm{d}r. \tag{3.13}$$

Integration of formula (3.13) gives

$$N_i k_B \left(ZT_e + T_i\right) = \frac{\mu_0}{4\pi} \left[\pi^2 j_z^2 \frac{r^4}{2}\right]_0^R = \frac{\mu_0}{4\pi} \frac{1}{2} \pi^2 j_z^2 R^4. \tag{3.14}$$

$$2N_i k_B \left(ZT_e + T_i\right) = \frac{\mu_0}{4\pi} (j_z \pi R^2)^2. \tag{3.15}$$

Since for constant j_z the total current is $I = j_z \pi R^2$, we obtain the Bennett relation

$$2N_i k_B \left(ZT_e + T_i\right) = \frac{\mu_0}{4\pi} I^2, \tag{3.16}$$

Thus, the average temperature of the equilibrium Z-pinch could be calculated knowing only the line density and current [20].

3.1.2 Pease-Braginskii Equilibrium

Whereas the Bennett equilibrium describes the pressure stability, the Pease-Braginskii equilibrium is related to the radiative energy losses. The Z-pinch is in steady-state equilibrium if the total radiative energy losses are equal to the energy released by the ohmic heating [6]. If the ohmic heating exceeds the radiative cooling, the Z-pinch will expand, and vice versa. In the hydrogen and deuterium plasma (this is the case of this thesis) the dominant energy losses are caused by the bremsstrahlung [6, 20]. The bremsstrahlung loss rate P_B per unit volume V is given by [20]

$$\frac{P_B}{V} = \beta_b Z n_e^2 \sqrt{T_e}, \tag{3.17}$$

where β_b is a constant equal to $1.69 \times 10^{-38}\,\mathrm{W\,m^3\,(eV)^{1/2}}$ and Z is the atomic number. The ohmic heating per unit volume is given by

$$\frac{P_j}{V} = \eta_\perp j^2, \tag{3.18}$$

where $\eta_\perp$ the plasma conductivity transverse to the magnetic field is given by the Spitzer formula:

$$\eta_\perp \approx \frac{1}{(4\pi\epsilon_0)^2} \frac{\pi Z^2 \sqrt{m_e}}{(k_B T_e)^{3/2}} \ln(\Lambda), \tag{3.19}$$

where m_e is the electron mass and Λ is the Coulomb logarithm defined as

$$\Lambda = \langle \lambda_D / r_0 \rangle, \tag{3.20}$$

where r_0 is the minimum of the distance between two colliding electrons. Assuming the uniform current density j, the equilibrium occurs if the Z-pinch current I is equal to the Peas-Braginskii current I_{PB} defined as [20]

$$I_{PB} = \frac{8\sqrt{3}k_B}{\mu_0\sqrt{\alpha\beta_b}}\frac{1+Z}{2Z} \approx 0.433\sqrt{\ln(\Lambda)}\left(\frac{1+\langle Z\rangle}{2\langle Z\rangle^{1/2}}\right) \text{ MA}, \tag{3.21}$$

where

$$\alpha = \left(1.03 \times 10^{-4} Z \ln(\Lambda)\right)^{-1}. \tag{3.22}$$

3.2 Dynamic Z-pinch

In this section, snowplow and slug models of the Z-pinch implosion are described. These models consider an implosion of plasma or gas cylindrical column with initially uniform density distribution like the gas-puff load in experiments presented in this thesis[2]. In both models, we assume that the current flows in an infinitesimal skin layer which acts as a piston [20, 24]. The fundamental difference between the snowplow and slug models is that in the case of snowplow model a strong plasma radiation is considered, whereas in the case of slug model a plasma radiation is neglected [24].

Therefore, the slug model is relevant for Z-pinch loads with a low atomic number, especially for deuterium or tritium gas-puffs. In the case of Z-pinch loads with a higher atomic number, the snowplow model is more suitable [24]. Since in the experiments presented in this thesis the deuterium gas-puff is used, the slug model is more important. For example, it is used for estimation of the mass of the imploding gas-puff. For clarity, the earlier and simpler snowplow model is described as well.

3.2.1 Snowplow Model

The snowplow model is the earliest zero-dimensional model which describes an implosion of strongly radiating plasma. This model was firstly published by Rosenbluth

[2]The snowplow and slug models could be used not only for gas-puffs bud also for various Z-pinch implosions with initially uniform density distribution like gas-embedded Z-pinches, foam cylinders, etc. [20, 24]

in 1955 in [69]. In the snowplow model, we assume a gas or plasma column of a cylindrical shape and a current which flows in an infinitesimal cylindrical skin layer with infinite conductivity. The layer radially implodes toward the z-axis due to the pinch effect and during the implosion, it swept up and accumulate the gas or plasma like a piston. Thus, the mass of the imploding layer is increased. The equation of motion is following

$$\mathbf{f}(t) = \frac{\mathrm{d}}{\mathrm{d}t}\left[m_l(t)\mathbf{v}(t)\right] = \frac{\mathrm{d}}{\mathrm{d}t}\left\{\rho_0\pi\left[R_0^2 - R^2(t)\right]\frac{\mathrm{d}\mathbf{R}(t)}{\mathrm{d}t}\right\} = -\frac{\mathbf{j}(t)\times\mathbf{B}(t)}{l_z}. \tag{3.23}$$

Where $\mathbf{f}$ is the force acting on the length element of the Z-pinch, $m_l(t)$ is the linear mass of the layer, $\mathbf{v}(t)$ is the layer velocity, ρ_0 is the mass density of the gas or plasma cylindrical column, $R(t)$ and R_0 are the radius and initial radius of the layer, respectively, $\mathbf{j}$ is the current density, $\mathbf{B}$ is the magnetic field, and l_z is the pinch length. Assuming that the layer is moving only in radial direction, the current flows only axially, and the magnetic field is only azimuthal, the equation of motion (3.23) could be simplified:

$$\frac{\mathrm{d}}{\mathrm{d}t}\left\{\rho_0\pi\left[R_0^2 - R^2(t)\right]\frac{\mathrm{d}R(t)}{\mathrm{d}t}\right\} = -\frac{\mu_0 I(t)^2}{4\pi R(t)}. \tag{3.24}$$

The general analytic solution of this second-order nonlinear ordinary differential equation has not been found. To solve equation (3.24), we will assume the linearly rising current, which is the approximation of a capacitor-inductor circuit discharge current [20]:

$$I = I_0\sin(\omega t) \approx I_0\omega t \equiv At, \tag{3.25}$$

where A is a constant. Using substitution

$$x = R(t)/R_0, \tag{3.26}$$

$$y = t/\tau_0, \tag{3.27}$$

where

$$\tau_0 = (4\pi^2\rho_0 R_0^4/\mu_0 A^2)^{1/4}, \tag{3.28}$$

we obtain the dimensionless equation of motion

$$\frac{\mathrm{d}}{\mathrm{d}y}\left\{\left[1 - x^2(y)\right]\frac{\mathrm{d}x(y)}{\mathrm{d}y}\right\} = -\frac{y^2}{x}. \tag{3.29}$$

The equation (3.29) can be integrated for the boundary conditions $x = 1$ and $\mathrm{d}x/\mathrm{d}y = 0$ at $y = 0$. The assumed form of the solution is

$$x = 1 - \sum_{n=1} a_{2n} y^{2n}, \tag{3.30}$$

where $a_2 = 1/\sqrt{12}$, $a_4 = 11/360$, etc, and a solution of the series (3.30) can be found [20]. The different solution of the snowplow model could be found in literature, for example, the constant current assumption is used in book [6], or approximation of the Z-pinch current by $I \approx I_{max}(\pi t/2\tau)^2$ is presented in Ryutov's review [24]. Despite the fact that the snowplow model is very simple, instabilities, etc., in many cases gives sufficient information.

3.2.2 Slug model

The slug model is zero-dimensional model devised by Potter [70]. In this model, the magnetic piston is also assumed in position $R_p(t)$ and at the same time, a very thin shock is in position $R_s(t) < R_p(t)$. The shock velocity v_s is higher than the piston velocity v_p. As well as in the case of the snowplow model, the uniform initial density ρ_0 and pressure p_0 are assumed. The relationship between the states on both sides of a shock wave in a one-dimensional flow in fluids is described by the Rankine-Hugoniot conditions [70]:

$$v_p = \frac{2}{\gamma + 1} v_s, \tag{3.31}$$

$$\rho_s = \frac{\gamma + 1}{\gamma - 1} \rho_0, \tag{3.32}$$

$$p_s = \frac{2}{\gamma + 1} \rho_0 v_s^2, \tag{3.33}$$

where γ is the Poisson constant (heat capacity ratio), ρ_s and p_s are the density and pressure immediately behind the shock, respectively. Between the moving shock and piston, there exists a compressed finite volume of hot plasma [70]. The time of sound propagation between the shock and piston given by formula

$$\tau_{sound} \approx \frac{r_p - r_s}{\sqrt{\dfrac{\gamma p_s}{\rho_s}}} = \frac{r_p - r_s}{\sqrt{\dfrac{2\gamma(\gamma - 1)}{(\gamma + 1)^2}}} \tag{3.34}$$

is much smaller than the Z-pinch implosion time given by

$$\tau_{imp} \approx \frac{R_0}{\langle v_s \rangle}. \tag{3.35}$$

Thus during the implosion, the sound waves propagate between the shock and the piston. Therefore, in this compressed region with volume $V(t)$, the spatially uniform pressure $p_s(t)$ could be assumed [70]. During the implosion, the pressure is changing in accordance with the adiabatic law:

$$p_s V^\gamma = const., \tag{3.36}$$

or,

$$\gamma p_s \, \mathrm{d}V + V \, \mathrm{d}p_s = 0, \tag{3.37}$$

where the pressure p_s is defined by the condition (3.33), thus

$$\mathrm{d}p = 2\frac{\mathrm{d}v_s}{v_s} p_s. \tag{3.38}$$

Obviously, the volume of the compressed region V bordered by shock and the piston is given by

$$V = \pi \left(R_p^2 - R_s^2 \right) \, l_z, \tag{3.39}$$

where l_z is the discharge length. A differential $\mathrm{d}V$ is given by consideration presented in Potter's paper [70]: "In considering the change of volume according to the adiabatic law (3.37), we must instantaneously refer to a fixed mass of gas. The plasma velocity relative to the piston is zero so that the piston position R_p is fixed in the Lagrangian frame. This is not true at the shock R_s through which the plasma moves. Thus, for a fixed mass instantaneously

$$\mathrm{d}V = 2\pi \left(R_p \, \mathrm{d}R_p - R_s \, \mathrm{d}\hat{R}_s \right) \, l_z. \tag{3.40}$$

where $\mathrm{d}\hat{R}_s$ is the change in the radius of the plasma evaluated at the shock. This is defined by the plasma velocity us at the shock relative to the shock velocity"[3]:

$$\mathrm{d}\hat{R}_s = \frac{2}{\gamma + 1} \, \mathrm{d}R_s \tag{3.41}$$

[3]The mathematical symbols in the cited text are changed to be consistent with other formulas in this thesis.

Using the formulas (3.38)-(3.41) in equation (3.37) we can express the boundary conditions at the shock [70]:

$$R_p \,\mathrm{d}R_p - \frac{2R_s}{\gamma+1}\mathrm{d}R_s + \frac{1}{\gamma\, v_s}\left(R_p^2 - R_s^2\right)\,\mathrm{d}v_s = 0. \tag{3.42}$$

As mentioned above, the uniform pressure between the shock and piston is assumed. Thus, the pressure behind the shock given by formula (3.33) must be equal to the magnetic pressure of the piston which carries the current I:

$$\frac{2}{\gamma+1}\,\rho_0 v_s^2 = \frac{\mu_0 I^2}{8\pi^2 R_p^2}, \tag{3.43}$$

thus,

$$v_s = \sqrt{\frac{\mu_0}{\rho_0}}\sqrt{\gamma+1}\,\frac{I}{4\pi R_p} \tag{3.44}$$

As well as in the case of the snowplow model the general solution of the slug model equation (3.44) has not been found. Considering the constant current I, a combination of equations (3.42) and (3.44) gives:

$$\left[\frac{\gamma-1}{\gamma} + \frac{1}{\gamma}\frac{R_s^2}{R_p^2}\right]\,\mathrm{d}R_p = \frac{2}{\gamma+1}\frac{R_s}{R_p}\,\mathrm{d}R_s. \tag{3.45}$$

Solving the equation (3.45) with the initial radius $R_s(t=0) = R_p(t=0) = R_0$, we obtain following formula [70]

$$R_p = R_0\left(\frac{\gamma}{\gamma+1-\frac{R_s^2}{R_p^2}}\right)^{\gamma/(\gamma-1)}. \tag{3.46}$$

If any shock reflections are not assumed, the final (minimum) pinch radius R_m is achieved when the shock radius is equal to zero, using (3.46) we obtain:

$$R_m = R_p(R_s=0) = R_0\left(\frac{\gamma}{\gamma+1}\right)^{\gamma/(\gamma-1)}. \tag{3.47}$$

Thus, the minimum pinch radius is defined only by the initial radius R_0 and ratio of specific heats γ. We note that for the ratio of specific heats of ideal monoatomic gas is $\gamma = 5/3$, the final radius achieves $R_m \doteq 0.3\,R_0$, thus the compression is very weak [70]. Different consideration is presented by S. Lee in [83, 84] where the shock reflection is assumed and the final pinch radius R_m is achieved when the piston meets the reflected shock. In such a case the predicted minimum pinch radius is $R_m \doteq 0.14\,R_0$.

Chapter 4

Nuclear Fusion Neutrons

The key topic of this thesis is the diagnostics and study of the neutrons produced by the nuclear fusion reactions which occur in the dense Z-pinch discharges. Therefore, the nuclear fusion reactions are briefly introduced in this section.

As far as the definition of the nuclear fusion is concerned, we could find several definitions. For example, in [71] the definition says "Nuclear fusion, process by which nuclear reactions between light elements form heavier elements (up to iron). In cases where the interacting nuclei belong to elements with low atomic numbers (e.g., hydrogen [atomic number 1] or its isotopes deuterium and tritium), substantial amounts of energy are released.". A very good example of exoenergetic fusion reactions can be found in stars. In stars with the size of the Sun or smaller, the reactions from the proton-proton chain which produces deuterium and helium dominate [72]. In bigger stars, the dominant energy-producing process is the carbon cycle (carbon-nitrogen-oxygen or CNO) [72]. Other elements are produced during the final stages of stars and their explosions. The heavier elements are formed by the supernova explosions. As far as the nuclear fusion on Earth is concerned, in laboratories, we can meet various reactions usually based on interactions of isotopes of hydrogen, helium, lithium, boron, etc. In plasma physics, probably the biggest emphasis is put on the D(d,n)^{3}He, D(d,p)T and T(d,n)^{4}He reactions[1]

$$\mathrm{D} + \mathrm{D} \rightarrow {}^3\mathrm{He} + \mathrm{n}\,(Q = 3.27\,\mathrm{MeV}), \tag{4.1}$$

$$\mathrm{D} + \mathrm{D} \rightarrow \mathrm{T} + \mathrm{p}\,(Q = 4.03\,\mathrm{MeV}), \tag{4.2}$$

[1]The established formulation of the nuclear reactions is generally A(a,b)B where A is a target nucleus, a is a projectile particle, b is an ejectile particle, and B is the final nucleus.

$$\mathrm{D} + \mathrm{T} \rightarrow^{4} \mathrm{He} + \mathrm{n}\,(Q = 17.59\,\mathrm{MeV}). \tag{4.3}$$

The total cross-sections of the reactions (4.1)-(4.3) are displayed in fig. 4.1. This

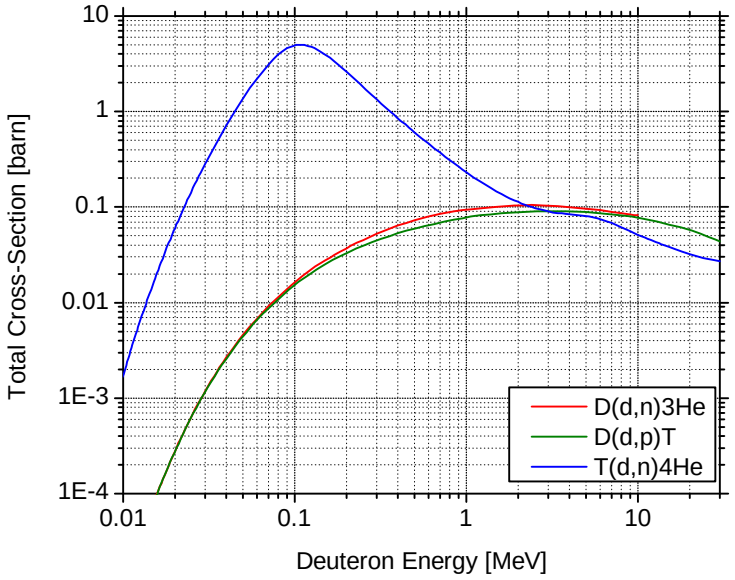

Figure 4.1: The total cross-sections of the D(d,n)^{3}He, D(d,p)T and T(d,n)^{4}He reactions.

thesis is mostly devoted to the measurement of neutrons produced from the reaction (4.1), this reaction is described in more detail in the following sections.

4.1 Energy of dd Neutrons

In D(d,n)^{3}He reaction, the energy of the ejectile neutron is dependent on the reaction energy Q ("Q-value"), projectile deuteron velocity v_d, and angle between the trajectory of the ejectile neutron and direction of the projectile deuteron (see fig. 4.2). The kinetics of the reaction (4.1) in the laboratory frame of reference is illustrated in fig. 4.2. In the laboratory system (see fig. 4.2(a)), where the zero target particle velocity is assumed and v_d is equal to the projectile deuteron energy, the energy balance of the reaction (4.1) is

$$E_d + Q = E_n + E_{He}. \tag{4.4}$$

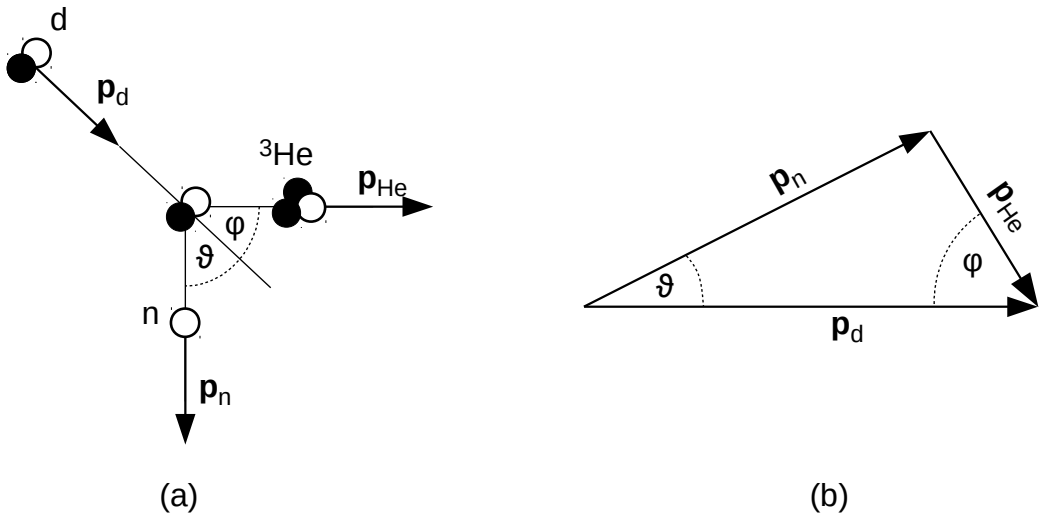

Figure 4.2: Kinetics of the D(d,n)^{3}He reaction in the laboratory frame of reference.

The energy of helium nucleus E_{He} is possible to express by its momentum p_{He}:

$$E_n + \frac{p_{He}^2}{2m_{He}} - E_d - Q = 0, \tag{4.5}$$

Where m_{He} is the mass of the helium nucleus. The law of the conservation of momentum gives

$$\mathbf{p_d} = \mathbf{p_n} + \mathbf{p_{He}}, \tag{4.6}$$

where $\mathbf{p_d}$, $\mathbf{p_n}$,, and $\mathbf{p_{He}}$ are momenta of the projectile deuteron, neutron, and helium nuclei, respectively. In accordance with fig. 4.2(b) we express equation (4.6) by the cosine law

$$p_{He}^2 = p_n^2 + p_d^2 - 2p_n p_d \cos(\vartheta). \tag{4.7}$$

Substituting helium nucleus momentum in (4.5) by (4.7) we obtain

$$E_n + \frac{p_n^2 + p_d^2 - 2p_n p_d \cos(\vartheta)}{2m_{He}} - E_d - Q = 0, \tag{4.8}$$

$$E_n + \frac{p_n^2}{2m_{He}}\frac{m_n}{m_n} + \frac{p_d^2}{2m_{He}}\frac{m_d}{m_d} - 2\frac{2p_n p_d}{\sqrt{2}\sqrt{2}\,m_{He}}\frac{\sqrt{m_n}}{\sqrt{m_n}}\frac{\sqrt{m_d}}{\sqrt{m_d}}\cos(\vartheta) - E_d - Q = 0, \tag{4.9}$$

$$E_n\left(1 + \frac{m_n}{m_{He}}\right) - 2\frac{\sqrt{E_d m_d m_n}}{m_{He}}\sqrt{E_n}\cos(\vartheta) - E_d\left(1 - \frac{m_d}{m_{He}}\right) - Q = 0, \tag{4.10}$$

where m_n and m_d are the ejectile neutron and projectile deuteron mass, respectively. The solution of the quadratic equation (4.10) with the variable $\sqrt{E_n}$ gives the neutron energy

$$[E_n(E_d,\vartheta)]_{1,2} = \left[\frac{\sqrt{E_d m_d m_n}}{m_{He}+m_n}\cos(\vartheta) \pm \right.$$

$$\left. \pm \sqrt{\frac{E_d m_d m_n}{(m_{He}+m_n)^2}\cos^2(\vartheta) + \frac{E_d(m_{He}-m_d)+Qm_{He}}{m_{He}+m_n}}\right]^2, \quad (4.11)$$

$$[E_n(E_d,\vartheta)]_{1,2} = \frac{E_d m_d m_n}{(m_{He}+m_n)^2}\left[\cos(\vartheta) \pm \right.$$

$$\left. \pm \sqrt{\cos^2(\vartheta) + \frac{E_d(m_{He}-m_d)(m_{He}+m_n)+Qm_{He}(m_n+m_{He})}{E_d m_d m_n}}\right]^2, \quad (4.12)$$

$$[E_n(E_d,\vartheta)]_{1,2} = \frac{E_d m_d m_n}{(m_{He}+m_n)^2}\left[\cos(\vartheta) \pm \right.$$

$$\left. \pm \sqrt{\cos^2(\vartheta) + \frac{E_d m_{He}(m_{He}+m_n-m_d)-E_d m_d m_n+Qm_{He}(m_n+m_{He})}{E_d m_d m_n}}\right]^2, \quad (4.13)$$

$$[E_n(E_d,\vartheta)]_{1,2} = \frac{E_d m_d m_n}{(m_{He}+m_n)^2}\left[\cos(\vartheta) \pm \right.$$

$$\left. \pm \sqrt{\cos^2(\vartheta) - 1 + \frac{E_d m_{He}(m_{He}+m_n-m_d)+Qm_{He}(m_n+m_{He})}{E_d m_d m_n}}\right]^2. \quad (4.14)$$

The sign $\pm$ before the square root does not mean that there are two possible energies of the ejectile neutron. The sign $\pm$ is the consequence of the derivation, where the energy E_d without any knowledge about the orientation of the collision has been used. Assuming that the deuteron before the collision flies in the direction towards the direction of the neutron detection, the sign + is valid [88].

Using formula $\sin^2(\vartheta) + \cos^2(\vartheta) = 1$ we obtain

$$E_n(E_d, \vartheta) = \frac{E_d m_d m_n}{(m_{He} + m_n)^2} \left[\cos(\vartheta) + \right.$$

$$\left. + \sqrt{\frac{E_d m_{He}(m_{He} + m_n - m_d) + Q m_{He}(m_n + m_{He})}{E_d m_d m_n} - \sin^2(\vartheta)} \right]^2 . \qquad (4.15)$$

The dependence of neutron energy (4.15) is displayed in fig. 4.3 and fig. 4.4.

4.2 Angular Distribution of dd Neutrons

The angular distribution of the neutron fluence produced by the deuterium Z-pinch is depended on the differential cross-section of the D(d,n)^{3}He reaction and on the angular and energy distribution of the deuterons. The differential cross-sections of D(d,n)^{3}He reaction are displayed in fig. 4.5. These cross-sections are exported from the DROSG-2000 database [73]. The distribution of the neutrons with energy of about 2.5 MeV is close to the isotropic distribution, since such neutrons are produced by the deuterons with a significantly lower energy than the Q-value of the D(d,n)^{3}He reaction (see fig. 4.3), where the cross-section is weakly dependent on the ejectile angle (see fig. 4.5). At the same time, the low-energy deuterons are deflected to all directions by the magnetic field of the Z-pinch. In contrast, the emission of the fast neutrons with an energy considerably higher than 2.5 MeV is significantly anisotropic. Such neutrons are produced by the collisions of the fast deuterons with an energy above 1 MeV. In such a case, the reaction cross-section is strongly dependent on the ejectile angle. Moreover, the deuterons are not so much affected by the magnetic field. Thus, it is assumed, that the most of such fast deuterons move more directly or they are affected just weakly in dependence on the magnetic field strength. At the experiments described in this thesis a large number of the neutrons with an energy significantly higher than 2.5 MeV are produced, thus their anisotropy should be taken into account.

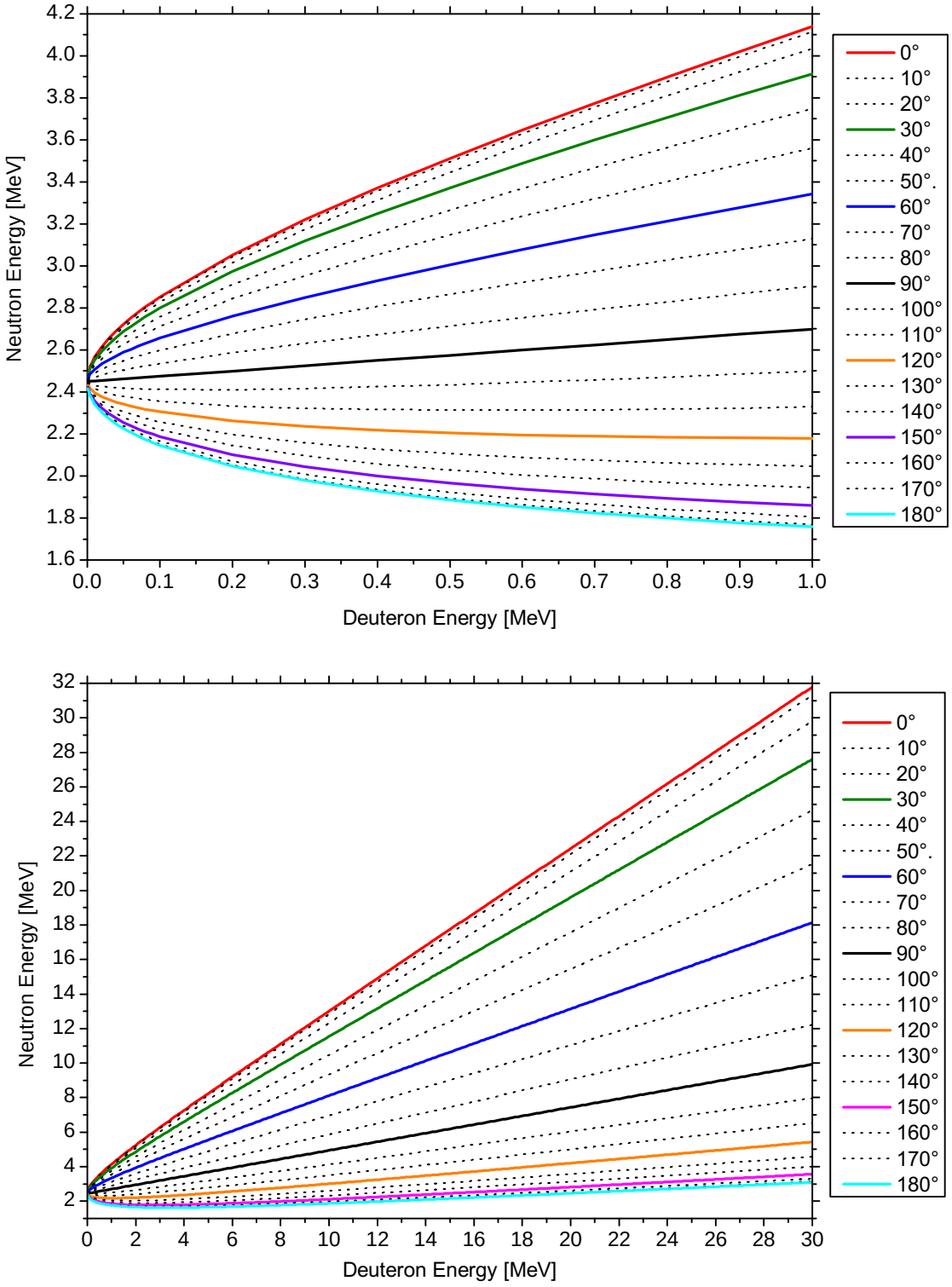

Figure 4.3: The dependence of dd neutron energy on the deuteron energy for several deuteron ejectile angles.

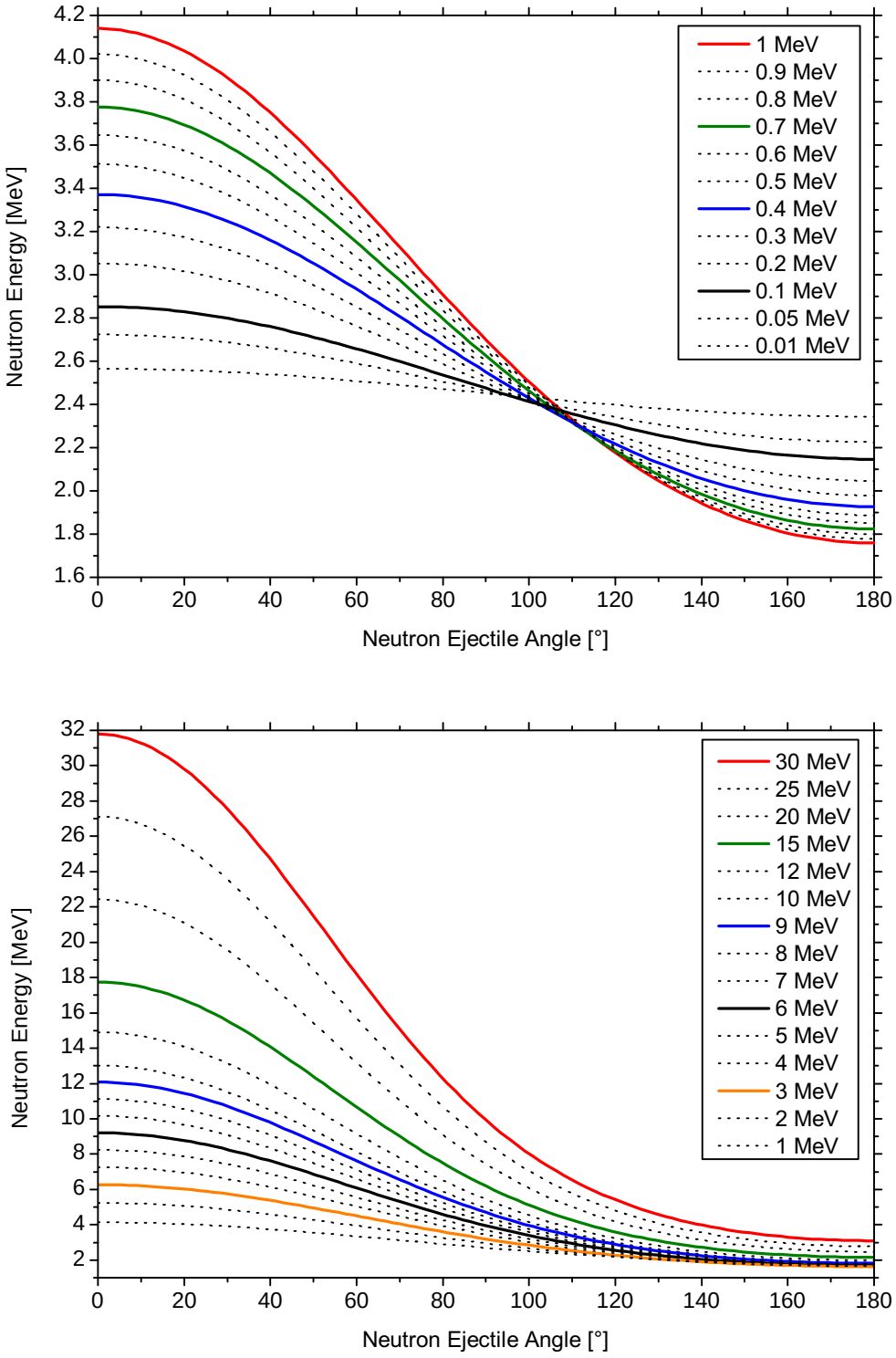

Figure 4.4: The dependence of dd neutron energy on the neutron ejectile angle for several deuteron energies.

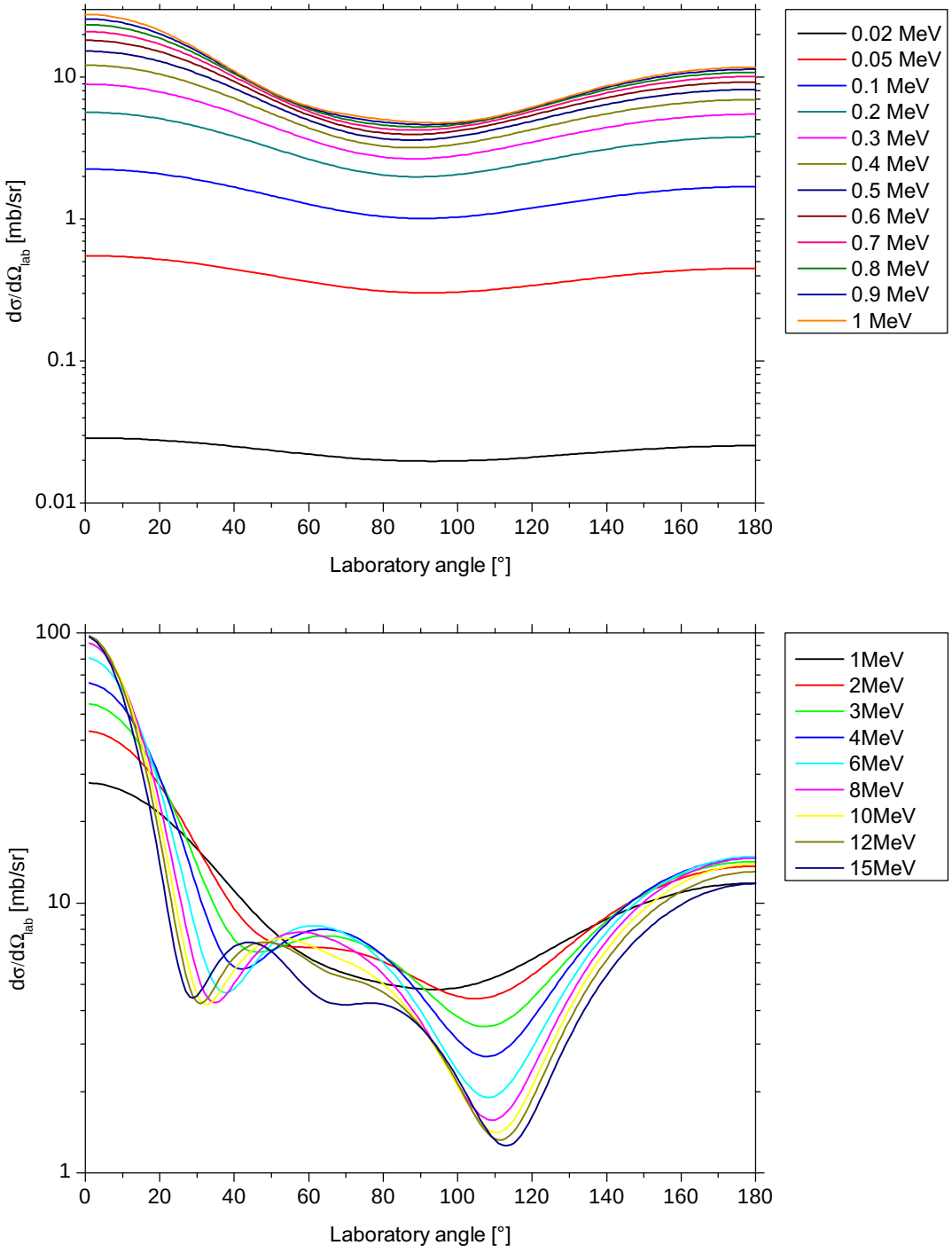

Figure 4.5: The differential cross-sections of D(d,n)^{3}He reaction for several deuteron energies in the laboratory system of coordinates [73].

Chapter 5

Radiation Interactions

The subject of this thesis is devoted to the diagnostics of high energy density plasmas using neutron and gamma-ray detectors. Knowledge of the radiation interactions and their principles are crucial for design and setup of the diagnostics, processing of the measured data, and physical interpretation. In this chapter, the basic interactions of photons and neutrons with a matter are briefly described.

5.1 Interactions of Photons

The photons detected in a frame of this work are of the gamma-ray, annihilation or bremsstrahlung origin and their energy is in the range of approximately (0.2-2) MeV[1]. In such a case the only photon interactions which we take into account are the photoelectric effect (photoelectric absorption), Compton effect (Compton scattering), pair production and photonuclear excitation, although other photon interactions are known.

5.1.1 Photoelectric Effect

In the photoelectric effect, the photon is completely absorbed by one electron bounded in an atom. The electron is ejected from its shell and escapes the atom. The energy of this emitted electron (photoelectron) is given by difference between the original

[1]Sometimes all photons in such energy range are considered as the gamma-ray photons, but correctly the gamma photons are only the photons emitted by a nucleus.

photon energy $h\nu$ and the binding energy E_B of the electron in its original shell

$$E_e = h\nu - E_B. \tag{5.1}$$

The vacancy in the shell of the original electron is filled by the capture of a free electron from the medium or rearrangement of electrons from other shells. Therefore, one or more characteristics X-ray photons may be emitted [92]. The photoelectric effect predominates up to the photon energy of a few hundred keV in dependence on an atomic number of an absorber material (see fig. 5.1).

5.1.2 Compton Effect

The Compton effect occurs when the incoming photon is deflected and part of its energy is transferred to a recoil electron. In accordance with the law of conservation of energy, E_{ke} kinetic energy of the recoil electron is given by

$$E_{ke} = h\nu - h\nu', \tag{5.2}$$

where $h\nu$ is the incoming photon energy and $h\nu'$ is the energy of the photon after the collision. The total energy of the recoil electron is represented by the relativistic energy-momentum relation:

$$E_e = \sqrt{m_0^2c^4 + p_e^2c^2}, \tag{5.3}$$

where m_0 is the rest mass of the electron, c is the light velocity, and p_e is the recoil electron momentum. At the same time, the total energy of the recoil electron is given by its rest energy before the collision $E_{e0} = m_0c^2$ increased by the E_{ke} kinetic energy transferred from the incoming photon. Thus, combining the above-mentioned formulas we obtain:

$$E_e = \sqrt{m_0^2c^4 + p_e^2c^2} = m_0c^2 + h\nu - h\nu'. \tag{5.4}$$

Square and modification of this equation [93] give:

$$p_e^2c^2 = (h\nu)^2 + (h\nu')^2 - 2(h\nu)(h\nu') + 2(h\nu)m_0c^2 - 2(h\nu')m_0c^2. \tag{5.5}$$

The p_e^2 is possible to express with help of the scalar product

$$p_e^2 = \mathbf{p}_e \cdot \mathbf{p}_e. \tag{5.6}$$

In accordance with the conservation of momentum, the momentum of electron $\mathbf{p}_e$ is given by difference of the incoming photon momentum $\mathbf{p}_{h\nu}$ and momentum of the photon after the collision $\mathbf{p}_{h\nu'}$

$$\mathbf{p}_e = \mathbf{p}_{h\nu} - \mathbf{p}_{h\nu'}. \tag{5.7}$$

Thus,

$$p_e = \mathbf{p}_e \cdot \mathbf{p}_e = (\mathbf{p}_{h\nu} - \mathbf{p}_{h\nu'}) \cdot (\mathbf{p}_{h\nu} - \mathbf{p}_{h\nu'}) = p_{h\nu}^2 + p_{h\nu'}^2 - 2p_{h\nu}p_{h\nu'}\cos(\vartheta), \tag{5.8}$$

where ϑ is the photon scattering angle. Multiplying this equation by square of the light velocity we obtain

$$p_e^2c^2 = p_{h\nu}^2c^2 + p_{h\nu'}^2c^2 - 2p_{h\nu}p_{h\nu'}c^2\cos(\vartheta). \tag{5.9}$$

Since $p_\nu c = h\nu$ and $p_{\nu'}c = h\nu'$, the equation (5.9) becomes

$$p_e^2c^2 = (h\nu)^2 + (h\nu')^2 - 2(h\nu)(h\nu')\cos(\vartheta). \tag{5.10}$$

The combination of the equations (5.5) and (5.10) gives

$$(h\nu)(h\nu') - (h\nu)m_0c^2 + (h\nu')m_0c^2 = (h\nu)(h\nu')\cos(\vartheta). \tag{5.11}$$

Modifying the expression (5.11) we obtain the scattered photon energy [92]:

$$h\nu' = \frac{h\nu}{1 + \dfrac{h\nu}{m_0c^2}(1 - \cos(\vartheta))} \tag{5.12}$$

As far as the probability of the Compton collision per atom is concerned, the differential scattering cross-section $\mathrm{d}\sigma/\mathrm{d}\Omega$ is predicted by the Klein-Nishina formula [92]:

$$\frac{\mathrm{d}\sigma}{\mathrm{d}\Omega} = Zr_0^2\left(\frac{1}{1+\alpha(1-\cos(\vartheta))}\right)^2\left(\frac{1+\cos^2(\vartheta)}{2}\right)\left(1 + \frac{\alpha^2(1-\cos(\vartheta))^2}{(1+\cos^2(\vartheta))(1+\alpha(1-\cos(\vartheta)))}\right), \tag{5.13}$$

where $\alpha \equiv h\nu/m_0c^2$ [92] and $r_0 = (1/4\pi\varepsilon_0)(e^2/m_0c^2) \doteq 2.81794 \times 10^{-15}$ m is the classical electron radius [94].

5.1.3 Pair Production

The production of the electron-positron pair is energetically possible if the interacting photon exceeds twice the electron rest-mass energy ($2 \times 0.511 = 1.022$ MeV). However, the pair production is significant if the photon energy $h\nu$ is much higher than the energetic threshold. This interaction occurs in the field of nuclei[2], the photon is completely absorbed and its energy is converted into the rest mass energy ($2m_0c^2$), kinetic energy E_{pp} of the electron-positron pair, and energy of the recoil nuclei. The energy and momentum transfer to the recoil nuclei is necessary to satisfy the law of conservation of the energy and momentum. However, the recoil nuclei energy and momentum is small. Thus, if we neglect recoil nuclei energy transfer, the kinetic energy of the electron-positron is [99, 100]

$$E_{pp} = h\nu - 2m_0c^2. \tag{5.14}$$

The produced positron is subsequently annihilated and two 511 keV annihilation photons are emitted. Also, the interaction of the annihilation radiation with matter is the important effect in the gamma-ray spectroscopy.

As far as the probability of the pair production per nucleus is concerned, no simple and exact formula exists [92]. We note only that this probability rises with the square of the atomic number of the interacting nuclei and also sharply rises with the original photon energy [92].

5.1.4 Interactions within Detector

All the introduced photon interactions (photoelectric effect, Compton effect, and pair production) occur in the photon detectors which are presented in this thesis. The relative importance of these effects is dependent on the photon energy and the absorber (detector) material.

The intensity of incident radiation is

$$I = \phi\, h\nu, \tag{5.15}$$

where ϕ is a number of primary photons per time unit (radiation flux) and $h\nu$ their energy [101]. In passing a distance dx within the absorber, the number of primary

[2]The pair production could occur also in the field of an electron, but the probability is much lower [99, 100]

photons suffering collisions is

$$d\phi = \phi\,\mu\,\mathrm{d}x, \tag{5.16}$$

where μ is the total linear attenuation coefficient [101]. Solution of this equation is as follows

$$\phi = \phi_0\, e^{-\mu d} \tag{5.17}$$

and

$$I = I_0\, e^{-\mu d}, \tag{5.18}$$

where ϕ_0 is the initial radiation flux, I_0 is the initial intensity of the radiation, and d is a passed distance in the detector. The total linear attenuation coefficient consists of all above-mentioned interactions of photons with matter [92, 99, 101]:

$$\mu = \tau + \sigma + \kappa \tag{5.19}$$

where τ is the photoelectric linear attenuation coefficient, σ is the Compton linear attenuation coefficient and κ is the pair production linear attenuation coefficient [101]. The Compton linear attenuation coefficient is given by σ_a and σ_s Compton linear absorption coefficient and Compton linear scattering coefficient, respectively [101]

$$\sigma = \sigma_a + \sigma_s. \tag{5.20}$$

As shown in fig. 5.1, each of linear attenuation components depends on the energy of the photons and material of the detector [101]. At low energies of the photons the photoelectric linear attenuation dominates, but it decreases rapidly with increasing energy and grows with the atomic number Z. However, at heavy elements, τ may be still significant up to photon energy of a few MeV. For photon energies of more than a few hundred keV and less than several MeV, the Compton effect component σ predominates. We note that the σ is significant at all energies of photons observed in this work. The coefficient κ predominates at the many-MeV photon energy [92, 100, 101].

In the photoelectric collisions, the energy of the photoelectrons is $(h\nu - B_e)$, where B_e is the average binding energy of the atomic electron [101]. In the Compton collisions, the average kinetic energy of the Compton electrons is $(h\nu\sigma_s/\sigma)$, and the Compton linear absorption coefficient σ_a is of the order of $^1/_2\sigma$ for (1 – 2)-Mev photons [101]. In the pair-production collisions, the total kinetic energy of the

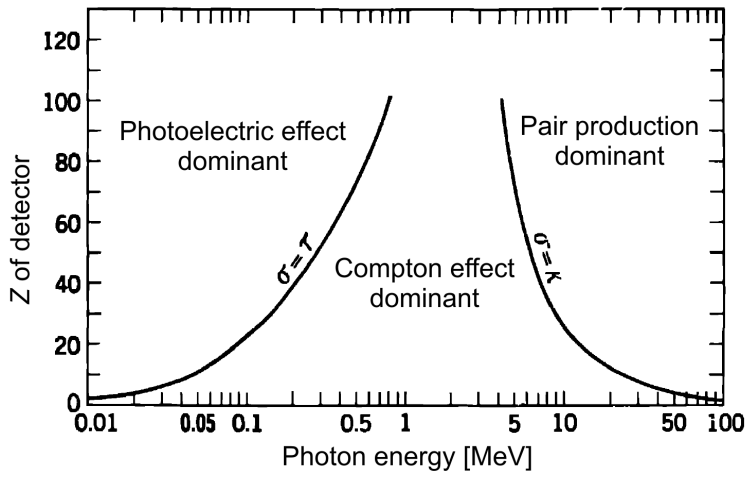

Figure 5.1: Relative importance of the three major photon interactions with a detector [101].

positron-electron pair is $(h\nu - 2m_0c^2)$ [101]. Combining these considerations with equations (5.16) and (5.19), we find the energy absorption in a thickness $\mathrm{d}x$ [101]:

$$\mathrm{d}I = n\left[\tau(h\nu - B_e) + \sigma h\nu\frac{\sigma_a}{\sigma} + \kappa(h\nu - 2m_0c^2)\right]\mathrm{d}x. \tag{5.21}$$

In the case of usual detector materials, B_e and $2m_0c^2$ could be neglected[3] [101]. Thus, the approximate expression of energy absorption becomes

$$\mathrm{d}I = I(\tau + \sigma_a + \kappa)\,\mathrm{d}x = I\mu_a\mathrm{d}x, \tag{5.22}$$

Where μ_a is the linear absorption coefficient. Obviously, μ_a is smaller than the total linear attenuation coefficient μ, since μ includes the linear absorption coefficient μ_a and the linear scattering coefficient μ_s [101]:

$$\mu = \mu_a + \mu_s \tag{5.23}$$

The linear absorption coefficient μ_a represents the photon energy which is converted into the kinetic energy of secondary electrons. The linear scattering coefficient μ_s represents the total energy of all secondary photons (Compton, x-rays, and annihilation radiation) [101].

[3]At the light elements, the electron binding energy is much smaller than the photon energy at the region in which the Compton effect is significant and $2m_0c^2 \doteq 1.02$ MeV is very small in comparison with photon energy in the region in which the pair production is significant [101].

In the real detector, all the mentioned photon interactions could contribute to the full-energy peak formation which is the most important in the gamma-ray spectroscopy, but especially the Compton collisions could lead also to the formation of continuum background or "false" peaks in the measured spectrum. Hypothetically, if the detector will be so large that each secondary photon has an opportunity to interact by any effect which we have mentioned, the total energy of entered photons will be completely converted into kinetic energy of electrons. Because a time scale of such process is much shorter than the response of the practical detector, each primary photon of a monoenergetic radiation will produce identical detector response and the full energy peak will be formed by all mentioned interactions. In the real detector with limited dimensions, some of scattered or annihilation photons may escape. Thus, the energy of an original photon is not always fully absorbed. The random losses of energy lead to the formation of continuum background, meanwhile, the precise losses lead to the formation of peaks in the measured spectrum.

The most significant continuum is caused by the Compton interaction of primary photons when the secondary photons are not absorbed. The Compton continuum is spread out between the zero energy (when the primary photon is scattered to the infinitely small angle) and the Compton edge (when the primary photon is backscattered to 180°) [99]. Substituting $h\nu = E_\gamma$, $E_{CE} = h\nu - h\nu'$, and $\vartheta = 180°$ in formula (5.12) we obtain the Compton edge energy

$$E_{CE} = \frac{2E_\gamma^2}{m_e\,c^2 + 2E_\gamma} \tag{5.24}$$

where E_γ is the energy of the primary photon, m_e is the rest-mass of electron and c the speed of light ($m_e\,c^2 = 0.511$ MeV). It should be noted that the second Compton edge may be formed by the Compton edge of double Compton scattering to 180°:

$$E_{2CE} = \frac{4E_\gamma^2}{m_e\,c^2 + 4E_\gamma}. \tag{5.25}$$

Between the Compton edge and the full energy peak is the continuum of multiple Compton events. The background with an energy above the full-energy peak is caused by pile-up effects which rest in false coincidence summing (detecting of two photons at the same time from different decays) and true coincidence summing (detecting of photons from the same decay). If both coincidence photons are fully absorbed, a "false" peak is formed. Other "false peaks" could be associated with the

electron-positron pair production interaction of the primary photons. The resulting positron is immediately annihilated emitting two photons. If one annihilation photon is not absorbed so-called single escape peak is formed [99]. If both annihilation photons are not absorbed so-called double escape peak is formed [99]. Obviously, the energy of single escape E_{SE} and double escape E_{DE} peak is determined as

$$E_{SE} = E_\gamma - m_0c^2 \tag{5.26}$$

$$E_{DE} = E_\gamma - 2m_0c^2 \tag{5.27}$$

where $m_0c^2 = 0.511$ MeV is the annihilation photon energy.

Moreover, the detector shielding and other surrounding matter could contribute to the background too. In the surrounding matter the Compton scattering, pair production, and photoelectric absorption are followed by emission of characteristics x-rays[4]. The Compton effect in the surrounding matter may lead to the formation of a backscatter peak. The energy of this peak is equal to the maximum energy of the photons backscattered to 180° by the surrounding matter. In accordance with formula (5.12) we obtain the energy of the backscatter peak [107]:

$$E_{BS} = \frac{E_\gamma m_e c^2}{m_e c^2 + 2E_\gamma}. \tag{5.28}$$

Another contribution to the spectrum continuum could be caused by the bremsstrahlung of β-particles. This effect is practically significant if the energy of β-particles exceeds 1 MeV [99].

Last but not least, we should mention the contribution of ubiquitous natural radioisotopes (^{222}Rn and ^{40}K and others) and cosmic radiation. Such background could be efficiently reduced using suitable shielding.

5.2 Interactions of Neutrons

The most important forces which cause interactions of a neutron with matter are the nuclear forces[5] [108]. Many kinds of neutron interactions with matter are known.

[4]The shielding is usually made of lead which produces a number of x-ray peaks in the region of 70-85 keV [99]. Therefore, it is not disturbing the measurement presented in this work since the energy of detected photons is significantly higher.

[5]Neutron, of course, could interact also by gravitation force since it has a mass and electromagnetic force since he has a magnetic moment [108]. However, in the experiments presented in this thesis, these interactions are insignificant.

The probability of all these interactions is strongly dependent on a neutron energy. In the case of a stationary target, the original energy of the dd fusion neutron is always higher than 1.7 MeV (see figs. 4.3 and 4.4). However, due to the scattering, the neutrons with a significantly lower energy may enter detectors. Obviously, the neutron scattering is often undesirable. For example, the measurement could be affected by neutrons scattered by the experimental chamber and surrounding hardware, laboratory walls and floor, etc. Nevertheless, in some diagnostic systems (for example Silver activation counter or Bonner spheres) the neutrons are moderated deliberately because many interactions are more probably at the lower neutron energies. In our Z-pinch experiments, we assume the occurrence of neutrons with an energy significantly lower than the original fusion neutron energy (due to the neutron scattering) and at the same time neutrons with an energy up to several tens of MeV. Interactions of such neutrons are described in this section.

5.2.1 Elastic Scattering

The neutron elastic scattering is an interaction in which a total kinetic energy of the projectile neutron and target nucleus before the collision is equal to the total kinetic energy after the collision. During the collision, part of the projectile neutron energy is transferred to the kinetic energy of the target nucleus and the remaining energy is carried by the scattered neutron. If the target nucleus is hydrogen ^{1}H (a proton), all the neutron energy could be transferred. For heavier nuclei, only a partial energy transfer is possible [92]. For the non-relativistic kinetic energies, the conservation of momentum and energy gives the energy of the recoil nucleus E_R in the laboratory coordinate system [92]

$$E_R = \frac{4A}{(1+A)^2}(\cos^2\theta)E_n, \tag{5.29}$$

where A is the mass number of the target nucleus, θ is the scattering angle of the recoil nucleus, and E_n is the neutron energy. The recoil nucleus interacts with the matter primary through the Coulomb forces between its positive charge and negative charge of the electrons in the material atoms [92]. The energy of the recoil nucleus is transferred to the electrons in accordance with the specific energy loss $-\mathrm{d}E/\mathrm{d}x$ (linear stopping power). Depending on the energy transferred to the electron, the excitation or ionization occurs.

5.2.2 Neutron-Induced Nuclear Reactions

Neutron-induced nuclear reactions are reactions in which a new nucleus is formed or the original nucleus is excited. The cross-sections of all these reactions depend on the neutron energy. In this section, only the basic reactions which are important for the diagnostics used in this work are presented. We note that generally very important group of neutron reactions is also the nuclear fission, however, its description is beyond the scope of this thesis.

5.2.2.1 Radiative Capture

Neutron radiative capture (n,γ) is a nuclear reaction in which the projectile neutron is absorbed by a target nucleus forming a heavier nucleus of the same chemical element as the original nuclei. Subsequently, the formed nucleus decays to its ground state by gamma emission. Notwithstanding the neutron radiative capture could occur at all neutron energies, usually the probability of this interaction drops rapidly at the neutron energies above 1 MeV. The cross-section of neutron capture reaction usually contains the resonance region. The resonances are related to the energy levels of the nucleus. In these resonances, the neutron capture cross-section is highest.

5.2.2.2 Nuclear Excitation

Nuclear excitation (n,n') is the inelastic scattering in which a part of the incident neutron energy is transferred to the nucleus which remains in the higher energetic level (excited state). In contrast to the neutron radiative capture, the nuclear excitation is a threshold reaction. The energy of the incident neutron must be higher than the energy difference between the ground and excited state. The half-life of the excited state could be very short (less than a nanosecond) bud also we can found the reactions in which the nuclei remain in a metastable state with a half-life on the order of hours.

5.2.2.3 Charged Particle Ejection

This category of the neutron-induced reactions are the collisions in which the incident neutron is absorbed and a charged particle is ejected. The most common such reactions are (n,p) and (n,α). However other reactions, for example (n,d), (n,t),

(n,^{3}He), etc. are also possible. The formed nucleus may or may not exist in an excited state. This group of collisions includes both endo-energetic and exo-energetic reactions.

5.2.2.4 Neutron Multiplication

The neutron multiplication reactions as (n,2n), (n,3n), etc are the threshold nuclear reactions. The energy threshold of these reactions may reach tens of MeV. If the produced nucleus is unstable or excited with a half-life in order of minutes or hours, the reaction is useful for the fast or ultrafast neutron activation diagnostics.

Chapter 6

Experimental Apparatus

Since 2011, the Czech-Russian join experiments have been performed on the GIT-12 device in Tomsk. The main aims of these experiments are the investigation of the nuclear-fusion plasma, production of nuclear-fusion neutrons, and principles of acceleration of ions up to the energy of tens of MeV. The GIT-12 device is supposed to work with various loads. However, all experiments which are presented in this thesis are performed with a gas-puff load with an outer plasma shell. The GIT-12 generator and experimental load used in the experiments presented in this thesis are described in the following sections.

6.1 GIT-12 Generator

The GIT-12 is a terawatt-class pulsed power device at the Institute of High Current Electronics (IHCE) of the Siberian Branch of the Russian Academy of Sciences (SB RAS) in Tomsk. The overall view of the GIT-12 device is shown in fig. 6.1. The

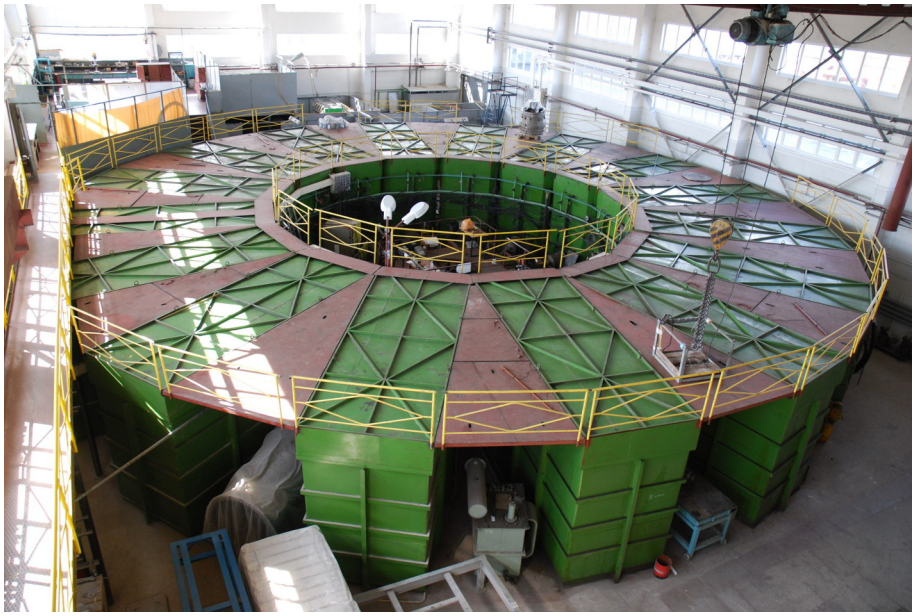

Figure 6.1: Overall view of the GIT-12 device

device contains 12 modules with Marx generators[1]. The modules are placed around a circle having an external diameter of 22 m. Outputs of the modules are coupled to the central node with the help of magnetically insulated transmission lines (MITL). In the central node, the MITL outputs are connected in parallel and coupled to a load. Charging the capacitors of Marx generators to the voltage of 50 kV, the total stored energy corresponds to 2.6 MJ and the maximum short-circuit current achieves 4.7 MA in 1.7 μs [68]. The rise time of the current in a load could be reduced to 200 ns using plasma opening switches (POS). The comparison of the generator current with and without the POS is in fig. 6.2.

[1]In fig. 6.1 we can see 16 containers. However, 4 containers do not contain any modules with Marx generators.

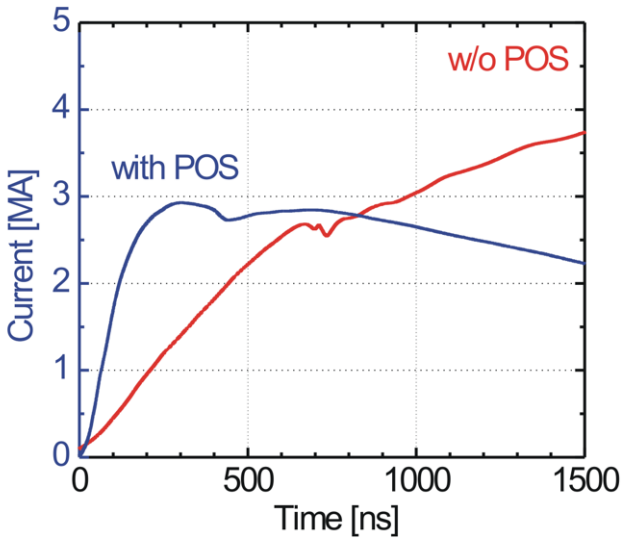

Figure 6.2: The comparison of the generator current with and without the plasma opening switches.

6.2 Experimental Load

The experimental load is composed of a gas-puff and an outer plasma shell generated by plasma guns. This type of experimental load was developed at the IHCE [81]. The deuterium gas was firstly used in such a load on the GIT-12 device in 2013 [2, 4]. The scheme of the experimental load is shown in fig. 6.3. The electrode system is composed of the anode and cathode meshes with a transparency of about 70%. An anode-cathode gap[2] varied typically between 23 and 27 mm. Above the anode mesh, the single-shell or multi-shell supersonic nozzle is placed [47]. The gas-puff injected by this nozzle spreads in the direction of the z-axis through the anode and cathode meshes. The gas flow formed by the nozzle was simulated with a help of ANSYS Fluent software by Jiří Stodůlka [82]. By these simulations, a temporally depended spatial distribution of the injected gas was evaluated. The gas-puff is surrounded by the outer plasma shell. The outer shell is generated by 48 coaxial-type plasma guns which are placed on the circle with a center on the z-axis. The diameter of the circle is 35 cm. As far as the outer-shell plasma composition is concerned, it consists of hydrogen (H^+) and carbon (C^+,C^{++}) ions [81].

[2]Shots with the anode-cathode gap up to 4 cm have been performed. However, for this work, the crucial shots have been performed with the anode-cathode gap of 23-27 mm.

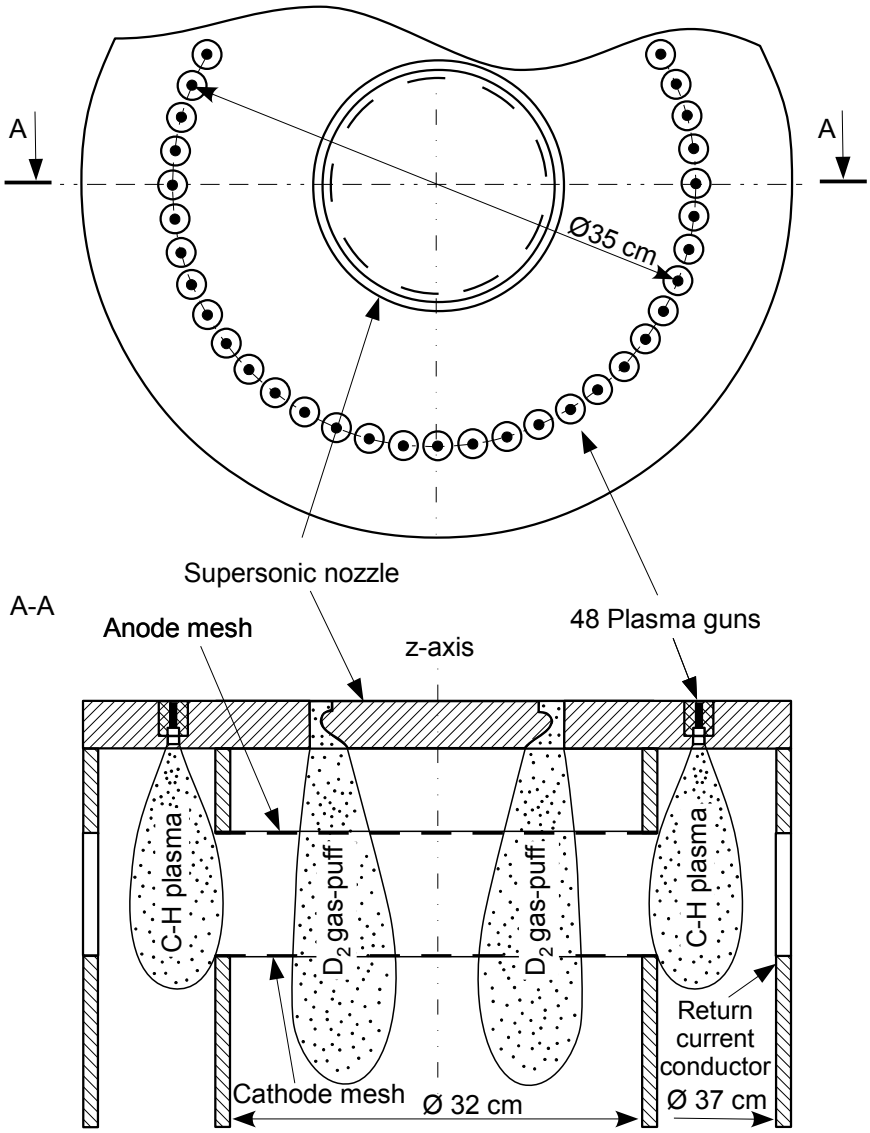

Figure 6.3: Scheme of the experimental load

During the shot, firstly the gas-puff valve opening mechanism is triggered at the time of about 350 μs before the main trigger of the GIT-12 generator. After the valve trigger, the plasma guns are triggered (1.7 – 1.9) μs before the GIT-12 trigger. The masses of the gas-puff and outer plasma shell are depended on the trigger delays. It makes us possible to vary the masses. The linear mass of the gas-puff is usually (60-100) μg/cm and the linear mass of the outer plasma shell is about 5 μg/cm.

We note, that the anode and cathode meshes are always damaged by the discharge and we mount the new electrode meshes before every shot. For illustration,

photos of the vacuum chamber and cathode mesh before and after the experimental shot are displayed in fig. 6.4.

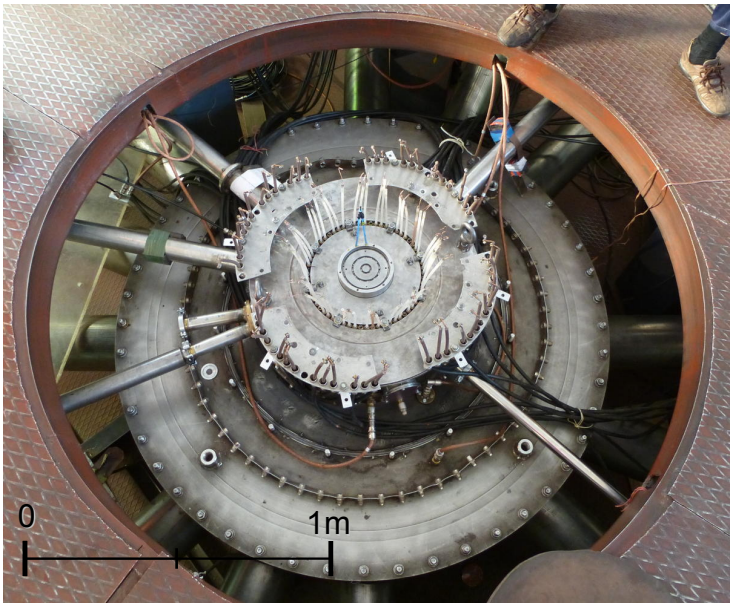

(a) Vacuum chamber

(b) Before shot

(c) After shot

Figure 6.4: (a) Photo of the vacuum chamber, (b) cathode mesh before the experimental shot, and (c) cathode mesh after the experimental shot.

Chapter 7

Diagnostic Techniques and Arrangement

The experiments on the GIT-12 device include a comprehensive set of diagnostics. Standard diagnostic instruments are used, for example, voltage and current probes, B-dot probes, an optical streak camera and an extensive system of extreme ultraviolet (EUV) and soft x-ray (SXR) diagnostics including the pinhole camera with four-channel gated microchannel plate. An emphasis is also put on the ion diagnostics. The ion emission is studied using pinhole cameras with stacks of radiochromic films (RCF) and CR-39 nuclear track detectors and ion absorbers [4]. The description of the whole diagnostic system which is used in the experiments on the GIT-12 device is beyond the scope of this thesis. The detail description of the neutron diagnostics which is the focal point of this thesis is presented in the following sections.

7.1 Neutron Bubble Detectors

The bubble detectors are a passive time-integrated neutron measurement method practically insensitive to other radiations such as hard x-rays (HXRs) and electromagnetic pulses (EMPs).

7.1.1 Bubble Detector Personal Neutron Dosimeters

In the experiments presented in this thesis, the neutron bubble detectors are mainly based on the Bubble Detector Personal Neutron Dosimeters (BD-PNDs) [90]. The

BD-PND consists of $10^4 - 10^5$ droplets of superheated liquid dispersed throughout 8 cm^3 of clear, elastic polymer medium. A diameter of the droplets is on the order of tens of microns. A pressure of the surrounding medium suppresses the normal boiling. If the BD-PND is exposed to a neutron flux, recoil ions are produced by reactions of the neutrons with atom nuclei within the detector volume (see fig. 7.1). The recoil ions are slowed down in accordance with the stopping power ($\mathrm{d}E_i/\mathrm{d}x$).

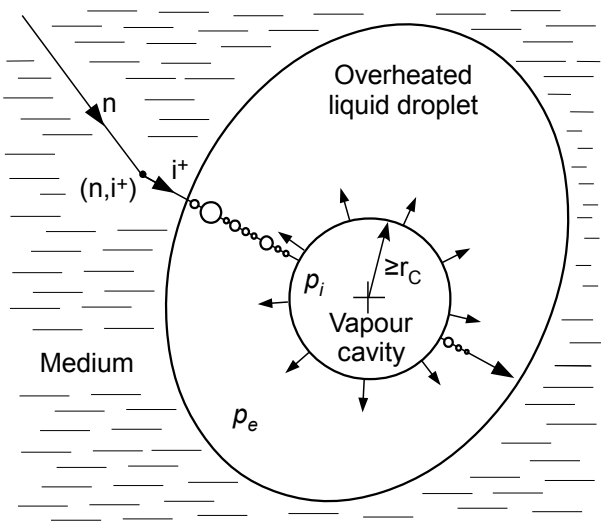

Figure 7.1: Formation of the bubbles in the neutron bubble detector.

These energy dissipations give rise to the production of highly localized hot regions, so-called "thermal spikes". If some recoil ion traverses the overheated liquid droplet, the "thermal spikes" with a temperature above the superheat limit lead to the formation of microscopic vapor cavities. If a radius of some such cavity exceeds the critical value (typically a few tens of nm [90]) then the cavity will rapidly expand to a form of a macroscopic bubble which fills the whole droplet [90]. If the cavity radius is bellow r_C, the cavity will be compressed by external pressure and disappears. If the cavity radius is equal to the r_C the pressure equilibrium occurs [90]:

$$p_e + \frac{2\sigma}{r_c} = p_i \tag{7.1}$$

where σ is the surface tension of the liquid, p_i is the internal thermodynamic pressure of the cavity, and p_e is the external pressure. Rearranging (7.1) and substituting $p_i - p_e = \Delta p$ we obtain:

$$r_c = \frac{2\sigma}{\Delta p} \tag{7.2}$$

In accordance with the classical thermodynamic theory, the minimum amount of energy required to form a vapor cavity of a radius r is approximately [90]:

$$E_{min} = 4\pi\sigma r_c^2 + \frac{4}{3}\pi r_c^3 \rho_v \frac{H}{M}, \tag{7.3}$$

where ρ_v is the density of the vapor, H is the molar heat of vaporization and M is the molecular mass. Combining equations (7.2) and (7.3) we obtain:

$$E_{min} = 16\pi \frac{\sigma^3}{(\Delta p)^2} \left[1 + \frac{2}{3}\frac{\rho_v}{\Delta p}\frac{H}{M}\right] \tag{7.4}$$

To exceed the critical radius of the cavity, the energy deposited by an ion over the effective length L_{eff} must achieve E_{min}. Assuming that L_{eff} is much shorter than a total particle track length, the deposited energy is given by [90]:

$$E_d = L_{eff} \left\langle \frac{\mathrm{d}E_i}{\mathrm{d}x} \right\rangle, \tag{7.5}$$

where $\langle \frac{\mathrm{d}E_i}{\mathrm{d}x} \rangle$ is the mean stopping power over L_{eff}. The effective length is proportional to the critical radius [90]. Thus,

$$E_d = k\, r_C \left\langle \frac{\mathrm{d}E_i}{\mathrm{d}x} \right\rangle, \tag{7.6}$$

where k is a constant. Equating (7.4) and (7.6) we obtain a threshold of the mean stopping power:

$$\left\langle \frac{\mathrm{d}E_i}{\mathrm{d}x} \right\rangle_{Th} = 8\frac{\pi}{k}\frac{\sigma^2}{\Delta p}\left[1 + \frac{2}{3}\frac{\rho_v}{\Delta p}\frac{H}{M}\right] \tag{7.7}$$

The mean stopping power increases with the ion energy and the initial ion energy increases with the energy of the neutron which interacts with this ion. Thus, the stopping power threshold is related to the neutron energy threshold. We should mention that the dimensions of the bubble are not dependent on any property of the incident neutron.

As far as the detection efficiency of the bubble detector is concerned, it is given by following formula [90]:

$$\eta(E_n, \vartheta) = V \sum_{i=0}^{n} N_i \sum_{j=0}^{m} \sigma_{ij} F_{ij}(E_n, \vartheta), \tag{7.8}$$

where V is the total volume of the superheated droplets, n is the number of isotopes in the superheated liquid, N_i is the atomic density of each isotope, m is the number

of considered reactions, σ_{ij} is the relevant cross-section, F_{ij} is the probability that the ij interaction leads to the formation of a bubble, E_n is the neutron energy, and ϑ is the detector temperature. The dependence of the BD-PND efficiency on the neutron energy is shown in fig. 7.2 where the data are used from [90]. The

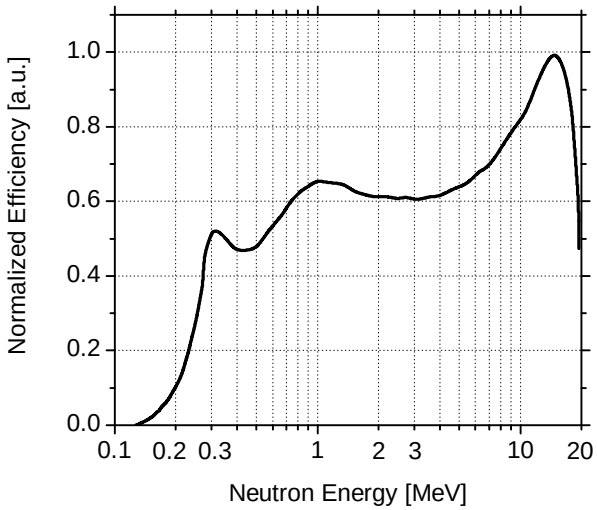

Figure 7.2: Detection efficiency of the BD-PND detector. Data used from [90].

neutron energy threshold of the BD-PND is of about 100 keV and the upper energy limit of the sensitivity is approximately 20 MeV. From the formula (7.8) it is clear that the efficiency is dependent on the temperature. (The threshold is as well dependent on the temperature.) However, the dosimeter has built-in compensation for temperature effects on the response of bubble detectors [90]. The temperature compensation is accomplished by a material with appropriate thermal expansion properties. This material is separated from the medium by a thin rubber membrane. The temperature range of the correct detector function is (20 – 37)°C [91]. The BD-PND detectors are equipped with a temperature indicator (see fig. 7.3). The screw cap servers to increase the external pressure, then the bubbles are compressed, removed, and the BD-PND could be used again.

As far as the calibration is concerned, it was found that the factory calibration is rough, moreover, the BD-PNDs are rapidly aging. The aging is dependent on the time elapsed from fabrication and also on the number of recompressions. This phenomenon must be taken into account in the experiments with duration of several weeks. Therefore our BD-PNDs have been calibrated in-situ using an Am-Be neutron source.

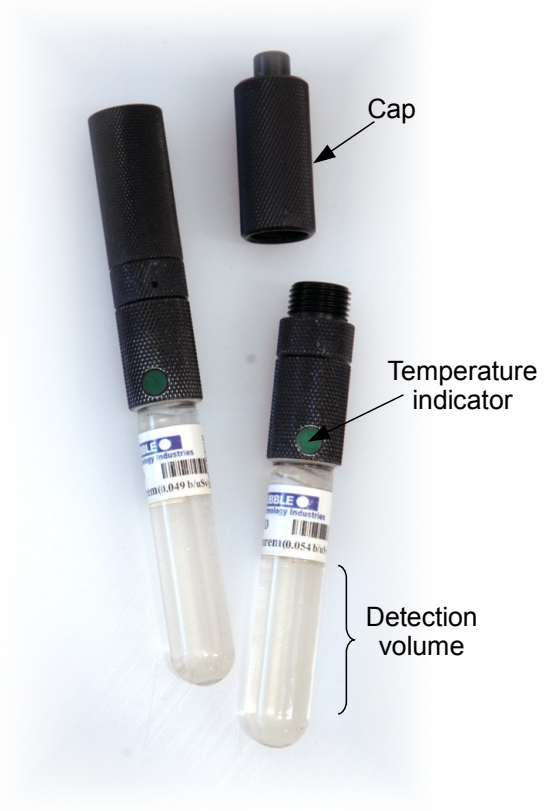

Figure 7.3: Buble Detector Personal Neutron Dosimeter

7.1.2 BDS Detectors

The BDS (Bubble Detector Spectrometer) represents a series of detectors with neutron energy thresholds from 10 keV to 10 MeV. However, if the factory calibration is used the result neutron spectra are coarse only. To use this type of diagnostics as a precise neutron spectrometer, several detectors of each threshold for better statistics should be used and their accurate calibration is required.

In the experiments on the GIT-12 generator, the BDS-10000 detector has been used in order to detect high-energy neutrons. The detection principle of the BDS-10000 is the same as in the case of BD-PND, but they are designed for the 10 MeV threshold. In contrast to the BD-PND, the BDS-10000 is strongly temperature dependent. The correct function is guaranteed only if the temperature is $(20.5 \pm 0.5)^{o}$C. For the recompression of the bubbles, the external compression chamber is required.

7.1.3 Bubble Detectors Arrangement

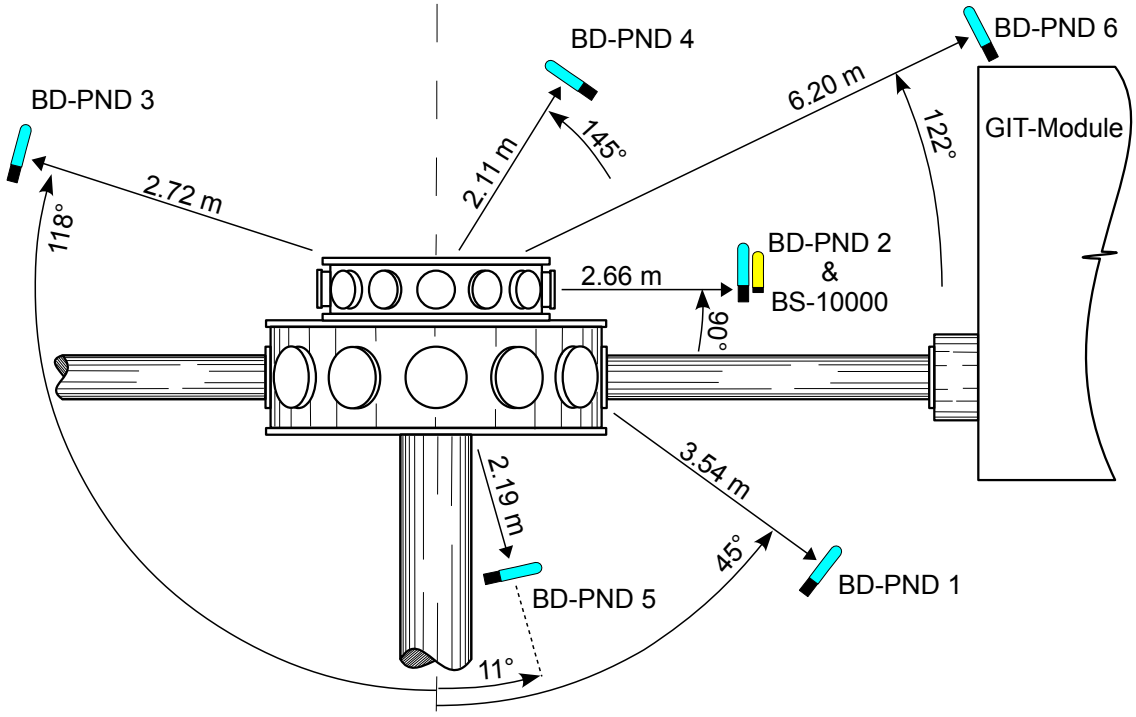

Figure 7.4: Arrangement of the Neutron Bubble Detectors

During the experiments on the GIT-12, six BD-PNDs and one BDS-10000 were used. The sensitivities of the BD-PNDs were in the range of $(2-7) \times 10^4$ bubble/neutron/cm^2 and sensitivity of the BDS-10000 was 3.1×10^4 bubble/neutron/cm^2. The BD-PNDs were arranged in order to include almost all neutron radiation directions to take into account an anisotropy. The BDS-10000 was placed in the radial direction, where an average neutron flux was assumed. The arrangement of the

BD-PNDs and BD-10000 is shown in fig. 7.4.

During the in situ calibration by the ^{241}Am-Be source with a strength of 10^6 neutrons per second, the detectors were placed at the same positions as during the experimental shots to include a neutron scattering.

7.1.4 Advantages of BD-PND detectors

For clarity, the advantages and disadvantages of the BD-PNDs are summarized in the following list.

Advantages:

+ The BD-PNDs are sensitive only to neutrons (insensitive to HXRs and EMPs).
+ They are sensitive to neutrons in the broad neutron energy range.
+ They are suitable for the measurement of short neutron pulses.
+ Detector versions with various sensitivities are available.

Disadvantages:

- The rapid aging must be taken into account during the experimental campaign.
- The factory calibration is rough, thus a precise calibration is needed.
- The sensitivity is dependent on a neutron energy.
- An exact counting of the bubbles is time-consuming.

7.2 Neutron Time-of-Flight Diagnostics

In the experiments described in this thesis, the neutron time-of-flight (nToF) detectors are based on the conversion of a neutron flux into an electrical signal using a plastic scintillator and photomultiplier or photodiode. The nToF detectors provide information about the neutron flux with a temporal resolution of a few nanoseconds. The original nToF signal, which is a function of the time, could be transformed into neutron energy spectrum if we know the distance from the neutron source to the detector, time of the neutron generation, time of the neutron detection, and energy response of the nToF detector. Obviously, some other effects as neutron scattering

could affect the neutron measurement. This section is focused on the implementation of the nToF detectors, their properties, experimental set-up, and transformation of the time signal to the energy spectrum.

7.2.1 Neutron Time-of-Flight Method

As mentioned above, the time-resolved signal of the neutron time-of-flight (nToF) detector is possible to transform into the neutron energy spectrum. Now, we show how to find and provide this transformation. We will describe the nToF method with a help of illustration in fig. 7.5. The nToF detector with a detection surface

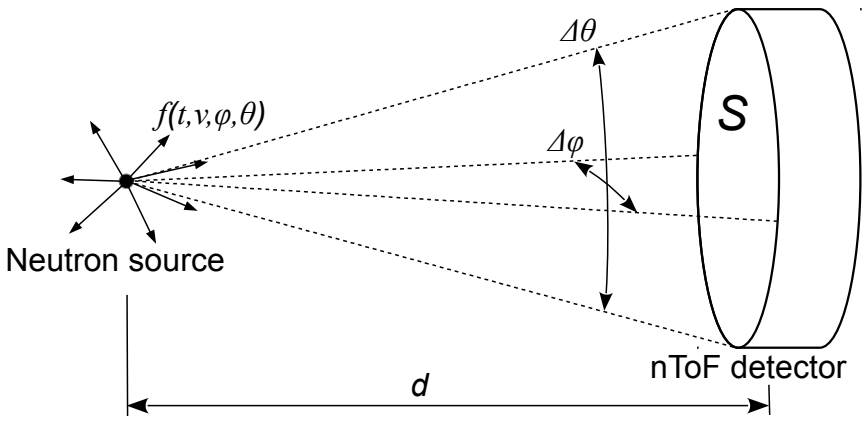

Figure 7.5: The nToF detector with a detection surface S is placed at the distance d from the neutron source with a distribution function $f(t, v, \varphi, \theta)$.

S is placed at the distance d from the neutron source with a velocity distribution $f(t, v, \varphi, \theta)$. The probability, that the emitted neutron will have a velocity v is possible to calculate if we know the time of neutron emission t and emission direction defined by φ and θ angles (see fig. 7.5). Then, the number of neutrons detected by the nToF detector $N_D(\tau, d)$ is given by the integral

$$N_D(\tau, d) = \int_t \int_v \int_{\Delta\varphi} \int_{\Delta\theta} f\,(t, v, \varphi, \theta)\, \delta\left(t + \frac{d}{v} - \tau\right)\, \mathrm{d}\varphi\, \mathrm{d}\theta\, \mathrm{d}v\, \mathrm{d}t, \qquad (7.9)$$

In the experiments reported in this thesis, the duration of neutron production is negligible in comparison with neutron time-of-flight. Therefore, in the calculations, we use the infinitesimal duration of the neutron emission in the time t_0. This approach

is called the basic time-of-flight method [88][1]. In this method, the velocity distribution in (7.9) is approximated as $f(t, v, \varphi, \theta) = \hat{f}(\hat{v}, \varphi, \theta)\,\delta(t - t_0)$. Integrating equation (7.9) with respect to t we obtain

$$N_D(\tau, d) = \int_{\hat{v}} \int_{\Delta\varphi} \int_{\Delta\theta} \hat{f}(\hat{v}, \varphi, \theta)\,\delta\left(t_0 + \frac{d}{\hat{v}} - \tau\right) \mathrm{d}\varphi\,\mathrm{d}\theta\,\mathrm{d}\hat{v}, \tag{7.10}$$

Now, we will integrate the equation (7.10) with respect to φ and θ angles. The integration limits are defined by the detector distance and dimensions (see fig. 7.5). The dimensions of the detector are on the order of centimeters and the distance of the detector is on the order of meters or tens of meters. Thus, $\Delta\varphi$ and $\Delta\theta$ are very small. Therefore, we assume that due to such very small changes in the angles the $\hat{f}$ distribution function is constant and the formula (7.10) becomes to

$$N_D(\tau, d) = \int_{\hat{v}} \hat{f}(\hat{v})\,\delta\left(t + \frac{d}{\hat{v}} - \tau\right) \frac{S}{d^2}\,\mathrm{d}\hat{v}, \tag{7.11}$$

where $S = d^2\Delta\varphi\Delta\theta$. To integrate the formula (7.10) we will use the following substitution [85, 89]:

$$\delta(g(\hat{v})) = \delta(\hat{v} - v)\,\frac{1}{|g'(\hat{v})|}, \tag{7.12}$$

where $g(\hat{v}) = t_0 + \frac{d}{\hat{v}} - \tau$ and v is the root of the g. Thus,

$$\delta\left(t_0 + \frac{d}{\hat{v}} - \tau\right) = \delta(\hat{v} - v)\frac{v^2}{d}. \tag{7.13}$$

Therefore, we can express (7.11) as

$$N_D(\tau, d) = \int_{\hat{v}} \hat{f}(\hat{v})\,\delta(\hat{v} - v)\,v^2\frac{S}{d^3}\,\mathrm{d}\hat{v}. \tag{7.14}$$

After the integration, we can express the neutron velocity spectrum

$$\hat{f}(v) = \frac{\mathrm{d}N_n}{\mathrm{d}v} = N_D(\tau, d)\,\frac{d^3}{v^2}\frac{1}{S}, \tag{7.15}$$

[1]If we assume a significantly long duration of neutron emission with respect to neutron time-of-flight, for example in plasma foci, we will need to use the extended ToF method presented in [86, 87, 88, 89]. However, in the experiments on the GIT-12 device the neutron production is very short in comparison with neutron time-of-flight. Moreover in the extended ToF method a lower deuteron energy than in our experiments (below 300 keV) is assumed. Therefore, we use the basic time-of-flight method.

where N_n is a number of the emitted neutrons with velocity in the interval of $\langle v, v + \mathrm{d}v\rangle$. The neutron velocity in (7.15) could be written using the neutron time of flight $(\tau - t_0)$ and the detector distance d:

$$\hat{f}(v) = \frac{\mathrm{d}N_n}{\mathrm{d}v} = N_D(\tau, d)\, d\, (\tau - t_0)^2 \frac{1}{S}. \tag{7.16}$$

The neutron velocity spectrum is very closely related to an energy spectrum. In the case of the non-relativistic energy of neutrons, the neutron energy is equal to $E_n = \frac{1}{2} m_n v^2$, where m_n is the neutron mass[2]. Thus, the neutron energy can be expressed by formula

$$f(E_n) = \frac{\mathrm{d}N_n}{\mathrm{d}E_n} = \hat{f}(v) \left| \frac{\mathrm{d}v}{\mathrm{d}E_n} \right| = \hat{f}(v) \frac{1}{m_n\, v}. \tag{7.17}$$

Combining the equations (7.16) and (7.17) we obtain the neutron energy spectrum:

$$f(E_n) = N_D(\tau, d) \frac{(\tau - t_0)^3}{m_n} \frac{1}{S} \tag{7.18}$$

Thus, if we assume the instantaneous neutron emission, the detection time τ corresponds exactly to the neutron energy E_n. As mentioned above, the scintillator is coupled with the photomultiplier. Assuming that, the multiplier is in the linear regime with an amplification A (including the attenuating optical filters mentioned above), the nToF detector output signal $s(\tau, d)$ is given only by $N_D(\tau, d)$, A, and the scintillator neutron response $\eta(E_n)$. Therefore, we can evaluate $f(E_n)$ neutron energy spectrum from the nToF detector output signal $s(\tau, d)$:

$$f(E_n) = s(\tau, d) \frac{A}{\eta(E_n)} \frac{(\tau - t_0)^3}{m_n} \frac{1}{S}. \tag{7.19}$$

As far as the time of neutron emission t_0 is concerned, we assume that it corresponds to the time of HXRs emission. The determination of t_0 significantly influences the accuracy of the neutron energy by the basic time-of-flight method. Generally, the uncertainty u of some determined value $Y = y(x_1, x_2, ..., x_i, ..., x_M)$ is defined as [74]:

$$u^2(Y) = \sum_{i=0}^{M} \left(\frac{\partial y}{\partial x_i} \right)^2 u^2(x_i), \tag{7.20}$$

[2]The non-relativistic approximation causes neutron energy error of 3% at the highest considered neutron energy of 18 MeV in our reconstructed nToF spectra.

where $u^2(x_i)$ is the uncertainty of the measured value x_i. In the case of nToF method $Y = E_n = \frac{1}{2}m_n v^2 = \frac{1}{2}m_n \left(d/t_{ToF}\right)^2$ where $t_{ToF} = \tau - t_0$ is the neutron time-of-flight. Obviously, the neutron mass m_n is exactly known, the detector distance d is also possible to measure relative precisely. Thus, an uncertainty of neutron energy ΔE_n is mostly given by the uncertainty of the determination of neutron time-of-flight Δt_{ToF}. Using 7.20 we obtain the uncertainty of energy ΔE_n:

$$\Delta E_n = \left| \frac{\partial}{\partial t_{ToF}} \left[\frac{1}{2} m_n \left(\frac{d}{t_{ToF}} \right)^2 \right] \Delta t_{ToF} \right| = \frac{2E_n}{t_{ToF}} \Delta t_{ToF}. \tag{7.21}$$

Thus, the uncertainty of the time-of-flight method is dependent on the time resolution of the nToF detector and duration of the neutron emission Δt which is corresponding to the duration of HXR pulse. As mentioned above, the time resolution of the nToF detector is about 5.7 ns. The full width at half maximum (FWHM) of the HXR pulse is about 10.5 ns. In accordance with (7.20) the $\Delta t_0 \doteq 12$ ns. Using formula (7.21) we obtain the neutron energy uncertainty displayed in fig. 7.6. The uncertainties in fig. 7.6 are plotted for the nToF detectors at the distances of

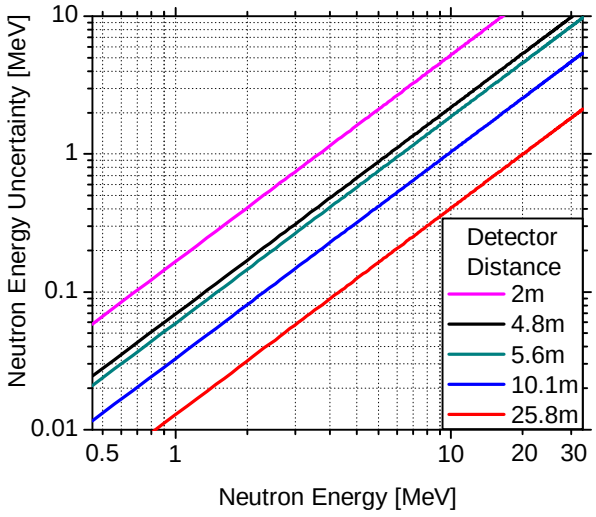

Figure 7.6: The uncertainty of the neutron energy evaluation by the basic time-of-flight method dependent on the detector distance.

2.0 m, 4.8 m, 5.6 m, 10.1 m, and 25.8 m. Such distances correspond to the nToF diagnostics set-up in the GIT-12 experiments (more in the following section). The neutron spectrum is usually evaluated from the signal of the furthermost detector at

the distance of 25.8 m. From fig. 7.6 is apparent that the energy resolution for the dd fusion neutron energy 2.45 MeV is of about 0.05 MeV and for the high-energy neutrons with the energy of 20 MeV, the resolution is of about 1 MeV. Such a resolution is sufficient and the extended time-of-flight method is not necessary. We note that the resolution of the real nToF diagnostics is slightly worse than the calculation in fig. 7.6 due to an EMP interference.

7.2.2 nToF Detectors

During the experiments presented in this thesis, two kinds of neutron time-of-flight (nToF) detectors were used. The first one is the nToF detector with the photomultiplier and the second one is the nToF detector with the vacuum photodiode. The simplified scheme of these detectors is displayed in fig. 7.7. The detection principle is based on the elastic scattering of neutrons on nuclei of the plastic scintillator. In the case of plastic scintillators, the scattering nuclei are represented by protons. The elastic interaction transfers a part of the neutron kinetic energy into a recoil proton[3] [92]. The energy of a recoil proton is fully deposited in the scintillator because the recoil proton free path length is negligible in comparison with dimensions of the scintillator. The deposited energy is converted into light flashes (scintillations) by excitation of the scintillator atoms and subsequent fluorescence.

In our nToF detectors, we use the Sant Gobain BC-408 polyvinyltoluene scintillators. The maximum of scintillation spectrum corresponds to a wavelength of 425 nm (visible violet light) and pulse duration (FWHM) is about 2.5 ns [95].

The scintillations are usually detected by the photomultiplier (see fig. 7.7(a)). We use the Hamamatsu H1949-51 assembly with the Hamamatsu R1828-01 fast photomultiplier tube (PMT) with a bialkali photocathode. The wavelength of maximum sensitivity of this PMT is 420 nm and an anode pulse rise time is 1.3 ns (at a supply voltage of 2.6 kV) [96]. The PMT response is linear with deviation up to 5% at anode currents below 500 mA [96]. The photomultiplier is coupled with the scintillator using neutral density optical filters to avoid a saturation of the photomultiplier by an intensive neutron flux and HXRs produced during the GIT-12 shot. The optical transparency coefficients of the filters vary from 1/512 to 1/15155 at

[3]The neutron scattering may occur also on another nucleus, but the proton is by far the most important nucleus [92].

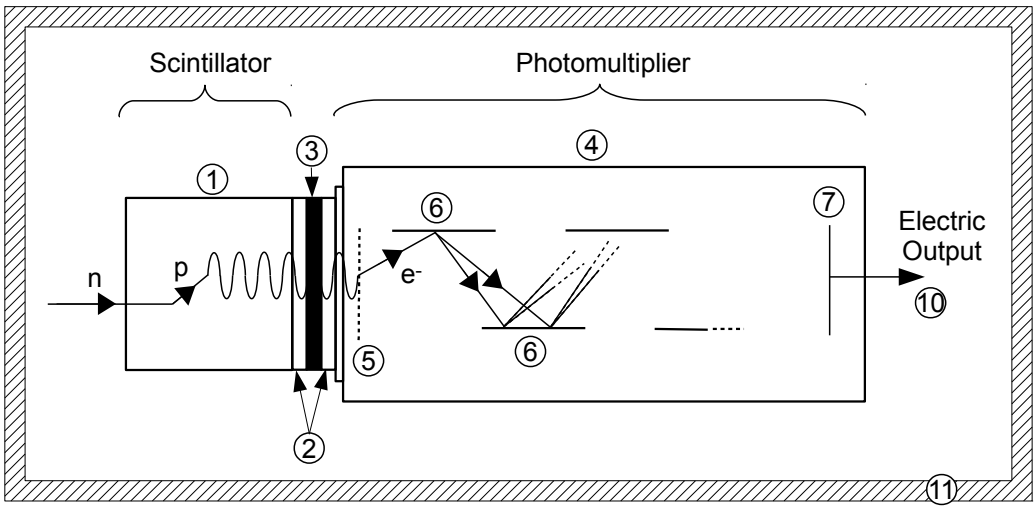

(a) Neutron Time-of-Flight Detector with Photomultiplier

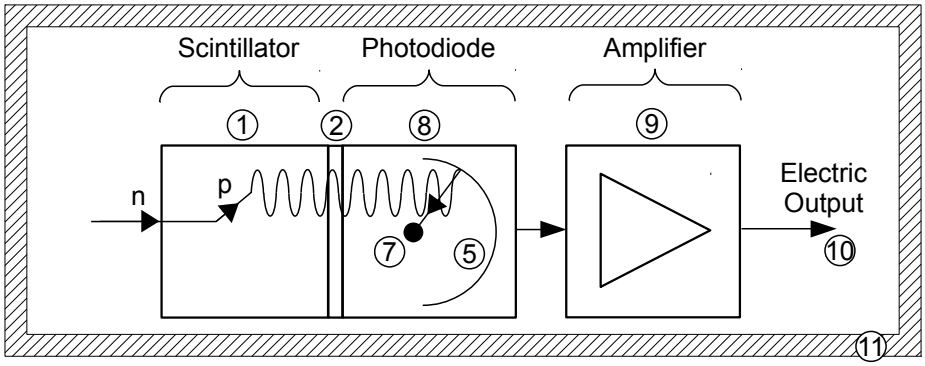

(b) Neutron Time-of-Flight Detector with Vacuum Photodiode

Figure 7.7: Simplified scheme of the neutron time-of-flight detector (a) with a photomultiplier, (b) with a vacuum photodiode. Description: 1 – Plastic scintillator BC408, 2 – Silicon emulsion, 3 – Neutral density optic filter, 4 – Photomultiplier, 5 – Photocathode, 6 – Electron multiplier dynodes, 7 – Anode, 8 – Photodiode, 9 – Solid state amplifier, 10 – Electrical output matched to 75 Ω coaxial cable, 11 – Lead shielding.

the furthest and nearest nToF detector, respectively. A photo of the nToF detector with the photomultiplier and its components is shown in fig. 7.8.

The high optical attenuation of the scintillations at the nearest detector led to the construction of the nToF detector where the photomultiplier was replaced

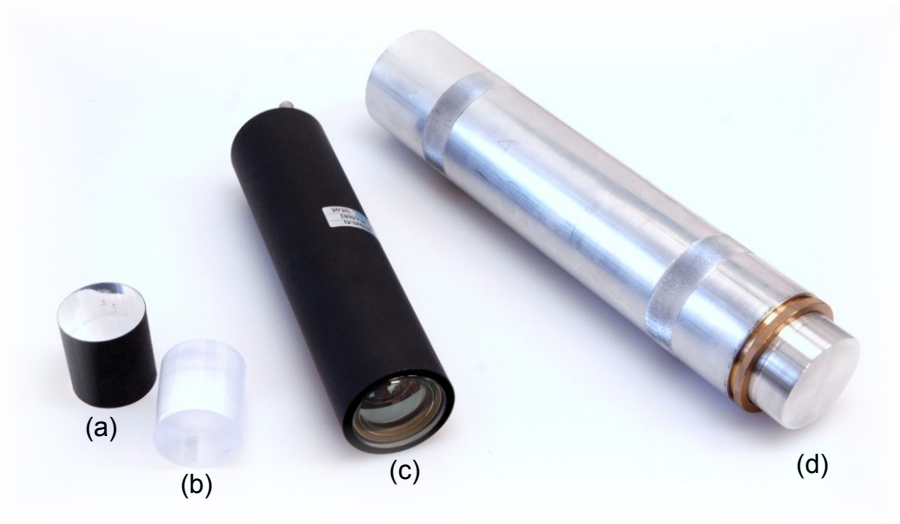

Figure 7.8: Photo of the neutron time-of-flight detector with a scintillator and a photomultiplier. (a) Scintillator with anti-reflective layer, (b) Scintillator BC-408, (c) Photomultiplier, (d) Assembled detector

by the vacuum photodiode coupled with a broadband solid-state amplifier (see fig. 7.7(b)). Such a detector is cheaper than the nToF detector with the photomultiplier. Moreover, no high-voltage power supply is required.

To avoid the saturation of both types of the nToF detectors by extreme intensive bremsstrahlung radiation which accompanies the neutron production, the detectors are shielded by 20 cm of lead on the front side and by 5 cm of lead from the other sides to eliminate backscattering and secondary radiation.

An example of the nToF detector output signal is displayed in fig. 7.9. The first short intensive pulse corresponds to the bremsstrahlung and the rest of the signal corresponds to the neutrons.

As far as a temporal resolution of the nToF detector is concerned, it has been investigated by Klir in [97]. The nToF detector with the identical scintillator and photomultiplier as in the experiments on GIT-12 was placed at the distance of 83.7 m from the pinch on the PF-1000 plasma focus at IPPLM in Warsaw. At such relatively great distance, it was possible to distinguish pulses corresponding to individual neutrons and obtain a single neutron response of the detector. A comparison of the measured single neutron response with the response predicted by the convolution of the PMT response and scintillator decay is displayed in fig. 7.10. The FWHM of

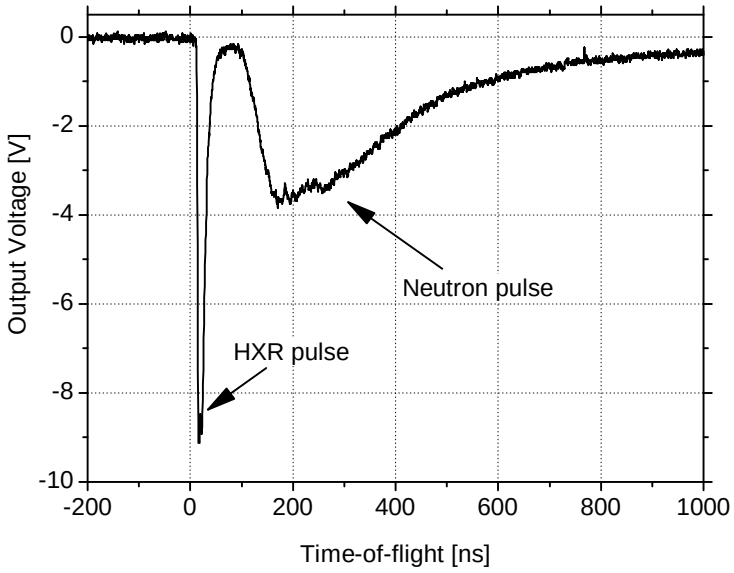

Figure 7.9: Signal of the N2 radial nToF detector at the distance of 5.6 m from the z-axis (shot no. 1844).

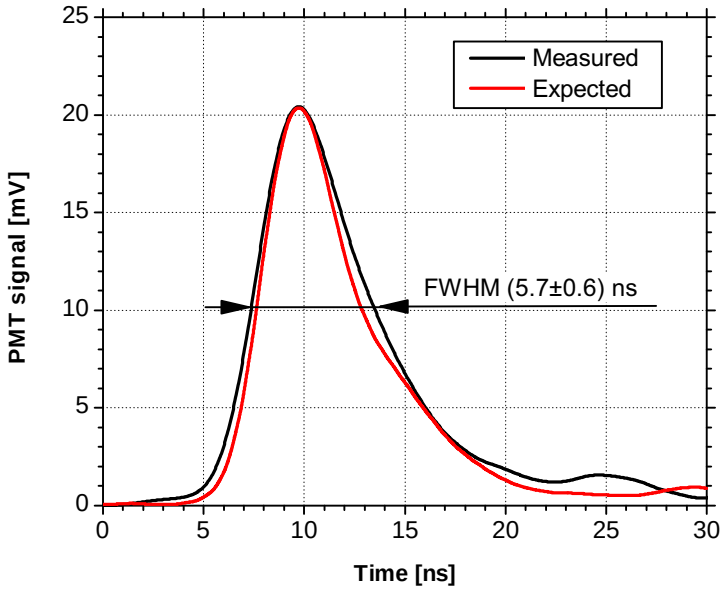

Figure 7.10: Response of the nToF detector to single neutron [97].

the neutron signal in fig. 7.10 is 5.7 ± 0.6 ns. The rise time and fall time are 2.9 ± 0.2 ns and 8 ± 1 ns, respectively. It allows us to distinguish two single neutrons when

the temporal shift is at least 5.7 ns [97].

Because the detectors operated in an environment with very harsh radio frequency EMPs, double shielded coaxial cables were used to transfer nToF detector signals to the Faraday cage with oscilloscopes.

7.2.2.1 Design of nToF Detector with Solid-State Amplifier

The nToF detector with a solid-state amplifier was developed in the frame of this thesis. A block scheme of this detector is shown in fig. 7.11. The detector is compatible with standard cylindrical scintillators with (44 – 45) mm in diameter and (40 – 57) mm in length which scintillate in the range of wavelengths from 200 nm to 600 nm. The range of the wavelengths of the scintillations which can be registered is limited by the vacuum photodiode used. The photodiode used is Hamamatsu R727 with a Sb-Cs photocathode and a UV-glass body (see fig. 7.12, curve 8). The parameters of Hamamatsu R727 are shown in table 7.1. The photodiode signal is amplified by the amplifier constructed from one or two integrated circuits with the current feedback. The complete electrical schemes of one-stage and two-stage amplifiers are shown in fig. 7.13 and 7.14, respectively.

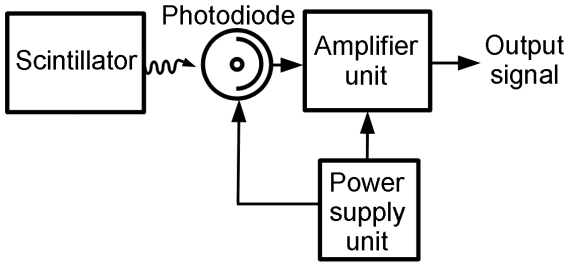

Figure 7.11: Conception of the probe

Description of the electrical schemes of the solid-state amplifiers is as follows. The charge of the cathode is drained by the R_{T1} resistor to the ground. The C_P interelectrode capacitance of the photodiode is about 2 pF [96](see table 7.1). Therefore the characteristic time of the detector τ is limited by the product of interelectrode capacitance C_P and resistance R_{T1}:

$$\tau = C_P\, R_{T1} = 2 \cdot 10^{-12}\mathrm{F} \cdot 1000\Omega = 2\,\mathrm{ns} \tag{7.22}$$

Photocathode material	Sb-Cs
Diameter of the photocathode	15 mm
Maximum anode supply voltage	100 V
Recommended operating voltage	15 V
Typical luminous sensitivity	40 μA/lm
Maximum peak cathode current	6 μA
Average cathode current	2 μA
Interelectrode capacitance	2 pF

Table 7.1: Parameters of the Hamamatsu R727 vacuum photodiode (Data from [96])

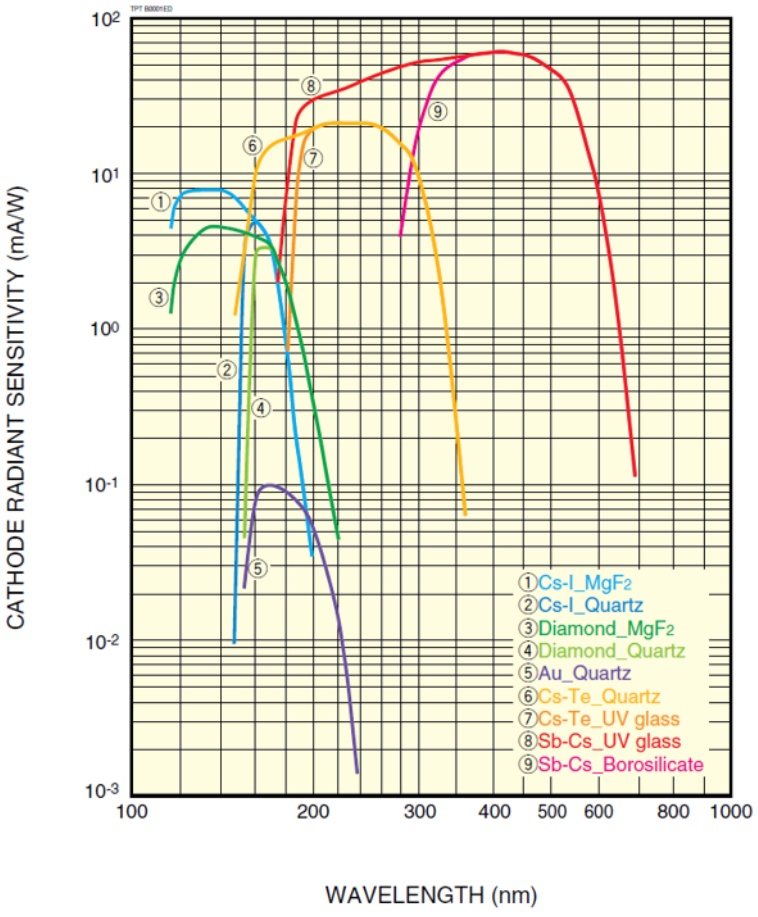

Figure 7.12: Spectral response characteristics of the Hamamatsu photodiodes [96]

At the same time, the sensitivity of the probe depends on the R_{T1} resistor. Because

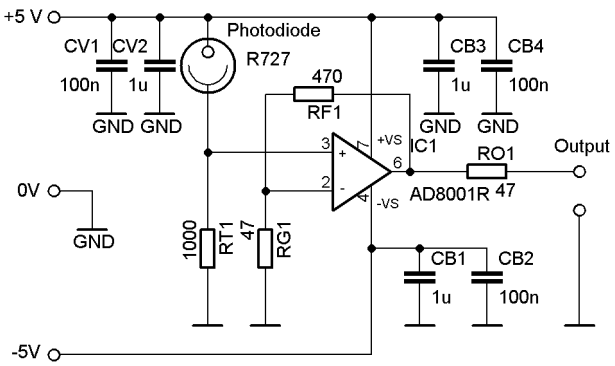

Figure 7.13: Electrical scheme of a one-stage amplifier

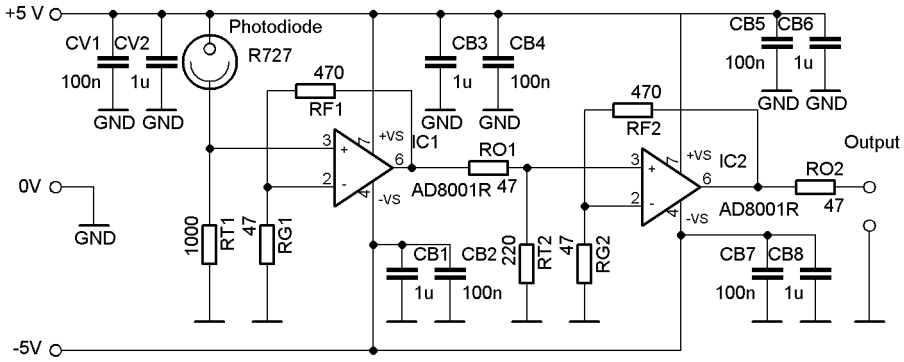

Figure 7.14: Electrical scheme of a two-stage amplifier

the voltage at the input of the amplifier is proportional to the photocurrent and to the value of the R_{T1} resistor

$$V_{IN} = I_P \, R_{T1}. \tag{7.23}$$

Hence, the sensitivity and time resolution are contradictory requirements. The characteristic time of 2 ns according to the FWHM of the scintillation pulses of the fast plastic scintillators [95] seems to be an optimal compromise.

The voltage of the R_{T1} resistor is amplified by a one-stage ore a two-stage amplifier composed of AD8001 integrated amplifiers in a noninverting configuration [98]. The theoretical voltage amplification A_{V1} of the one-stage amplifier is

$$A_{V1} = \frac{R_{F1}}{R_{G1}} + 1 = 11. \tag{7.24}$$

The voltage amplification of the second stage A_{V2} is

$$A_{V2} = \frac{R_{F2}}{R_{G2}} + 1 = 11. \tag{7.25}$$

Note that the total voltage amplification A_V is two times lower because the R_{O2} adapting resistor (or R_{O1} in the case of the one-stage amplifier) forms a 1/2 divider with a 50-Ω load. Therefore the total voltage amplification A_V of the one-stage amplifier is

$$A_V = \frac{A_{V1}}{2} = 5.5. \tag{7.26}$$

If we count the interstage divider from the R_{O1} and R_{T2} resistors and if we neglect the input impedance of the integrated circuits, the total voltage amplification A_V of the two-stage amplifier is

$$A_V = \frac{R_{T2}}{R_{T2} + R_{O1}} A_{V1} A_{V2} = 45. \tag{7.27}$$

The power amplification of the solid-state amplifier can be determined by the ratio of the electric power of the amplifier output and the electric power delivered to the amplifier input:

$$A_P = \frac{P_{out}}{P_{in}} = A_V^2 \frac{R_{T1}}{R_O + R_L} \tag{7.28}$$

where R_L is the resistance of the load, which is represented usually by the 50-Ω line. By substituting to (7.28) we obtain the power amplification of 250 for the one-stage amplifier and amplification of 20 250 for the two-stage amplifier.

The symmetrical power supply of the integrated circuits is filtered by blocking ceramic capacitors of capacitances of 100 nF and 1 μF (the capacitors: C_{B1}, C_{B2}, C_{B3}, C_{B4}, C_{B5}, C_{B6}, C_{B7}, C_{B8}) which are placed very close to the integrated circuit package (as close as possible). The power supply of the vacuum photodiode is filtered in the same way as well (capacitors: C_{V1}, C_{V2}).

The very important properties of the amplifiers are frequency characteristics since they influent a temporal resolution of the detector. The frequency characteristics of voltage amplification of the one-stage and two-stage amplifiers are shown in fig 7.15.

The measurements of frequency-depended amplification were done with the 50-Ω matching. The high-frequency generator output and the oscilloscope input were set to the 50-Ω coupling mode. From fig. 7.15 it is clear that in the range from 10 to 400 MHz the amplification change is negligible. The amplifier is able to work without

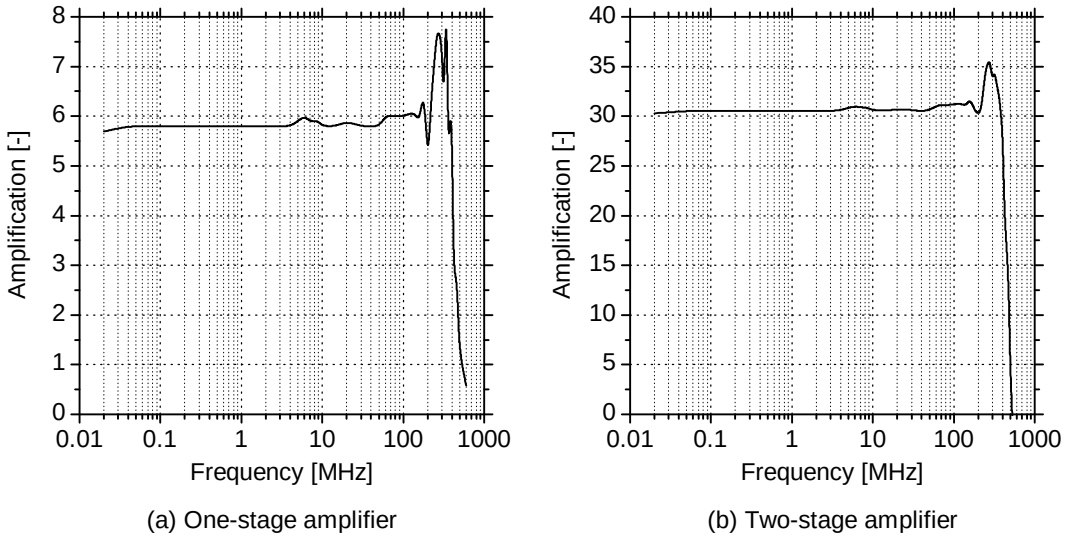

Figure 7.15: Measured frequency characteristics: (a) one-stage amplifier, (b) two-stage amplifier.

any significant distortion of the output signal up to the output voltage swing of 3 V. That means that the amplifier in this form can amplify unipolar pulses with a height of up to 1.5 V.

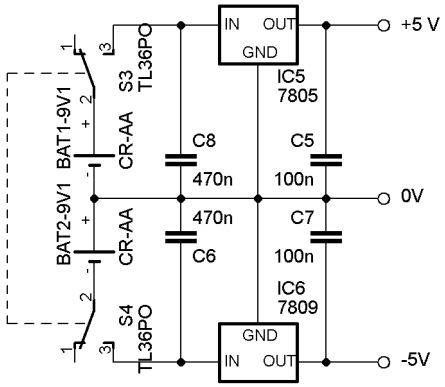

Figure 7.16: Electrical scheme of the power supply

As far as the symmetrical power supply unit is concerned, it is formed using two 9-V batteries and 7805 and 7905 integrated stabilizers for the positive and negative supplying branch, respectively. The electrical scheme of the power supply is shown in fig. 7.16. We should mention that the power supply is not ideal because of

the power losses. For a lower energy consumption, the DC/DC converter is more suitable. However, the simple power supply used is more reliable and does not generate any noise[4]. Therefore the prototype which is designed to test the new type of detector is equipped with the battery power supply displayed in fig. 7.16. When it was tested, the batteries showed a lifetime of many hours of a continuous detector operation.

The computer model of the scintillation probe prototype is shown in fig. 7.17. For illustration, the photo of the made prototype is shown in fig. 7.18.

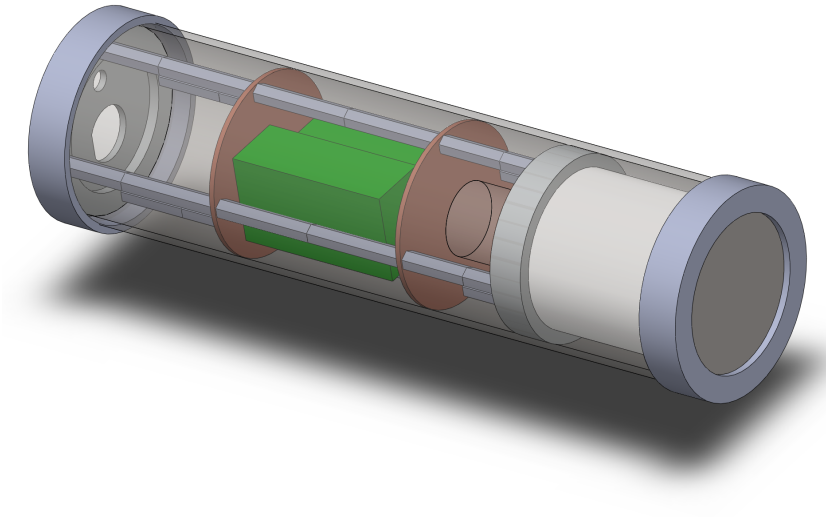

Figure 7.17: Model of the designed prototype of the scintillation probe

[4]The DC/DC converters contains AC generators which could be a source of noises if they are constructed in an inappropriate manner.

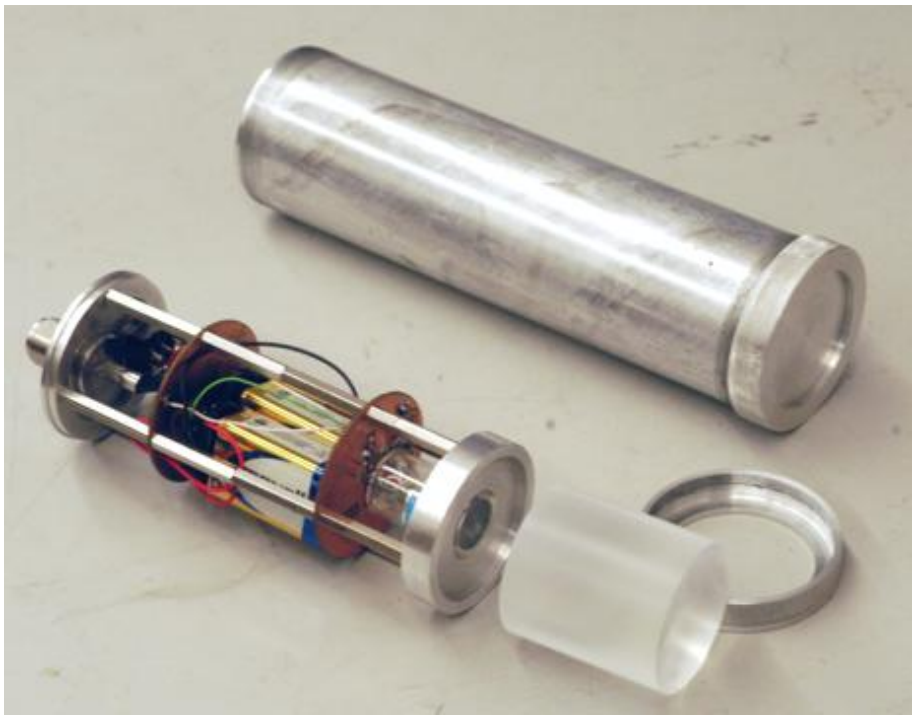

Figure 7.18: Photo of the scintillation photodiode probe

7.2.3 nToF Detectors Set-up

During the experiments on the GIT-12 device, we used four radial detectors and one axial nToF detector in the downstream direction (below cathode). The placement of the nToF detectors is shown in fig. 7.19. We note that fig. 7.19 is schematic and the dimensions are not in scale. The neutron source represented by the Z-pinch discharge is assumed on the z-axis between the anode and cathode inside the experimental vacuum chamber. All detector distances are related to this neutron source. The nearest nToF detector labeled N1 was placed at the distance of 2 m because this is the shortest distance where the HXRs pulse does not interfere with the neutron pulse. The N4 nToF detector is placed at the largest possible distance of 25.8 m which is limited by the facility building dimensions. To minimize a distortion of detected neutron energy by the scattering, there were no objects in the line of sight from the Z-pinch to the radial nToF detector except a stainless steel flange with a thickness of 0.5 cm.

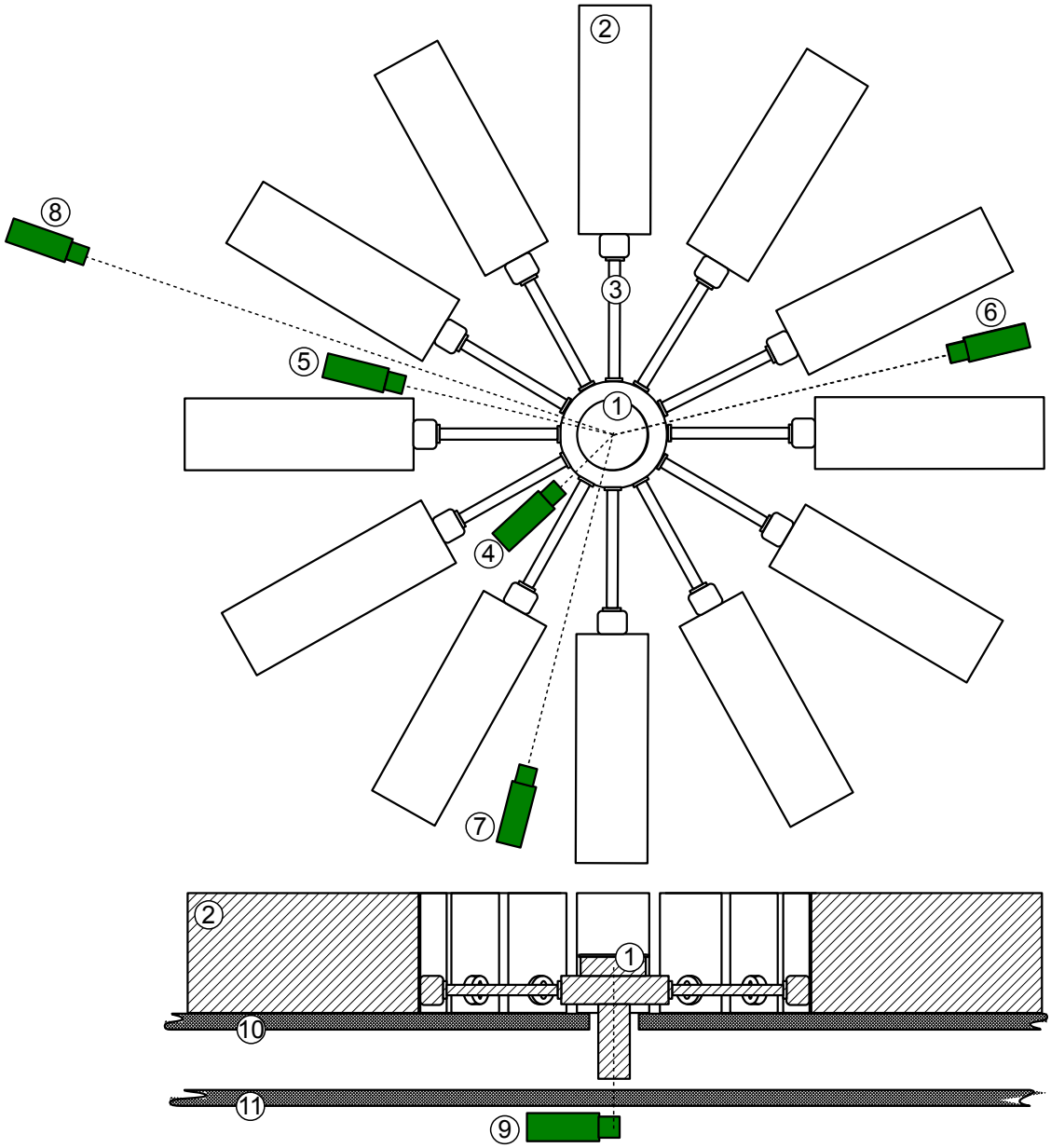

Figure 7.19: Arrangement of the neutron time-of-flight detectors displayed in top view and side view cross-section of the GIT-12 device. Description: 1 – Experimental vacuum chamber, 2 – Twelve modules of Marx generators, 3 – Magnetically insulated transmission line (MITL), 4 – nearest radial detector N1 (2 m), 5 – N2 radial detector (5.6 m), 6 – N3 radial detector (10.1 m) in 2015, 7 – N3 radial nToF detector (10.1 m) in 2016 and 2017, 8 – N4 radial detector (25.8 m), 9 – N5 axial detector (4.8 m), 10 – Concrete floor, 11 – Underground concrete floor.

7.2.4 Advantages and Disadvantages of nToF Diagnostics

Advantages:

+ The time-resolved signal is possible to transform to spectrum.

Disadvantages:

- Absolute calibration is complicated.

- Dependence of the scintillator response on neutron energy in the range important for the experiments reported in this thesis (up to 20 MeV) was estimated theoretically only.

- The nToF detector is sensitive to HXRs[5].

- Problems with the EMP interference.

7.3 Silver Activation Neutron Diagnostics

The silver activation counter is the established time-integrated neutron diagnostic method. The method is based on the activity of silver induced by neutron flux. A decay radiation of the produced unstable isotopes is detected. Since the activation process is very fast, this method is suitable for the detection of short neutron pulses. The detailed principle of the silver activation diagnostics is explained below.

7.3.1 Principle of Neutron Activation Diagnostics

During the exposure of an activation sample to a neutron flux, nuclear reactions might occur. Since we consider an activation sample with the thickness on the order of millimeters and the neutron energy on the order of MeV, the mean free path of the neutrons is much higher than the sample thickness. Thus, the reaction rate R is given by

$$R = \phi N_t \langle \sigma \rangle \tag{7.29}$$

[5]The sensitivity of the nToF detectors to HRXs is particularly also advantage, since the HXRs pulse in the nToF signal carries information about the time, when the neutrons were emitted.

where ϕ is the neutron flux (number of neutrons per unit area per unit time), N_t is the number of the target particles, and $\langle\sigma\rangle$ is the mean cross-section averaged over the neutron spectrum:

$$\langle\sigma\rangle = \frac{\int_{E_{Th}}^{\infty} \frac{\mathrm{d}\Phi(E)}{\mathrm{d}E}\,\sigma(E)\,\mathrm{d}E}{\int_{E_{Th}}^{\infty} \frac{\mathrm{d}\Phi(E)}{\mathrm{d}E}\mathrm{d}E}, \tag{7.30}$$

where E_{Th} is the reaction threshold energy and Φ is the time-integrated neutron fluence

$$\Phi = \int_0^{t_0} \phi \mathrm{d}t. \tag{7.31}$$

The produced radioactive isotopes undergo decay from the beginning of the exposure. The rate of decay is given simply by $\lambda N(t)$, where λ is the decay constant of the radioisotope and $N(t)$ is the number of the unstable nuclei at the time t. Thus the total rate of change $N(t)$ is given by the difference between the rate of radioisotope production and rate of decay [92]:

$$\frac{\mathrm{d}N(t)}{\mathrm{d}t} = R - \lambda N(t) \tag{7.32}$$

Assuming a constant R, constant N_t (neglecting any "burn-up"), zero radioactivity before the exposure $N(0) = 0$, and the begin of the exposure at the time $t = 0$, the solution of the equation 7.32 is following

$$N(t) = \frac{R}{\lambda}\left[1 - \exp\left(-\lambda t\right)\right] \tag{7.33}$$

and the activity $A(t)$ is given by

$$A(t) = R\left(1 - e^{-\lambda t}\right). \tag{7.34}$$

Thus, the maximum activity of the sample is limited. The saturated activity is given by limit

$$A_\infty = \lim_{t\to\infty} A(t) = R = \phi N_t \langle\sigma\rangle \tag{7.35}$$

If the exposure finishes at the time t_0, the initial activity is given by

$$A_0(t_0) = A_\infty\left(1 - e^{-\lambda t_0}\right) = R\left(1 - e^{-\lambda t_0}\right). \tag{7.36}$$

The time dependence of the activity during and after the exposure is shown in fig. 7.20. The temporal dependence during the exposure is important for a calibra-

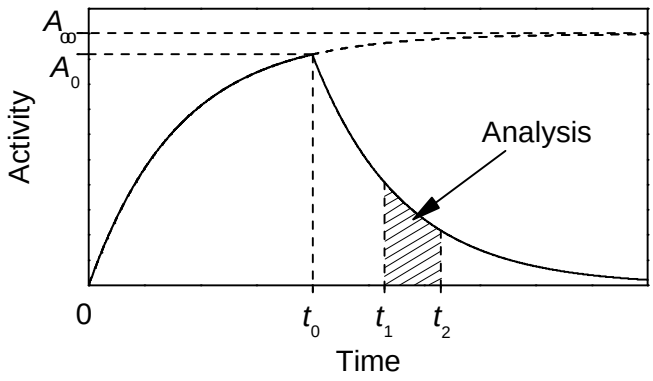

Figure 7.20: Activity of the activation sample.

tion by the ^{241}Am-Be neutron source. Since a length of the neutron pulse produced by the Z-pinch is on the order of tens of nanoseconds and the half-life of activated silver is on the order of tens of seconds or higher, we neglect a decay during the exposure[6]. Thus, the initial activity is approximated by the formula

$$A_0(t_0) = \lambda \Phi N_t \langle \sigma \rangle. \tag{7.37}$$

where Φ is the time-integrated neutron fluence.

After the exposure, we begin to measure or analyze the decay radiation of the sample. The rate of detected events for $t \geq t_0$ is given by

$$R_D(t) = \epsilon\, A(t) + C_B = \epsilon A_0\, e^{-\lambda(t-t_0)} + R_B, \tag{7.38}$$

where ϵ is the overall detection efficiency depending on the energy, self-absorption within the activation sample, geometric factors, and probability of the decay particle emission and R_B is the rate of counts caused by detection of a background radiation. The number of events counted between t_1 and t_2 for $t_1, t_2 \geq t_0$ is given by

$$C = \int_{t_1}^{t_2} R_D(t)\mathrm{d}t = \epsilon \frac{A_0}{\lambda}\, e^{\lambda t_0}\, \left(e^{-\lambda t_1} - e^{-\lambda t_2}\right) + R_B(t_2 - t_1) = \epsilon \frac{A_0}{\lambda}\, e^{\lambda t_0}\, \left(e^{-\lambda t_1} - e^{-\lambda(t_1+\Delta t)}\right) + C_B, \tag{7.39}$$

where $\Delta t = t_2 - t_1$ is the duration of the counting and $C_B = R_B \cdot \Delta t$ is the number of counts caused by detection of a background radiation.

[6]In the case of the tokamaks, continuous accelerators or repetitive plasma foci the decay during the exposure must be taken into account.

7.3.2 Silver Activation Counter

The silver activation counter (SAC) uses the natural silver with isotopic content 52% of ^{107}Ag and 48% of ^{109}Ag. The significant nuclear reactions of neutrons with the natural silver are represented by neutron radiative captures:

$$^{107}\mathrm{Ag}(\mathrm{n},\gamma)^{108}\mathrm{Ag}\left(T_{1/2}=142.9\,\mathrm{s}\right)\longrightarrow^{108}\mathrm{Cd}+\beta^{-}\,(97.2\%) \tag{7.40}$$

and

$$^{109}\mathrm{Ag}(\mathrm{n},\gamma)^{110}\mathrm{Ag}\left(T_{1/2}=24.6\,\mathrm{s}\right)\longrightarrow^{110}\mathrm{Cd}+\beta^{-}\,(99.7\%) \tag{7.41}$$

The neutron radiative captures by ^{107}Ag and ^{109}Ag result in the production of ^{108}Ag and ^{110}Ag unstable isotopes with half-lifes of 142.9 s and 24.6 s, respectively. The total cross-sections of the corresponding reactions are shown in fig. 7.21. From fig. 7.21

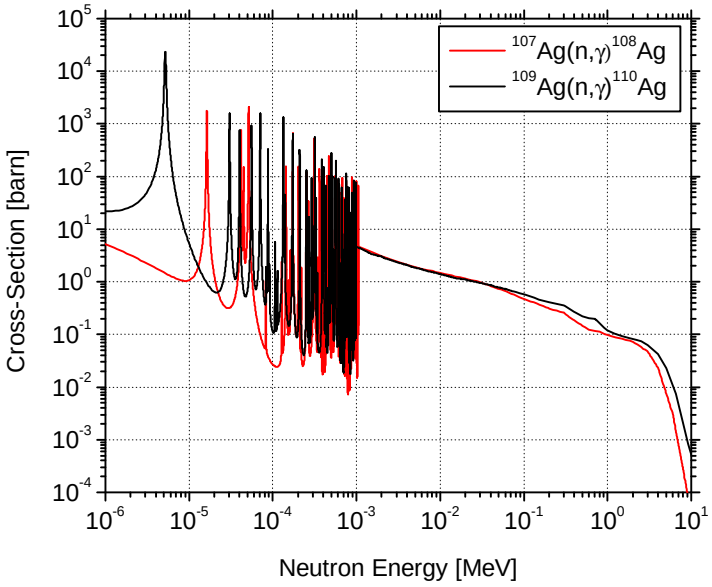

Figure 7.21: The total cross-sections of the radiative neutron capture reactions of natural silver isotopes

it is clear that the activation cross-section for the neutrons with dd fusion energy of 2.45 MeV is relatively low in comparison with the cross-section at the energies on the order of keV or lower. Therefore to detect the high-energy dd fusion neutrons, a polyethylene moderator is used to achieve higher reaction probability (see fig. 7.22). The moderator is designed for the energies of the dd fusion neutrons. It is assumed,

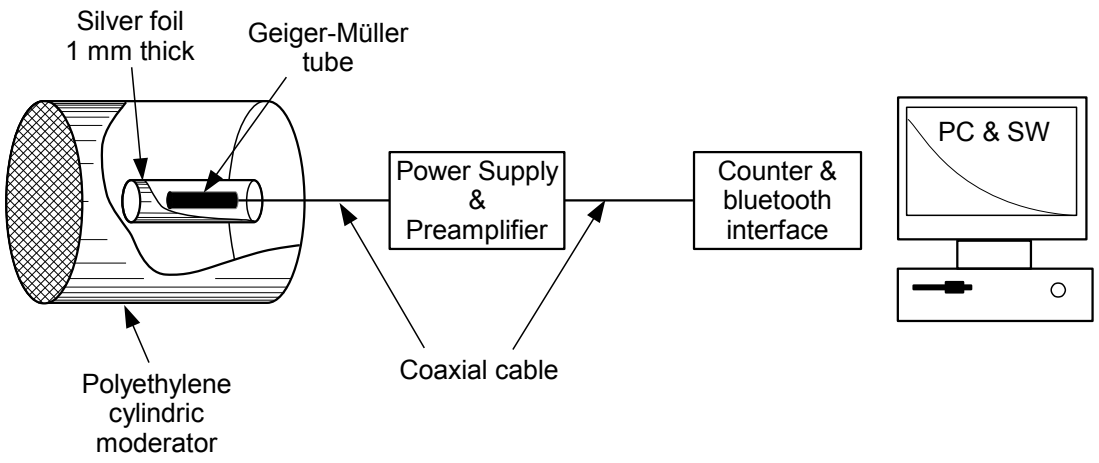

Figure 7.22: Scheme of the silver activation counter

that it works correctly up to neutron energies of 4 MeV. The moderated neutrons are captured by the silver foil with a thickness of 1 mm. The silver foil is surrounding the Geider-Müller tube (G-M Tube) СБМ-19 (SBM-19) which detects the β^- decay radiation. In accordance with (7.38), assuming $t \geq t_0$ and superposition of ^{108}Ag and ^{110}Ag decay radiation, for $t \geq t_0$ the count rate is given by

$$R_{Ag}(t) = \epsilon_1 A_{01}\, e^{-\lambda_1 (t-t_0)} + \epsilon_2 A_{02}\, e^{-\lambda_2 (t-t_0)} + R_B, \tag{7.42}$$

where index 1 corresponds to ^{108}Ag and index 2 corresponds to ^{110}Ag isotope. In accordance with (7.39), for $t_1 \geq t_0$ the number of counts is

$$\begin{aligned} C_{Ag} &= \epsilon_1 \frac{A_{01}}{\lambda_1}\, e^{\lambda_1 t_0}\, \left(e^{-\lambda_1 t_1} - e^{-\lambda_1 (t_1+\Delta t)}\right) \\ &+ \epsilon_2 \frac{A_{02}}{\lambda_2}\, e^{\lambda_2 t_0}\, \left(e^{-\lambda_2 t_1} - e^{-\lambda_2 (t_1+\Delta t)}\right) + C_B, \end{aligned} \tag{7.43}$$

where t_1 is the start of counting and Δt is the duration of counting. A signal of the G-M tube is amplified by the preamplifier and analyzed by the counter in control room.

The silver activation counter has been placed in the radial direction at the distance of 4.55 m from the z-axis.

We note that the G-M tube could be saturated by the radiation of activated silver if the neutron yield from the GIT-12 shot exceeds 10^{12} neutrons per shot. Such saturation could be corrected by extrapolation of the decay exponential curve if the neutron yield is below 5×10^{12}. Theoretically, this range could be increased by

placing the SAC at a greater distance, but it is complicated due to bulky oil tanks with Marx generators which surround the experimental chamber[7].

7.3.3 Calibration of SAC

The silver activation counter (SAC) has been calibrated by Dr. Padalko using ^{241}Am-Be neutron source with the strength of 10^6 neutrons per second and neutron energy spectrum displayed in fig. 7.23[8]. The calibration counting was performed after the exposure to avoid some influence of gamma-rays produced by ^{241}Am-Be to the G-M tubes. During the exposure, the saturation of SAC was achieved. Consequently, the neutron source was removed and the decay radiation was detected with $\Delta t =$ 1 s. Obviously, $A_{01} = A_{\infty 1}$ and $A_{02} = A_{\infty 2}$. Substituting the saturated activities $A_{\infty 1}, A_{\infty 2}$ in equation (7.43) by formula (7.35) we obtain

$$\begin{aligned} C_{Ag} = \epsilon_1 \frac{\phi \sigma_1 N_{t1}}{\lambda_1} e^{\lambda_1 t_0} \left(e^{-\lambda_1 t_1} - e^{-\lambda_1 (t_1 + \Delta t)} \right) \\ + \epsilon_2 \frac{\phi \sigma_2 N_{t2}}{\lambda_2} e^{\lambda_2 t_0} \left(e^{-\lambda_2 t_1} - e^{-\lambda_2 (t_1 + \Delta t)} \right) + C_B. \end{aligned} \tag{7.44}$$

Where C_{Ag} is the number of counts caused by the decay of the activated silver, C_B is the number of counts caused by the background radiation, and ϕ is the neutron flux given by the ^{241}Am-Be source and its distance from the SAC. The SAC was calibrated placing the ^{241}Am-Be source at the distances of 0, 20, 40, and 60 cm from the SAC. The detection efficiencies ϵ_1, ϵ_2, cross-sections σ_1, σ_1 and numbers of ^{107}Ag and ^{109}Ag nuclei we assumed constant. Thus, we merge the constants in 7.44: $K_1 = \epsilon_1 \, N_{t1} \, \sigma_1$ and $K_2 = \epsilon_2 \, N_{t2} \, \sigma_2$ and equation (7.44) becomes

$$\begin{aligned} C_{Ag} = K_1 \frac{\phi}{\lambda_1} e^{\lambda_1 t_0} \left(e^{-\lambda_1 t_1} - e^{-\lambda_1 (t_1 + \Delta t)} \right) \\ + K_2 \frac{\phi}{\lambda_2} e^{\lambda_2 t_0} \left(e^{-\lambda_2 t_1} - e^{-\lambda_2 (t_1 + \Delta t)} \right) + C_B, \end{aligned} \tag{7.45}$$

where K_1 and K_2 represent the calibration coefficients. Fitting equation (7.45) to the measured decay, we found the calibration factors K_1 and K_2.

Moreover, the SAC has been in-situ cross-calibrated with the BD-PNDs.

[7] It is possible to place the SAC to narrow gaps between the oil tanks, but in such a case the SAC will be strongly affected by neutrons scattered by oil.

[8] The energy spectrum of the ^{241}Am-Be neutrons was measured by Thompson and Taylor [109].

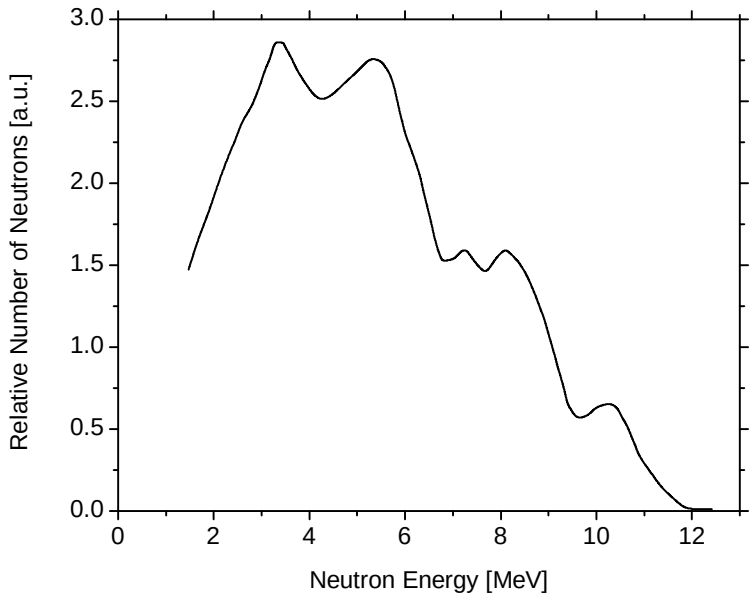

Figure 7.23: Neutron spectrum of the ^{241}Am-Be source [109].

7.3.4 Advantages and Disadvantages of SAC detectors

Advantages:

+ SAC is well known and established method.

+ SAC is not affected by HXRs or EMP[9].

+ It is suitable for the measurement of short neutron pulses.

Disadvantages:

- The calibration by a suitable neutron source is needed.

- Design and calibration of the SAC for a broad neutron energy spectrum are complicated.

7.4 Fast Neutron Activation Diagnostics

In most of similar Z-pinch and plasma focus deuterium fusion experiments, the neutron diagnostics is designed for the energy of 2.45 MeV. However, as mentioned

[9]In the experiments described in this thesis, the SAC is not affected by EMP and HXRs since the measurement result is evaluated by processing of the post-shot decay counting.

above, the energy spectrum of neutron emission in the experiments presented in this work is very broad. In the spectrum we found sub-MeV energies corresponding to scattered neutrons [111] and at the same time neutron energies above 20 MeV [2, 4]. Therefore, the diagnostics which is dedicated to detection of neutrons with the energy in a specific energy range, should not be affected by neutrons with the energy out of this range. This requirement is met by the fast-neutron activation diagnostics based on nuclear reactions with an energy threshold.

The fast neutron activation diagnostics is based on similar principles as the silver activation counter with following differences:

There is an energy threshold at the activation reactions.

The neutrons which activate a sample of some material are not moderated.

In the experiments described in this thesis, we detect only the gamma-rays emitted by the activated sample.

Gamma-ray spectrum analysis is necessary.

7.4.1 Used Neutron Activation Samples

The energy threshold of the nuclear reaction is given by an isotopic content of the sample. For the choice of the sample element, the following requirements are given:

- suitable reaction energy threshold,
- sufficiently high reaction cross-section,
- reasonable half-life of the reaction product,
- product gamma-ray energy in a measurable range,
- sufficient probability of the gamma-ray photon emission,
- isotopic content,
- chemical purity,
- availability and cost.

Obviously, the fundamental requirement is the suitable energy threshold of the nuclear reaction. Another very important parameter is the dependence of the reaction cross-section on the neutron energy. The slope of the cross-section from the threshold energy to the cross-section maximum should be sharp for the better neutron energy resolution. There are also requirements on the value of the reaction cross-section, product half-life, intensity of the gamma-ray lines, isotopic abundance, chemical purity, etc. These requirements are only approximate and typical in the practice (see examples in [92, 112, 113, 114, 117, 118]). For example, a very high cross-section of some reaction could compensate a low isotopic abundance, etc. The sufficient value of the cross-section is dependent on the assumed fluence of neutrons above the energy threshold. Usually, it shouldn't be much less than 0.1 barn. In our experiments, it was shown that the cross-section of about 0.09 barn of the ^{27}Al(n,p)^{27}Mg with the threshold of 3.8 MeV is sufficient. As far as a product of the reaction is concerned, it must be unstable. In the experiments described in this thesis, at least one minute is needed to transport the irradiated activation samples to the gamma-ray spectrometer which is in a different room than the GIT-12 device. Therefore, a half-life of the activated samples should not be less than a minute to make the gamma-ray spectrum analysis possible. At the same time, its half-life shouldn't be longer than a few days due to the weak radioactivity of long-lived isotopes. The energies of gamma-ray photons of the decaying product must allow the gamma-ray analysis by available NaI(Tl) and HPGe gamma-ray spectrometers. The energy of the observed gamma-lines is usually higher than 200 keV. The intensity of these gamma-ray lines in terms of the gamma-ray emission probability is usually higher than 20%. As far as the isotopic abundance is concerned, in our case, the samples were always of the natural content. Usually, the abundance of the isotope acting in the observed nuclear reactions is higher than 20%. At the same time, the natural element mustn't contain any unstable isotopes which affect the gamma-ray spectrum analysis. To prevent any other disturbing reactions we use chemical purity of the samples as high as possible. Since material samples with a chemical purity better than 99% are commercially available we used the samples with such high purity. Of course, the essential requirement is also the cost and availability of samples.

To obtain information about the substantial part of the neutron spectrum, based on these requirements, indium, aluminum, niobium, and copper samples were used.

The total cross-sections of reactions corresponding to these samples are shown in fig. 7.24. The basic features of the fast neutron activation samples are summarized

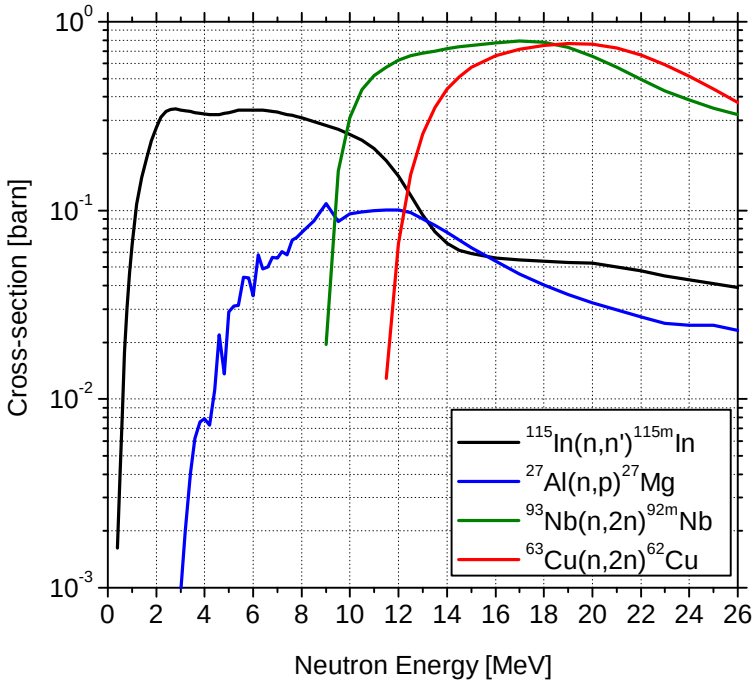

Figure 7.24: Total nuclear reaction cross-sections of the used fast-neutron activation samples: black – indium [119, 120], blue – aluminium [115, 116], green – niobium [115, 116], and red – copper [115, 116].

in table. 7.2.

We will describe the neutron detection from the highest energy threshold to the lowest threshold. In order to evaluate the number of the neutrons with the energy above 12 MeV Y_{12}, the natural copper sample was used. Such a method has been used also on the Z Accelerator at SNL [112] and on the National Ignition Facility (NIF) at LLNL [113, 114]. The copper sample was placed in the radial direction at the distance of 36 cm from the z-axis. The natural copper contains 69% of the ^{63}Cu isotope and 31% of the ^{65}Cu isotope. The only significant reactions of the neutrons with the natural copper which produce unstable isotopes are ^{63}Cu(n,2n)^{62}Cu and ^{65}Cu(n,2n)^{64}Cu. The copper ^{62}Cu undergoes the $\beta+$ decay into ^{62}Ni with the half-life of 9.67 minutes [122]. The half-life of the unstable ^{64}Cu product of the second reaction is 12.7 hours and the decay occurs in two ways: β^+ decay into ^{64}Ni or β^- decay into stable ^{64}Zn with the probabilities of 31.5% and 68.5%, respectively [122].

Isotope	Indium ^{115}In	Aluminum ^{27}Al	Niobium ^{93}Nb	Copper ^{63}Cu
Natural Abundance	96%	100%	100%	69%
Reaction	^{115}In(n,inl)^{115m}In	^{27}Al(n,p)^{27}Mg	^{93}Nb(n,2n)^{92m}Nb	^{63}Cu(n,2n)^{62}Cu
Energy Threshold [MeV]	0.5	3.8	9.5	11.9
Max. Cross-section [barn]	0.32	0.09	0.45	0.8
Product half-life	4.5 hours	9.45 min.	10 days	9.8 min
γ Energy [MeV] (intensity)	0.335 (48%)	0.843 (71.8%) 1.014 (28.2%)	0.934 (99%)	0.511

Table 7.2: The physical parameters of the threshold neutron activation samples used at the experiments on the GIT-12 device in 2015. We used values presented in [92, 115, 116, 122].

Therefore, the annihilation radiation of the irradiated copper sample includes the decay radiation of ^{64}Cu as well as the decay radiation of ^{62}Cu. However, the contribution of ^{64}Cu could be neglected due to 79 times longer half-life and 5.6 times lower relative intensity of the 511 keV annihilation line. As is shown in fig. 7.24, there is the threshold of 11.9 MeV for the ^{63}Cu(n,2n)^{62}Cu reaction. The threshold of the ^{65}Cu(n,2n)^{64}Cu reaction is 10 MeV [115, 116]. Consequently, the copper sample could be activated only by the neutrons with the energy above 10 MeV and neglecting the second reaction, it is above 11.9 MeV or rounded up to 12 MeV. In

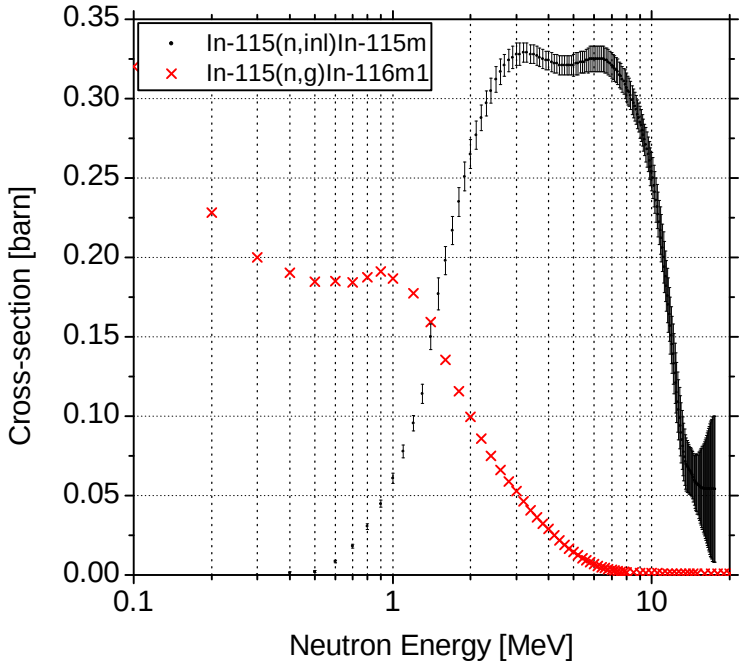

Figure 7.25: Comparison of the cross-section of ^{115}In(n,n')^{115m}In nuclear excitation reaction (dotes) [119, 120] and ^{115}In(n,γ)^{116m1}In neutron radiative capture (crosses) [115, 116].

the same manner as Y_{12}, the yields Y_{10} and Y_4 of neutrons with the energy above 10 MeV and 4 MeV were determined using the niobium and aluminum activation sample, respectively. The only natural isotope of niobium is ^{93}Nb and the observed reaction is ^{93}Nb(n,2n)^{92m}Nb. In the case of natural aluminum, there are two reactions which lead to a significant neutron induced activity, namely ^{27}Al(n,α)^{24}Na and ^{27}Al(n,p)^{27}Mg reactions. Because the half-life of the ^{24}Na isotope is 15 hours, its initial activity is much smaller than the activity of the resulting ^{27}Mg with the

half-life of 9.5 min. Thus, the ^{27}Al(n,α)^{24}Na reaction was neglected and we took into account only the reaction ^{27}Al(n,p)^{27}Mg. We should mention that the interference of gamma radiation from the decay of ^{24}Na to gamma-ray lines on ^{27}Mg decay is excluded because the spectrum of the gamma rays is strongly different. Finally, the indium sample is used to measure the yield of the neutrons with the energy above 0.5 MeV. The indium sample is also applied in order to measure the neutron yield on the PF-1000 plasma focus [117, 118] and at the NIF laser facility [113]. Because the natural indium contains almost 96% of ^{115}In, our diagnostics is based on the reactions with this isotope only. In such a case, there are two significant reactions: the neutron-induced nuclear excitation to the metastable state ^{115}In(n,n')^{115m}In and the neutron radiative capture ^{115}In(n,γ)^{116m1}In. Since a half-life of the ^{115m}In metastable nuclei is 4.5 hours [122], there is sufficient time to perform the gamma-ray spectrum analysis. The deexcitation is accompanied by the gamma photons with the energy of 336.2 keV with the relative intensity of 48% [122].

The product of the radiative capture ^{115}In(n,γ)^{116m1}In with the half-life of 54 minutes is decaying into ^{116}Sn [122]. The gamma-ray spectrum accompanying this β^- decay is more complicated than the previous one. It consists of many lines with different relative intensities. The dependences of the total cross section on the neutron energy of these nuclear reactions are shown in fig. 7.25. The cross-section data plotted in fig. 7.24 of the ^{115}In(n,n')^{115m}In reaction are evaluated by Lapenas and Bondars [119, 120] and exported from the EXFOR nuclear data library. The cross-section of ^{115}In(n,γ)^{116m1}In is exported from the TENDL-2014: TALYS-based Evaluated Nuclear Data Library [115, 116]. As we can see in fig. 7.24, there is not any energy threshold at the ^{115}In(n,γ)^{116m1}In reaction. Therefore, the ^{115}In(n,γ)^{116m1}In reaction is not used for our measurement. To prevent the interference of ^{116m1}In gamma-rays, the indium samples are analyzed the next day after a shot, when the activity of ^{116m1}In is negligible in comparison with ^{115m}In with the quintuple longer half-life. It might be interesting to mention the initial activity of the irradiated samples. The initial activity of the samples is always below 20 kBq. For example, the activity of the sample "In-Big", which is given by a sum of the activities of ^{115m}In and ^{116m1}In is approximately 2 kBq in a typical shot with the neutron yield of about 10^{12}. Therefore, the manipulation of the samples is harmless to our health. As far as the gamma spectrometer is concerned, the $\varnothing$150 mm $\times$ 100 mm cylindrical and $10 \times 10 \times 40$ cm^3 cuboid NaI(Tl) scintillation crystal detectors

Sample name	Material	Shape	Dimensions [mm]	Thickness [mm]	Mass [g]
In 1	Indium	Disk	⌀15.0	4.0	4.849
In 2	Indium	Disk	⌀15.0	4.0	4.822
In 3	Indium	Disk	⌀15.1	4.0	4.848
In 4	Indium	Disk	⌀15.1	4.1	4.994
In 5	Indium	Disk	⌀15.1	4.1	4.977
In 6	Indium	Disk	⌀15.1	4.1	4.849
In 7	Indium	Disk	⌀15.1	4.1	5.000
In A	Indium	Disk	⌀26.0	1.6	5.257
In B	Indium	Disk	⌀26.1	1.6	5.283
In C	Indium	Disk	⌀30.0	1.0	5.113
In D	Indium	Disk	⌀30.0	1.0	5.174
In V	Indium	Rectangle	50.2×35.3	3.0	35.4
In VI	Indium	Rectangle	50.3×35.5	3.0	36.2
In Big	Indium	Rectangle	103.1×69.2	3.0	108.7
Al	Aluminum	Rectangle	101.2×81.0	2.8	31.7
Cu	Copper	Rectangle	103.0×69.2	3.1	215.7
Nb	Niobium	4× Cylinder	$4 \times ⌀12 \times 50$	-	34.1

Table 7.3: The used neutron activation samples.

and HPGe detector Canberra are used. The experiments showed that for the analysis of the copper, aluminum and indium samples, the NaI(Tl) spectrometers with a lower spectral resolution than the HPGe are sufficient. However, we used the HPGe detector always when it was possible. As far as the analysis of the niobium sample is concerned, the HPGe detector must be used every time, because of the 10-days long half-life of the ^{93}Nb.

The list of all activation samples with their geometry and mass is presented in table 7.3. The various indium samples were placed at different distances and angles with respect to the Z-pinch discharge in order to evaluate an anisotropy of the neutron production and other features like the point of neutron production, the influence of the photo-activation of the indium sample, etc.

The indium samples V, VI, Big, Aluminum sample, and Copper sample were placed outside the vacuum chamber in the radial direction at the distance of 37 cm in each experimental shot. The Niobium sample was placed outside the chamber in the radial direction at the distance of 32 cm. The layout of the activation samples which are placed outside the chamber is displayed in fig. 7.26. As far as the indium

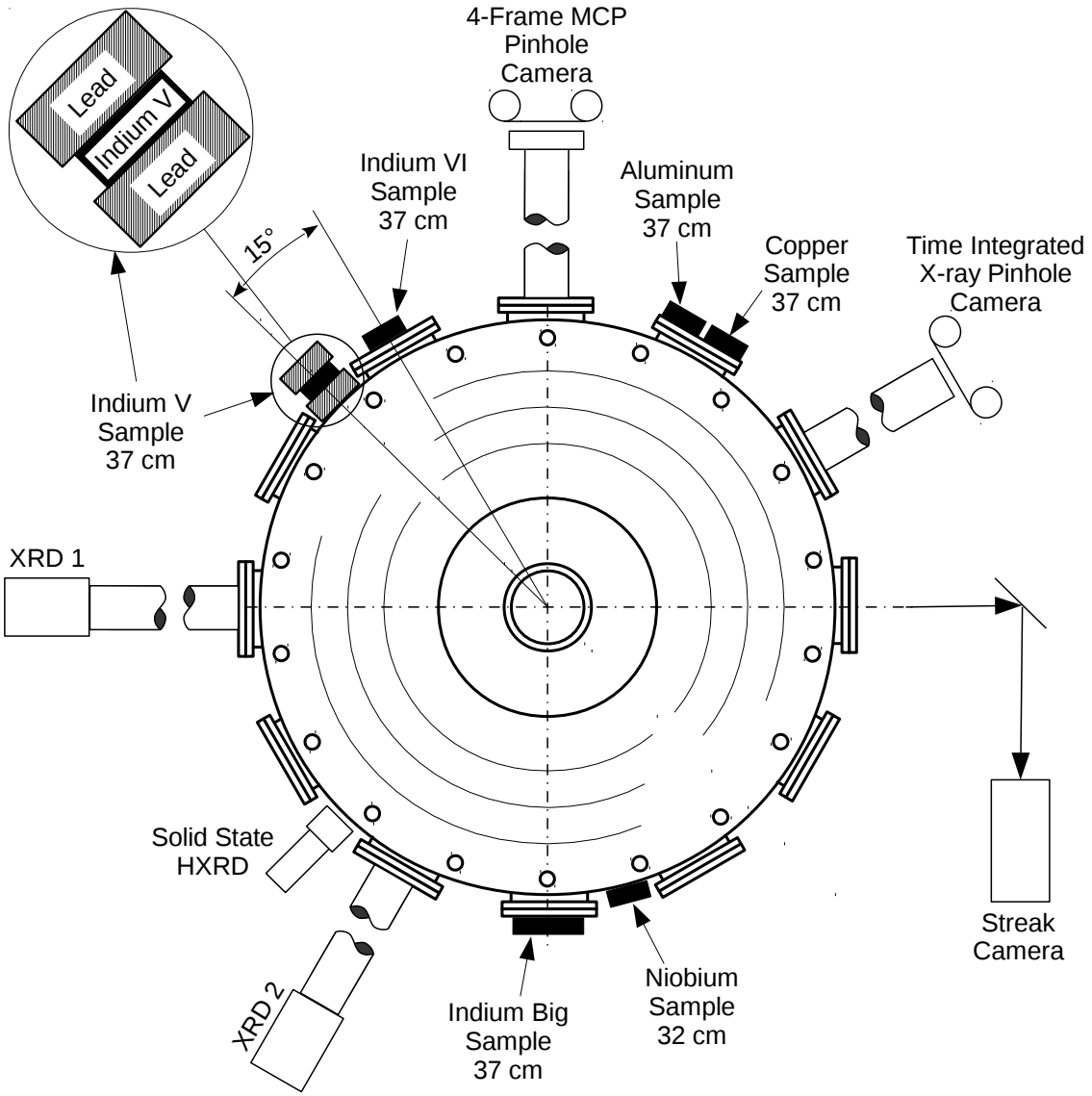

Figure 7.26: Layout of the activation samples which are placed outside the vacuum chamber and other diagnostics.

samples A-D and 1-7 are concerned, their arrangement often differs in dependence on the experimental shot settings. Their layout is described individually in the

following sections.

To have a better information about the experiment, other diagnostics as vacuum x-ray diodes (XRD1 and XRD2), a Hard x-ray solid-state diode (HXRD), time-integrated x-ray pinhole camera, and gated 4-frame soft x-ray and ultraviolet MCP pinhole camera are displayed in fig. 7.26.

7.4.2 Gamma-ray Spectrometers

Gamma-rays of the irradiated activation samples are analyzed by gamma-ray spectrometers. The gamma-ray spectrometers are systems composed of the detector, electronic circuits, and data acquisition software. The first stage in this chain is the gamma-ray detector. In the experiments reported in this thesis, the HPGe and NaI(Tl) detectors are used. Such detectors are the most common detectors in the gamma-ray spectroscopy and they are described in more detail in the following sub-subsections.

The next part of the spectrometer is a preamplifier, however, in the case of NaI(Tl) with PMT, it could be omitted. While in the case of NaI(Tl) spectrometry, if it is used, the preamplifier could be voltage-sensitive or current-sensitive, in the case of HPGe the preamplifier is always charge-sensitive. Essentially, the charge-sensitive preamplifier is an integrating amplifier (integrator). After every collision of a photon with the detector, the integrator collects the charge carried from the detector. The height of the preamplifier output pulse is proportional to the charge. Usually, the integrator is composed of low-noise voltage amplifier with passive resistor-capacitor feedback. The capacitor is collecting the charge during the integration and resistor slowly discharges the capacitor and reset the integrator to be ready for the next integration (detected photon). In the case of high rate spectrometers, the integrator is reset by active feedback with a transistor. A rise time of the passive feedback preamplifier is on the order of tens or hundreds of nanoseconds and decay on the order of tens or hundreds of microseconds [99]. Obviously, due to the long decay of the preamplifier output, a pile-up of pulses may occur. Therefore, the preamplifier output pulses must be shaped before the pulse height analysis. Earlier it was achieved using analog shaping circuit with differentiation-integration circuit embedded in an amplifier module. It should be noted that to conserve the linearity, the circuits had to be very precise. We can still meet such shaping amplifiers at

NaI(Tl) spectrometers. The modern high-resolution HPGe spectrometers use for pulse shaping a digital signal processing [99]. Besides amplification and shaping, the amplifier module also detects the pile-up pulses and restores the output baseline [99].

The signal processed in amplifier module is coupled to the pulse height analyzer. In the multichannel analyzer, the pulses are sorted by height and the number of pulses within the individual pulse height intervals is counted [92, 99]. Afterwards, this histogram is processed with a help of computer software.

All types of detectors are characterized by the following basic parameters.

Energy Resolution

Obviously, the most fundamental parameter of the detector is the energy range and energy resolution. The energy resolution of the detector characterizes its ability to resolve two energetically close peaks. It is closely related with FWHM of the full-energy peak in the spectrum [92, 99, 107]. Usually, it is assumed, that the peaks are clearly separated when the centroids of Gaussian peaks are 3 × FWHM apart. However, using a spectrum analysis software it is usually possible to resolve peaks only 1 × FWHM apart, see fig. 7.27 [99].

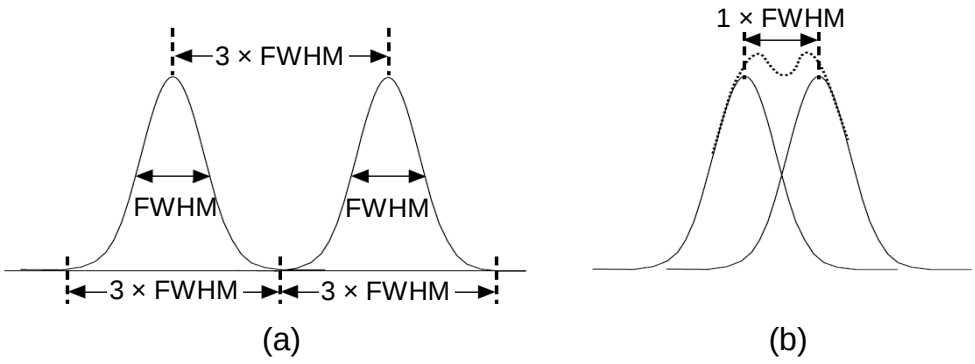

Figure 7.27: (a) Gaussian peaks 3 × FWHM apart, (b) Gaussian peaks 1 × FWHM apart [99].

Total Efficiency

The equally important feature as the energy resolution is the detection efficiency. The fundamental definition of absolute photon detection efficiency is [107]:

$$\epsilon_{tot} = \frac{N_{FEP}}{N_S} = \frac{N_{FEP}}{A\, I_\gamma}\Delta T \tag{7.46}$$

where N_{FEP} is a number of counts in the full-energy peak, N_S is a number of the photons emitted by the source, A is its activity in Becquerels, I_γ is the probability of the gamma-photon emission, and ΔT is the duration of the counting (analysis). The total efficiency is composed of the following components [107]:

$$\epsilon_{tot} = \epsilon_{geom}\epsilon_{absp}\epsilon_{sample}\epsilon_{int} \tag{7.47}$$

The first term ϵ_{geom} represents the geometric factor. For a point isotropic source, ϵ_{geom} is given by

$$\epsilon_{geom} = \frac{S}{4\pi d^2} \tag{7.48}$$

where S is an area of the detection surface projection and d is the distance from the source to the detector [107].

The absorption efficiency ϵ_{absp} includes the absorption of the radiation by matter between the radiation source and the detector. The absorption could be undesirable (detector housing, air, etc.) but also desirable (absorbers, filters, etc.) The undesirable absorption is usually significant in the case of the low-energy photon detection. It can be evaluated as

$$\epsilon_{absp} = \exp\left[-\sum \mu_i(E_\gamma)\rho_i x_i\right] \tag{7.49}$$

where μ_i is the mass absorption coefficient, ρ_i is the density, and x_i is the thickness of the i-th absorbing material [107].

The sample efficiency ϵ_{sample} represents the self-absorption of the sample. In the simple case of an area source, the self-absorption efficiency is approximately

$$\epsilon_{sample} = \frac{1 - e^{-\mu_s\rho_s x_s}}{\mu_s\rho_s x_s} \tag{7.50}$$

where μ_s is the mass absorption coefficient of the sample, ρ_s is the density of the sample, and x_s is the thickness of the plate source [107].

The last term in (7.47) is the intrinsic efficiency ϵ_{int} specifying the probability that a photon entering the detector will contribute to the full-energy peak [107]. It

is very complicated to determine this parameter because it is dependent on many factors such as geometry, chemical content, crystal structure, temperature of the detector, energy of the photon, noise of the detection and electronics, etc. However, in practice it could be approximated experimentally with a help of empirical power law [107]:

$$\epsilon_{int} \propto E_{\gamma}^{-b} \tag{7.51}$$

It should be noted that currently, the very precise evaluation of all efficiency components is using Monte Carlo codes, especially in the cases of geometrically complicated configurations. Nowadays, all manufacturers of the detectors usually provide simulation software based on Monte Carlo codes with models of the detectors.

Relative Efficiency

The relative efficiency is a practical comparison of efficiencies of various detectors with the standard NaI(Tl) scintillation detector. It is defined as the percent ratio of total efficiency ϵ_{tot} of a detector to the total efficiency $\epsilon_{NaI-tot}$ of the NaI(Tl) cylindrical scintillation detector with dimensions $\varnothing\, 3 \times 3$ inches ($\varnothing\, 7.62 \times 7.62$ centimeters) for the photon energy of 1332 keV from the standard ^{60}Co radiation source at 25-cm source-to-detector distance:

$$\epsilon_{rel} = 100\, \frac{\epsilon_{tot}(1332keV)}{\epsilon_{NaI-tot}(1332keV)} \tag{7.52}$$

Maximum Count Rate

The maximum count rate is related to a dead time of the detector. This is the time needed for relaxation (decay) of the detector and signal processing, thus it is dependent on the whole detecting system. In practice, if the maximum count rate is exceeded, two situations may occur. The first one occurs if a gamma-ray photon enters the detector in the dead time when the detecting system is insensitive. In such a case, the photon will not be detected and the dead time will not be extended. Another situation is if the photon enters the detector at the dead time when the detecting system is sensitive. In this case, the pile-up will occur and the dead time will be extended.

Other parameters

Many other parameters are defined for the detection of ionizing photon radiation. However, their description is beyond the scope of this thesis. We can shortly note the full-energy-peak/Compton-peak ratio, full-energy-peak/Compton-continuum ratio, spatial resolution, shape of the output pulse, etc.

Comparison of NaI(Tl) and HPGe

From point of view of the energy resolution, the HPGe detectors are much better than the NaI(Tl), see table 7.4. However, the NaI(Tl) detector has also some advantages. It is much cheaper, therefore in applications where high energy resolution is not needed the NaI(Tl) detector could be an economically preferable choice. The second advantage of NaI(Tl) is the availability of much larger dimensions than HPGe. The next advantage of NaI(Tl) is that the cryogenic cooling is not needed. It allows a simple construction of portable "hand-held" gamma-ray spectrometers. Nevertheless, in most of the applications of gamma-ray spectrometry the HPGe detectors are much better than NaI(Tl).

Detector type	FWHM at 0.661 MeV	FWHM at 1.332 MeV	Relative efficiency
NaI(Tl) cylinder 3×3 inch.	30 – 50 keV[a]	80 keV[b]	100 %
HPGe standard p-type coaxial	0.794 keV[b]	1.75 – 2.30 keV[c]	10 – 150%[c]

Table 7.4: The usual parameters of detectors used in gamma-ray spectrometry. These parameters could somewhat differ in various literature. Obviously, it is mostly dependent on the quality of the crystals and electronics (photomultipliers, multichannel analyzers, etc.) which is continuously improving. [a]Knoll and Gilmore [92, 99], [b]Gilmore [99] and [c]Web-sites and data-sheet of Ortec company[104].

7.4.3 HPGe Gamma-ray Spectrometer

The gamma-ray spectrometer with HPGe detector is a very important diagnostic instrument in the experiments reported in this thesis. Therefore, in this subsection,

the HPGe gamma-ray spectrometer is described. At the beginning, we shortly introduce the general principles of the detection of ionizing radiation by semiconductors. It is well known, that there is a band-gap of the order of eV between the valence and conduction band in the electronic band structure. The probability that an electron will be promoted to the conduction band is dependent on the temperature [99]:

$$p(T) \propto T^{3/2} \exp\left(-\frac{E_g}{2kT}\right) \tag{7.53}$$

where T is the temperature, E_g is the band-gap energy and k is the Boltzmann constant. Thus, in semiconductors which are absolutely pure (intrinsic semiconductors), the thermal excitation could promote a certain number of electrons from the valence band to the conduction band [99]. However, it is impossible to make such absolutely pure semiconductor and the impurities lead to significant conductivity and current flow. Such current is more significant than current related to collisions of gamma-ray photons with the semiconductor material [99]. Therefore the following structure is used. Adding a trivalent dopant (for example gallium or boron) to the tetravalent semiconductor, a hole able to maintain an electron arises in the crystal lattice. The hole is free and it behaves as a positive charge carrier. Such semiconductor is the positive-type or p-type. Similarly, adding a pentavalent dopant, for example, arsenic or phosphor, a free electron – negative charge carrier arises. Such semiconductor is the negative-type or n-type. If some piece of semiconductor contains both types of dopants, the type of semiconductor will be determined by the major charge carrier. Using a suitable technology, a semiconductor with p-n junction could be prepared and a diode is formed. Due to thermal diffuse, some of the holes from the p-side move to the n-side of the junction and electrons from the n-side to the p-side. Around the physical junction, the remaining holes meet the remaining electrons and combine together. Consequently, this region will be free of all charge carriers and across the junction the diffusion voltage arises (in germanium of about 0.4 V). It is called depletion region and it is the active region of the detector [99]. The number of hole-electron pairs produced in the depletion region is proportional to the energy expended by the incident photons in this region [102]. The width of the depletion region w can be approximated by following formula [92, 99]:

$$w \approx \sqrt{\frac{2\varepsilon\left(V_0 + V_b\right)}{en}} \tag{7.54}$$

where ε is the permittivity, e is the elementary charge, n is a concentration of impurities in the bulk semiconductor material, V_0 is the diffusion voltage and V_b is the bias voltage. The positive bias voltage is connected to the n-type semiconductor, therefore the junction is reverse biased. In accordance with (7.54), the width of the depletion region is increasing with the reverse bias voltage. Since, as mentioned above the depletion region is the active (sensitive) region, it is desirable to be as wide as possible. Thus, also the bias voltage should be as high as possible, but less than the breakdown voltage of the material. We note that a non-reverse biasing will lead to narrowing of the depletion region. If the non-reverse bias voltage exceeds the diffusion voltage, the depletion region disappears and diode current is uncontrolled. As far as the width of the depletion region is concerned, the other variable in (7.54) is the concentration of impurities n. In practice, the detectors must be manufactured from a material with extremely high purity approximately 10^{10} atoms per cm^3 [92]. Such purity is achieved only in germanium[10]. It is called high-purity germanium (HPGe)[11]. As far as the reverse bias voltage are concerned at the germanium detectors the reverse bias voltage is usually (1 – 3) kV.

In accordance with the equation (7.53), at the room temperature, some hole-electron pairs will be produced by thermal excitation. Such hole-electron pairs allow a current flow which at the mentioned high voltage bias will lead to the destruction of the semiconductor structure. Therefore the germanium detectors must be cooled by a liquid nitrogen[12].

The HPGe detectors are made in planar, semi-planar and coaxial configuration. The coaxial configuration could be fabricated in n-type coaxial and p-type coaxial (standard electrode) structure, see fig. 7.28.

When the semiconductor material is considered, both germanium and silicon are

[10]High-purity has not been achieved in the silicon, because of higher melting temperature (1410°C versus 959°C for germanium). This difference makes the purifying by zone refine more difficult.

[11]Sometimes the HPGe is called intrinsic germanium, this is incorrect, because the used semiconductor is not intrinsic [99].

[12]The HPGe detectors must be kept in cryogenic temperature when the bias voltage is connected, but earlier used lithium-drifted germanium detectors Ge(Li) must be kept at liquid lithium temperature always, even if they are not in operation. In Ge(Li), lithium is used to compensate p-type impurities in the germanium crystals. Violation of the cryogenic conditions a diffusion of lithium in the crystal occurs and the carefully created balance of impurities will be destroyed. The Ge(Li) detectors were fully superseded by the HPGe detectors [99].

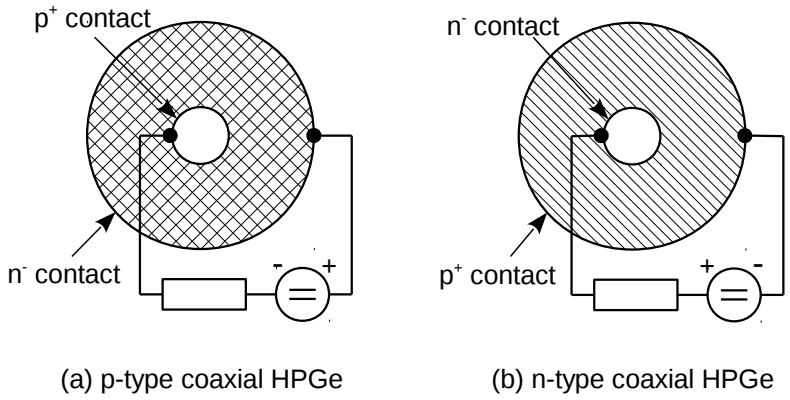

Figure 7.28: Structure of the HPGe detector [92].

used for ionizing photon detection. However, due to the lower atomic number of silicon (14 versus 32 of germanium), the absorption of gamma-ray photons is weaker than in the case of germanium. This is another reason why the most common gamma-ray spectrometer detectors are based on germanium[13]. The modern technologies allow a preparation of the high-purity germanium and the HPGe detectors have replaced the other types such as lithium-drifted germanium Ge(Li).

The HPGe gamma-ray spectrometer which is used in the experiments reported in this thesis is equipped with Canberra GC5019 p-type coaxial detector. A simplified scheme of the spectrometer with GC5019 is shown in fig 7.29. The HPGe detector is shielded by lead with a thickness of 5 cm. The amplifier, bias voltage supply, multichannel analyzer, and temperature diagnostic electronics are embedded in the Canberra DSA 1000 digital spectrum analyzer compact module. This module was connected to the personal computer by USB interface.

The scheme in fig. 7.30 describes the connection of detector to the electric circuit of the bias, signal output, and temperature protection. As far as the high-voltage bias is concerned, the output of the high-voltage source is filtered by the resistor-capacitor (RC) low-pass filter with a very large time constant which ensures that the voltage is gradually applied to the detector and protects the electronics from high-voltage spikes. The detector element is sealed in cryogenic vacuum enclosure together with a field-effect transistor (FET) and feedback elements of the charge-sensitive preamplifier and the temperature sensor. The FET represents a first stage

[13]Various silicon detectors are commonly used for detection of x-rays, electron and ion radiation.

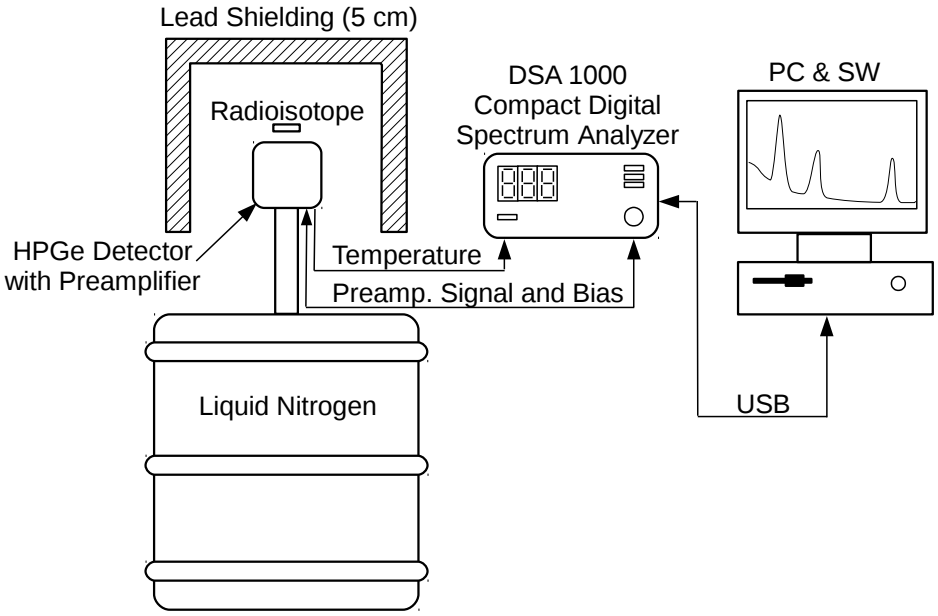

Figure 7.29: Scheme of the gamma-ray spectrometer with the HPGe Canberra GC5019 detector.

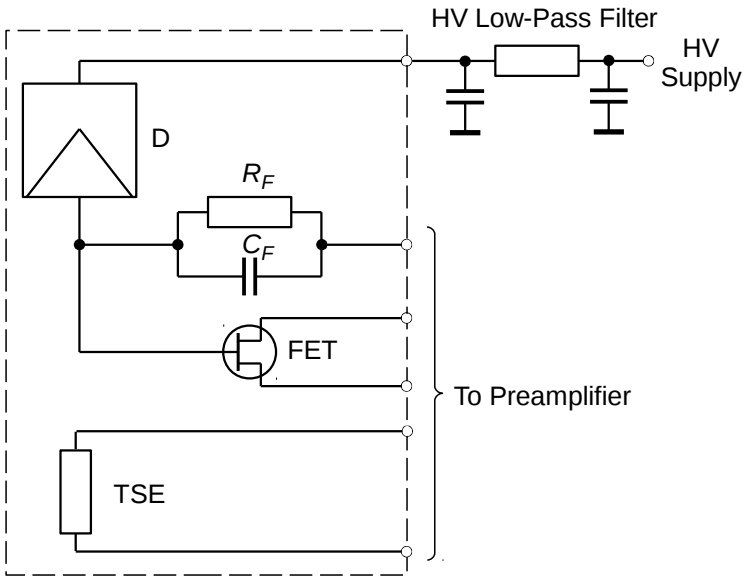

Figure 7.30: Simplified electric diagram of the HPGe detector: D - detector, C_F feedback - capacitor, R_F - feedback resistor, FET - Field effect transistor, TSE - Temperature-sensing element(thermistor) [104].

of the charge-sensitive preamplifier which is reset by the feedback[14]. The cryogenic temperature of these elements minimizes electronic noise [104]. If the temperature exceeds the allowed range it is detected by the temperature-sensing element and the protective circuit (usually embedded in the preamplifier housing) promptly unplugs the detector from the high-voltage power supply.

7.4.4 NaI(Tl) Gamma-ray Spectrometer

Although for our purpose the HPGe spectrometers significantly surpass the scintillation spectrometers (except the cost), sometimes the usage of the scintillation spectrometer could be sufficient. It is advantageous especially when a set of the activation samples with a short half-life is used and their simultaneous gamma-ray spectrum analysis is needed. Of course, it is necessary to know, when it is possible to use the scintillation spectrometer and at the same time, the accurate calibration is needed.

In the experiments reported in this thesis, the sodium-iodine crystal activated by thallium (NaI(Tl) or shortly NaI) was used. These scintillators excel in the efficiency of gamma detection. In accordance with the above-mentioned mechanisms of interaction of photons with a detector, the produced primary electrons raise secondary electrons to the conduction band, leaving holes in the valence band of the atoms of the detector. Because the band gap of sodium-iodine is large the de-excitation photons are far outside the visible light. Moreover, the sodium-iodine is not transparent to such photons. In order to make a detection of scintillation flashes easier, a suitable activator is used. In the case of sodium-iodine, of about 10^{-3} mol fraction of thallium activator creates defects in the crystal lattice and extra levels arise within the band gap [99]. The de-excitation photons from such levels are in visible range and the scintillator matter is transparent for them. If the transition from an excited state to the ground is allowed, its lifetime is short (in the case of NaI(Tl) on the order of 100 ns and in the case of organic scintillators it could be less than 1 ns). Such prompt emission is called fluorescence. If the transition from an excited state to the ground is forbidden, the lifetime of the excited state is much longer. The electron must be firstly promoted by thermal excitation to a level which allows

[14]The passive resistor-capacitor feedback is used up to rate of 75 000 collisions per second, for higher rates the transistor-reset amplifiers with active feedback are used [104].

the de-excitation. It is termed phosphorescence referred to as afterglow [99]. In the case of NaI(Tl) the decay time is 0.15 s and represents 9% of total light output [99]. It should be noted, that at NaI(Tl) only of about 12% of the total absorbed energy is converted to the visible light. Remaining energy is retained as lattice vibrations or heat [99]. The visible scintillations are usually converted into an electrical signal using a photomultiplier.

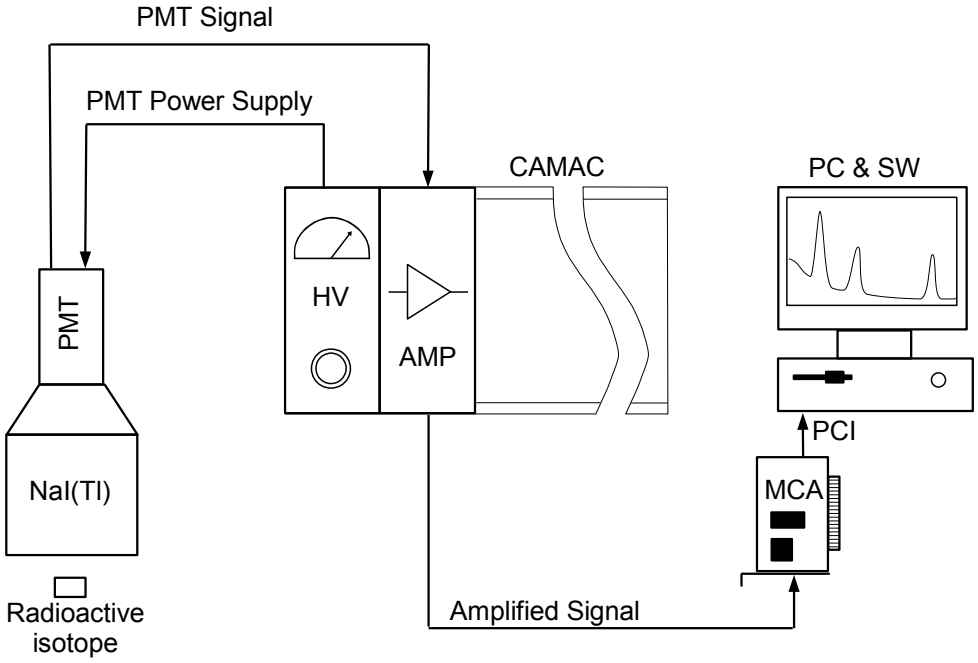

Figure 7.31: Scheme of the gamma-ray spectrometer with the NaI(Tl) detector. PMT - Photomultiplier Tube with a voltage divider, HV - High Voltage power supply, AMP - Active filter amplifier, MCA - Multichannel Analyser, PCI - Peripheral Component Interconnect

In the experiments reported in this thesis, two types of NaI(Tl) detectors were used. In 2014 and 2015, we used the cylindrical crystal with the diameter of 15 cm and height of 10 cm. This crystal was coupled to ФЭУ-49Б (FEU-49B) photomultiplier with an antimony-potassium-cesium photocathode with the diameter of 15 cm. In 2016 and 2017 we used the cuboid crystal with dimensions $10 \times 10 \times 40$ cm^3. We used the same electronics of both gamma-ray spectrometers. The output of the photomultiplier was thousandfold amplified with a help of the POLON 1101 active filter amplifier. The pulse height analysis was performed by АЦП-8К-П1 (ACP-

8K-P1) multichannel analyzer (MCA) manufactured by Amptek, Inc. The MCA is in form of computer PCI card and its resolution is 8 192 channels. The scheme of the gamma-ray spectrometer with the NaI(Tl) scintillation detector is shown in fig. 7.31.

The obtained spectra were processed by the Spectraline software which allows us to detect the peaks and evaluate their background radiation pedestal.

7.4.5 Background Radiation

The natural background radiation is omnipresent and includes the cosmic radiation and decay radiation of radionuclides. Whereas an energy of the cosmic gamma-ray photons is usually random, the spectrum of radionuclide decay could interfere with the gamma-ray spectrum of the analyzed activated sample. The origin of such radionuclides could be natural or artificial (anthropogenic). The natural radionuclides fall into three categories: primordial radionuclides, secondary radionuclides, and cosmogenic radionuclides. The primordial radionuclides, for example, ^{235}U, ^{238}U, and ^{232}Th have been produced in the stellar nucleosynthesis and supernova explosions. Such radionuclides still remain on Earth due to their long half-life. The products of the primordial radionuclides decay are the secondary radionuclides. The secondary radionuclides are represented for example by the ^{40}K, ^{226}Ra, ^{210}Pb, etc. The cosmogenic radionuclides, for example. ^{14}C, ^{7}Be, ^{3}H, etc. are produced by the interactions of cosmic rays with the atmosphere. As far as the artificial radionuclides are concerned, they are produced by the nuclear accidents, weapon tests, nuclear research, medicine, etc.

This radiation could be reduced, but even with a thick lead shielding (in our case 5 cm) we can not completely prevent the penetration of the background radiation to the detector. Therefore, the background radiation spectrum was measured in situ. The background radiation detected by the HPGe gamma-ray spectrometer is displayed in fig. 7.32. The live time of this measurement was 32 hours because the HPGe spectrometer was used also for the gamma-ray analysis of the relatively long-lived samples with a low activity (for example ^{92m}Nb with the half-life of 10.15 days) where such long measurement times were assumed. The list of the detected peaks with the numbers of counts and rates (number of counts per second) is shown in table 7.5. Some of the peaks were easily identified since they correspond to the decay of the common natural radionuclides like ^{226}Ra and ^{40}K (the most significant). Other peaks correspond to radionuclides of uranium decay chain (^{214}Pb and ^{214}Bi) and thorium decay chain (^{228}Ac). The 511 keV peak corresponds to every β^+ decay. Some peaks were not exactly identified. Such peaks correspond to the energy of gamma-rays of decay of the known radionuclides, but their abundance in nature is improbable. An explanation could be given by the used lead bricks with unknown history. We know only that, it was used in the nuclear reactor laboratory and

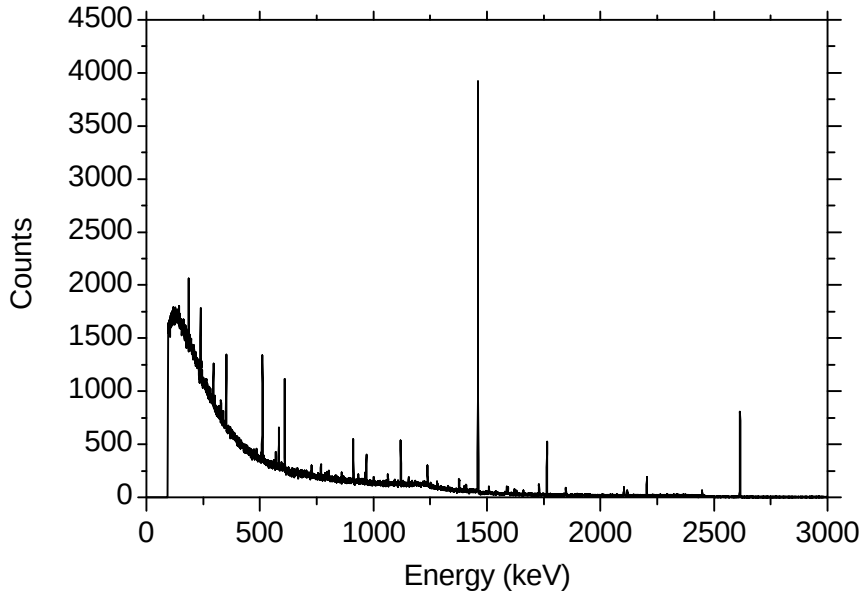

Figure 7.32: The background radiation of the Canberra GC5019 shielded by 5 cm of lead (live time of the measurement 32 hours).

the non-natural radionuclides may be produced by the neutron capture during a long exposition. The identification of these peaks is possible, nevertheless, for our purpose, it is sufficient to know their energy and rate. As we can see in table 7.5, the only possible interferences are at the energies 511 keV (interference with ^{62}Cu) and 911 keV (close to 934 keV ^{92m}Nb). In the case of 511 keV, the detection rate of the activated copper sample is usually much higher than the background. As far as the 911 keV peak is concerned, if the spectrometer is correctly calibrated it should be easy to distinguished 911 keV peak from the 934 keV peak of ^{92m}Nb since the resolution of the HPGe detector is of about 1 keV at this energy region (see table 7.4). However, the peak at energy of 934 keV from the ^{214}Bi decay collides with the peak of ^{92m}Nb decay. This contribution must be corrected.

As far as the background radiation of the NaI(Tl) spectrometers is concerned, it is displayed in fig. 7.33. This background radiation was measured for 30 minutes. We assume that the sources of the background radiation are the same as in the case of the HPGe spectrometer. As we can see in fig. 7.33, the only significant peaks are 352 keV (^{214}Pb), 511 keV, 609 keV (^{214}Bi), 1120 keV (^{214}Bi), strong 1460 keV corresponding to ^{40}K, 1764 keV (^{214}Bi), and peak which raised by merging of peaks with the energy of 911 keV, 934 keV and 969 keV.

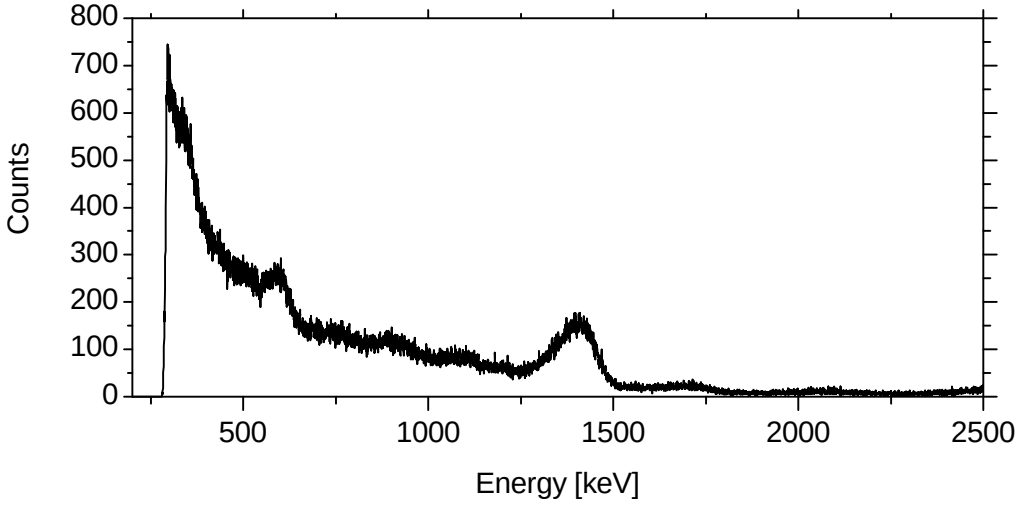

(a) ø15 cm x10 cm Cylindrical NaI(Tl)

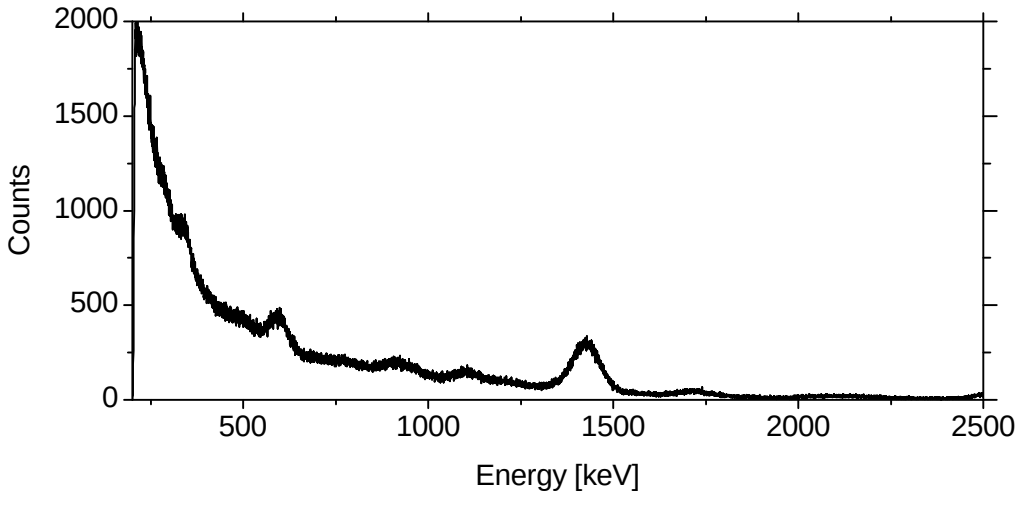

(b) 10 x10 x 40 cm^3 Cuboid NaI(Tl)

Figure 7.33: The background radiation of the gamma-ray spectrometers with NaI(Tl) detector (live time of the measurement 30 minutes).

Energy [keV]	Counts [-]	Rate [1/second]	Radionuclide	Possible Interference
186	1774	1.54×10^{-2}	^{226}Ra	no
238	1787	1.55×10^{-2}	^{214}Pb	no
241	485	4.20×10^{-3}	^{214}Pb	no
295	1204	1.04×10^{-2}	^{214}Pb	no
328	560	4.86×10^{-3}	^{228}Ac	no
352	2486	2.16×10^{-2}	^{214}Pb	no
511	3522	3.06×10^{-2}	-	^{62}Cu
529	492	4.27×10^{-3}	-	no
583	1268	1.10×10^{-2}	-	no
609	3192	2.77×10^{-2}	^{214}Bi	no
728	399	3.46×10^{-3}	^{214}Bi	no
768	579	5.03×10^{-3}	^{214}Bi	no
911	1730	1.50×10^{-2}	^{228}Ac	Close to ^{92m}Nb
934	579	3.75×10^{-3}	^{214}Bi	^{92m}Nb
969	1038	9.01×10^{-3}	^{228}Ac	no
1120	1852	1.62×10^{-2}	^{214}Bi	no
1239	886	7.69×10^{-3}	^{214}Bi	no
1377	578	5.02×10^{-3}	^{214}Bi	no
1407	304	2.64×10^{-3}	^{214}Bi	no
1460	22265	1.93×10^{-1}	^{40}K	no
1509	326	2.83×10^{-3}	^{214}Bi	no
1729	465	4.04×10^{-3}	^{214}Bi	no
1764	2696	2.34×10^{-2}	^{214}Bi	no
2103	447	3.88×10^{-3}	-	no
2203	1058	9.18×10^{-3}	^{214}Bi	no
2614	5430	4.71×10^{-2}	-	no

Table 7.5: List of the detected peaks in the background radiation spectrum (Live time of measurement 32 hours)

.

7.4.6 Calibration of Gamma-ray Spectrometers

In the neutron activation diagnostics, the correct calibration of the gamma-ray spectrometer is crucial. The efficiency of the gamma-ray detection is dependent on the photon energy, material of the activated sample, its thickness, shape, and mutual position of the sample and detector.

7.4.6.1 Calibration of HPGe Spectrometer

The gamma-ray spectrometer with the Canberra GC5019 HPGe was calibrated with the help of the Canberra LabSOCS (Laboratory Sourceless Object Calibration Software). The LabSOCS uses the Monte Carlo modeling code for the determination of the energy/efficiency/spatial response profile [105]. This software allows the very precise calibration which includes the geometry and absorption (for illustration see fig. 7.34). The influence of the lead shielding is not included in this model because

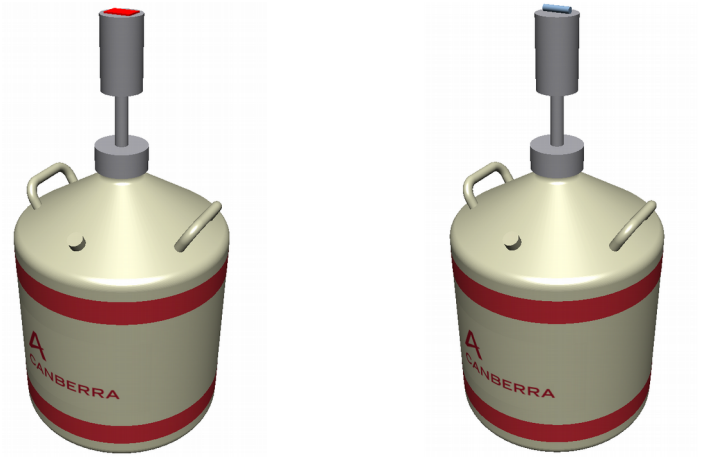

(a) Rectangle indium sample (b) Cylindrical niobium sample

Figure 7.34: Model of the geometry of the indium and niobium sample during the analysis by the HPGe spectrometer.

we have access only to a limited version which did not allow to include it. Nevertheless, we assume that the influence of the lead shielding is negligible for our purpose. The efficiency characteristics of the GC5019 HPGe detector for each used activation sample are displayed in fig. 7.35. The highest detection efficiency is evaluated for the samples In-A, In-B, In-C, and In-D since they are much smaller than the

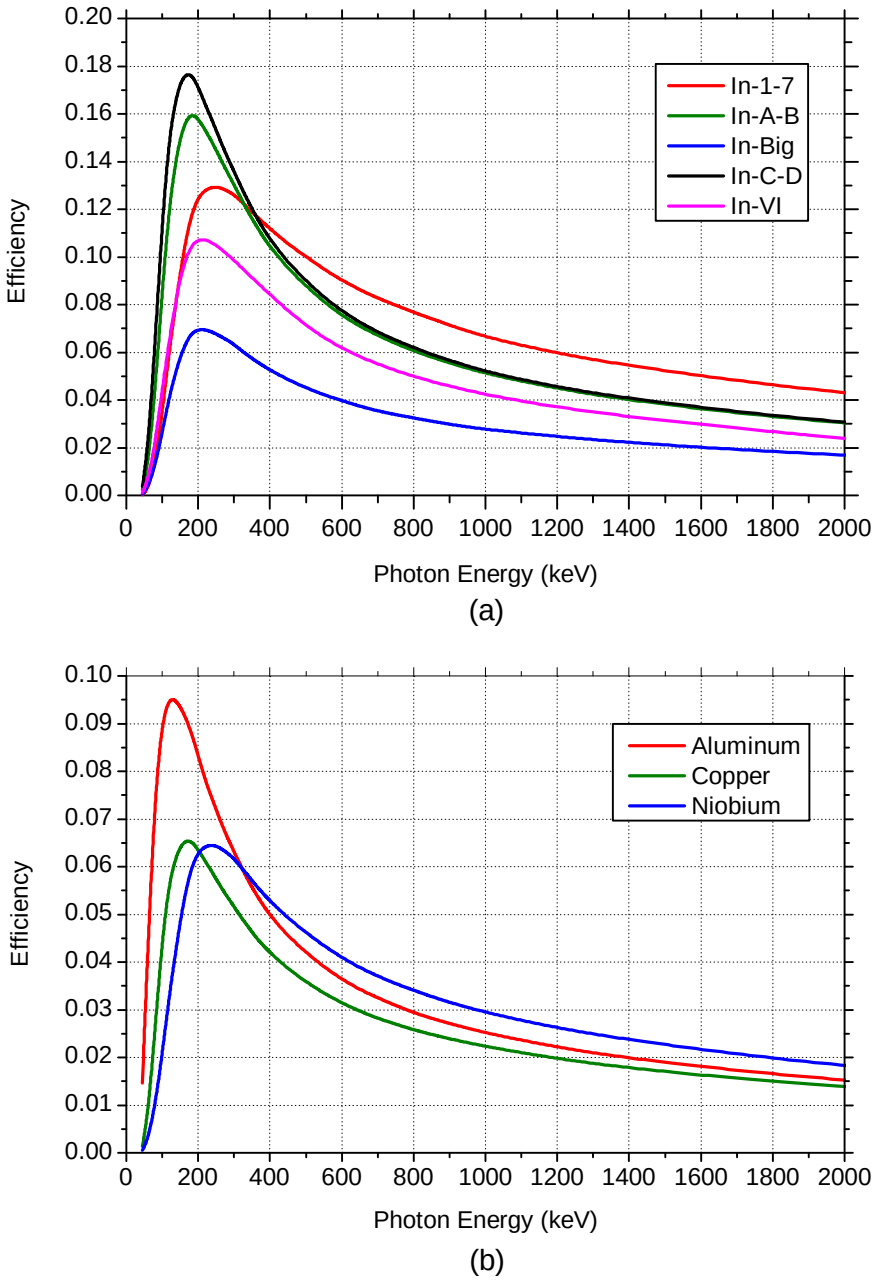

Figure 7.35: Full energy peak efficiency calibration of the HPGe gamma-ray spectrometer Canberra.

detector surface and they are thin in comparison with the other indium samples. The samples In-1-7 are also relatively small, but they are thicker than the samples In-A-D, therefore a bigger portion of the gamma-rays is absorbed within the sample volume and the detection efficiency is lower. Even smaller detection efficiency is

obtained for samples In-V and In-VI since they are also thick and their dimensions are close to the dimensions of the detector. The lowest detection efficiency of the indium sample In-big is caused by the large sample dimensions which overlap the dimensions of the detector.

To be sure, that there is not any systematic error in our calibration simulations, we tested the fidelity of the simulations using the laboratory calibration radionuclides with known activity. The calibration simulations were performed analogously to the case of the activation samples. The testing was performed by the measurement of the sample activity. We tested two geometries for each laboratory sample: when the sample was tightly attached (at the distance of 0 mm from the detector surface) and when the sample was placed at the distance of 80 mm from the detector. In both cases, the sample was placed on the axis of the detector. The results of such measurement are presented in table 7.6. The uncertainties of the measured activities

Sample	Nominal Activity	Measured Activity	
		0 mm	80mm
Cs-137 no. N278	(47.3 ± 5.0) kBq	(47.2 ± 1.0) kBq	(49.5 ± 2.2) kBq
Co-60 no. V210	(1.04 ± 0.10) kBq	(0.99 ± 0.10) kBq	(1.21 ± 0.10) kBq

Table 7.6: Verification of the LabSOCS software modeling.

were evaluated by the Genie 2000 software including the LabSOCS calibration and peak surface error. The measured activities of the laboratory samples correspond to the nominal values in limits of sample activity tolerance and the uncertainties of the measurements. Therefore, we assume that the calibration is correct also for the activation samples.

7.4.6.2 Calibration of NaI(Tl) Spectrometer

The dimensions of the used NaI(Tl) detectors were relatively large, namely: $10 \times 10 \times 40$ cm^3 and $\varnothing 15$ cm $\times$ 10 cm. The limited version of the LabSOCS calibration software which was available for our experiment did not allow the calibration of NaI(Tl) detectors with such dimensions and the full version of this software is relatively expensive. Therefore the NaI(Tl) spectrometers were calibrated with the set of laboratory calibration sources and cross-calibrated with the HPGe detector.

As far as the calibration sources are concerned, we used ^{152}Eu, ^{137}Cs, and ^{60}Co established gamma-ray sources. The surface of these sources was much smaller than the surface of the NaI(Tl) detector. The sources were encapsulated in a plastic foil with a thickness of 50 μm. The calibration was performed for the tight position of radioactive samples with the NaI(Tl) detectors because a weak activity of the irradiated neutron detectors was assumed and any long gamma-ray analysis was impossible due to the relatively short half-life of the activated samples. The calibration sources were placed in the center of the detection surface. The efficiency was evaluated using the following formula

$$\epsilon\,(E_\gamma) = \frac{C(E_\gamma) - C_B(E_\gamma)}{I_\gamma\, t_{real}\, A\, C_{coi}(E_\gamma)} \tag{7.55}$$

where C is the total number of counts of a peak in the energy spectrum, A is the activity of the calibration source, C_B is the number of counts of a pedestal of the peak, I_γ is the probability of the gamma photon emission, t_{real} is the real time of the analysis and C_{coi} is a coincidence correction factor.

The coincidence occurs when two or more gamma-ray photons enter the detector during a time shorter than a time resolution of the detector. In this case, the output of the detector corresponds to the sum of the coincidence photon energies absorbed by the detector. This effect may lead to increase or decrease of the peak area in the energy spectrum. We can express the coincidence correction factor as [110]:

$$C_{coi}(E_\gamma) = \frac{C(E_\gamma) - C_B(E_\gamma)}{C_{correct}(E_\gamma)} = [1 - L(E_\gamma)][1 - S(E_\gamma)], \tag{7.56}$$

where $C_{correct}(E_\gamma)$ is the correct number of photons which was absolutely absorbed by the detector, $L(E_\gamma)$ is the coincidence loose coefficient, and $S(E_\gamma)$ is the coincidence summing coefficient.

The loose occurs when the energy of one coincidence photon is absorbed absolutely and energy of the other coincidence photon is absorbed particularly. Then, the detector response does not contribute to the full energy peak.

The increase of the full energy peak occurs when an energy of two or more coincidence photons are fully absorbed and the sum of their energies is equal to the energy of a different transition. Then the full energy peak of this transition is increased.

The coincidences are very significant at the decays with a high probability of the gamma photon emission, for example in the case of ^{60}Co radioactive cobalt. The

decay scheme of ^{60}Co is shown in fig. 7.36. At ^{60}Co an emission probability of

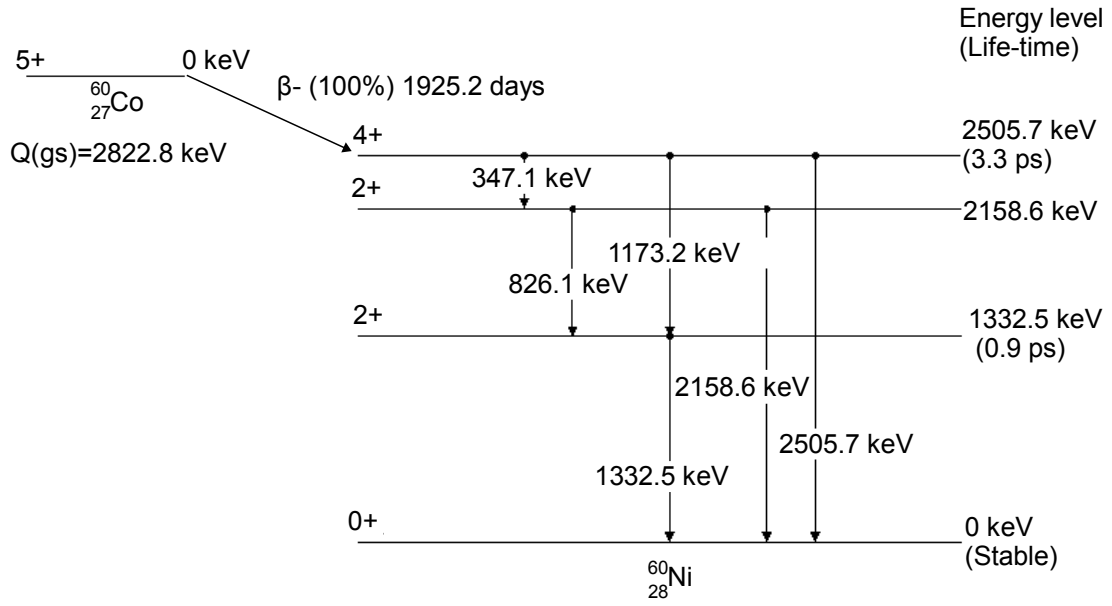

Figure 7.36: Decay scheme of ^{60}Co radioactive cobalt, data used from [122]

1173.2 keV and 1332.5 keV photons is almost 100%. An emission probability of the gamma photons with a different energy is on the order of thousandths of a percent. Thus, the only considered coincidence is the real cascade coincidence of 1173.2 keV and 1332.5 keV photons corresponding to transitions from 2505.7 keV energy level to 1332.5 keV level and transitions to the ground state, respectively. The life-time of the state between these transitions is 0.9 ps. Therefore, if both photons enter the detector, we can't distinguish them. It leads to the decrease of the peak area. The coincidence loose coefficient of 1173.2 keV peak is defined as

$$L_c(1173) = p_c\, I_\gamma(1332)\, p_a(1332), \tag{7.57}$$

where p_c is a probability that the transition related to the 1173.2 keV photon emission is followed by the transition related to the 1332.5 keV photon emission, $I_\gamma(1332)$ is the probability that the 1332.5 keV photon will be emitted and $p_a(1332)$ is a probability that the 1332.5 keV photon will enter the detector and some part of its energy which is bigger than the energy resolution will be absorbed. Analogously, the loose coefficient of the 1332.5 keV peak is defined as

$$L_c(1332) = p_c\, I_\gamma(1173)\, p_a(1173). \tag{7.58}$$

From the decay scheme in fig. 7.36 it is evident that the only transition from the 1332.5 keV state is related to the emission of the 1332.5 keV photon. Thus, the p_c probability is 100% (equal to 1). As mentioned above, the emission probabilities of 1173.2 keV and 1332.5 keV photons are also 100%. As far as the p_a probability is concerned, we could estimate it by following considerations. Because of a high volume of the used NaI(Tl) crystals, we assume that always when a gamma-ray photon enters the detector some part of its energy is absorbed. Further, the sample of ^{60}Co which is tightly attached to the detector is very small. Thus, due to isotropy of the gamma-rays, practically half of the emitted photons must enter the detector. Therefore, the $L_c(1173) = L_c(1332) \doteq 0.5$. Due to the very low emission probability of the 347.1 keV and 826.1 keV photons the full energy peak of the 1173.2 keV transition is not increased. The full energy peak of 1332.5 keV is not increased because the sum of energy of any photons is not equal to this energy. Thus, $S_c(1173) = S_c(1332) = 0$. In accordance with formula (7.56) we obtain $C_{coi} = 0.5$.

In the same manner, the coincidence correction factor for ^{152}Eu was evaluated. In the case of ^{137}Cs and ^{115m}In any coincidence does not occur. Using formula (7.55) we obtained the efficiency calibration of the cuboid and cylindrical NaI(Tl) detectors, as shown in fig. 7.37.

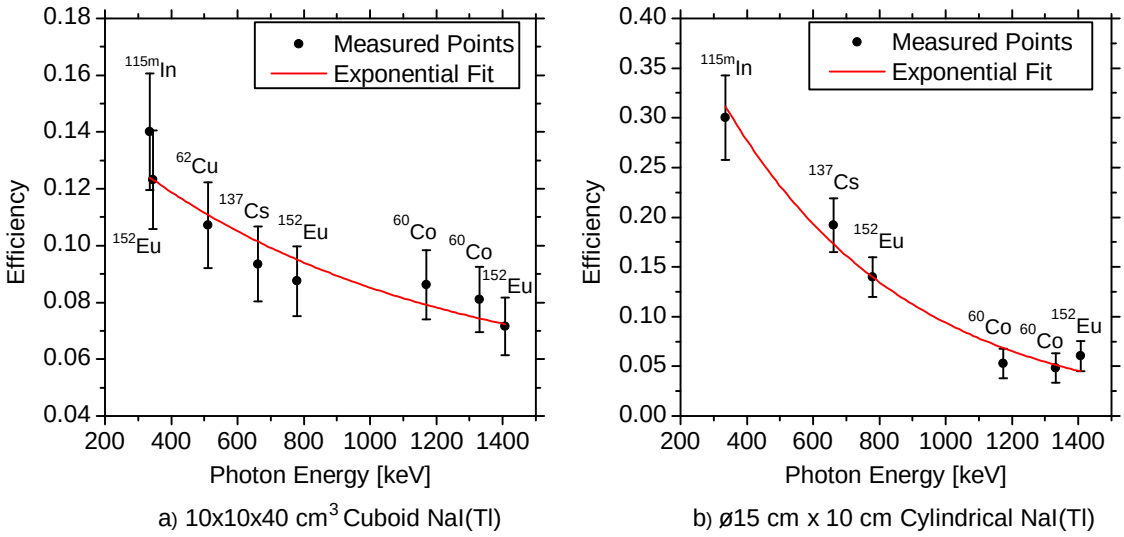

Figure 7.37: Full energy peak efficiency calibration of the gamma-ray spectrometers. a) $10 \times 10 \times 40$ cm^3 cuboid NaI(Tl) detector. b) $\varnothing 15$ cm $\times$ 10 cm cylindrical NaI(Tl) detector.

We assume that the small source detection efficiency is dependent on its position due to geometric factors. This dependence is displayed in fig. 7.38, where the origin of the xy-coordinates is in the center of the detector surface, z is the distance from the detector surface, and normed efficiency is $\epsilon_{tot}(x, y, z)/\epsilon_{tot}(0, 0, 0)$. The photomultiplier is coupled to the NaI(Tl) crystal in the center of xz-plane of the NaI(Tl) crystal, therefore we assume, that the dependence on the x-coordinate is symmetrical with respect to $x = 0$.

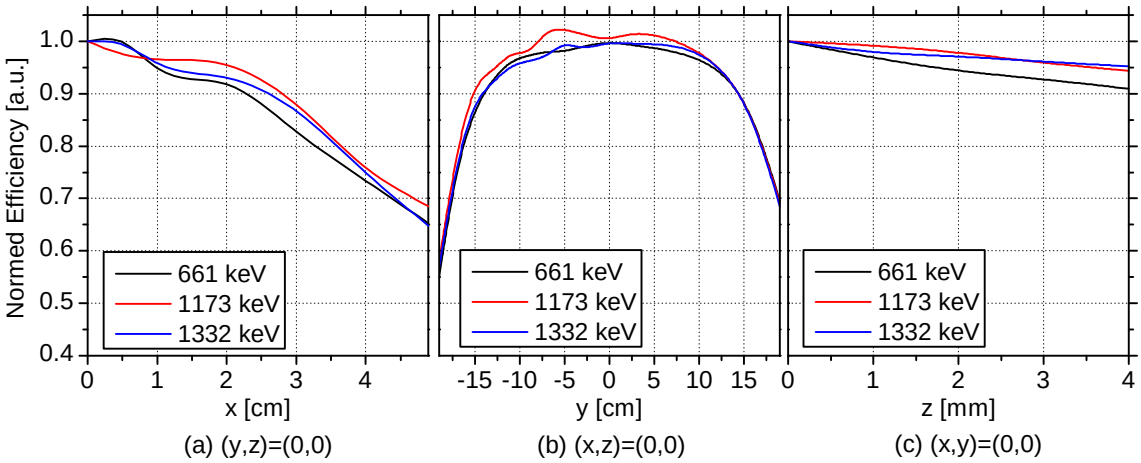

Figure 7.38: The dependence of the $10\times10\times40\text{cm}^3$ cuboid NaI(Tl) detector efficiency on the point source position. The xy-coordinate origin is the center of the detector surface and z is the distance from the detector surface.

As we can see in fig. 7.38(a,b), in the center of the detection surface we found the rectangular area with dimensions approximately 4.4×28 cm^2 in which the normed efficiency is in the range of $0.9 - 1.0$. If we place the small source to this area, the additional error in calibration will be better than 10%. Therefore, if a real radioactive sample which is represented by many very small samples, is placed in this area, we can use the calibration for the very small sample to evaluate the activity of the real sample. Since the Al and Cu samples were not sufficiently narrow, they were split into two identical samples. Additionally, such calibration of the cuboid NaI(Tl) detector was verified by cross-calibration with the HPGe detector. The cylindrical NaI(Tl) detector which was used in 2015 was not cross-calibrated with the HPGe detector, but since it is bigger than the cuboid detector we assume that the calibration with the help of the small sources is sufficient.

7.4.7 Gamma-ray Spectra Examples

The gamma-ray spectra obtained by the NaI(Tl) and HPGe spectrometers were processed using the Spectraline 2010 and Genie 2000 software, respectively. The examples of the gamma-ray spectra measured by the NaI(Tl) and HPGe detectors are displayed in fig. 7.39. The gamma-ray spectra of the indium sample shown

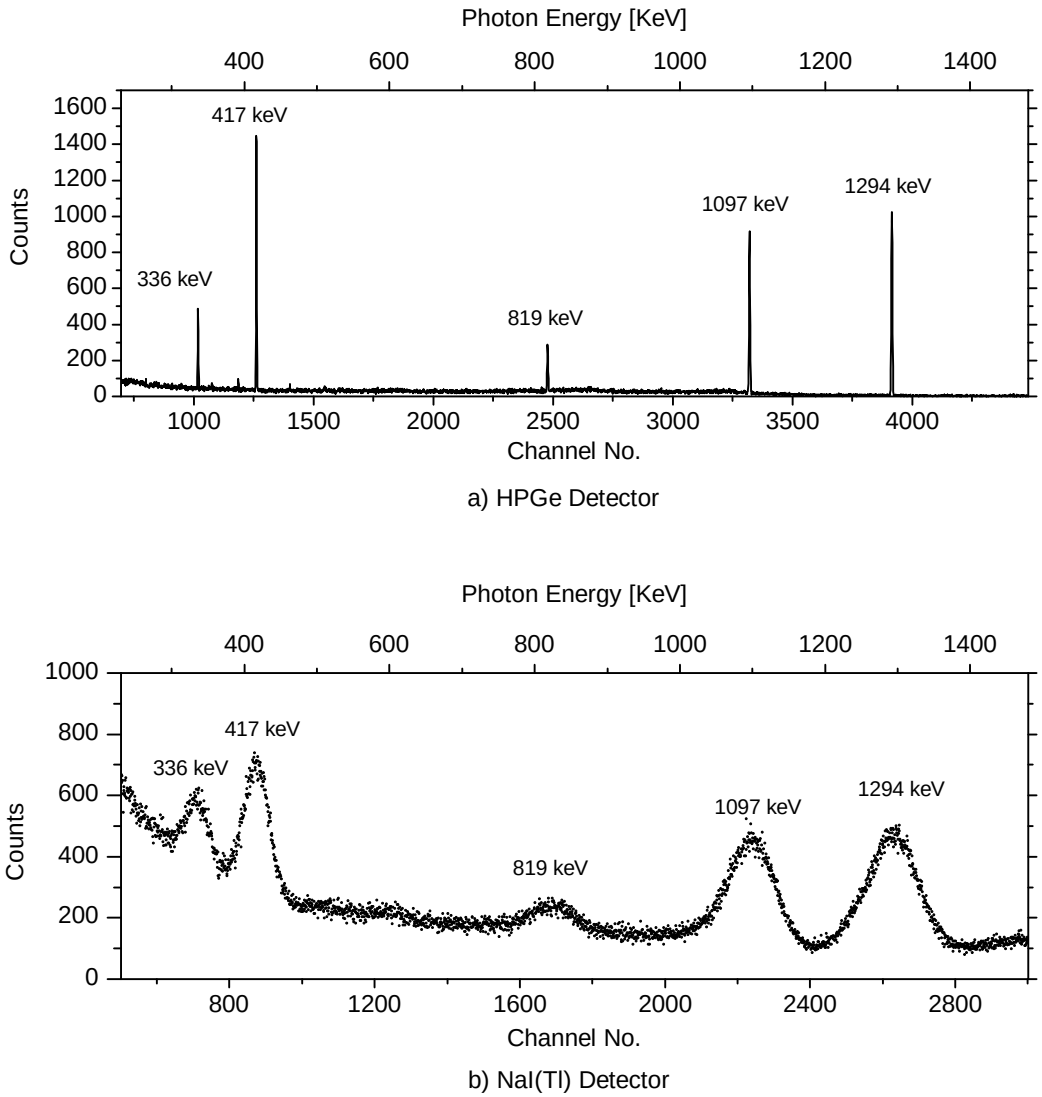

Figure 7.39: Gamma-ray spectra measured by HPGe and NaI(Tl) detector.

in fig. 7.39(a,b) were measured of about 15 minutes after the shot 1774 with the analysis live time of 600 s. The gamma line with the energy of 336 keV corresponds

to the decay of ^{115m}In and the other lines correspond to the decay of ^{116m1}In. As mentioned above, we evaluate the total neutron yield from the ^{115m}In decay with the half-life of about 4.5 hours. Therefore, the neutron yield was usually evaluated using the spectra which were measured a few hours after the shot to eliminate the background radiation of ^{116m1}In with a half-life of about 54 minutes.

To be sure that we correctly identified the radioisotopes in the gamma-ray spectrum, the decay of the induced radioactivity of the fast neutron activation samples was observed. The decays of activated indium, aluminum and copper samples measured by the NaI(Tl) spectrometer are plotted in fig. 7.40. The decays of the indium detector were measured in shot no. 1834 with a neutron yield of 2.7×10^{12}. The decay of the aluminum and copper detectors was measured in shot no. 1839 with a neutron yield of about 6.3×10^{12}. As far as the half-life of a niobium sample is concerned, it was not measured because of its long duration (10 days), instead of that, the niobium was irradiated at every experimental shot. The remanent activity from the previous shots was taken into account during the processing of the results.

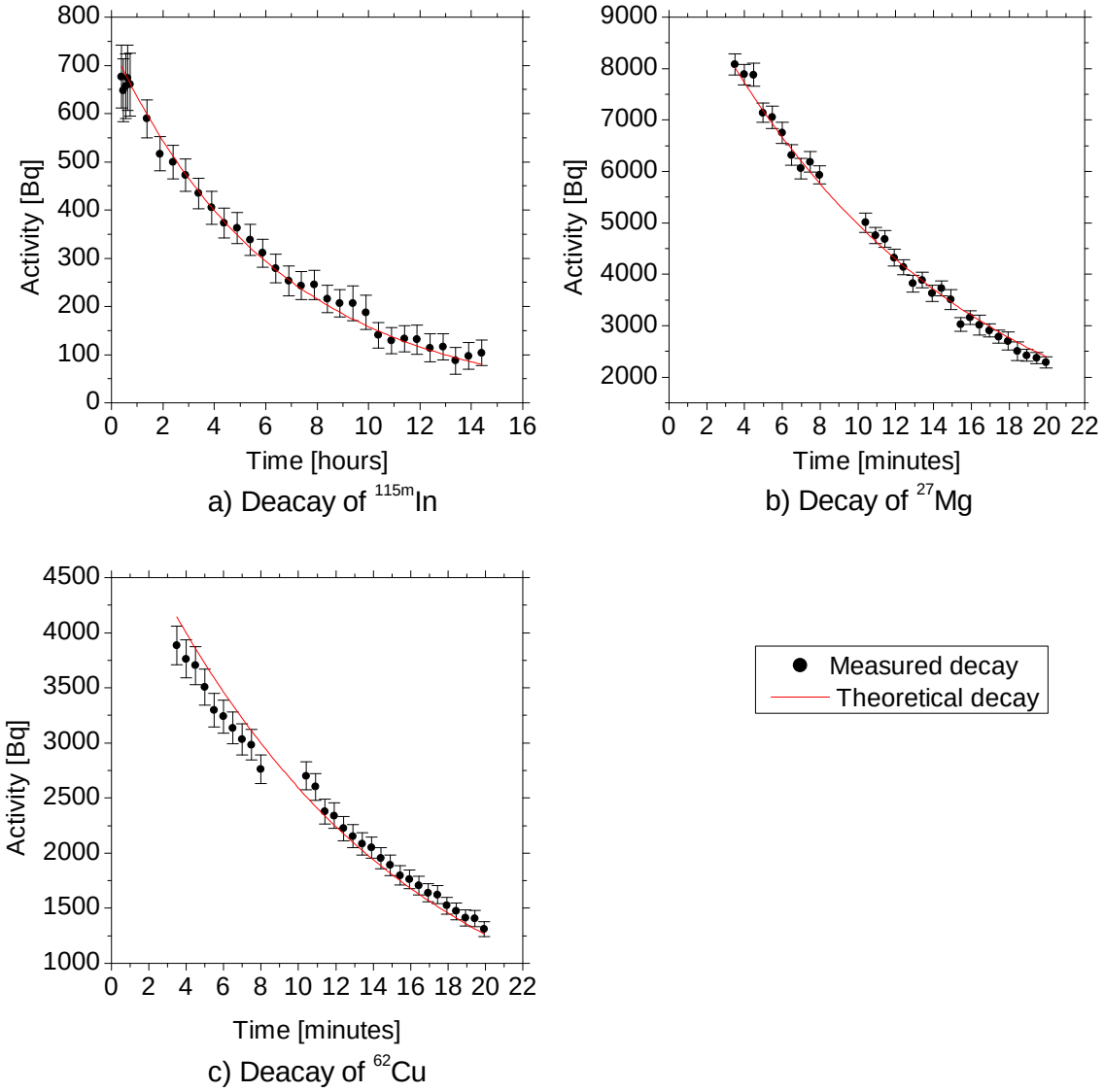

Figure 7.40: The measured and theoretical decays of the fast neutron detectors: (a) indium detector in the shot 1834, (b) aluminum detector in the shot 1839 and (c) copper detector in the shot 1839.

Chapter 8

Experimental Results

In this chapter, the results of diagnostics described in the previous chapter are reported. Using the bubble detectors, silver activation counter, and neutron activation samples, the neutron yields are evaluated and the number of neutrons produced by reactions of deuterons with hardware (non-dd) is estimated. With a help of several indium activation samples placed in different directions and distances from the pinch, we investigate an angular distribution of the non-dd neutrons. The absolute neutron energy spectrum is evaluated by the fitting of the nToF spectrum to the spectrum measured by the set of activation samples (indium, aluminum, niobium, and copper). These results and their evaluations are presented in the following sections.

8.1 Neutron Yields

The neutron yields measured by the fast neutron activation detectors are presented in this section. The neutron yield is a very important parameter which allows us to evaluate the number of dd fusion reactions and compare the efficiency of the neutron production for various experimental configurations. In the case of GIT-12, an energy spectrum of the produced neutrons is very broad. The neutrons with an energy above 20 MeV have been observed [2, 4]. Therefore the measurement of the neutron yield is more complicated than at the experiments where the neutron energy is not significantly different from the energy of 2.45 MeV. The energy dependence of the neutron detectors must be taken into account and a few independent method should be used to prove the measurement results.

The measurement of the total neutron yields in experiments presented in this thesis is based on the bubble detectors (BD-PNDs), silver activation counter (SAC) and fast neutron activation diagnostics. The comparison of the neutron yields from the campaign on the GIT-12 device in 2016 and 2015 measured by these detectors is presented in fig. 8.1.

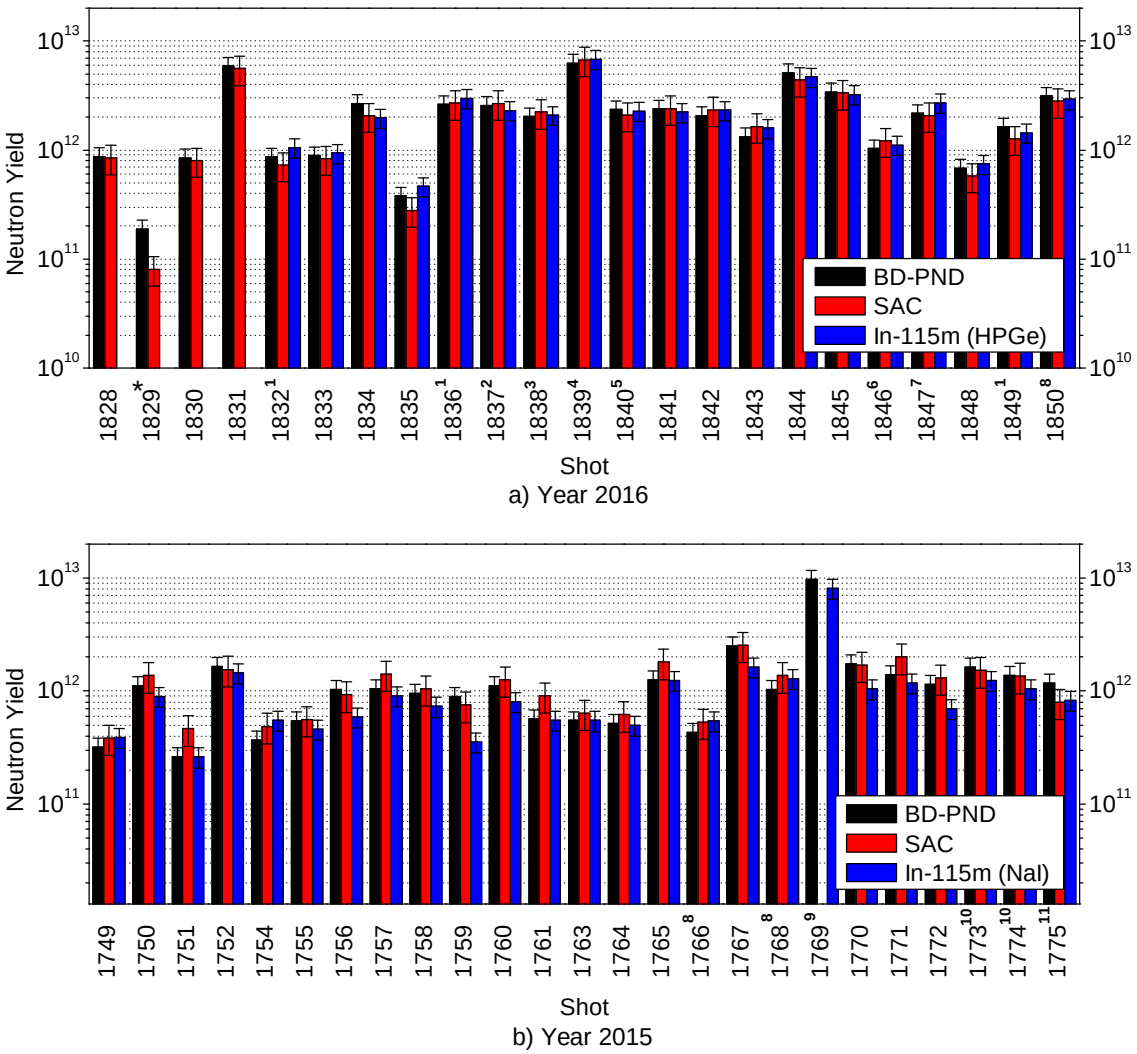

Figure 8.1: Neutron yields from the experimental campaigns on the GIT-12 device in 2016 and 2015.

In the shots marked in fig. 8.1 by a numeric upper index, diagnostics catchers are used. These catchers take the form of LiF or CD_2 tablets. The catchers were mounted below the cathode mesh in order to convert the fast deuterons into neu-

trons. In the case of shots in 2016 small catchers were used and their contribution to the total neutron yield is below 30%. Thus, these small diagnostic catchers did not affect the total neutron yield significantly[1], but we distinguished neutrons with energy above 10 MeV from ^{7}Li(d,n) and ^{7}Li(d,n+α) reactions in the nToF signals, BDS-10000, and copper activation sample. In the case of the shots in 2015, the bigger catchers were used and their contribution to the total neutron yield is more significant.

The neutron yields evaluated by ^{115}In(n,n')^{115m}In reaction in 2016 (fig. 8.1(a)) were measured using the HPGe gamma-ray spectrometer. In 2015 (fig. 8.1(b)) we used the NaI(Tl) spectrometer because the HPGe spectrometer was not available for most of the shots. However, examining fig. 8.1 we can see, that the neutron yields evaluated by ^{115}In(n,n')^{115m}In reaction correspond to the neutron yields evaluated by SAC and BD-PNDs. Thus, it seems that in our experiments, the NaI(Tl) spectrometer is sufficient. The neutron yield evaluated by the indium excitation is missing in the shots 1828-1831 because the gamma-ray spectrometer was not available. Nevertheless, the neutron yields evaluated by other diagnostics are included in the fig. 8.1(a) to have information about the shot-to-shot neutron yield fluctuation during the whole experimental campaign.

As far as the fluctuation of the neutron yield is concerned, the lowest neutron yield of 1.9×10^{11} (evaluated by BD-PNDs) was achieved in shot no. 1829 (in fig. 8.1 marked by *). The reason for such a deviation is that it was the only shot without the outer plasma shell. The neutron yield of the other shots varied approximately from 4×10^{11} to 6×10^{12} in 2016. The average neutron yield at the shots with the outer plasma shell was 2.3×10^{12}. The neutron yield in the range of $2.3\times10^{12}\pm50\%$ was measured at 52% of the shots with the outer plasma shell. In the case of the year 2015, all shots were performed with the outer plasma shell. The total neutron yield at the shots without any catcher varied from 2.6×10^{11} to 2.5×10^{12} (by BD-PNDs) and the average value was of about 1×10^{12}. The neutron yield in the range of $1 \times 10^{12} \pm 50\%$ was measured at 68% of the shots without any catcher.

Thus, the average neutron yield in 2016 was more than two times higher than in 2015. However, the fluctuation was a little bit better in the shots in 2015. The reason of this difference is not clear. We speculate that the high neutron yields in

[1]The contribution of the LiF and CD_2 diagnostic catchers to the total neutron yield is of the same level as the uncertainty of our neutron yield measurement.

2016 were caused by precise arranging of the experimental load.

In fig. 8.1, one can see small differences between the neutron yields evaluated by the BD-PND, SAC, and ^{115m}In at the same shot. These differences could be caused by the following reasons. First, each kind of the detector has a different dependence of the sensitivity on the neutron energy. Comparing the normalized dependencies of the sensitivities on the neutron energy in fig. 8.2, it is apparent, that the BD-PND is more sensitive to the neutrons with an energy below 1 MeV than the indium detector. We note that in fig. 8.2, the data of sensitivity of BD-PND are used from [90] and sensitivity of the indium detector is assumed to be proportional to the ^{115}In(n,n')^{115m}In reaction cross-section. Second, the measurement could be affected by the neutron scattering. Each detector is placed at a different place and, as a result, the scattering rate could be also different. Third, the BD-PNDs are aging during the experimental campaign. Fourth, the sensitivity of the SAC to the neutrons with energy above 4 MeV is not known because of the moderator is designed for the 2.45 MeV neutrons. However, as we can see in fig. 8.1, the

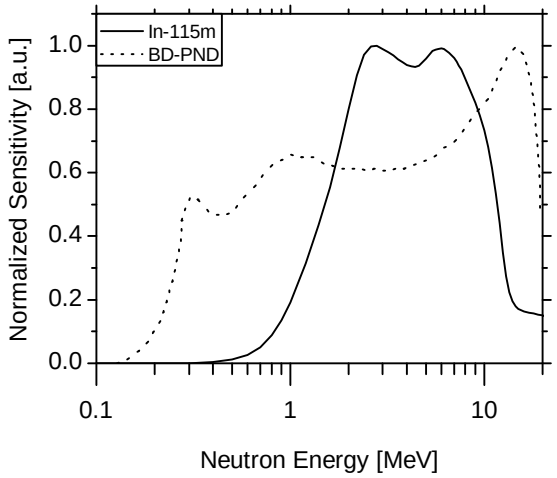

Figure 8.2: Comparison of the efficiencies of the BD-PND and indium fast neutron activation detector.

neutron yields measured by all techniques correspond to each other in the limits of uncertainties. Thus, it seems that our measurement of the neutron yield is correct.

As far as the high energy neutrons are concerned, the yields of neutrons with energy above 12 MeV were detected with the help of the copper activation sample. These yields are displayed in fig. 8.3. In this graph some of the high-energy neutron

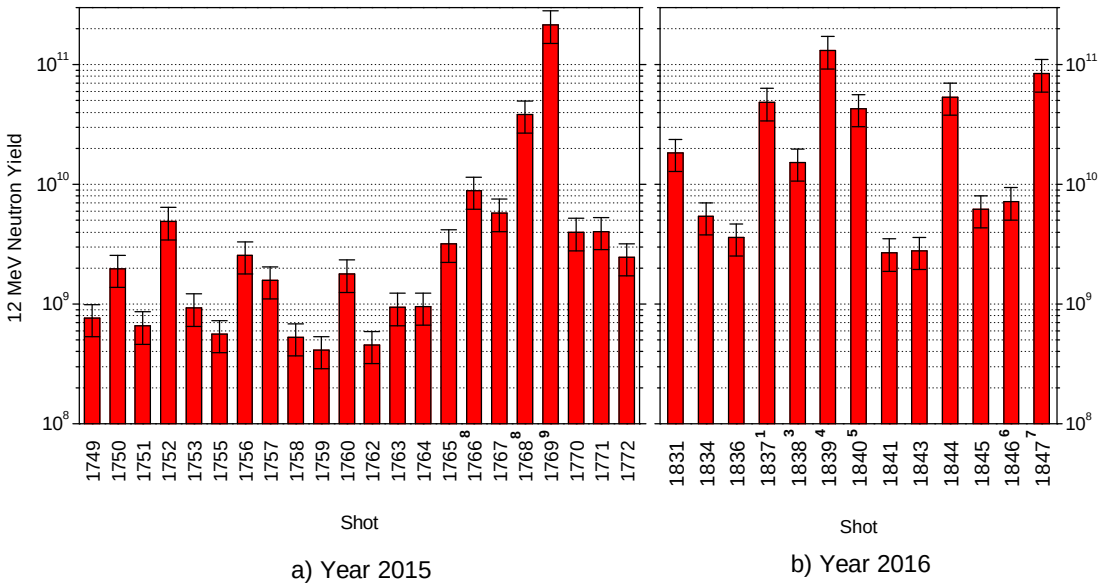

Figure 8.3: Yields of the neutrons with energy above 12 MeV.

yields are missing, because of excessive uncertainty in the gamma-ray analysis in several shots. We note that the high-energy neutron yields are affected by the LiF catchers because the reactions ^{7}Li(d,n) with Q = 15.0 MeV and ^{7}Li(d,n+α) with Q = 15.1 MeV produce the neutrons with the energy above the threshold of the copper activation detector (see fig. 7.24). In the shots where the LiF catcher was not used, the neutrons with such high energy should be produced by D(d,n)^{3}He reactions of the multi-MeV deuterons. We note, that sometimes the neutron yield of D(d,n)^{3}He could be also influenced by the catcher due to the reflection of the injected gas by the catcher. Thus, the linear mass of the imploding Z-pinch is affected. Excluding the shots with the catcher, we obtain the dependence of the $>$ 12 MeV neutron yield on the total neutron yield displayed in fig. 8.4, where the total neutron yield is evaluated by ^{115}In(n,n')^{115m}In reaction. In all shots with the outer plasma shell and without any catcher, the yield of the neutrons with energy above 12 MeV exceeds 10^{9}. This yield is evidently increasing with the total neutron yield. However, any function which reasonable fits this dependence has not been found yet. It should be noted, that such yields of the neutrons with energy above 12 MeV has been achieved only in the shots with the outer plasma shell presented in section 6.3.

Some of the neutrons contributing to the neutron yields could be produced by the non-dd reactions. The contribution of such neutrons is discussed in the following section.

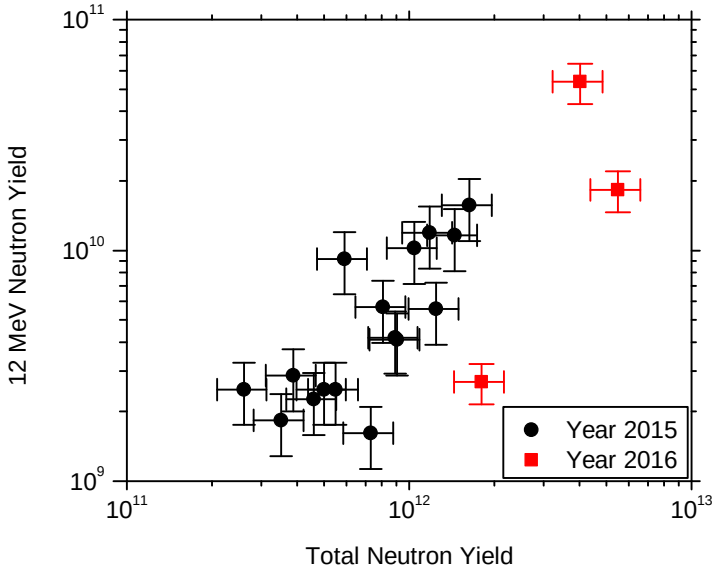

Figure 8.4: Dependence of the > 12 MeV neutron yield measured by copper activation on the total neutron yield measured by indium activation.

8.2 Non-dd Neutrons

The neutron yield in the experiments with the deuterium gas-puff and the outer plasma shell on the GIT-12 device reached fairly high values on the order of 10^{12} (see fig. 8.1). At the same time, a relatively high number of neutrons with energy above 12 MeV was detected. Examining fig. 8.3(b) we found that in the shots without any catcher, the number of >12 MeV neutrons is usually on the order of $10^9 - 10^{10}$. The higher number of >12 MeV neutrons reaches of about 8×10^{10} in shot no. 1844. These high energy neutrons imply a significant number of reacting multi-MeV deuterons. A high number of the multi-MeV deuterons have been observed not only indirectly by the neutron diagnostics but also by the nuclear track detectors (CR-39), radiochromic films (RCF), and ion activation samples [2, 4, 123]. The question arises as to the fraction of the measured neutrons produced by the interaction of deuterons with the materials inside the discharge vacuum chamber. There are several materials that could be struck by the deuterons: the duralumin housing of the axial ion detectors, the stainless steel electrode system, the walls of the vacuum chamber made of stainless steel, the brass nozzle of the gas-puff, and two radial glass diagnostic windows at the distance of 37 cm from the pinch. Using the RCF, CR-39, and ion activation samples, which were placed on the brass nozzle behind the anode mesh and on the inner side of the radial diagnostic port, we found out that the number of the multi-MeV deuterons flying in the upstream and radial direction was insufficient to achieve significant non-dd neutron production. Moreover, the total surface of brass and glass components is negligible in comparison with the surface of the surrounding stainless steel chamber. In most of the shots, the duralumin housing of the ion detector with a surface of up to 49 cm^2 was placed below the cathode mesh at the distance of about 10 cm from the ion source. As a result, some of the fast ions, which escaped the discharge, struck the duralumin and almost all other deuterons struck stainless steel. In both cases, the neutrons could be produced by reactions of deuterons with the solid metal. The most significant neutron-producing reactions of deuterons with duralumin and stainless steel are ^{27}Al(d,n)^{28}Si (Q=9.4 MeV) and ^{56}Fe(d,n)^{57}Co (Q = 3.8 MeV), respectively. The deuteron break-up reactions ^{27}Al(d,n+p)^{27}Al (Q=-2.2 MeV) and ^{56}Fe(d,n+p)^{56}Fe (Q=-2.2MeV) could be also significant. The total cross-sections of the neutron-producing reactions and spectra of the emitted neutrons for the reactions which are

the most significant in our experiment are displayed in fig. 8.5. Examining the

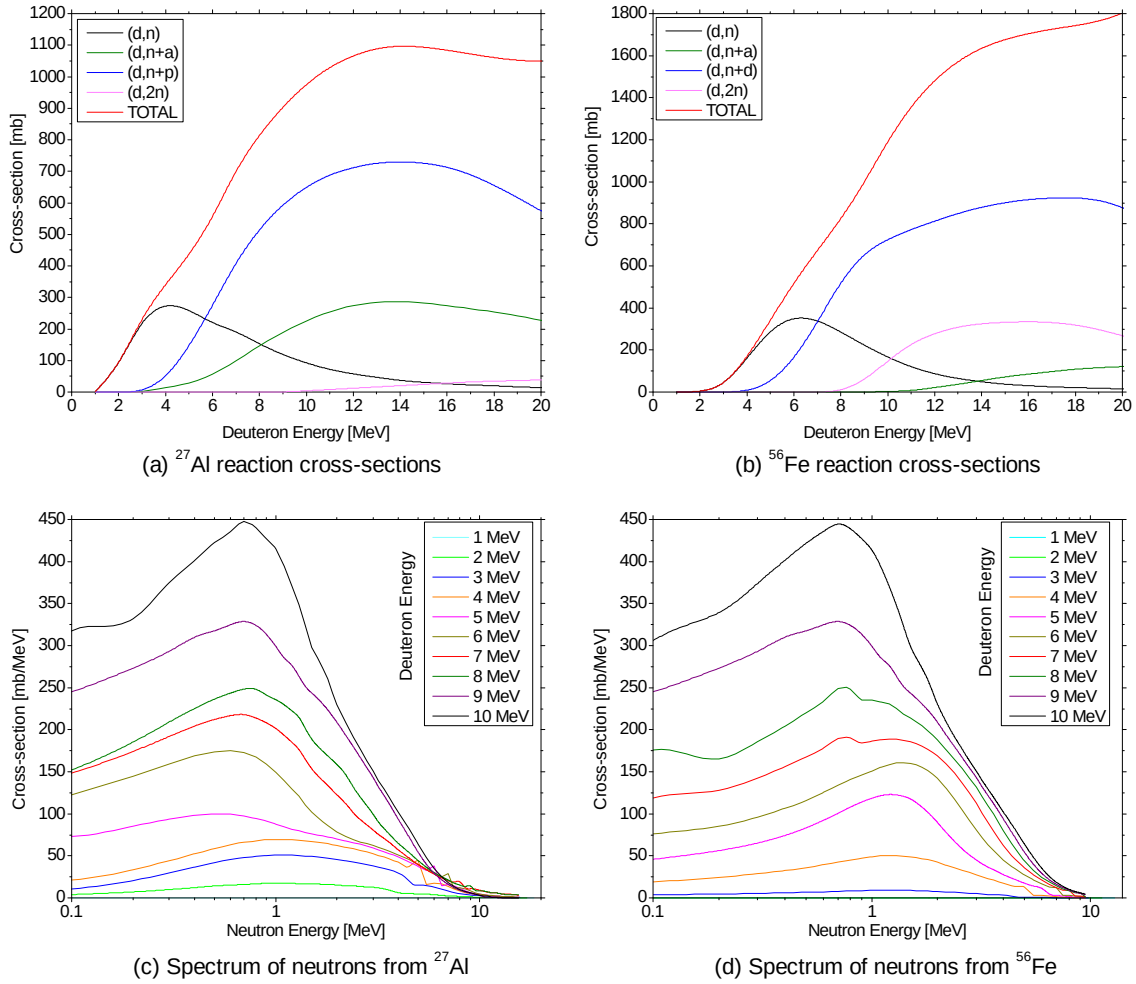

Figure 8.5: The total cross-sections of the significant neutron-producing reactions of deuterons with the solid metal and the spectra of produced neutrons from all reactions. Data exported from [115, 116].

spectra of neutrons originated from such reactions in fig. 8.5(c,d), we see that it is very complicated to distinguish neutrons produced by the non-dd reactions from the neutrons produced by D(d,n)^{3}He reaction. The number of these non-dd neutrons depends on a thick-target yield Y_{TT} which can be calculated from the total cross-section $\sigma(E_d)$ of the reaction and the stopping cross-section $s(E_d)$ of the target as follows [124]

$$Y_{TT}(E_i) = \int_0^L \sigma(E_d)\, n \,\mathrm{d}x = n \int_0^{E_i} \frac{\sigma(E_d)}{|\mathrm{d}E_d/\mathrm{d}x|}\,\mathrm{d}E_d = \int_0^{E_i} \frac{\sigma(E_d)}{s(E_d)}\,\mathrm{d}E_d, \qquad (8.1)$$

where E_i is the incident energy of the deuteron, and n is the concentration of target nuclei. The cross-sections of the (d,n) reactions are taken from the TENDL 2014 TALYS-based Evaluated Nuclear Data Library [115, 116]. The stopping powers $\mathrm{d}E/\mathrm{d}x$ are evaluated by the SRIM software [121]. The obtained thick target yields are shown in fig. 8.6(a). The above-mentioned reactions are significant at the

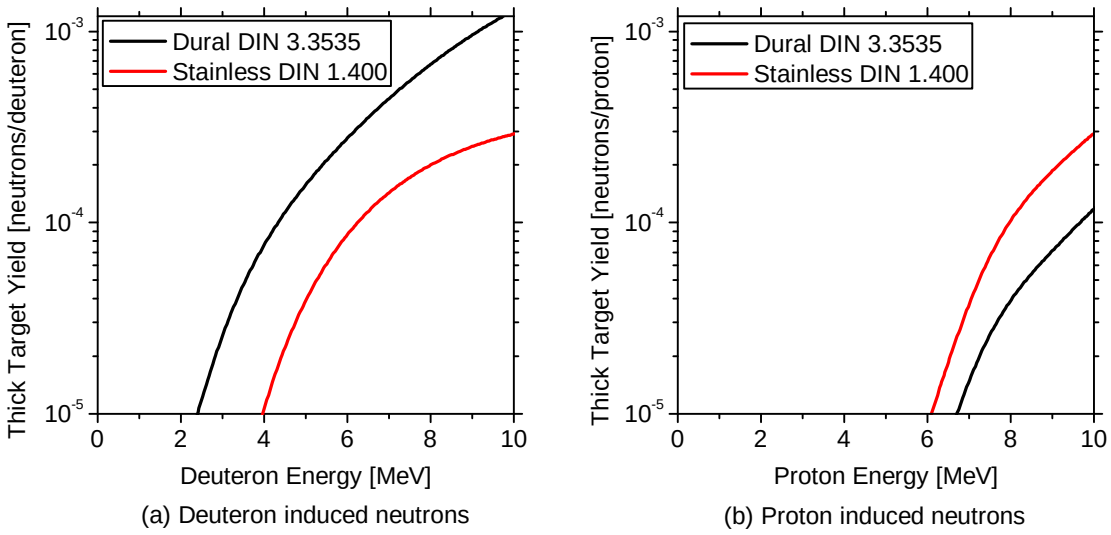

Figure 8.6: Thick target yields of the deuteron and proton induced neutron-producing reactions in duralumin and stainless steel.

energies of the deuterons above 2 MeV (see fig. 8.6). At such energies, it was shown in [77, 78, 79], that the deuterons in our experiments follow the power-law distribution $\mathrm{d}N_d/\mathrm{d}E_d \propto E_d^{-\kappa}$. We assume that the κ parameter is in the range from 1.6 to 3 up to the deuteron energy of about 10 MeV [77, 78, 79, 123]. The number of multi-MeV deuterons which struck the duralumin or stainless steel could be estimated with the help of the LiF deuteron-neutron converter. In the shot 1697, a 3 × 3 cm^2 LiF sample was placed 3 mm below the cathode mesh. The neutrons were produced by ^{7}Li(d,n)^{8}Be and ^{7}Li(d,n+α)^{4}He reactions [123]. The number of the neutrons produced by these reactions is given by the integration of a Y_{TT-LiF} thick target yield of the LiF sample and deuteron energy distribution:

$$Y_{LiF} = \int_0^{10\,\mathrm{MeV}} \frac{\mathrm{d}N_d(E_d)}{\mathrm{d}E_d}\, Y_{TT-LiF}(E_d)\,\mathrm{d}E_d. \tag{8.2}$$

The neutrons from ^{7}Li(d,n) and ^{7}Li(d,n+α) reactions could be distinguished from the dd neutrons due to the different energy spectrum [123]. Using fast neutron

diagnostics, D. Klir in [123] estimates that the number of neutrons generated by the LiF converter Y_{LiF} is approximately 2×10^{12} in the shot 1697. On the basis of the neutron yield from LiF, we are now able to estimate the neutron yield from the interaction of fast deuterons with the duralumin and stainless steel. If we assume that the same deuteron beam which interacted with LiF in shot no. 1697 interacts with the experimental chamber and diagnostic elements, we can estimate the neutron yield from non-dd reactions as follows:

$$Y_n' = Y_{LiF} \frac{\int_0^{10\,\mathrm{MeV}} E_d^{-\kappa}\, Y_{TT}(E_d)\,\mathrm{d}E_d}{\int_0^{10\,\mathrm{MeV}} E_d^{-\kappa}\, Y_{TT-LiF}(Ed)\,\mathrm{d}E_d}, \tag{8.3}$$

where Y_{TT} is the thick target yield of the duralumin or stainless steel. In calculation (8.3), the κ parameter was not evaluated by the neutron spectrum at the shot 1697, because of the high number of non-dd neutrons produced by the LiF converter. However, we could assume that κ lies in the range from 1.6 to 3.0 [77, 78, 79, 123]. The dependence of the non-dd neutron yield on the κ parameter for the extreme situations, when all deuterons strike the duralumin or stainless steel hardware is displayed in fig. 8.7. If we consider that all multi-MeV deuterons strike the duralumin and including 70% transparency of the cathode mesh, we obtain $(2.9 - 3.2) \times 10^{11}$ non-dd neutrons. Similarly, if the duralumin equipment is not used and considering that all the multi-MeV deuterons strike the stainless steel, the yield of non-dd neutrons achieves approximately $(1.2-1.9)\times 10^{11}$. However, if the duralumin equipment is used, it is unlikely that all the deuterons strike only the duralumin. Therefore, the non-dd neutron yield should be smaller than 3.2×10^{11}. On the other hand, the number of non-dd neutrons is higher than 1.2×10^{11}. Thus if the duralumin housing of the ion diagnostics is placed below the cathode mesh, the number of non-dd neutrons lies between the curves corresponding to duralumin and stainless steel. As we can see in fig. 8.7, if we consider an extreme situation when all the deuterons with energy above 2 MeV strike the duralumin and at the same time, the κ parameter will have the unlikely low value of $\kappa \approx 1.6$, only about 15% of the detected neutrons will be produced by the non-dd reactions. As mentioned in section 8.1, the shots in our experiments are well reproducible. Thus we can assume that in all shots in our experiments, more than 85% of the neutrons were produced by the dd reactions. This estimation is important since for evaluation of the κ parameter of the deuteron energy distribution approximation $\mathrm{d}N_d/\mathrm{d}E_d \propto E_d^{-\kappa}$ using nToF diagnostics, most

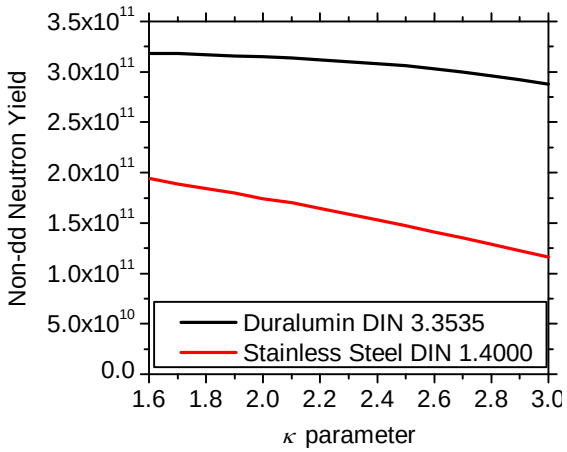

Figure 8.7: Dependence of the neutron yields of (d,n) reactions with the duralumin and stainless steel on the κ parameter.

of the detected neutrons must be produced by the D(d,n)^{3}He reactions. Now, we have proved that this condition is fulfilled.

The same effect which produces the non-dd neutrons occurs in the shots with the natural hydrogen gas. The natural hydrogen gas-puff was used in the shot no. 1698. In this shot, we used optimal initial conditions similarly as in the case of deuterium gas-puff [123]. The neutron yield measured by the bubble detectors (BD-PND) in the shot with natural hydrogen achieved about 10^{11}. Such a neutron yield cannot be explained by the presence of deuterium atoms in the natural hydrogen gas because its abundance is about 0.015% only. Therefore, the neutrons were probably produced by the reactions of protons with the stainless steel. The thick target yields of neutrons from the ^{27}Al(p,n)^{27}Si and ^{56}Fe(p,n)^{56}Co proton-induced reactions are shown in fig. 8.6(b). The estimation in fig. 8.6(b) is also calculated using the TENDL 2014 TALYS-based Evaluated Nuclear Data Library [115, 116] and SRIM software [121]. In the same manner, as in the case of a deuterium gas-puff, the dependence of the neutron yield from the proton-induced reaction on the κ parameter was evaluated. The result of this evaluation is displayed in fig. 8.8. In the shot with the natural hydrogen gas-puff, the used aluminum housing of ion detector below cathode was much smaller than in the shots with the deuterium gas-puff. At the same time, in this shot, the ion detector was placed at a greater distance from the cathode mesh than in the shots with the deuterium gas-puff. Therefore,

we could assume that most of the protons struck the stainless steel. To obtain the neutron yield of about 10^{11} in the same manner as at the reaction with deuterons, the proton distribution should correspond to $E_p^{-\kappa}$ with $\kappa \approx 1.8$.

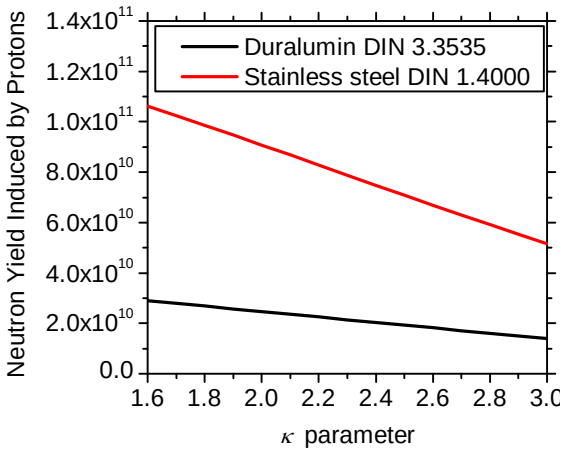

Figure 8.8: The dependence of neutron yields of the (p,n) reactions with duralumin and stainless steel on the κ parameter in the shot with the natural hydrogen gas-puff.

Finally, we should note that in the case of the deuterium gas-puff, a fraction of the neutron yield could be produced by deuterons interacting with the neutral gas below the cathode mesh. To evaluate the number of these neutrons, we need to know the number of sub-MeV deuterons which could produce neutrons in dd reactions. However, we can assume that the number of these neutrons is not significant because simulations in the ANSYS Fluent software indicate the low density of the natural gas below the cathode mesh [82]. Evaluation of the number of these neutrons will be one of the goals of the following investigation of the deuterium gas-puff.

8.3 Neutron Fluence Anisotropy Close to Pinch

Anisotropy of the neutron production in the experiments on the GIT-12 device was investigated using indium activation samples. These samples were placed on the z-axis in the downstream direction (below cathode), in the upstream direction (above anode), and in the radial direction. The arrangement of the activation indium samples is schematically displayed in fig. 8.9. The indium samples In A or In B

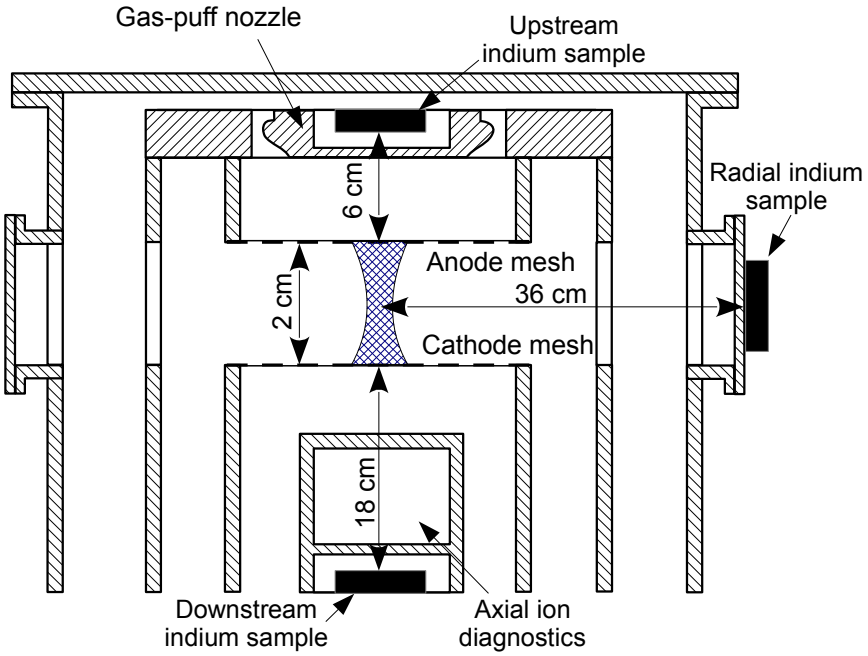

Figure 8.9: Arrangement of the indium activation samples in the radial, upstream, and downstream direction (not in scale).

were used as the upstream samples, In V as the radial samples and In C or In D as the downstream samples (see the list of the indium activation samples in table 7.3)[2]. Using the activation samples the angular neutron fluences were measured. We defined the angular neutron fluence as a number of neutrons per solid angle:

$$\frac{\mathrm{d}N}{\mathrm{d}\Omega} \approx \frac{\Delta N}{\Delta \Omega} \approx \Phi(d_S, \phi)\mathrm{d}S_S, \tag{8.4}$$

[2]When the indium samples In A and In D was ready to shot inside the vacuum chamber, the samples In B and In D were prepared and mounted to the diagnostic housing for next shot and vice versa.

where N is a number of dd neutrons passed an indium sample, Ω is the solid angle, $\Phi(d_S, \phi)$ is the neutron fluence detected by the indium sample, S_S is the surface of the indium sample, and d_S is the distance of the indium sample from the neutron source (pinch). The angular neutron fluences $\Phi(0^o)$ (downstream fluence), $\Phi(90^o)$ (radial fluence), $\Phi(180^o)$ (upstream fluence), and their ratios are reported in table 8.1 and graphically displayed in fig. 8.10.

Shot no.	Angular neutron fluence [1/sr]			Differential neutron yield ratio		
	Downstream (0^o)	Radial (90^o)	Upstream (180^o)	D/U ($0^o/180^o$)	D/R ($0^o/90^o$)	R/U ($180^o/90^o$)
1833	3.4×10^{11}	6.1×10^{10}	4.0×10^{10}	8.5	5.6	1.5
1835	6.6×10^{10}	3.0×10^{10}	2.9×10^{10}	2.3	2.2	1.1
1837	1.1×10^{12}	1.5×10^{11}	1.4×10^{11}	8.2	7.4	1.1
1838	8.4×10^{11}	1.4×10^{11}	9.3×10^{10}	9.1	6.2	1.5
1839	2.7×10^{12}	5.8×10^{11}	3.7×10^{11}	7.4	4.8	1.5
1840	5.2×10^{11}	1.5×10^{11}	1.1×10^{11}	5.0	3.5	1.4
1841	1.0×10^{12}	1.5×10^{11}	8.8×10^{10}	11.7	7.1	1.6
1845	1.4×10^{12}	2.1×10^{11}	9.0×10^{10}	13.5	6.8	2.0
1847	4.1×10^{11}	1.8×10^{11}	1.2×10^{11}	3.5	2.3	1.5
1850	6.6×10^{11}	1.9×10^{11}	1.6×10^{11}	4.1	3.5	1.2
Average	9.2×10^{11}	1.8×10^{11}	1.2×10^{11}	7.3	4.9	1.4

Table 8.1: Results of measurement of the neutron emission anisotropy

.

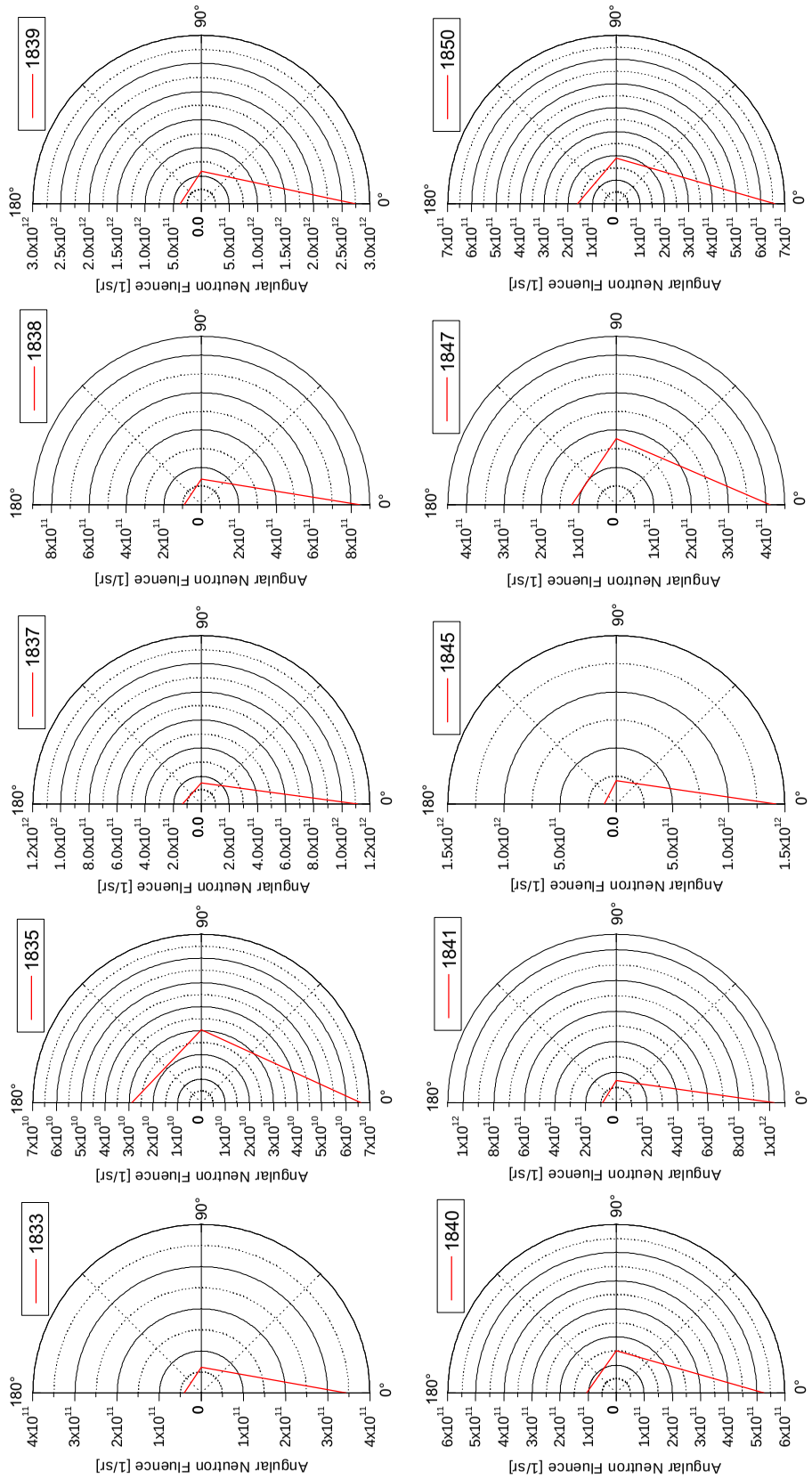

Figure 8.10: Neutron emission anisotropy represented by the angular neutron fluences.

Dependence of the angular neutron fluence in the downstream and upstream direction on the total neutron yield evaluated by the radial indium sample is displayed in fig. 8.11. This dependence includes only the shots without LiF or CD_2 catcher. Examining the fig. 8.11 it seems that the downstream and upstream angular neutron

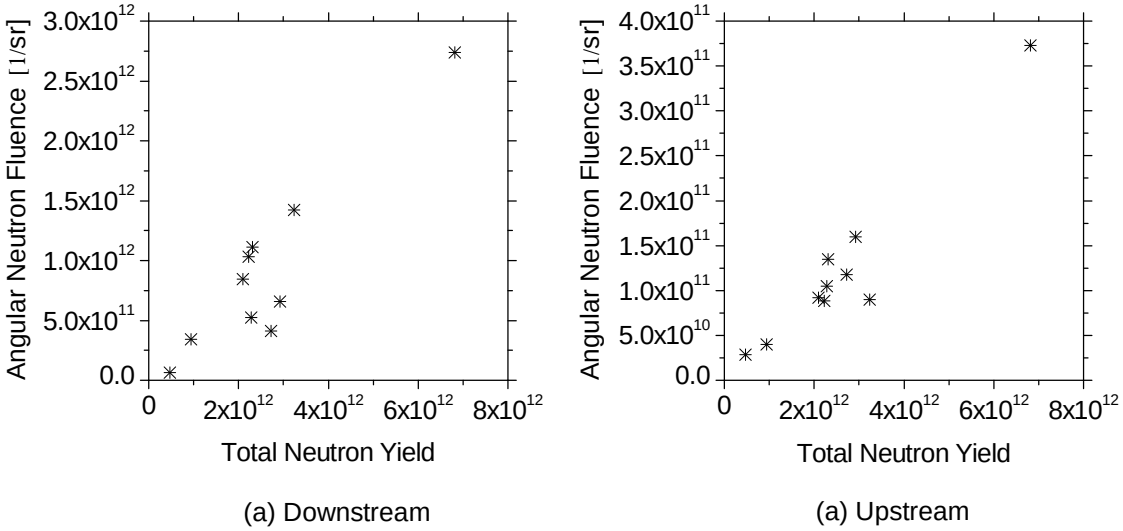

Figure 8.11: Dependence of the angular neutron fluence in the downstream and upstream direction on the total neutron yield evaluated by the radial indium activation diagnostics.

fluences are linearly dependent on the total neutron yield. In fig. 8.12 we can see the anisotropy represented by the radial/upstream and downstream/radial angular neutron fluence ratio. The fig. 8.12 includes only the shots without the LiF or CD_2 catcher. It seems, that these ratios are independent on the neutron yield. In the case of the radial/upstream ratio, it seems, that it is almost constant close to the average value of 1.4. On the other hand, the downstream/radial ratio varies in a wide range approximately from 2 to 7.5. Such results were proved during the recent experiments in 2017.

Examining the scheme in fig. 8.9 we can see that the indium sample below cathode (downstream) is relatively close (of about 8 cm) to the aluminum cover of the axial ion diagnostics housing. By the calculations presented in section 8.2, we estimated that approximately 15% of the measured neutrons are produced by the non-dd reactions of the multi-MeV deuterons which escape the pinch and duralumin cover of the axial ion diagnostics. Such non-dd neutrons influenced the measurement

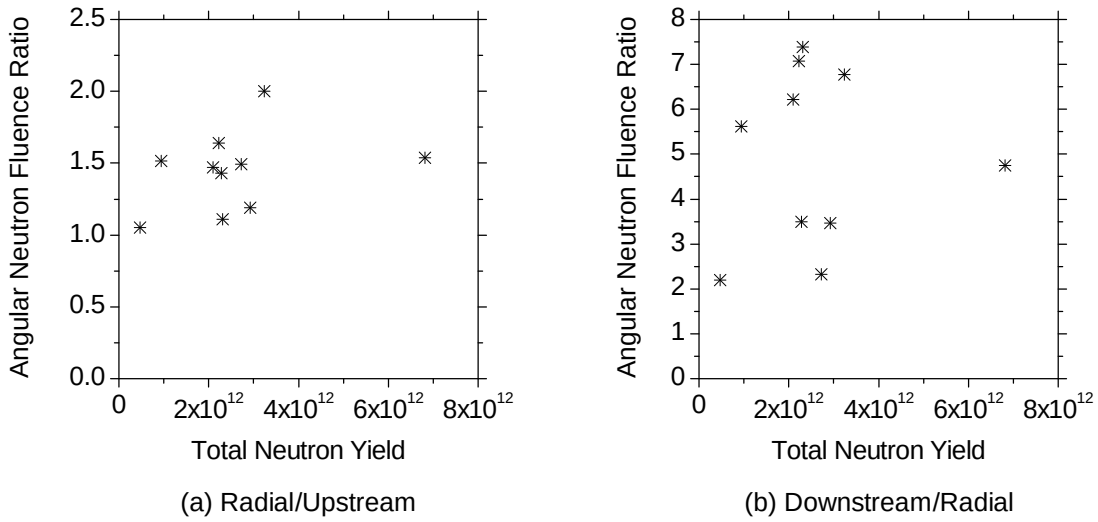

Figure 8.12: Dependence of the radial/upstream and downstream/radial differential neutron yield ratio on the total neutron yield evaluated by the radial indium activation diagnostics.

of dd neutron emission anisotropy in the close distances of 6 cm and 18 cm to the electrodes (see fig. 8.9). Therefore, the measurements reported in the following section were performed.

8.4 Dependence of Neutron Fluence on Distance

The anisotropy of neutron fluence at the close distance from the pinch presented in section 8.3 is probably affected by the non-dd neutrons.

In order to evaluate the number of the non-dd neutrons and prove their assumed origin, the dependence of the neutron fluence on the distance from the pinch was measured in the radial and axial direction. For this purpose, two radial and three downstream indium activation samples were used. The arrangement of the samples is displayed in fig. 8.13. We note that all indium samples, which were placed inside the vacuum chamber were shielded by the metallic housing to avoid an activation by ions. The distortion of the neutron measurement by the housing was taken into account with the help of the MCNP simulations performed by Ondřej Šíla. These simulations show that the influence of the neutron scattering to measurement reported in this section is insignificant.

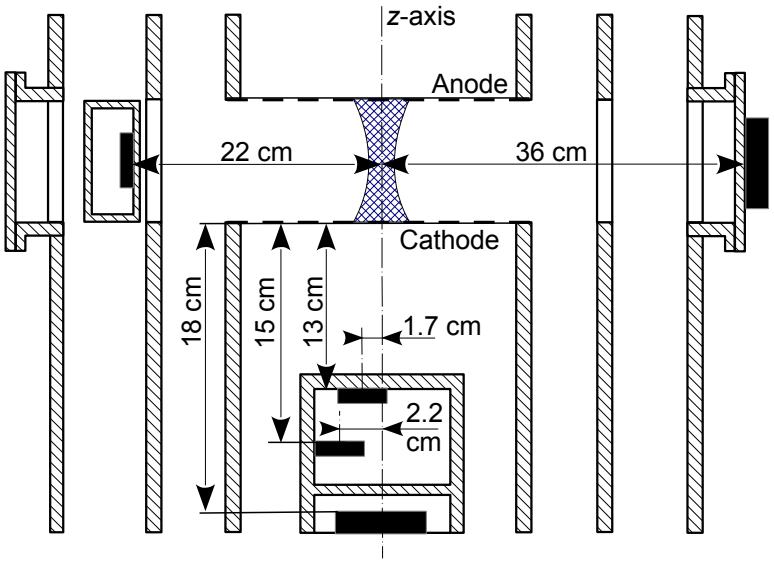

Figure 8.13: Arrangement of the indium activation samples in the radial and downstream direction (not in scale).

8.4.1 Radial Dependence of Neutron Fluence

The dependence of the neutron fluence in the radial direction was measured using indium samples labeled 1-7 (see table 7.3)[3] at the distance of 22 cm and sample VI at the distance of 36 cm. The center of the samples was placed at the same height as the center between the anode and cathode mesh. We evaluated the angular differential neutron yields at the distances of 22 cm and 36 cm from the z-axis. The comparison of the differential neutron yields is displayed in fig. 8.14. As we can see in fig. 8.14, the number of neutrons per solid angle is in both distances similar and mostly is different only in the scope of the detection uncertainty[4]. Since the differential neutron yields at 22 cm correspond to the differential neutron yields in 36 cm, we could assume that most of the neutrons emitted in the radial direction are generated close to the Z-pinch axis (up to 1.5 cm) and between the electrodes or close to them (up to 8 cm).

[3]In each shot, just one sample from the set 1-7 was used.

[4]The uncertainty of the measurement at the distance of 22 cm is somewhat higher than at the distance of 36 cm. The reason of different uncertainties is that the mass of the closer indium sample is approximately 7 times lower.

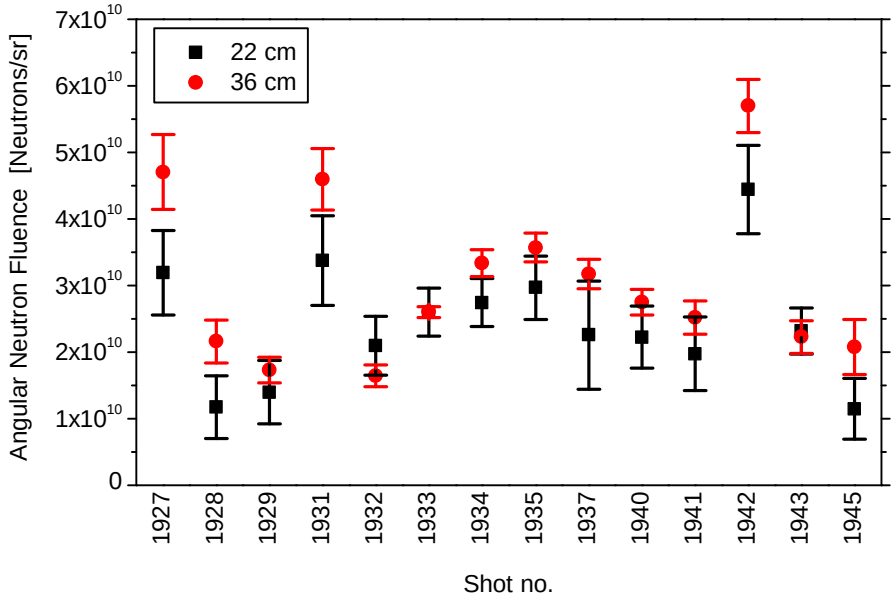

Figure 8.14: Difference between the angular neutron fluence in the radial direction at the distance of 22 cm and 36 cm from the z-axis (without non-dd neutron corrections).

8.4.2 Downstream Dependence of Neutron Fluence

The dependence of neutron fluence in the downstream direction was measured with a help of the indium sample 1-7[5] placed at the distance of 13 cm from the cathode mesh, sample 1-7 at the distance of 15 cm, and the sample C or D at the distance of 18 cm from the mesh (see fig. 8.13). It should be noted, that the distances mentioned above are rounded. The real distances of the samples vary up to 1 mm due to the need of assembling and disassembling of the electrode system after each experimental shots. All the experimental results which are reported in this thesis are calculated with the help of the real distances which were measured before each shot. As in the case of radial indium samples, the downstream samples are protected from the ions by the metallic cover.

As far as the differential neutron yields (without non-dd neutron corrections) are concerned, the measurement shows that in the case of the downstream direction, they are significantly dependent on the distance from the cathode mesh. We assume that significant number of neutrons is produced by the non-dd reactions of the fast

[5]One sample from the set 1-7 was placed in each position (distance from the pinch).

deuterons with the diagnostic housing, as mentioned in the subsection 8.3. We can evaluate the fluence of the non-dd neutrons produced by the duralumin cover in the place of the downstream indium sample by the following manner. If we assume the isotropic neutron emission of the non-dd reactions and homogeneous irradiation of the duralumin cover by deuterons, we can approximate the non-dd neutron source as a disk with the radius R and surface S. The number of the non-dd neutrons emitted by each dS surface element of the disk is

$$\mathrm{d}Y' = \psi' \mathrm{d}S, \tag{8.5}$$

where ψ' is the surface density of the non-dd neutron emission:

$$\psi' = \frac{Y'}{S}, \tag{8.6}$$

where Y' is the total number of the emitted non-dd neutrons. The downstream indium sample is placed on the disk axis at the distance l (see fig. 8.15). The

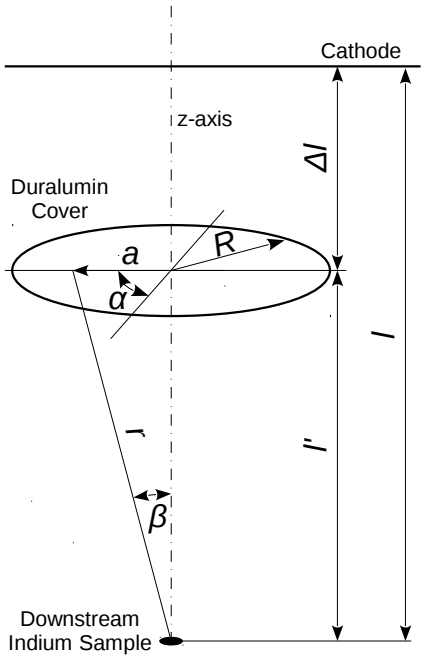

Figure 8.15: Geometry of the duralumin cover and the downstream indium sample.

distance of the activation sample from the duralumin cover is given by

$$l' = l - \Delta l, \tag{8.7}$$

where Δl is the distance of the duralumin cover from the cathode mesh. In accordance with fig. 8.15, the neutron fluence in the downstream direction at the distance l' from the duralumin disk is

$$\mathrm{d}\Phi'(\varphi = 0^{\mathrm{o}}) = \frac{\psi'}{4\pi r^2}\ \cos\beta\ \mathrm{d}S. \tag{8.8}$$

Substituting r by $\sqrt{a^2 + l'^2}$, $\cos\beta$ by $l'/\sqrt{a^2 + l'^2}$, and $\mathrm{d}S$ by $a\,\mathrm{d}\alpha\,\mathrm{d}a$ we obtain:

$$\mathrm{d}\Phi'(\varphi = 0^{\mathrm{o}}) = \frac{\psi'}{4\pi}\ \frac{l'\,a}{\left(a^2 + l'^2\right)^{3/2}}\ \mathrm{d}\alpha\ \mathrm{d}a. \tag{8.9}$$

The total non-dd fluence in through the downstream indium sample area is given by the expression:

$$\Phi'(\varphi = 0^{\mathrm{o}}) = \int_0^R \int_0^{2\pi} \frac{\psi' l'}{4\pi}\ \frac{a}{\left(a^2 + l'^2\right)^{3/2}}\ \mathrm{d}\alpha\ \mathrm{d}a, \tag{8.10}$$

$$\Phi'(\varphi = 0^{\mathrm{o}}) = \int_0^R \frac{\psi' l'}{2}\ \frac{a}{\left(a^2 + l'^2\right)^{3/2}}\ \mathrm{d}a, \tag{8.11}$$

and finally,

$$\Phi'(\varphi = 0^{\mathrm{o}}) = \frac{\psi'}{2} - \frac{\psi' l'}{2}\frac{1}{\sqrt{R^2 + l'^2}}. \tag{8.12}$$

Since the indium sample is significantly smaller than the duralumin cover, we assume that the non-dd neutron fluence is constant on the indium sample front surface.

We used the formula (8.12) to evaluate the dependence of the non-dd neutron fluence on the distance from the aluminum cover of the diagnostic housing. Thus, the total neutron fluence in the downstream direction is given by the superposition of the dd and non-dd neutrons:

$$\Phi(\varphi = 0^{\mathrm{o}}) = \frac{\psi'}{2} - \frac{\psi' l'}{2}\frac{1}{\sqrt{R^2 + l'^2}} + \frac{Y}{4\pi l^2} \tag{8.13}$$

where l' is the distance of the non-dd neutron source (housing cover) and l is the distance of the dd neutron source (assumed close to the cathode). The expression (8.13) was fitted with the measured neutron fluences. The number of non-dd neutrons was used as the fitting parameter for each individual shot. Such fitted dependencies of the neutron fluence are displayed in fig. 8.16. As we can see in fig. 8.16, formula (8.13) allows the relatively good fit. The number of non-dd neutrons is very different for each individual fit. We can express the fitting parameter by the percent fraction

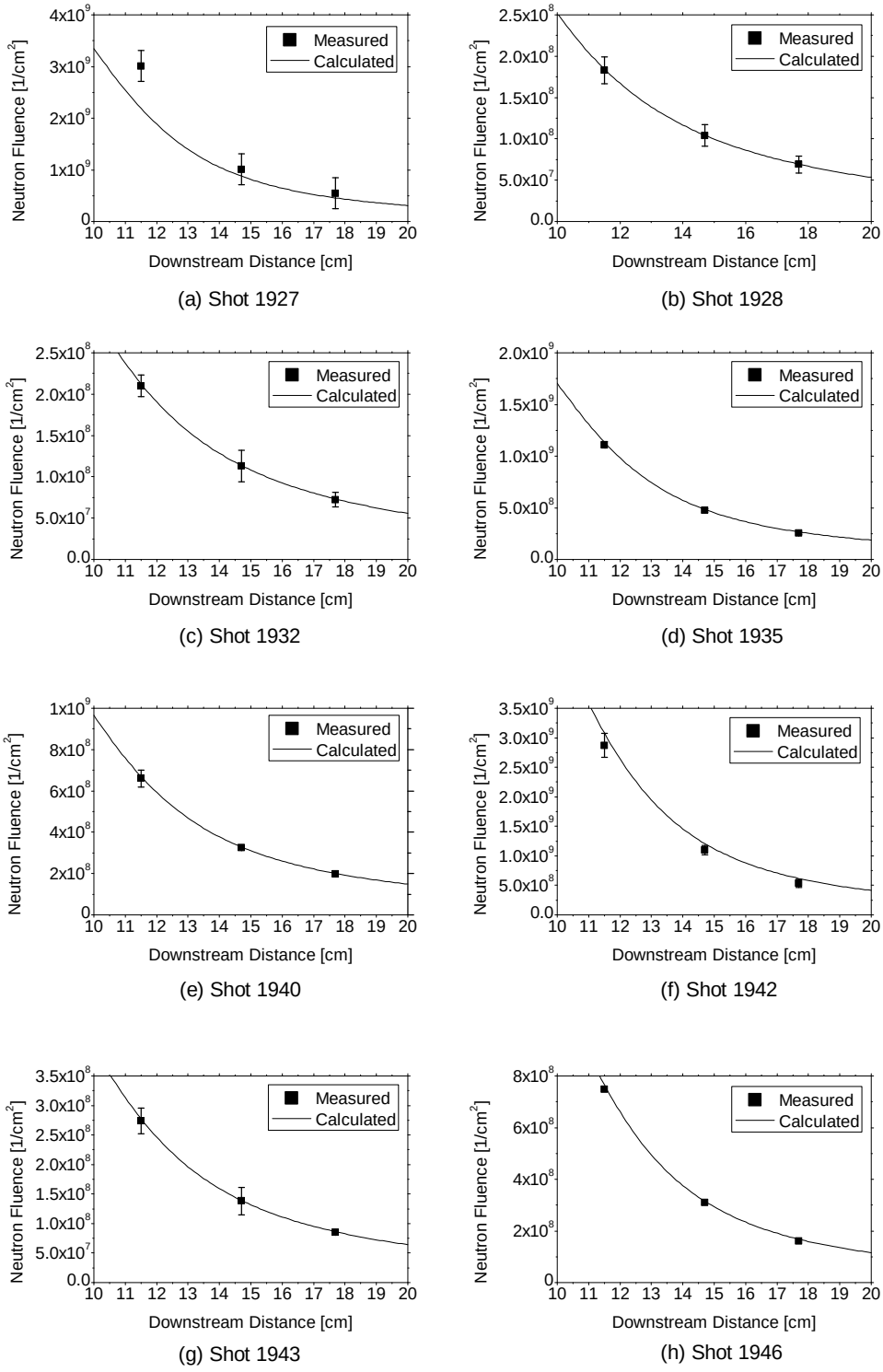

Figure 8.16: Comparison of the calculated and measured neutron fluence in the downstream direction.

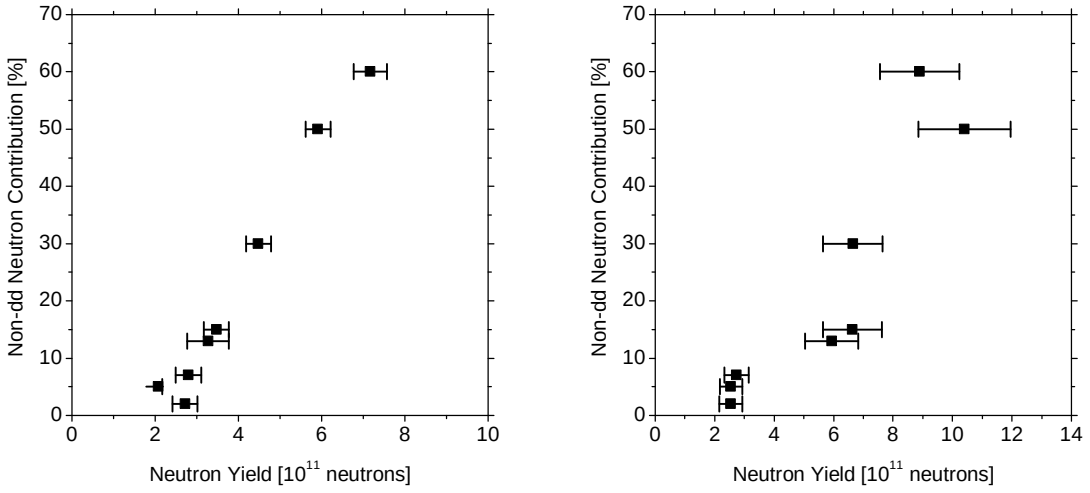

(a) Neutron Yield by Indium Activation (b) Neutron Yield by BD-PND

Figure 8.17: Dependence of the non-dd neutrons on the total neutron yield.

of the total measured neutron yield. If we plot the dependence of this fitting parameter used in fig. 8.16 on the total neutron yield we obtain fig. 8.17. Examining the dependencies in fig. 8.17, it seems that the contribution of the non-dd neutrons is growing with the total neutron yield. However, such high contributions of the non-dd neutrons to the total neutron yield are not in accordance with the estimations in section 8.2. Therefore, the assumption of the isotropic neutron emission of the nuclear reactions of deuterons with the diagnostic cover seems to be incorrect. It indicates that the non-dd neutrons are emitted rather in the downstream direction than in the radial direction. In such a case, the vertical axis in fig. 8.17 represents a number of the non-dd neutrons emitted in the downstream direction in arbitrary units instead of the fraction of the total neutron yield. This hypothesis is in accordance with the calculated and measured differential neutron yields reported in Araki's paper [125]. These thick target angular differential neutron yields from a thick aluminum target are displayed in fig. 8.18 [125]. As we can see in fig. 8.18, the neutron emission induced by reactions of deuterons with the aluminum thick target is relatively anisotropic, with a maximum at the angle of 0°. It could explain the significant neutron fluence anisotropy measured in the short distances from the electrodes reported in section 8.3 (see fig. 8.10).

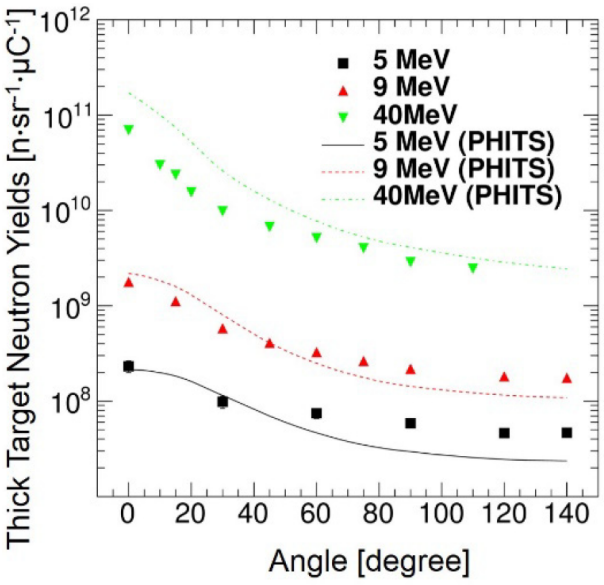

Figure 8.18: Angular differential neutron yields from a thick aluminum target [125].

8.5 Neutron Spectra

In the previous sections, the neutron time-of-flight diagnostics, fast neutron activation diagnostics, and their experimental results were presented. This information helps us to evaluate the neutron spectrum. As mentioned in section 8.1, the number of neutrons with the energy above 12 MeV was estimated by the copper activation sample. Obviously, the number of the neutrons with an energy in the range from 10 MeV to 12 MeV was evaluated from the difference between the yields determined by the niobium and copper samples. Analogously, subtracting the yields evaluated by the niobium sample from the yield evaluated by the aluminum sample, the number of the neutrons with energies in the range from 3.8 MeV to 9.5 MeV was obtained. Finally, when we subtract the yields evaluated by the aluminum sample from the yield evaluated by the indium sample, we obtain the number of the neutrons with energy in the range from 0.5 MeV to 3.8 MeV. The example of such neutron spectra with the yields of neutrons corresponding to the energy intervals mentioned above and the fitted neutron spectrum obtained by the nToF detector is shown in fig. 8.19. The example in fig. 8.19 represents neutron spectrum measured in the radial direction at the distance of 37 cm from the z-axis in shot no. 1760. In this shot, the neutron yield achieves $(1.1 \pm 0.2) \times 10^{12}$, the current at stagnation reached 2.8

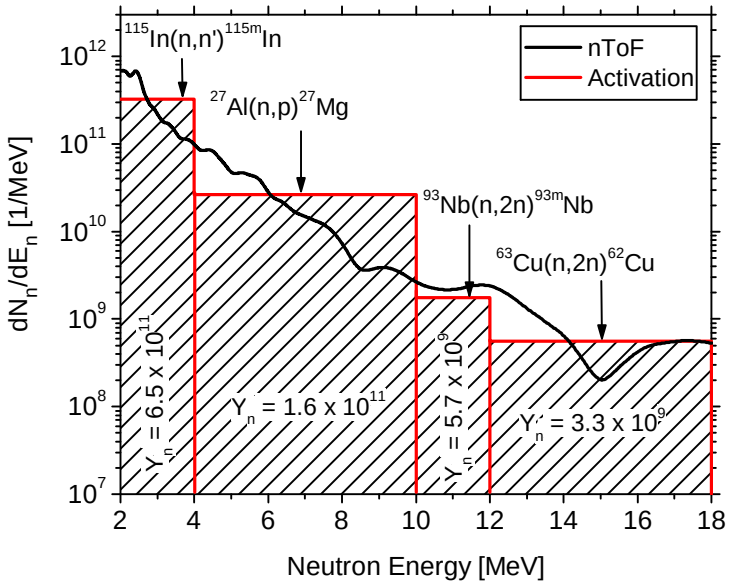

Figure 8.19: Neutron spectrum in shot no. 1760 with the total neutron yield of 1.1×10^{12}. The line represents the neutron spectrum obtained by nToF detector and the bars represent the neutron spectrum obtained by the set of the activation samples with corresponding yields.

MA and the injected mass of the gas-puff was about 75 μg/cm. The bars in fig. 8.19 are labeled by the threshold reaction. As far as the nToF is concerned, the relative spectrum is obtained using the nToF detector in 25.8 m. The measured nToF signal $s(\tau)$ was transformed into the neutron spectrum $\mathrm{d}N_n/\mathrm{d}E_n$ [86, 87, 88] using the transformation (7.19) derived in the section 7.2. Since the neutron spectrum in our experiment is very broad, term $\eta(E_n)$ scintillator neutron response in (7.19) is very important. A theoretical determination of $\eta(E_n)$ is complicated [75]. An experimental evaluation of the $\eta(E_n)$ is presented in [76]. However, the vicinity of our detectors, especially the lead shielding significantly differs from the case described in [76]. Therefore, it was needed to find the $\eta(E_n)$ of our nToF detectors. We assume that the $\eta(E_n)$ could be approximated as

$$\eta(E_n) \approx A_S \, E_n^P, \tag{8.14}$$

where A_S is a proportional parameter, E_n is the neutron energy and P is the power factor. Thus, the neutron spectrum can be approximated by

$$\frac{dN_n}{dE_n} = s(\tau, d)\frac{A_P}{A_S\, E_n^P}\frac{(\tau - t_0)^3}{m_n}\frac{1}{S}, \tag{8.15}$$

where E_n is the neutron energy, A_P is a photomultiplier amplification, τ is the time of the detection, t_0 is the time of the neutron generation, m_n is the neutron mass, and S is the surface of the detector. As far as P factor is concerned, the first estimation including the lead shielding performed Ondřej Šíla with a help of the MCNP simulation. Using this simulation, we obtain P approximately equal to 1. P was also evaluated from the experimental data. The transformation of nToF detector signals into neutron energy (7.19) was performed with several different P power factors in the range from 0.5 to 2. The obtained neutron spectra were fitted into the spectrum evaluated by the activation diagnostics (see fig. 8.19 for $P = 1$). The numbers of neutrons in each energy range were compared. The averaged differences between the areas under the nToF and activation spectra are displayed in fig. 8.20. Examining fig. 8.20 it seems that the best fit of the nToF

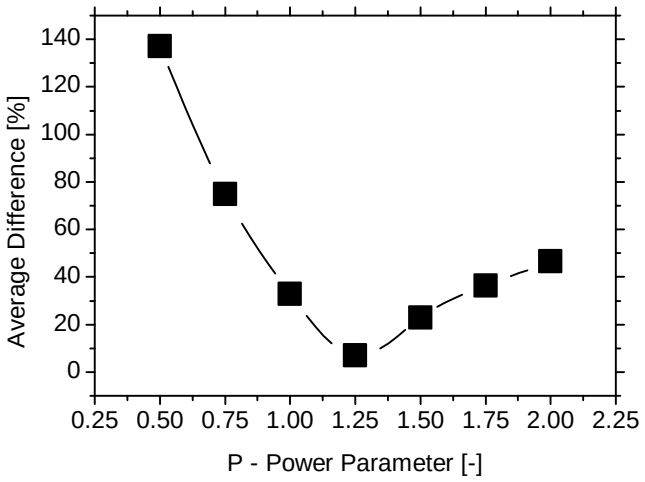

Figure 8.20: The difference between the spectrum evaluated by the fast activation diagnostics and fitted nToF spectrum.

and activation spectrum was achieved with $P = 1.25$. However, taking into account the inaccuracy of such fit, in our experiments we use $P = 1$ found by the MCNP simulation. Practically, the difference between $P = 1$ and $P = 1.25$ should not be decisive in the result interpretation.

To put it shortly, the relative nToF spectrum with a high energy resolution was calibrated by the absolute spectrum with the low energy resolution evaluated by the fast neutron activation samples. We assume that such calibration is valid in every shot where the setting of the nToF detector is the same.

If we take into account the gamma-ray analysis error, the uncertainty of the results in fig. 8.19 is about 30%.

In fig. 8.19 we can see, that a very significant number of the neutrons with energy above 2.45 MeV are in the neutron spectrum. Such a high-energy nature of the neutron spectrum could be explained by the high number of the suprathermal deuterons.

In conclusion of this subsection, it should be noted that the spectrum in fig. 8.19 represents the spectrum in the radial direction only. In the downstream direction, the neutron energies should be significantly higher. Also, the neutron spectrum in the upstream direction is certainly different. So far, the spectrum in the upstream and downstream directions has not been precisely measured due to the mechanical equipment. In particular, the massive gas-puff hardware with a brass nozzle and a copper coil in the upstream direction and the vacuum system in the downstream direction complicate the measurement by the significant scattering of the neutrons.

8.6 Photoexcitation of Indium Activation Sample

In work presented in this thesis, the indium activation samples are used to measure the neutron fluence by nuclear excitation reaction ^{115}In(n,n')^{115m}In. As mentioned in section 7.4, the decay of the metastable ^{115m}In is accompanied by gamma-rays with the energy of 335 keV (see table. 7.2). It should be mentioned, that ^{115m}In could be produced also by the interaction of high-energy photons with the indium sample by photoexcitation reaction $^{115}\mathrm{In}(\gamma,\gamma')^{115m}\mathrm{In}$ [126]. Obviously, it is impossible to distinguish ^{115}In(n,n')^{115m}In and reaction $^{115}\mathrm{In}(\gamma,\gamma')^{115m}\mathrm{In}$ by the gamma-ray spectra. Therefore, the photoexcitation could affect the neutron measurement.

In our experiments, the disruption of Z-pinch by instabilities is accompanied by MeV bremsstrahlung [123]. Using TLF-700 thermoluminescence dosimeters we measured a dose up to 100 Gy of 200 keV photons per single shot at the distance of 3 cm behind the anode surface [123]. Due to the short intensive pulsed character of the bremsstrahlung the evaluation of its spectrum is complicated. Since the measured

anode-cathode voltage maximum achieves about 1 MV, we assume, that energy of most of the bremsstrahlung photons is below 1 MeV. On the other hand, the detected multi-MeV deuterons indicate that also electrons and photons with multi-MeV energies are produced. Thus, it seems that the duration of the multi-MeV charged particle and bremsstrahlung emission is shorter than the time resolution of our voltage measurement of about 2 ns. Since the FWHM of the bremsstrahlung pulse measured by the scintillation detectors is about 20 ns, a contribution of multi-MeV photons to the total number of bremsstrahlung spectrum could be insignificant in comparison with the sub-MeV photons.

In order to prove that our indium activation diagnostics is not affected by $^{115}\mathrm{In}(\gamma,\gamma')^{115\mathrm{m}}\mathrm{In}$ reaction, the following measurement was performed. Two identical indium samples V and VI were placed in the radial direction at the distance of 37 cm from the z-axis. Sample V was shielded in the front and rear side by lead with a thickness of 5 cm whereas the sample VI was without any lead shielding. The experimental arrangement is shown in fig. 7.26.

In book [101], the experimental transmission of gamma-rays of ^{60}Co (gamma-ray photon energy 1.17 MeV and 1.33 MeV) through the thick lead shielding is presented. The radiation dose rate of ^{60}Co is attenuated approximately ten times by the lead with the thickness of 5 cm. Photons with an energy lower than the energy of ^{60}Co radiation should be attenuated even more.

Therefore if $^{115}\mathrm{In}(\gamma,\gamma')^{115\mathrm{m}}\mathrm{In}$ reaction influences activity of an indium sample, the neutron fluence measured by the sample indium V (with lead shielding) should be significantly lower than the activity of the sample indium VI (without lead shielding). To evaluate the neutron fluence by the sample V, the scattering of neutrons by the lead shielding must be taken into account. Using the MCNP simulation, Ondřej Šíla determined the neutron attenuation coefficients for our experimental neutron spectrum and neutron energy threshold of 0.5 MeV. According to these simulations, the lead shielding attenuates the neutron fluence approximately 1.85 times.

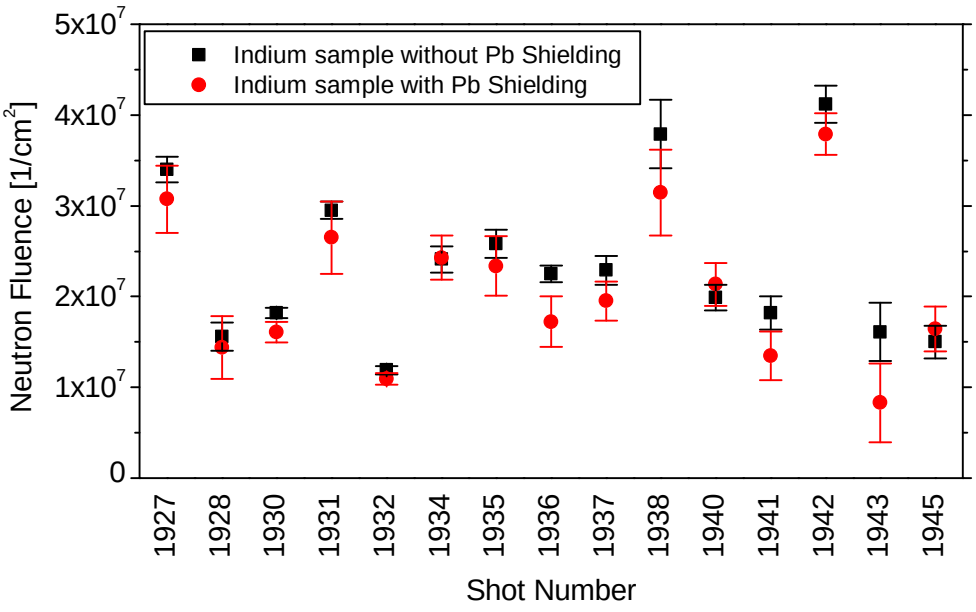

Figure 8.21: Comparison of neutron fluences measured by the indium samples with and without the lead shielding with a thickness of 5 cm including the neutron attenuation coefficient evaluated by MCNP.

A comparison of neutron fluences measured by the indium samples with and without the 5 cm lead shielding is reported in fig. 8.21. In this comparison the neutron attenuation coefficient is included. Examining fig. 8.21 we can see, that the neutron fluences evaluated by the sample indium V correspond to the neutron fluences evaluated by the sample indium VI. Therefore, we could assume that in our experiments the photoexcitation reaction $^{115}\mathrm{In}(\gamma,\gamma')^{115\mathrm{m}}\mathrm{In}$ influences the indium activation diagnostics in radial direction insignificantly.

Chapter 9

Discussion

In this chapter, results of our experiments are summarized and results of the measurements are discussed and put into context.

9.1 Most Important Experimental Results

The neutron yields were measured by several independent methods: neutron bubble detectors (BD-PND), silver activation counter (SAC), and fast neutron activation diagnostics. The results of these diagnostic techniques are relatively consistent (see fig. 8.1).

As mentioned in section 8.2, in our experiments some portion of neutrons is produced by interactions of multi-MeV deuterons with duralumin and stainless steel experimental hardware. The energy of such non-dd neutrons can range from 0 to more than 10 MeV (see cross-sections in fig. 8.5). For the physics of the hot deuterium plasma, it is important to evaluate the contribution of the non-dd neutrons to the total neutron yield. In section 8.2, the contribution of the non-dd neutrons was estimated with a help of the cross-sections of the neutron-producing reactions of deuterons with ^{27}Al and ^{56}Fe and number of the multi-MeV deuterons which was determined with a help of the LiF deuteron-neutron converter. By this estimation, the number of the non-dd neutrons achieves up to 15% of the total neutron yield. The analogous estimation was performed for neutrons produced by (p,n) reactions in the shot with the natural hydrogen where dd neutrons can be ruled out. The result of the estimation of neutron yield from (p,n) reactions is in good agreement with the measured neutron yield (see section 8.2). The measurement of neutron fluence

at different distances from the pinch in downstream and radial direction shows that the non-dd neutrons are emitted mostly in the downstream direction.

As far as the measured neutron spectra are concerned, the neutrons with relatively high energies (12 – 20) MeV were detected in the radial direction. There are three possibilities how to explain such high-energy neutron emission in the radial direction.

The first possibility is that the high-energy neutrons are produced by the dd reactions of deuteron beam streaming from the anode to the cathode. Examining the dependence of the ejectile neutron energy on the projectile deuteron energy of D(d,n)^{3}He reaction to the angle of 90^o (see fig. 4.3), we see that for the emission of 12 MeV neutrons the deuteron energy of 38 MeV is needed. An occurrence of the deuterons with such energy was not proved. However, hydrogen ions (deuterons or protons) with an energy above 39 MeV were detected using a stack of radiochromic films, CR-39 nuclear track detectors and metallic absorbers [2]. It is not excluded that deuterons with even higher energy are also generated. On the other hand, the 90^o ejection angle is not very probable in comparison with the ejection angle of 0^o (see angular differential cross-section in fig. 4.5).

Another possibility is that the 12 MeV neutrons in the radial direction are emitted by the deuterons with an energy of about 7 MeV which are moving in the radial direction. The deuterons could be deflected to the radial direction by the Z-pinch magnetic field. Considering the MCP images and results of ion pinholes, the discharge radius is of about 5 mm at the stagnation. If we assume, that the half of the discharge current ($0.5 \times 3 = 1.5$) MA is compressed on or below this radius, the Larmor radius of the 7 MeV deuterons is 9 mm. Such relatively small Larmour radius indicates that the deflection of the 7 MeV deuterons to the radial direction is possible.

The last possibility is that the high-energy neutrons in the radial direction are produced by the reactions of deuterons with ^{27}Al and ^{56}Fe, especially (d,n), (d,n+p), (d,n+α), and (d,2n). Nevertheless, an energy of the most of produced neutrons is bellow 10 MeV (see fig. 8.19). The number of neutrons, in this region of neutron spectrum, is significantly higher than than the estimated number of non-dd neutrons (chapter 8.2). Therefore, the approximation of the deuteron energy distribution $f(E_d) \propto E_d^{-\kappa}$ should not be affected even if the >12 MeV neutrons are of the non-dd origin since the κ parameter is given by the neutron spectrum bellow 10 MeV.

9.2 Neutron Production of Deuterium Plasma

As far as the neutrons produced by the D(d,n)^{3}He reaction are concerned, from the neutron spectra, anisotropy, neutron time-of-flight signals, and many other considerations, it is undoubted that their majority is produced by the beam-target mechanism. To achieve the observed neutron energy spectrum, the neutrons must be produced by collisions of the deuterons with much higher energy than the deuteron temperature. Such high-energy tail of the deuteron distribution could be approximated as $f(E_d) \propto E_d^{-\kappa}$ [77, 78, 79]. Using the procedure described by Knapp et al., $\kappa = 1.8 - 2.0$ was evaluated from the dd neutron energy spectrum in the radial direction for the deuteron energy above 20 keV [2, 4]. For the validity of this evaluation, the following conditions must be fulfilled. The first condition is the known dependence of the neutron time-of-flight detector response on the neutron energy. This is important especially in the GIT-12 experiments where the neutron spectrum is very broad. The second condition is that most of the detected neutrons should be of the dd origin. The experimental results presented in this thesis indicate that these conditions are fulfilled.

Since we know the κ parameter of the deuteron distribution, we could evaluate the average energy of deuterons which produce neutrons by D(d,n)^{3}He reaction [4]:

$$\langle E_d \rangle_{\text{reacting}} = \frac{\int_{>20\,\text{keV}} \sigma_{dd}(E_d)\, E_d\, f(E_d)\, \mathrm{d}E_d}{\int_{>20\,\text{keV}} \sigma_{dd}(E_d)\, f(E_d)\, \mathrm{d}E_d} = \frac{\int_{>20\,\text{keV}} \sigma_{dd}(E_d)\, E_d\, E_d^{-\kappa}\, \mathrm{d}E_d}{\int_{>20\,\text{keV}} \sigma_{dd}(E_d)\, E_d^{-\kappa}\, \mathrm{d}E_d} \doteq 1\text{MeV}, \tag{9.1}$$

where $\sigma_{dd}(E_d)$ is the cross-section of D(d,n)^{3}He reaction, $f(E_d)$ is the energy distribution of reacting deuterons.

As far as the number of deuterons with the fusion energy is concerned, it could be calculated by the following formula [4]:

$$N_{tail} = \frac{Y_{dd}}{n_d\, l_d \int_{>20\,\text{keV}} \sigma_{dd}(E_d)\, f(E_d)\, \mathrm{d}E_d}, \tag{9.2}$$

where Y_{dd} is a number of deuterons produced by D(d,n)^{3}He reaction, n_d is a deuteron density, l_d is a path length of deuterons. Assuming that the contribution of non-dd neutrons should be less than 15% (see section 8.2) and most of the non-dd neutrons are emitted in the downstream direction (see section 8.4.2), we could consider that the total neutron yield evaluated by the radial neutron diagnostics is approximately equal to Y_{dd}. We could evaluate the deuteron density n_d from the deuteron line

density $n_l = 3 \times 10^{19}$ deuterons/cm and the final pinch radius $R = 0.5$ cm as $n_d = n_l/\pi R^2 = 4 \times 10^{19}$ cm^{-3} [4]. The estimation of l_d is somewhat more complicated. If we assume, that l is approximately equal to the anode-cathode gap of 2 cm, we obtain $N_{tail} \doteq 10^{18}$ with the total energy

$$E_{\text{tail}} = N_{\text{tail}} \int_{>20keV} E_d \, f(E_d) \, \mathrm{d}E_d \doteq 60\,\text{kJ} \tag{9.3}$$

for a good shot with the neutron yield of about 2×10^{12}. Such energy is almost equal to the total energy input into plasma during the implosion [4]:

$$E_{\text{plasma}} = \frac{1}{2} \int \dot{L} I^2 \mathrm{d}t \doteq 65\,\text{kJ}. \tag{9.4}$$

It is very unlikely since less than 2% of all deuterons belong to the high-energy tail [4]. Therefore, the deuteron path length should be much higher than 2 cm. During the neutron emission (15-20 ns), deuterons with the energy $\langle E_d \rangle_{\text{reacting}} \doteq 1$ MeV could travel the distance of about 10 cm [4]. Using formulas (9.2) and (9.3) for $l_d = 10$ cm we obtain the total energy of deuterons in high-energy tail of about 10 kJ [4]. Such an energy seems to be quite realistic. The prolongation of deuteron path length could be explained by the magnetization. Such assumption is in accordance with the neutron energy spectra in the radial direction mentioned above.

9.3 Scaling and Efficiency of Neutron Production

It could be interesting to compare the neutron yields achieved in our experiments with other deuterium Z-pinch and plasma focus experiments with a different current and type of load. Such a comparison is displayed in fig. 9.1. Our experiment on the GIT-12 generator is marked by the red square, other deuterium gas-puff experiments are marked by blue squares, deuterated fiber and cryogenic deuterium fiber experiments are marked by green triangles, and deuterium plasma foci experiments are marked by black circles. In fig. 9.1 the neutron yield scaling laws $Y_n \propto I^3$ and $Y_n \propto I^4$ are represented by the blue and red line, respectively. In fig. 9.1, the neutron yield from the fiber Z-pinches is significantly lower than the neutron yield from the plasma foci and gas-puffs at the currents of above 1 MA. In the case of plasma foci, a saturation of the neutron yield was observed at the currents above 2 MA [16]. As far as the deuterium gas-puffs are concerned, any saturation of neutron

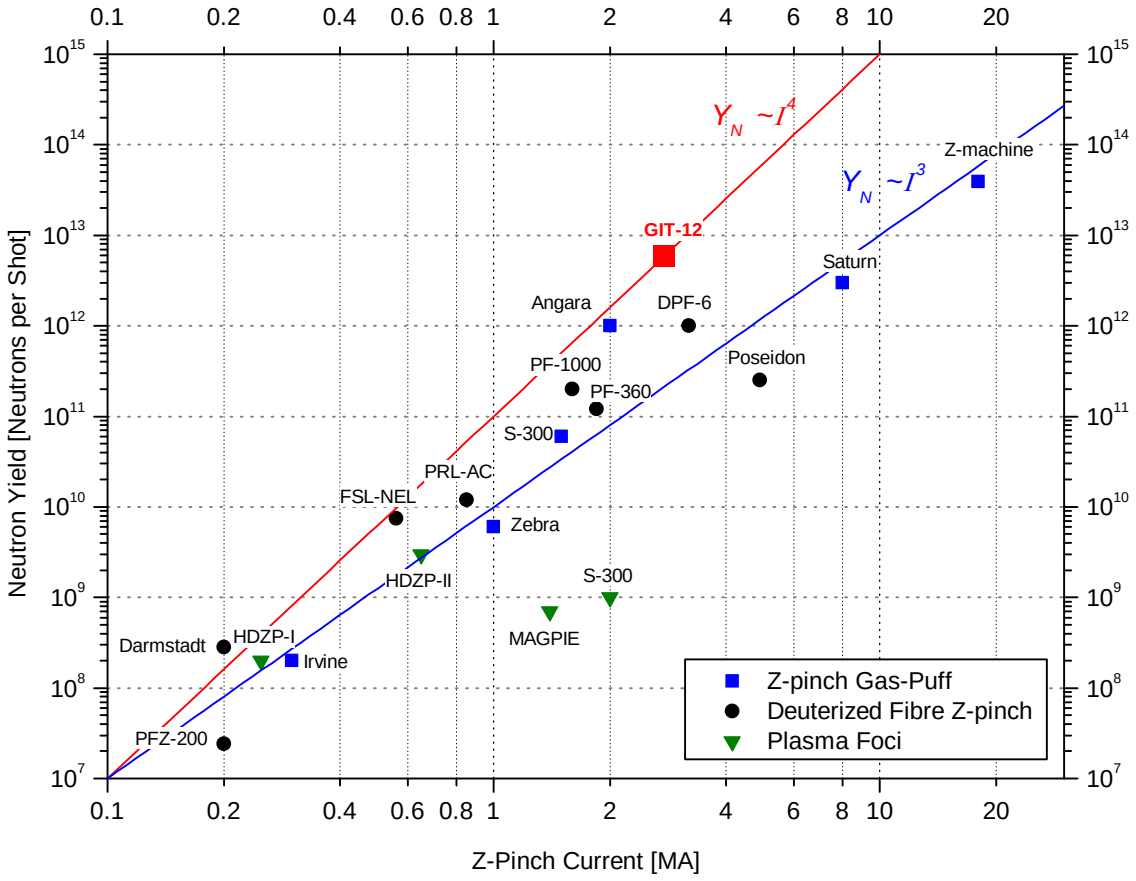

Figure 9.1: Comparison of the neutron yields from experiments on the GIT-12 generator and other Z-pinch and plasma focus experiments. Data are used from [16, 35, 36, 39, 40, 67, 128, 129, 130, 131, 132, 133, 134, 135].

yield has not been observed. The experiments on the Saturn [32] and Z machine [39] indicate that the neutron yield corresponds to the $Y_n \propto I^3$ scaling law. However, in the experiments on Angara [36, 37] and our experiments it seems, that the neutron yield scaling corresponds to $Y_n \propto I^4$ at the currents $(2-3)$ MA. It should be noted, that all neutron yields in fig. 9.1 are of the beam-target origin.

The experiments shown in fig. 9.1 are different in many parameters as in the time of implosion, the mass of imploding pinch, electric parameters of the current generator, etc. Therefore, the neutron yields should be compared also taking into account the total stored electrical energy in capacitors of the generator. The neutron yields of above-mentioned experiments related to the total stored electric energy are

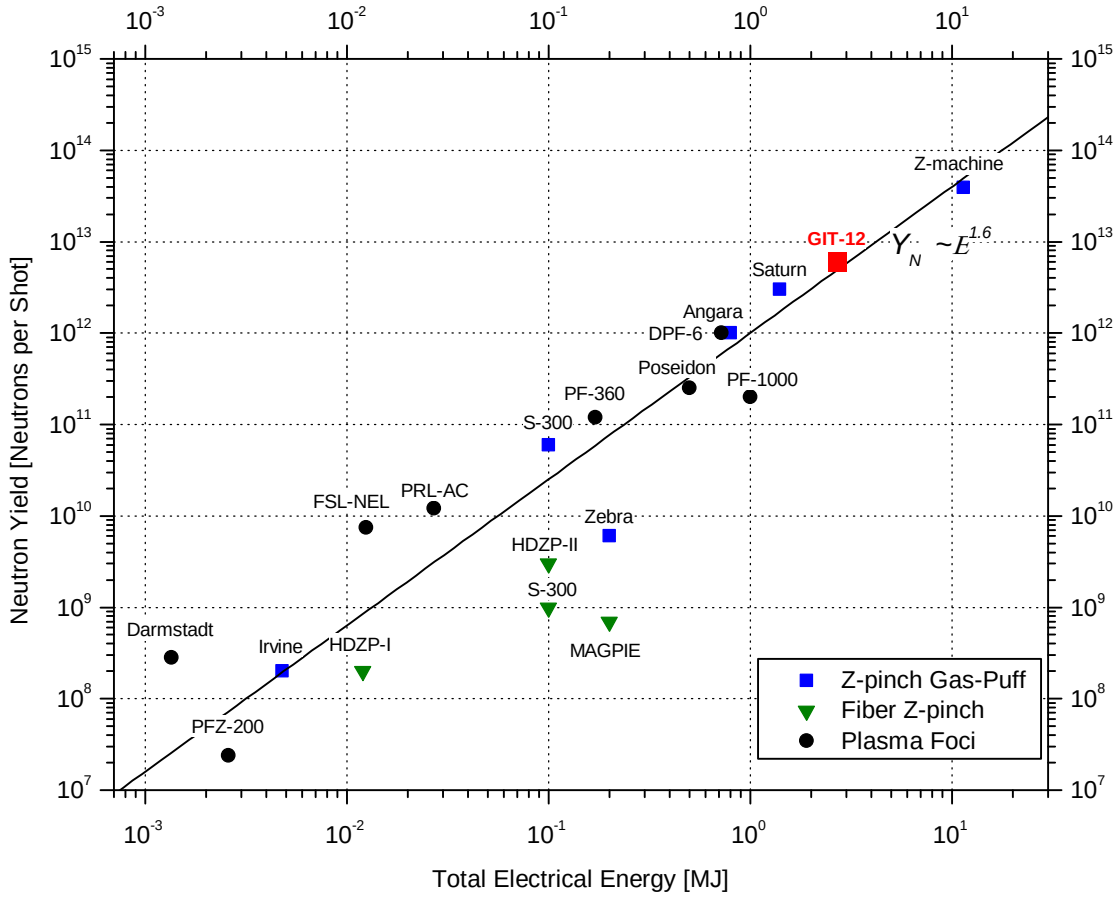

Figure 9.2: Comparison of the neutron yields from experiments on the GIT-12 generator and other Z-pinch and plasma focus experiments. Data are used from [16, 35, 36, 39, 40, 67, 128, 129, 130, 131, 132, 133, 134, 135]

displayed in fig. 9.2.

In fig. 9.2 the neutron yield scaling $Y_n \propto E^{1.6}$ is shown. In the case of plasma foci, the saturation of neutron yield occurs at the energy of about 1 MJ [16, 136]. It should be noted that in the gas-puff experiments on the Angara [36], Saturn [32], and Z-machine [39], the current rise times are about 100 ns, 40 ns, and 100 ns, respectively, whereas, in our experiments, the rise time of the GIT-12 generator is about 1.5 μs. Thus, for the high neutron emission efficiency, the very short rise times up to 100 ns is not necessary. It allows an easier design and construction of the pulsed power generators for neutron producing Z-pinches. Moreover, in our experiments, the Z-pinch stagnation and disruption occur at the time of about 700

ns. During the remaining time of 800 ns the current is rising up to the value of about 5 MA, but in this phase, the generator energy does not contribute to the neutron production[1]. Therefore, we could assume, that if we use a generator with the maximum current of 3 MA, rise time of 700 ns and thus significantly lower stored electrical energy, to drive the same Z-pinch load, the neutron production efficiency (neutrons/energy ratio) would be better than in the case of the GIT-12 generator.

9.4 Applications of Deuterium Gas-puff Z-Pinch

The main goal of our experiments is the fundamental research, but in future, the deuterium gas-puff Z-pinch could be used also in applications. As mentioned in chapter 8, the deuterium gas-puff in our experiments produces an intensive beam of multi-MeV deuterons. It could be used for the production of radioisotopes with a short half-life and high activity. For example, ^{13}N isotopes with a half-life of 10 min are used in the positron-emission tomography (PET) in medicine [137]. The ^{13}N could be produced by reaction ^{12}C(d,n)^{13}N [4]. If we place a carbon sample below the cathode mesh, the number of produced ^{13}N nuclei $N_{\mathrm{N}-13}$ could be estimated with a help of the shot with LiF catcher described in section 8.2. Analogously to the calculation (8.3) we obtain

$$N_{\mathrm{N}-13} = Y_{LiF} \frac{\int_0^{10\,\mathrm{MeV}} E_d^{-\kappa}\, Y_{TT-C}(E_d)\,\mathrm{d}E_d}{\int_0^{10\,\mathrm{MeV}} E_d^{-\kappa}\, Y_{TT-LiF}(Ed)\,\mathrm{d}E_d}, \tag{9.5}$$

where Y_{LiF} is the thick target yield of ^{7}Li(d,n) and ^{7}Li(d,n+α) reactions from the LiF catcher, Y_{TT-C} is a thick target yield of ^{12}C(d,n)^{13}N reaction from the carbon sample and deuteron energy distribution $f(E_d) \propto E_d^{-\kappa}$. The thick target yield for the carbon sample Y_{TT-C} could be calculated analogously to formula (8.1). Assuming $\kappa = 2$ we obtain a number of ^{13}N nuclei of about 5×10^{11}. It corresponds to the activity of about 0.6 GBq after the shot.

Another possibility is to use the deuterium gas-puff for a neutron radiography with a short exposition time on the order of tens of nanoseconds. In our experiments we, placed two nuclear track detectors CR-39 behind samples of lead, stainless steel, and duralumin in the radial direction at the distance of 25 cm from the z-axis. These

[1]The GIT-12 was originally designed to drive implosions of heavier loads where the implosion is longer than in our experiments with the deuterium gas-puff.

samples were 3.5 cm long and 4 cm high. The experimental arrangement, the result image, and the simulation in the MCNP performed by Ondřej Šíla are displayed in fig. 9.3. To obtain the first Z-pinch neutron radiography image shown in fig. 9.3(e),

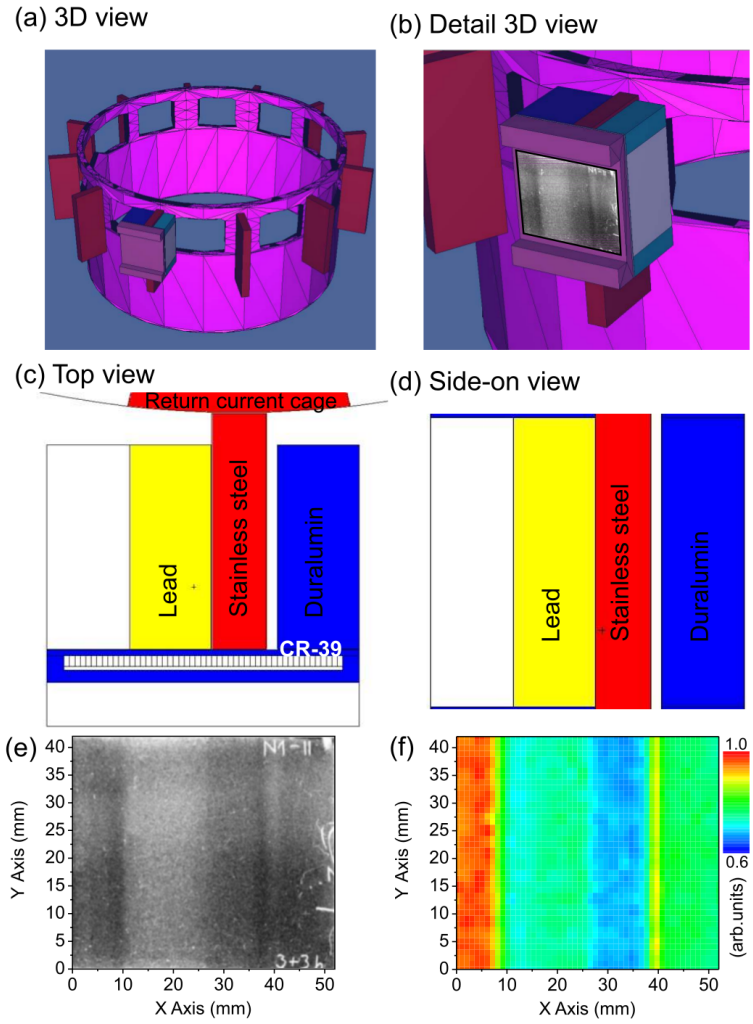

Figure 9.3: Neutron radiography: (a) 3D view of experimental arrangement, (b) Detail of 3D view of experimental arrangement, (c) Top view of experimental arrangement, (d) Side-on view of experimental arrangement, (e) Scan of the etched CR-39 detector, (f) MCNP simulation of neutron fluence at the CR-39 detector [4].

we accumulated 20 shots with a total neutron yield of 3×10^{13}. The accumulation of 20 shot is not necessary for our neutron source. Using more sensitive neutron detector, a single shot should be sufficient to obtain a neutron radiography image. For example, in [138] a fast scintillating fiber array gated neutron imager is used [139]

for imaging of a similar testing sample as in our experiments by a neutron source with an output up to 10^{10} neutrons/sr per single shot. In our experiments, the average neutron output in the radial direction is of about 1.8×10^{10} neutrons/sr and in the downstream direction of about 9.2×10^{11} neutrons/sr (see table 8.1). Moreover, using a LiF catcher, the neutron output of our Z-pinch could be significantly higher.

Chapter 10

Conclusions and Prospects

The deuterium gas-puff with the outer plasma shell on the GIT-12 device is a very efficient source of high energy neutrons and deuterons with relatively good reproducibility.

In the frame of the work reported in this thesis, the scintillation neutron time-of-flight detector with the solid state amplifier was developed. The NaI(Tl) and HPGe gamma-ray spectrometers were calibrated and the fast neutron activation diagnostics was established in the experiments on the GIT-12 device. It was proven that the indium neutron activation sample is not significantly activated by the photo-excitation reactions. Using the neutron activation diagnostics, the neutron fluences at different distances and directions were measured. The neutron yields evaluated by the fast neutron activation diagnostics are in agreement with neutron yields evaluated by the silver activation counter and neutron bubble detectors. The broad-energy radial neutron spectra were measured by indium, aluminum, niobium, and copper neutron activation samples and scintillation neutron time-of-flight detectors. The high-energy neutrons (up to 20 MeV) were emitted in the radial direction probably due to collisions of magnetized multi-MeV deuterons. The interactions of multi-MeV deuterons with the duralumin and stainless steel hardware led to the production of non-dd neutrons. A number of the non-dd neutrons could achieve 15% of the total neutron yield. It seems that most of the non-dd neutrons are emitted in the downstream direction (below cathode). Therefore, they should not significantly affect the radial neutron diagnostics.

Many questions remain to be answered in the neutron emission at the Z-pinches. Therefore, the future work should be focused on a more precise determination of the

number of non-dd neutrons. It would help to a better interpretation of the experimental results as the high neutron emission anisotropy and origin of the high-energy neutrons. If we found neutron activation materials with a different suitable cross-section of neutron-induced reactions, the more precise neutron spectrum could be obtained. Such experimental results could help with the explanation of the deuteron acceleration mechanism which accelerates the deuterons to multi-MeV energies at the experiments with the generator with the output voltage of 600 kV. This fundamental mechanism is important in other physical disciplines for example, in laser physics, astrophysics, tokamak research, etc.

Appendix A

Personal Contribution to Experiments

The author of this thesis actively participated in the experiments on the GIT-12 generator from 2012 to 2017. During these experiments, he installed and operated the neutron time-of-flight diagnostics, neutron bubble detectors, multi-channel plate soft x-ray pinhole camera, ion diagnostics etc.

As far as the fast neutron diagnostics is concerned, he performed the calibration of the HPGe gamma-ray spectrometer with help of the Canberra LabSOCS (Laboratory Sourceless Object Calibration Software) calibration software and laboratory radiation sources and calibration of the NaI(Tl) spectrometers using laboratory radiation sources and cross-calibration with the HPGe spectrometer. He was responsible for the activation sample selection, placement, and their gamma-ray spectrum analysis.

From the experimental results of the neutron activation diagnostics and neutron time-of-flight signals, he evaluated the neutron yields, neutron energy spectra, neutron anisotropy, dependencies of the neutron fluence on the distance from the pinch in radial and downstream directions, etc. By fitting the spectra obtained by the neutron time-of-flight method to the spectra given by the neutron activation diagnostics, he evaluated the dependence of the neutron time-of-flight detector response on the neutron energy. He designed the neutron time-of-flight detector with the photodiode and solid-state amplifier.

Based on the experimental results, he estimated the number of the neutrons which were produced by the reactions of multi-MeV deuterons with the stainless

steel experimental chamber and stainless steel or duralumin diagnostics housing inside the chamber.

Appendix B

List of Publications

B.1 Publications in Journals with Impact Factor

The publications which follow are the papers, where the author of this thesis is the corresponding author.

1. J. Cikhardt, D. Klir, K. Rezac, A. V. Shishlov, R. K. Cherdizov, B. Cikhardtova, G. N. Dudkin, F. I. Fursov, V. A. Kokshenev, J. Kravarik, P. Kubes, N. E. Kurmaev, A. Yu. Labetsky, V. N. Padalko, N. A. Ratakhin, O. Sila, K. Turek, V. A. Varlachev, *Neutron Spectrum Measured by Activation Diagnostics in Deuterium Gas-Puff Experiments on the 3 MA GIT-12 Z pinch*, IEEE Transactions on Plasma Science - Accepted for publication, Digital Object Identifier: 10.1109/TPS.2017.2763641

2. J. Cikhardt, J. Krása, M. De Marco, M. Pfeifer, A. Velyhan, E. Krouský, B. Cikhardtová, D. Klír, K. Řezáč, J. Ullschmied, J. Skála, P. Kubeš, J. Kravárik, *Measurement of the target current by inductive probe during laser interaction on terawatt laser system PALS*, Review of Scientific Instruments **85**, 103507, 2014.

3. J. Cikhardt, B. Batobolotova, P. Kubes, J. Kravarik, D. Klir, K. Rezac, *Influence of an external magnetic field on the dynamics of a modified plasma focus*, Physica Scripta **T161**, 014042, 2014.

In the following publications, the author of this thesis is a coauthor. We note the publications no. 5 and 23 which are published in the multidisciplinary journals

with impact factor 8.701 and 7.645, respectively.

1. J. Krasa, M. De Marco, J. Cikhardt, M. Pfeifer, A. Velyhan, D. Klir, K. Rezac, J. Limpouch, E. Krousky, J. Dostal, J. Ullschmied, R. Dudzak, *Spectral and temporal characteristics of target current and electromagnetic pulse induced by nanosecond laser ablation*, Plasma Physics and Controlled Fusion **59**, 6, 065007, 2017

2. J. Krasa, E. Giuffreda, D. Delle Side, V. Nassisi, D. Klir, J. Cikhardt, K. Rezac, *Target current: a useful parameter for characterizing laser ablation*, Laser and Particle Beams **35**, 1, 170-176, 2017.

3. P. Kubes, M. Paduch, J. Cikhardt, B. Cikhardtova, D. Klir, J. Kravarik, K. Rezac, E. Zielinska, M. J. Sadowski, A. Szymaszek, K. Tomaszewski, D. Zaloga, *Filamentation in the pinched column of the dense plasma focus*, Physics of Plasmas **24**, 3, 032706, 2017.

4. P. Kubes, M. Paduch, B. Cikhardtova, J. Cikhardt, D. Klir, J. Kravarik, K. Rezac, J. Kortanek, E. Zielinska, M. J. Sadowski, K. Tomaszewski, *Interferometry and x-ray diagnostics of pinched helium plasma in a dense plasma focus with an Al-wire on the axis*, Physics of Plasmas **23**, 11, 2016

5. D. Margarone, A. Velyhan, J. Dostal, J. Ullschmied, J. P. Perin, D. Chatain, S. Garcia, P. Bonnay, T. Pisarczyk, R. Dudzak, M. Rosinski, J. Krasa, L. Giuffrida, J. Prokupek, V. Scuderi, J. Psikal, M. Kucharik, M. De Marco, J. Cikhardt, E. Krousky, et al., *Acceleration Driven by a Nanosecond Laser from a Cryogenic Thin Solid-Hydrogen Ribbon*, Physical Review X, **6**, 4, 2016.

6. J. Krasa, D. Klir, A. Velyhan, K. Rezac, J. Cikhardt, *Generation of fast neutrons through deuteron acceleration at the PALS laser facility*, Journal of Instrumentation **11**, 3, 2016.

7. D. Klir, A. V. Shishlov, V. A. Kokshenev, P. Kubes, K. Rezac, J. Cikhardt, B. Cikhardtova, J. Kravarik, O. Sila, *z-pinch as a powerful source of multi-MeV ions and neutrons for advanced applications* **23**, 3, 2016.

8. B. Cikhardtova, P. Kubes, J. Cikhardt, M. Paduch, J. Kravarik, K. Rezac, J. Kortanek, *Evolution of the small ball-like structures in the plasma focus discharge*, Nukleonika **61**, 2, 2016.

9. M. De Marco, J. Krasa, J. Cikhardt, M. Pfeifer, J. Limpouch, *Measurement of electromagnetic pulses generated during interactions of high power lasers with solid targets*, Journal of Instrumentation **11**, 6, 2016.

10. M. Akel, J. Cikhardt, P. Kubes, H. J. Kunze, S. Lee, M. Paduch, S. H. Saw, *Experiments and simulations on the possibility of radiative contraction/collapse in the PF-1000 plasma focus*, Nukleonika **61**, 2, 145–148, 2016.

11. P. Kubes, M. Paduch, B. Cikhardtova, J. Cikhardt, D. Klir, J. Kravarik, K. Rezac, J. Kortanek, E. Zielinska, M. J. Sadowski, K. Tomaszewski, *The influence of the nitrogen admixture on the evolution of a deuterium pinch column*, Physics of Plasmas **23**, 2016.

12. P. Kubes, M. Paduch, B. Cikhardtova, J. Cikhardt, D. Klir, J. Kravarik, K. Rezac, E. Zielinska, D. Zaloga, M. J. Sadowski, K. Tomaszewski, *Influence of the Al wire placed in the anode axis on the transformation of the deuterium plasma column in the plasma focus discharge*, Physics of Plasmas **23**, 2016.

13. P. Kubes, M. Paduch, J. Cikhardt, D. Klir, J. Kravarik, K. Rezac, B. Cikhardtova, J. Kortanek, E. Zielinska, *The evolution of the plasmoidal structure in the pinched column in plasma focus discharge*, Plasma Physics and Controlled Fusion **56**, 2016.

14. P. Kubes, M. Paduch, J. Cikhardt, D. Klir, K. Rezac, J. Kravarik, B. Cikhardtova, J. Kortanek, E. Zielinska, *Puffing Deuterium Compressed by a Neon Plasma Sheath at the Initial Poloidal Magnetic Field in Plasma Focus Discharge*, IEEE Transactions on Plasma Science **53**, 8, 2015.

15. B. Cikhardtova, P. Kubes, J. Cikhardt, M. Paduch, E. Zielinska, J. Kravarik, K. Rezac, J. Kortanek, O. Sila, *Temporal distribution of linear densities of the plasma column in a plasma focus discharge*, Nukleonika **60**, 2, 2015.

16. M. De Marco, J. Cikhardt, J. Krasa, A. Velyhan, M. Pfeifer, E. Krousky, D. Klir, K. Rezac, J. Limpouch, D. Margarone, J. Ullschmied, *Electromagnetic*

pulses produced by expanding laser-produced Au plasma, Nukleonika **60**, 2, 2015.

17. O. Sila, D. Klir, K. Rezac, J. Cikhardt, B. Cikhardtova, *MCNP calculations of neutron emission anisotropy caused by the GIT-12 hardware*, Nukleonika **60**, 2, 323–326 2015.

18. D. Klir, J. Krasa, J. Cikhardt, R. Dudzak, E. Krousky, M. Pfeifer, K. Rezac, O. Sila, J. Skala, J. Ullschmied, A. Velyhan, *Efficient neutron production from sub-nanosecond laser pulse accelerating deuterons on target front side*, Physics of Plasmas **22**, 9, 2015.

19. A. Kasperczuk, T. Pisarczyk, T. Chodukowski, Z. Kalinowska, W. Stepniewski, K. Jach, R. Swierczynski, O. Renner, M. Smid, J. Ullschmied, J. Cikhardt, D. Klir, P. Kubes, K. Rezac, E. Krousky, M. Pfeifer, J. Skala: *Efficiency of ablative plasma energy transfer into a massive aluminum target using different atomic number ablators*, Laser and Particle Beams, 2015.

20. D. Klir, A. V. Shishlov, V. A. Kokshenev, P. Kubes, A. Yu. Labetsky, K. Rezac, R. K. Cherdizov, J. Cikhardt, B. Cikhardtova, G. N. Dudkin, F. I. Fursov, A. A. Garapatsky, V. M. Kovalchuk, J. Kravarik, N. E. Kurmaev, H, Orcikova, V. N. Padalko, N. A. Ratakhin,O. Sila, K. Turek, V. A. Varlachev: *Efficient generation of fast neutrons by magnetized deuterons in an optimized deuterium gas-puff z-pinch*,Plasma Physics and Controlled Fusion **57**, 4, ISSN: 0741-3335, 2015.

21. J. Krása, D. Klir, A. Velyhan, E. Krouský, M. Pfeifer, K. Řezáč, J. Cikhardt, K. Turek, J. Ullschmied, K. Jungwirth: *Generation of high-energy neutrons with the 300-ps-laser system PALS*, High Power Laser Science and Engineering, **2**, (2014).

22. P. Kubes, M. Paduch, J. Cikhardt, J. Kortanek, etc.: *Filamentary structure of plasma produced by compression of puffing deuterium by deuterium or neon plasma sheath on plasma-focus discharge*, Physics of Plasmas **21**, 12, ISSN: 1070-664X, 2014.

23. D. Klir, P. Kubes, K. Rezac, J. Cikhardt, etc.: *Efficient Neutron Production*

from a Novel Configuration of Deuterium Gas-Puff Z-Pinch, Physical Review Letters **112**, 9, ISSN: 0031-9007, 2014.

24. M. De Marco, M. Pfeifer, E. Krousky, J. Krasa, J. Cikhardt, D. Klir, V. Nassisi: *Basic features of electromagnetic pulse generated in a laser-target chamber at 3-TW laser facility PALS*, PPLA2013, Journal of Physics Conference Series**508**, 012007, ISSN: 1742-6588, 2014.

25. P. Kubes, M. Paduch, D. Klir, J. Kravarik, K. Rezac, J. Cikhardt, etc.: *Correlation of x-ray emission with interferometry and neutron diagnostics at tungsten anode face and deuterium filling in plasma-focus discharge*, Plasma Phys. Control. Fusion **55**, 11, 2013.

26. M. Paduch, E. Zielinska, P. Kubes, D. Klir, J. Kravarik, K. Rezac, J. Cikhardt, J. Kortanek, M. Scholz, L. Karpinski: *Influence of the external magnetic field on pinch evolution and neutron production in plasma-focus discharge*, Plasma Phys. Control. Fusion **55**, 11, 2013.

27. D. Klir, A. V. Shishlov, V. A. Kokshenev, P. Kubes, A. Y. Labetsky, K. Rezac, J. Cikhardt, etc.: *Characterization of neutron emission from mega-ampere deuterium gas puff Z-pinch at microsecond implosion times*, Plasma Phys. Control. Fusion **55**, 8, 2013.

28. A. Kasperczuk, T. Pisarczyk, T. Chodukowski, Y. Kalinowska, S. Gus'kov, N. Demchenko, J. Ullschmied, E. Krousky, M. Pfeifer, J. Skala, D. Klir, J. Kravarik, P. Kubes, J. Cikhardt, K. Rezac, P. Pisarczyk: *Plastic plasma interaction with plasmas with growing atomic number*, Cent. Eur. J. Phys. **11**, 5, 2013.

29. D. Klír, J. Kravárik, P. Kubeš, K. Řezáč, J. Cikhardt, etc.: *Efficient production of 100 keV deuterons in deuterium gas puff Z-pinches at 2MA current.* In: Plasma Physics and Controlled Fusion. **52**, 6, 2010.

Appendix C

List of Conference Contributions

The chronological list of poster presentations on the international conferences during the Ph.D. study period is as follows.

1. J. Cikhardt, D. Klir, K. Rezac, B. Cikhardtova, J. Kravarik, P. Kubes, O. SILA, A.V. Shishlov, R.K. Cherdizov, F.I. Fursov, V.A. Kokshenev, N.E. Kurmaev. A.Yu. Labetsky, N.A. Ratakhin, G.N. Dudkin, A.A. Garapatsky, V.N. Padalko, V.A. Varlachev, K. Turek, *Neutron Activation Diagnostics in Deuterium Gas-Puff Experiments on the 3 MA GIT-12 Z-Pinch*, 58th Annual Meeting of the APS Division of Plasma Physics, Volume 61, Number 18 Monday–Friday, October 31 – November 4 2016, San Jose, California.

2. J. Cikhardt, D. Klir, K. Rezac, B. Cikhardtova, J. Kravarik, P. Kubes, O. Sila, A.V. Shishlov, R.K. Cherdizov, F.I. Frusov, V.A. Kokshenev, N.E. Kurmaev, Yu.A. Labetsky, N.A. Ratakhin, G.N. Dudkin, A.A. Garapatsky, V.N. Padalko, V.A. Varlachev, K. Turek, K. Krasa, *Neutron production in deuterium gas-puff z-pinch with outer plasma shell at current of 3 MA*, 57th Annual Meeting of the APS Division of Plasma Physics, Volume 60, Number 19 Monday–Friday, November 16-20, 2015, Savannah, Georgia.

3. J. Cikhardt, D. Klir, K. Rezac, P. Kubes, J. Kravarik, B. Batobolotova, O. Sila, K. Turek, A.V. Shishlov, A.Yu. Labetsky, V.A. Kokshenev, R.K. Cherdizov , V.N. Padalko, N. Ratakhin, *Diagnostics of deuterium gas-puff z-pinch experiments on the GIT-12 generator*, 56th Annual Meeting of the APS Division of Plasma Physics, Volume 59, Number 15, Monday–Friday, October 27-31, 2014, New Orleans, Louisiana.

4. J. Cikhardt J. Krása, M. De Marco, M. Pfeifer, E. Krouský, A. Velyhan, B. Batobolotova, D. Klír, K. Řeazáč, P. Kubeš, J. Kravárik, J. Ullschmied, *Measurement of target currents generated during the interaction of terawatt laser with solid targets*, 26th Symposium on Plasma Physics and Technology, 16-19 June 2014 in Prague, Czech Republic.

5. J. Cikhardt, B. Batobolotova, J. Kravárik, P. Kubeš, D. Klír, K. Řezáč, O. Šíla, *Influence of an external magnetic field on dynamics of a modified plasma focus*, Plasma-2013: International Conference on Research and Applications of Plasmas, 2–6 September 2013, Warsaw, Poland.

6. J. Cikhardt, P. Kubeš, J. Kravárik, D. Klír, K. Řezáč, A.V. Shishlov, A.Yu. Labetsky, S.A. Chaikovsky,

7. The construction of the fast resistive bolometer for a SXR measurement on the GIT-12 Z-pinch, 25th Symposium on Plasma Physics and Technology, 18-21 June 2012 in Prague, Czech Republic.

The chronological list of oral presentations on the international conferences is as follows.

1. J. Cikhardt, D. Klír, K. Řezáč, B. Cikhardtová, P. Kubeš, J. Kravárik, O. Šíla, K. Turek, J. Krása, A.V. Shishlov, R.K. Cherdizov, F.I. Frusov, V.A. Kokshenev, N.E. Kurmaev, Yu.A. Labetsky, N.A. Ratakhin, G.N. Dudkin, A.A. Garapatsky, V.N. Padalko, V.A. Varlachev, *Neutron Production in 3 MA Deuterium Gas-puff Zpinch Experiments at GIT-12 Device*, International Centre for Dense Magnetised Plasma - Workshop and Expert Meeting On Dense Magnetised Plasmas, 14-15 October 2016 in Warsaw, Poland.

2. J. Cikhardt, D. Klir, K. Rezac, A.V. Shishlov, R.K. Cherdizov, B. Cikhardtova, G.N. Dudkin, A.A. Garapatsky, V.A. Kokshenev, J. Kravarik, P. Kubes, A.Yu. Labetsky, V.N. Padalko, N.A. Ratakhin, O. Sila, K. Turek, V.A. Varlachev, *Neutron Production from Deuterium Gas-puff Z-pinch on GIT-12 Generator at Current of 3 MA*, 27th Symposium on Plasma Physics and Technology, 20-23 June 2016 in Prague, Czech Republic.

3. J. Cikhardt, D. Klír, K. Řezáč, B. Cikhardtová, P. Kubeš, J. Kravárik, O. Šíla, K. Turek, J. Krása, A.V. Shishlov, R.K. Cherdizov, F.I. Fursov, V.A. Kokshenev, N.E. Kurmaev, Yu.A. Labetsky, N.A. Ratakhin, G.N. Dudkin, A.A. Garapatsky, V.N. Padalko, V.A. Varlachev, *Joint Czech-Russian Z-Pinch Experiments On GIT-12 Device*, International Centre for Dense Magnetised Plasma - Workshop and Expert Meeting On Dense Magnetised Plasmas, 11-12 September 2015 in Warsaw, Poland.

4. J. Cikhardt, D. Klir, K. Rezac, B. Cikhardtova, O. Sila, P. Kubes, J. Kravarik, K. Turek, A.V. Shishlov, A.Yu. Labetsky, V.A. Kokshenev, R.K. Cherdizov, V.N. Padalko, N. Ratakhin, *Nuclear Activation Diagnostics of deuterium gas-puff z-pinch experiments on the GIT-12 generator*, Plasma-2015: International Conference on Research and Applications of Plasmas, 7-11 September 2015, Warsaw, Poland.

The chronological list of oral presentations on the international summer schools is as follows. We noted, that the contribution no. 1 was awarded.

1. J. Cikhardt, J. Krása, M. De Marco, M. Pfeifer, A. Velyhan, E. Krouský, B. Batobolotova, P. Kubeš, D. Klír, K. Řezáč, J. Ullschmied, J. Skála, *Measurement of the Target Current and EMP on Terawatt Laser System PALS*, 12th Kudowa Summer School "Towards Fusion Energy", 9-13th June 2014 in Kudowa Zdrój, Poland.

2. J. Cikhardt, P. Kubeš, D. Klír, J. Kravárik, K. Řezáč, A.V. Shishlov, A.Yu. Labetsky, S.A. Chaikovsky, *The SXR Bolometer Design for Measurement on the Power Z-Pinches*, 11th Kudowa Summer School "Towards Fusion Energy", 11-15th June 2012 in Kudowa Zdrój, Poland.

Appendix D

List of Internships

The list of active experimental internships during the Ph.D. study period is as follows.

1. Institute of High Current Electronics, Siberian Branch, Russian Academy of Sciences, 2/3 Akademichesky Avenue Tomsk 634055, Russia, 1-30 April 2017 (29 days).

2. Institute of Plasma Physics and Laser Microfusion, Hery Street 23, 01-497 Warsaw, Poland, 12-24 February 2017 (12 days).

3. Institute of Plasma Physics and Laser Microfusion, Hery Street 23, 01-497 Warsaw, Poland, 2-15 October 2016 (13 days).

4. Institute of High Current Electronics, Siberian Branch, Russian Academy of Sciences, 2/3 Akademichesky Avenue Tomsk 634055, Russia, 2 April - 7 May 2016 (35 days).

5. Institute of Plasma Physics and Laser Microfusion, Hery Street 23, 01-497 Warsaw, Poland, 8-19 February 2016 (11 days).

6. Institute of Plasma Physics and Laser Microfusion, Hery Street 23, 01-497 Warsaw, Poland, 13-26 October 2015 (13 days).

7. Institute of High Current Electronics, Siberian Branch, Russian Academy of Sciences, 2/3 Akademichesky Avenue Tomsk 634055, Russia, 28 March - 12 May 2015 (45 days).

8. Institute of Plasma Physics and Laser Microfusion, Hery Street 23, 01-497 Warsaw, Poland, 1-14 February 2015 (13 days).

9. Institute of Plasma Physics and Laser Microfusion, Hery Street 23, 01-497 Warsaw, Poland, 13-18 October 2014 (5 days).

10. Institute of Plasma Physics and Laser Microfusion, Hery Street 23, 01-497 Warsaw, Poland, 1-13 September 2014 (12 days).

11. GSI Helmholtzzentrum für Schwerionenforschung GmbH, Planckstraße 1, 64291 Darmstadt, 5-18 May 2014 (13 days).

12. Institute of High Current Electronics, Siberian Branch, Russian Academy of Sciences, 2/3 Akademichesky Avenue Tomsk 634055, Russia, 16 March - 26 April 2014 (41 days).

13. Institute of Plasma Physics and Laser Microfusion, Hery Street 23, 01-497 Warsaw, Poland, 2-15 February 2014 (13 days).

14. Institute of Plasma Physics and Laser Microfusion, Hery Street 23, 01-497 Warsaw, Poland, 8-21 September 2013 (13 days).

15. Institute of High Current Electronics, Siberian Branch, Russian Academy of Sciences, 2/3 Akademichesky Avenue Tomsk 634055, Russia, 20 May - 1 July 2013 (42 days).

16. Institute of Plasma Physics and Laser Microfusion, Hery Street 23, 01-497 Warsaw, Poland, 14-27 April 2013 (13 days).

17. Institute of Plasma Physics and Laser Microfusion, Hery Street 23, 01-497 Warsaw, Poland, 14-27 October 2012 (13 days).

Bibliography

[1] R. P. Drake. *High-Energy-Density Physics*. Springer, 2006.

[2] D. Klir, P. Kubes, K. Rezac, J. Cikhardt, J. Kravarik, O. Sila, A. V. Shishlov, B. M. Kovalchuk, N. A. Ratakhin, V. A. Kokshenev, A. Yu. Labetsky, R. K. Cherdizov, F. I. Fursov, N. E. Kurmaev, G. N. Dudkin, B. A. Nechaev, V. N. Padalko, H. Orcikova, and K. Turek. Efficient neutron production from a novel configuration of deuterium gas-puff z-pinch. *Phys. Rev. Lett.*, 112:095001, Mar 2014.

[3] J. Krása, D. Klír, A. Velyhan, E. Krouský, M. Pfeifer, K. Řezáč, J. Cikhardt, K. Turek, J. Ullschmied, and K. Jungwirth. Generation of high-energy neutrons with the 300-ps-laser system pals. *High Power Laser Science and Engineering*, 2, 2014.

[4] D. Klir, A. V. Shishlov, V. A. Kokshenev, P. Kubes, A. Yu Labetsky, K. Rezac, R. K. Cherdizov, J. Cikhardt, B. Cikhardtova, G. N. Dudkin, F. I. Fursov, A. A. Garapatsky, B. M. Kovalchuk, J. Kravarik, N. E. Kurmaev, H. Orcikova, V. N. Padalko, N. A. Ratakhin, O. Sila, K. Turek, and V. A. Varlachev. Efficient generation of fast neutrons by magnetized deuterons in an optimized deuterium gas-puff z-pinch. *Plasma Physics and Controlled Fusion*, 57(4), APR 2015.

[5] W. M. Parsons, W. A. Reass, J. R. Griego, D. W. Bowman, C. Thompson, R. F. Gribble, J. S. Shlachter, C. A. Ekdahl, P. D. Goldstone, and S. M. Younger. Atlas-a facility for high energy density physics research at los alamos national laboratory. In *Digest of Technical Papers. Tenth IEEE International Pulsed Power Conference*, volume 1, pages 593–600 vol.1, July 1995.

[6] M. A. Liberman, J.S. De Groot, A. Toor, and R.B. Spielman. *Physics of High-Density Z-Pinch Plasmas*. Springer New York, 1998.

[7] D. Klir. The study of a fibre z-pinch, ph.d. thesis, 2005. `http://arxiv.org/abs/physics/0703207`.

[8] M. G. Haines, S. V. Lebedev, J. P. Chittenden, F. N. Beg, S. N. Bland, and A. E. Dangor. The past, present, and future of z pinches. *Phyiscs of Plasmas*, 7, May 2000.

[9] L. Soto, H. Chuaqui, M. Favre, and E. Wyndham. Novel gas embedded compressional z-pinch configuration. *Phyiscal Review Letters*, 72, May 1994.

[10] Dangor A. E. High density z-pinches. *Plasma Phys. Control. Fusion*, 28, Dec 1986.

[11] F. N. Beg, R. B. Stephens, H.-W. Xu, D. Hass, S. Eddinger, G. Tynan, E. Shipton, B. DeBono, and K. Wagshal. Compact x-pinch based point x-ray source for phase contrast imaging of inertial confinement fusion capsules. *Applied Physics Letters*, 89, Jul 2006.

[12] T. A. Shelkovenko, D. B. Sinars, S. A. Pikuz, K. M. Chandler, and D. A. Hammer. Point-projection x-ray radiography using an x pinch as the radiation source. *Review of Scientific Instruments*, 72, Jan 2001.

[13] A. Shishlov, S. Chaikovsky, A. Fedunin, F. Fursov, V. Kokshenev, N. Kurmaev, A. Labetsky, V. Oreshkin, A. Rousskikh, and N. Zhidkova. Microsecond planar wire array implosions on the GIT-12 generator. In *2007 IEEE PULSED POWER CONFERENCE, VOLS 1-4*, pages 649–653. IEEE, 2007. 16th IEEE International Pulsed Power Conference, Albuquerque, NM, JUN 17-22, 2007.

[14] N.V. Filippov, T.I. Filippova, and V.P. Vinogradov. Dense high-temperature plasma in a non-cylindrical z-pinch compression. *Nucl. Fusion, Suppl.*, Jan 1962.

[15] J. W. Mather. Formation of a high-density deuterium plasma focus. *The Physics of Fluids*, 8(2):366–377, 1965.

[16] H. Herold, A. Jerzykiewicz, M. Sadowski, and H. Schmidt. Comparative analysis of large plasma focus experiments performed at ipf, stuttgart, and ipj, swierk. *Nuclear Fusion*, 29(8):1255, 1989.

[17] V Krauz, K Mitrofanov, M Scholz, M Paduch, L Karpinski, E Zielinska, and P Kubes. Experimental study of the structure of the plasma-current sheath on the pf-1000 facility. *Plasma Physics and Controlled Fusion*, 54(2):025010, 2012.

[18] S. Lee and S. H. Saw. Pinch current limitation effect in plasma focus. *Applied Physics Letters*, 92(2), JAN 14 2008.

[19] D. Klir, V. A. Kokshenev, P. Kubes, A. Yu Labetsky, M. Paduch, K. Rezac, and A. V. Shishlov. Search for Drive Parameter of Neutron-Optimized Z-Pinches and Dense Plasma Foci. *IEEE Transactions on Plasma Science*, 41(11):3129–3134, NOV 2013.

[20] M. G. Haines. A review of the dense z-pinch. *Plasma Physics and Controlled Fusion*, 53, Mar 2011.

[21] J. A. Pollock and S. Barraclough. Note on a hollow lightning conductor crushed by the discharge. *Journal and proceedings of the Royal Society of New South Wales*, 39:131, 1905.

[22] E. F. Northrupp. Some newly observed manifestations of forces in the interior of an electric conductor. *Physical Review*, 24:474, 1907.

[23] W. H. Bennet. Magnetically self-focussing streams. *Physical Review*, 45:474, Jun 1934.

[24] D. D. Ryutov, M. S. Derzon, and M. K. Matzen. The physics of fast z pinches. *Rev. Mod. Phys.*, 72:167–223, Jan 2000.

[25] M. G. Haines. Fifty years of controlled fusion research. *Plasma Physics and Contorlled Fusion*, 34:643–656, 1996.

[26] United Nations. *Proceedings of the Second United Nations International Conference on the Peaceful Uses of Atomic Energy*, volume 31, Geneva, Switzerland, 1 September - 13 September 1958 1958.

[27] C. Stallings, K. Nielsen, and R. Schneider. Multiplewire array load for high-power pulsed generators. *Applied Physics Letters*, 29(7):404–406, Oct 1976.

[28] P. J. Turchi and W. L. Baker. Generation of highenergy plasmas by electromagnetic implosion. *Journal of Applied Physics*, 44(11):4936–4945, Nov 1973.

[29] J Shiloh, A Fisher, and N Rostoker. Z-Pinch of a Gas-Jet. *Physical Review Letters*, 40(8):515–518, 1978.

[30] A. Fisher, F. Maco, and J. Shiloh. Fast valve for gas injection into vacuum. *Review of Scientific Instrument*, 49(6):872–873, Jun 1978.

[31] C. Stallings, K. Childers, I. Roth, and A. Schneider. Imploding argon plasma experiments. *Applied Physics Letters*, 35(7):524–526, Oct 1979.

[32] R. B. Spielman, D. L. Hanson, M. A. Palmer, M. K. Matzen, T. W. Hussey, and J. M. Peek. Efficient x-ray production from ultrafast gass-puff z-pinches. *Journal of Applied Physics*, 57(3):830–833, Feb 1985.

[33] A. Krejčí. Gas-puff z-pinch experiment. *Czechoslovak Journal of Physics*, 40:182–187, 1988.

[34] C. Deeney, M. R. Douglas, R. B. Spielman, T. J. Nash, D. L. Peterson, P. L'Eplattenier, G. A. Chandler, J. F. Seamen, and K. W. Struve. Enhancement of X-ray Power from a Z Pinch Using Nested-Wire Arrays. *Phycal Review Letters*, 81(22):4883–4886, NOV 1998.

[35] J. Bailey, Y. Ettinger, A. Fisher, and N. Rostoker. Gas-puff z pinches with o_2 and 0_2-ar mixtures. 40(6):460–462, Mar 1982.

[36] Z. A. Albikov, E. P. Velikhov, A. I. Veretennikov, V. A. Glukhin, E. V. Grabovski, G. M. Gryaznov, O. A. Gusev, G. N. Zhemchuznikov, V. I. Zaitsev, O. A. Zolotoskii, Yu. A. Istomin, O. V. Kozlov, I. S. Krashneninnikov, S. S. Kurochkin, G. M. Latmanizova, V. V. Matveev, G. V. Mineev, V. N. Mikhailov, S. L. Nedoseev, G. M. Oleinik, V. P. Pevchev, A. S. Perlin, O. P. Pecherskii, V. D. Piśmennyi, L. I. Rudakov, V. P. Smirnov, V. Ya. Tsarfin, I. R. Yampolskii. Angara-5-1 experimental complex. *Atomic Energy*, 68(1):26–35, January 1990.

[37] A. V. Batyunin, A. N. Bulatov, V. D. Vikharev, G. S. Volkov, V. I Zaytsev, S. V. Zakharov, S. A. Komarov, Nedoseev S. L., L. B. Nikandrov, G. M. Oleynik, V. P. Smirnov, S. V. Trofimov, E. G. Utyugov, M. V. Fedulov, I. N. Frolov, and V. Ya. Carfin. Issledovanie sverkhbystrogo deiterievogo z-pincha na ustanovke "angara-5-1". *Fizika Plazmy*, 16(9):1027–1035, 1990.

[38] R. B. Spielrnan, G. T. Baldwin, G. Cooper, D. Hebron, R. J. Leeper, S. F. Lopez, J. S. McGurn, D. J. Muron, C. L. Ruiz, A. Schmidlapp, and M. Vargas. D-d fusion experiments using fast z pinches. *Sandia Report*, (SAND98-0705), Mar 1998.

[39] C. A. Coverdale, C. Deeney, A. L. Velikovich, R. W. Clark, Y. K. Chong, J. Davis, J. Chittenden, C. L. Ruiz, G. W. Cooper, A. J. Nelson, J. Franklin, P. D. LePell, J. P. Apruzese, J. Levine, J. Banister, and N. Qi. Neutron production and implosion characteristics of a deuterium gas-puff Z pinch. *Phzsics Of Plasmas*, 14(2), FEB 2007.

[40] D. Klir, J. Kravarik, P. Kubes, K. Rezac, J. Cikhardt, E. Litseva, T. Hyhlik, S. S. Ananev, Yu L. Bakshaev, V. A. Bryzgunov, A. S. Chernenko, Yu G. Kalinin, E. D. Kazakov, V. D. Korolev, G. I. Ustroev, A. A. Zelenin, L. Juha, J. Krasa, A. Velyhan, L. Vysin, J. Sonsky, and I. V. Volobuev. Efficient Production of 100 keV Deuterons in Deuterium Gas Puff Z-pinches at 2 MA Current. *Plasma Physics and Controlled Fusion*, 52(6), JUN 2010.

[41] V. V. Ivanov, E. S. McKee, B. D. Hammel, T. W. Darling, K. J. Swanson, and A. M. Covington. Note: Infrared laser diagnostics for deuterium gas puff z pinches. *Review of Scientific Instruments*, 88(7):076111, 2017.

[42] P. Kubes, M. Paduch, J. Cikhardt, J. Kortanek, B. Batobolotova, K. Rezac, D. Klir, J. Kravarik, W. Surala, E. Zielinska, M. Scholz, L. Karpinski, and M. J. Sadowski. Neutron production from puffing deuterium in plasma focus device. *Physics of Plasmas*, 21(8):082706, 2014.

[43] D. R. Zaloga, E. Skladnik-Sadowska, M. Kubkowska, M. S. Ladygina, K. Malinowski, R. Kwiatkowski, M. J. Sadowski, M. Paduch, E. Zielinska, and V. A. Makhlaj. Comparison of optical spectra recorded during DPF-1000U plasma experiments with gas-puffing. *Nukleonika*, 60(2):309–314, JUN 2015.

[44] D. Klir, A. V. Shishlov, P. Kubes, K. Rezac, F. I. Fursov, V. A. Kokshenev, B. M. Kovalchuk, J. Kravarik, N. E. Kurmaev, A. Yu Labetsky, and N. A. Ratakhin. Deuterium Gas Puff Z-pinch at Currents of 2 to 3 Mega-Ampere. *Phyisics of Plasmas*, 19(3), MAR 2012.

[45] D. Klir, A. V. Shishlov, V. A. Kokshenev, P. Kubes, A. Yu Labetsky, K. Rezac, J. Cikhardt, F. I. Fursov, B. M. Kovalchuk, J. Kravarik, N. E. Kurmaev, N. A. Ratakhin, O. Sila, and J. Stodulka. Characterization of neutron emission from mega-ampere deuterium gas puff Z-pinch at microsecond implosion times. *Plasma Physic And Controlled Fusion*, 55(8), AUG 2013.

[46] S. A. Sorokin. Gas-puff liner implosion in the configuration with helical current return rods. *Plasma Physics Reports*, 39(2):139–143, Feb 2013.

[47] A. Yu. Labetsky, V. A. Kokshenev, N. E. Kurmaev, V. A. Oreshkin, A. G. Rousskikh, A. V. Fedyunin, F. I. Fursov, S. A. Chaikovsky, A. V. Shishlov, and N. A. Zhidkova. Study of the current-sheath formation during the implosion of multishell gas puffs. *PLASMA PHYSICS REPORTS*, 34(3):228–238, MAR 2008. 12th All-Russian Conference on Plasma Diagnostics, Troitsk, Russia, JUN 03-09, 2007.

[48] MK Matzen. Z Pinches as Intense X-Ray Sources for High-Energy Density Physics Applications. *Physics of Plasmas*, 4(5, 2):1519–1527, MAY 1997. 38th Annual Meeting of the Division-of-Plasma-Physics of the American-Physical-Society, DENVER, CO, NOV 11-15, 1996.

[49] S. A. Slutz, M. C. Herrmann, R. A. Vesey, A. B. Sefkow, D. B. Sinars, D. C. Rovang, K. J. Peterson, and M. E. Cuneo. Pulsed-power-driven cylindrical liner implosions of laser preheated fuel magnetized with an axial field. *Physics of Plasmas*, 17(5), MAY 2010. 51st Annual Meeting of the Division-of-Plasma-Physics of the American-Physics-Society, Atlanta, GA, NOV 02-06, 2009.

[50] M. E. Cuneo, M. C. Herrmann, D. B. Sinars, S. A. Slutz, W. A. Stygar, R. A. Vesey, A. B. Sefkow, G. A. Rochau, G. A. Chandler, J. E. Bailey, J. L. Porter, R. D. McBride, D. C. Rovang, D. C. Rovang, M. G. Mazarakis, E. P. Yu, D. C. Lamppa, K. J. Peterson, C. Nakhleh, S. B. Hansen, A. J. Lopez, M. E. Savage, C. A. Jennings, M. R. Martin, R. W. Lemke, B. W. Atherton,

I. C. Smith, P. K. Rambo, M. Jones, M. R. Lopez, P. J. Christenson, M. A. Sweeney, B. Jones, L. A. McPherson, E. Harding, M. R. Gomez, P. F. Knapp, T. J. Awe, R. J. Leeper, C. L. Ruiz, G. W. Cooper, K. D. Hahn, J. McKenney, A. C. Owen, G. R. McKee, G. T. Leifeste, D. J. Ampleford, E. M. Waisman, A. Harvey-Thompson, R. J. Kaye, M. H. Hess, S. E. Rosenthal, and M. K. Matzen. Magnetically Driven Implosions for Inertial Confinement Fusion at Sandia National Laboratories. *IEEE Transactions on Plasma Science*, 40(12, 2, SI):3222–3245, DEC 2012.

[51] M. R. Gomez, S. A. Slutz, A. B. Sefkow, D. B. Sinars, K. D. Hahn, S. B. Hansen, E. C. Harding, P. F. Knapp, P. F. Schmit, C. A. Jennings, T. J. Awe, M. Geissel, D. C. Rovang, G. A. Chandler, G. W. Cooper, M. E. Cuneo, A. J. Harvey-Thompson, M. C. Herrmann, M. H. Hess, O. Johns, D. C. Lamppa, M. R. Martin, R. D. McBride, K. J. Peterson, J. L. Porter, G. K. Robertson, G. A. Rochau, C. L. Ruiz, M. E. Savage, I. C. Smith, W. A. Stygar, and R. A. Vesey. Experimental Demonstration of Fusion-Relevant Conditions in Magnetized Liner Inertial Fusion. *Physical Review Letters*, 113(15), OCT 6 2014.

[52] S. A. Slutz, W. A. Stygar, M. R. Gomez, K. J. Peterson, A. B. Sefkow, D. B. Sinars, R. A. Vesey, E. M. Campbell, and R. Betti. Scaling magnetized liner inertial fusion on Z and future pulsed-power accelerators. *Physics of Plasmas*, 23(2), FEB 2016.

[53] S. A. Slutz, C. A. Jennings, T. J. Awe, G. A. Shipley, B. T. Hutsel, and D. C. Lamppa. Auto-magnetizing liners for magnetized inertial fusion. *Physics of Plasmas*, 24(1):012704, JAN 2017.

[54] W. A. Stygar, T. J. Awe, J. E. Bailey, N. L. Bennett, E. W. Breden, E. M. Campbell, R. E. Clark, R. A. Cooper, M. E. Cuneo, J. B. Ennis, D. L. Fehl, T. C. Genoni, M. R. Gomez, G. W. Greiser, F. R. Gruner, M. C. Herrmann, B. T. Hutsel, C. A. Jennings, D. O. Jobe, B. M. Jones, M. C. Jones, P. A. Jones, P. F. Knapp, J. S. Lash, K. R. LeChien, J. J. Leckbee, R. J. Leeper, S. A. Lewis, F. W. Long, D. J. Lucero, E. A. Madrid, M. R. Martin, M. K. Matzen, M. G. Mazarakis, R. D. McBride, G. R. McKee, C. L. Miller, J. K. Moore, C. B. Mostrom, T. D. Mulville, K. J. Peterson, J. L. Porter, D. B.

Reisman, G. A. Rochau, G. E. Rochau, D. V. Rose, D. C. Rovang, M. E. Savage, M. E. Sceiford, P. F. Schmit, R. F. Schneider, J. Schwarz, A. B. Sefkow, D. B. Sinars, S. A. Slutz, R. B. Spielman, B. S. Stoltzfus, C. Thoma, R. A. Vesey, P. E. Wakeland, D. R. Welch, M. L. Wisher, and J. R. Woodworth. Conceptual designs of two petawatt-class pulsed-power accelerators for high-energy-density-physics experiments. *Physical Review Special Topics-Accelerators and Beams*, 18(11), NOV 30 2015.

[55] R. B. Spielman, C. Deeney, G. A. Chandler, M. R. Douglas, D. L. Fehl, M. K. Matzen, D. H. McDaniel, T. J. Nash, J. L. Porter, T. W. L. Sanford, J. F. Seamen, W. A. Stygar, K. W. Struve, S. P. Breeze, J. S. McGurn, J. A. Torres, D. M. Zagar, T. L. Gilliland, D. O. Jobe, J. L. McKenney, R. C. Mock, M. Vargas, T. Wagoner, and D. L. Peterson. Tungsten wire-array z-pinch experiments at 200 tw and 2 mj. *Physics of Plasmas*, 5(5):2105–2111, 1998.

[56] V. V. Aleksandrov, E. A. Bolkhovitinov, G. S. Volkov, E. V. Grabovski, A. N. Gritsuk, S. F. Medovshchikov, G. M. Oleinik, A. A. Rupasov, and I. N. Frolov. Implosion Dynamics of a Megampere Wire-Array Z-Pinch with an Inner Low-Density Foam Shell at the Angara-5-1 Facility. *Plasma Physics Reports*, 42(12):1091–1100, DEC 2016.

[57] V. V. Aleksandrov, G. S. Volkov, E. V. Grabovski, A. N. Gritsuk, Ya. N. Laukhin, K. N. Mitrofanov, G. M. Oleinik, I. N. Frolov, A. P. Shevel'ko, and V. A. Barsuk. Study of the Formation, Stability, and X-ray Emission of the Z-Pinch Formed during Implosion of Fiber Arrays at the Angara-5-1 Facility. *Plasma Physics Reports*, 42(11):1024–1036, NOV 2016.

[58] V. V. Alexandrov, G. S. Volkov, E. V. Grabovsky, A. N. Gritsuk, K. N. Mitrofanov, G. M. Oleinik, and A. P. Shevelko. Experimental Study of Emission Z-pinch Spectra in the Axial and Radial Directions at the Angara-5-1 Facility. 132, 2017. 25th Congress on Spectroscopy, Troitsk, RUSSIA, OCT 03-07, 2016.

[59] F. Lassalle, A. Loyen, A. Georges, B. Roques, H. Calamy, Ch. Mangeant, J.-F. Carnbonie, S. Laspalles, D. Cadars, G. Rodriguez, J.-M. Delchie, Ph. Combes,

R. Lample, Th. Chanconie, and J. Saves. Status on the Sphinx machine based on the 1-mu s LTD technology. *IEEE Transactions on Plasma Science*, 36(2, 1):370–377, APR 2008.

[60] T. d'Almeida, F. Lassalle, A. Morell, J. Grunenwald, F. Zucchini, A. Loyen, T. Maysonnave, and A. Chuvatin. Ramp Compression of a Mmetallic Liner Driven by a Shaped 5 MA Current on the SPHINX Machine. 500, 2014. 18th Joint Int Conf of the APS Topical-Grp on Shock Compress of Condensed Matter / 24th Int Conf of the Int-Assoc-for-the-Advancement-of-High-Pressure-Sci-and-Technol, Seattle, WA, JUL 07-12, 2013.

[61] Z. Huang, J. Yang, R. Xu, Z. Li, S. Jiang, F. Ye, Q. Hu, J. Ning, and Z. Xu. Axially Resolved Radiation of Tungsten Wire-array Z-pinches on JULONG-I. *High Eneregy Density Physics*, 21:1–7, DEC 2016.

[62] A. S. Safronova, V. L. Kantsyrev, M. E. Weller, V. V. Shlyaptseva, I. K. Shrestha, A. Stafford, M. T. Schmidt-Petersen, M. Y. Lorance, K. A. Schultz, and A. S. Chuvatin. Larger Sized Planar Wire Arrays of Complex Configuration on 1.5-1.8 MA Z-pinch Generator. *Physics of Plasmas*, 23(10), OCT 2016. 3rd International Workshop on Radiation from High Energy Density Plasmas (RHEDP), Stateline, NV, JUN 09-12, 2015.

[63] John L. Giuliani and Robert J. Commisso. A Review of the Gas-Puff Z-Pinch as an X-Ray and Neutron Source. *IEEE Transactions on Plasma Science*, 43(8, SI):2385–2453, AUG 2015.

[64] J. P. Apruzese, J. L. Giuliani, N. D. Ouart, V. Tangri, A. J. Harvey-Thompson, B. Jones, C. A. Jennings, S. B. Hansen, D. J. Ampleford, G. A. Rochau, and C. A. Coverdale. Effects of a Xe dopant on an Ar gas-puff implosion on Z. *Physics of Plasmas*, 23(12), DEC 2016.

[65] F. Zucchinia, H. Calamy, F. Lassalle, A. Loyen, P. Maury, J. Grunenwald, A. Georges, A. Morell, J. P. Bedoch, S. Ritter, P. Combes, O. Smaniotto, R. Lample, P. L. Coleman, and M. Krishnan. First Argon Gas Puff Experiments With 500 ns Implosion Time On Sphinx Driver. In Hammer, DA and Kusse, BR, editor, *DENSE Z-PINCHES*, volume 1088 of *AIP Conference Proceedings*, pages 247+. US DOE, Natl Nucl Secur Agcy; US DOE, Off Fus

Energy Sci; US Naval Res Lab; Sandia Natl Lab, 2009. 7th International Conference on Dense Z-Pinches, Alexandria, VA, AUG 12-21, 2008.

[66] J. L. Giuliani, J. W. Thornhill, E. Kroupp, D. Osin, Y. Maron, A. Dasgupta, J. P. Apruzese, A. L. Velikovich, Y. K. Chong, A. Starobinets, V. Fisher, Yu. Zarnitsky, V. Bernshtam, A. Fisher, T. A. Mehlhorn, and C. Deeney. Effective versus ion thermal temperatures in the Weizmann Ne Z-pinch: Modeling and stagnation physics. *Physics of Plasmas*, 21(3), MAR 2014.

[67] M. Krishnan. The dense plasma focus: A versatile dense pinch for diverse applications. *IEEE Transactions on Plasma Science*, 40(12):3189–3221, Dec 2012.

[68] S.P. Bugaev, A.M. Volkov, A.A. Kim, V.N. Kiselev, B.M. Kovaľchuk, N.F. Kovsharov, V.A. Kokshenev, N.E. Kurmaev, S.V. Loginov, G.A. Mesyats, F.I. Fursov, and A.P. Khuzeev. GIT16: A megajoule pulse generator with plasma switch for a Z-pinch load. *Russian Physics Journal*, 40(12):1154–1161, 1997.

[69] M. Rosenbluth, R Garvin, and A. Rosenbluth. Infinite conductivity theory of the pinch. *Los Alamos Scientific Report*, (LA-1850), Mar 1955.

[70] D. Potter. The formation of high-density z-pinches. *Nuclear Fusion*, 18(6):813, 1978.

[71] Robert W. Conn. Nuclear fusion. `https://www.britannica.com/science/nuclear-fusion`, April 2016.

[72] G. McCracken and P. Stott. *Fusion – The Energy of the Universe*. Mladá fronta, 1st edition, 2006.

[73] M. Drosg. Drosg-2000: Neutron source reactions, data files with computer codes for 60 accelerator-based neutron source reactions.

[74] Zpracování fyzikálních měření. 2013.

[75] S. A. Pozzi, J. A. Mullens, and Mihalczo J. T. Analysis of neutron and photon detection position for the calibration of plastic (bc-420) and liquid

(bc-501) scintillators. *Nuclear Instruments and Methods in Physics Research A*, (524):92–101, 2004.

[76] S. R. Mirfayzi, S. Kar, H. Ahmed, A. G. Krygier, A. Green, A. Alejo, R. Clarke, J. Freeman, R. R. amd Fuchs, D. Jung, A. Kleinschmidt, J. T. Morrison, Z. Najmudin, H. Nakamura, P. Norreys, M. Oliver, M. Roth, L. Vassura, M. Zepf, and M. Borghesi. Calibration of time of flight detectors using laser-driven neutron source. *Rev. Sci. Instrum.*, 86(7), 2015.

[77] V. V. Vikhrev and V. D. Korolev. Neutron generation from z-pinches. *PLASMA PHYSICS REPORTS*, 33(5):356–380, 2007.

[78] V. V. Vikhrev and A. D. Mironenko-Marenkov. On the spectrum of z-pinch plasma neutrons. *PLASMA PHYSICS REPORTS*, 38(3):225–234, 2012.

[79] P. F. Knapp, D. B. Sinars, and K. D. Hahn. Diagnosing suprathermal ion populations in z-pinch plasmas using fusion neutron spectra. *Physics of Plasmas*, 20(062701), 2013.

[80] M. Řípa, J. Mlynář, V. Weinzettl, and F. Žáček. *Řízená termojaderná fúze pro každého.* 2011.

[81] V. A. Kokshenev, A. Yu. Labetsky, B. M. Kovalchuk, S. A. Chaikovsky, A. V. Fedunin, F. I. Fursov, N. E. Kurmaev, A. G. Rousskikh, A. V. Shishlov, and N. A. Zhidkova. Multi-shell plasma flow switch experiments on the git-12 generator. *14th Symposium on High Current Electronics*, pages 272–275, SEP 2006. Tomsk, Russia.

[82] J. Stodůlka. CFD simulace nestacionárního stlačitelného proudění tryskou pulsního generátoru pro fuzní experimenty. Master's thesis, Master Thesis, Faculty of Mechanics, Czech Technical University in Prague, 2012.

[83] S. Lee. Energy balance and the radius of electromagnetically pinched plasma columns. *Plasma Physics*, 25(4):571–576, 1832.

[84] S. Lee. Application of energy balance to compute plasma pinch ratios. *J. Appl. Phys.*, 54(6):3603–3605, JUN 1983.

[85] *Mathematical Methods for Physicists: A Comprehensive Guide*. Burlington: Elsevier Academic Press, 2005.

[86] M. Vlad. A time resolving spectrometry method for particles emitted in intense bursts. *Nuclear Instruments and Methods in Physics Research*, 227:327–334, 1985.

[87] I. Tiseanu, G. Deckerb, and Kies W. A monte-carlo technique for the reconstruction of time dependent spectra of short-pulse neutron sources. *Nuclear Instruments and Methods in Physics Research A*, 373:73–80, 1996.

[88] K. Rezac. *Reconstruction of Neutron Energy Spectra in Z-pinch Fusion Experiments*. PhD thesis, Czech Technical University in Prague, Faculty of Electrical Engineering, 2011.

[89] K. Rezac, D. Klir, P Kubes, and J. Kravarik. Improvement of time-of-flight methods for reconstruction of neutron energy spectra from d(d,n)3he fusion reactions. *Plasma Phys. Control. Fusion*, 54, 2012.

[90] H Ing, RA Noulty, and TD McLean. Bubble detectors - A maturing technology. *Radiation Measurements*, 27(1):1–11, FEB 1997.

[91] BTI Bubble Technology Industries. *Bubble Detector Neutron Dosimeters Manual*.

[92] G. F. Knoll. *Radiation detection and measurement*. Wiley, 4th edition, 2010.

[93] I. V. Saveliev. *Kurs Obshey Fiziki*, volume 3. AST/Astrel, 2001.

[94] National Institute of Standards and Technology. Classical electron radius. `https://physics.nist.gov/cgi-bin/cuu/Value?re`, 2017.

[95] Bc-400,bc-404,bc-408,bc-412,bc-416 premium plastics scintillators data sheet. `http://www.crystals.saint-gobain.com/sites/imdf.crystals.com/files/documents/sgc-bc400-404-408-412-416-data-sheet.pdf`, 2016.

[96] Photomultiplier tubes r1828-01, r2059. `https://www.hamamatsu.com/resources/pdf/etd/R1828-01_R2059_TPMH1259E.pdf`, 2016.

[97] D. Klir, J. Kravarik, P. Kubes, K. Rezac, E. Litseva, K. Tomaszewski, L. Karpinski, M. Paduch, and M. Scholz. Fusion neutron detector for time-of-flight measurements in z-pinch and plasma focus experiments. *REVIEW OF SCIENTIFIC INSTRUMENTS*, 82(3), MAR 2011.

[98] Analog Devices: 800 MHz, 50 mW Current Feedback Amplifier AD8001, One Technology Way, 2003.

[99] G. R. Gilmore. *Practical Gamma-ray Spectrometry*. Wiley, 2nd edition, 2008.

[100] J. B. Briks. *The Theory and Practice of Scintillation Counting*. Pergamon Press, 1st edition, 1964.

[101] R. D. Evans. *The Atomic Nucleus*. Krieger Pub Co, 1982.

[102] K. Siegbahn. *Alpha-, Beta- and Gamma-ray Spectroscopy*. North-Holland Publishing Company, 1968.

[103] R. J. Lanter and D. E. Bannerman. *The Silver Counter A Detector for Bursts of Neutrons*. Los Alamos Scientific Laboratory of the University of California, la-3498-nms edition, 1966.

[104] *Phton Detecotor Assembly*. Ortec manual.

[105] Technical Advantages of ISOCS™/LabSOCS™, Canberra, Miron Tehcnologies. `http://www.canberra.com/literature/isocs/application_notes/ISOCS-LabSOCS-App-Note-C39530.pdf`.

[106] S. A. Dyer. *Survey of instrumentation and measurement*. Wiley, 2001.

[107] D. Reilly, N. Ensslh, and H. Smith. *Passive Nondestructive Assay of Nuclear Materials*. Los Alamos National Laboratory, 1991.

[108] N. A. Vlasov. *Neitrony (Neutrons)*. State technical and theoretical literature press, Moscow, 1955.

[109] M. N. Thompson and J. M. Taylor. Neutron Spectra from Am-α-Be and Ra-α-Be sources. *Nuclear Instruments and Methods*, 37:305–308, 1965.

[110] O. Svoboda. *Experimental Study of Neutron Production and Transport for ADTT*. Dissertation Thesis, Faculty of Nuclear Sciences and Physical Engineering, Czech Technical University in Prague, 2011.

[111] Ondrej Sila, Daniel Klir, Karel Rezac, Balzhima Cikhardtova, and Jakub Cikhardt. MCNP calculations of neutron emission anisotropy caused by the GIT-12 hardware. *Nukleonika*, 60(2):323–326, JUN 2015.

[112] K. D. Hahn, G. W. Cooper, C. L. Ruiz, G. A. Fehl, D. L. ans Chandler, P. F. Knapp, R. J. Leeper, A. J. Nelson, R. M. Smelser, and J. A. Torres. Fusion-neutron-yield, activation measurements at the z accelerator: Design, analysis, and sensitivity. *Rev. Sci. Instrum.*, 85(4):043507, 2014.

[113] G. W. Cooper and C. L. Ruiz. Nif total neutron yield diagnostic. *Rev. Sci. Instrum.*, 72(1), 2001.

[114] D. L. Bleuel, C. B. Yeamans, L. A. Bernstein, R. M. Bionta, J. A. Caggiano, D. T. Casey, G. W. Cooper, O. B. Drury, J. A. Frenje, C. A. Hagmann, R. Hatarik, J. P. Knauer, M. Gatu Johnson, K. M. Knittel, R. J. Leeper, J. M. McNaney, M. Moran, C. L. Ruiz, and D. H. G. Schneider. Neutron activation diagnostics at the national ignition facility. *Rev. Sci. Instrum.*, 83(10D313), 2012.

[115] D. Rochman. Talys-based evaluated nuclear data library. *Sandia meeting, Albuquerque, NM, USA*, November 2014.

[116] A.J. Koning and D. Rochman. Modern nuclear data evaluation with the talys code system. *Nuclear Data Sheets*, 113(12):2841–2934, 2012.

[117] S. Jednorog, A. Szydlowski, B. Bienkowska, and R. Prokopowicz. The application of selected radionuclides for monitoring of the d-d reactions produced by dense plasma-focus device. *Journal of Radioanalytical and Nuclear Chemistry*, 301:23–31, 2014.

[118] S. Jednorog, M. Paduch, K. Szewczak, and E. Laszynska. Ti radioindium and determination of neutron radial asymmetry for the pf-1000 plasma focus device. *Journal of Radioanalytical and Nuclear Chemistry*, 303:1009–1014, 2015.

[119] A.A. Lapenas, Kh.Ja. Bondars, and Ja.K. Vejnbergs. Neutron spectrum measurement by activation. *Riga, USSR*, 1975.

[120] Kh.Ja. Bondars, Ja.K. Vejnbergs, and A.A. Lapenas. Cross-sections of neutron thresh-hold reactions. *Yadernye Konstanty*, 15(63), 1974.

[121] J. F. Ziegler. Srim-2003. *Nuclear Instruments and Methods in Physics Research Section B: Beam Interactions with Materials and Atoms*, 219–220:1027–1036, 2004.

[122] Nudat 2.6, national nuclear data center, brookhaven national laboratory. `http://www.nndc.bnl.gov/nudat2/chartNuc.jsp`.

[123] D. Klir, A.V. Shishlov, V.A. Kokshenev, P. Kubes, A.Yu. Labetsky, K. Rezac, R. Cherdizov, J. Cikhardt, B. Cikhardtova, G. N. Dudkin, F. I. Fursov, A. A. Garapatsky, B.M. Kovalchuk, J. Krása, J. Kravarik, N.E. Kurmaev, H. Orcikova, V. N. Padalko, N. A. Ratakhin, O. Sila, K. Turek, V.A. Varlachev, A. Velyhan, and R. Wagner. Deuterium z-pinch as a powerful source of multi-mev ions and neutrons for advanced applications. *Physics of Plasmas*, 23(032702), 2016.

[124] F. C. Young, J. Golden, and C. A. Kapetanakos. Diagnostics for intense pulsed ion beams. *Rev. Sci. Instrum.*, 48(4), 1977.

[125] Shouhei Araki, Yukinobu Watanabe, Tadahiro Kin, Nobuhiro Shigyo, and Kenshi Sagara. Measurement of double differential neutron yields from thick aluminum target irradiated by 9 mev deuteron. *Energy Procedia*, 71(Supplement C):197 – 204, 2015. The Fourth International Symposium on Innovative Nuclear Energy Systems, INES-4.

[126] J Goldemberg and L. Katz. High Energy Gamma-Gamma Cross Section of ^{115m}In. *Physical Review*, 90(2):308–314, Apr 1953.

[127] National Institute of Standards and Technology. X-ray mass attenuation coefficients. `https://physics.nist.gov/PhysRefData/XrayMassCoef/tab3.html`, 2017.

[128] P. Kubes, D. Klir, J. Kravarik, and K. Rezac. Neutron Production at the Small Plasma-Focus Device With Antianode. *IEEE Transactions on Plasma Science*, 37(9):1786–1791, SEP 2009.

[129] P. Kubes, J. Kravarik, D. Klir, K. Rezac, M. Bohata, M. Scholz, M. Paduch, K. Tomaszewski, I. Ivanova-Stanik, L. Karpinski, and M. J. Sadowski. Determination of deuteron energy distribution from neutron diagnostics in a plasma-focus device. *IEEE Transactions on Plasma Science*, 37(1):83–87, Jan 2009.

[130] Pavel Kubes, Jozef Kravarik, Daniel Klir, Jiri Kortanek, and Karel Rezac. Neutron Production From a Small Modified Plasma Focus Device. *IEEE Transactions on Plasma Science*, 40(12, 2, SI):3298–3302, DEC 2012.

[131] L. Michel, K. H. Schönbach, and Heinz Fischer. Neutron emission from a small 1-kj plasma focus. *Applied Physics Letters*, 24(2):57–59, 1974.

[132] A. Bernard, H. Bruzzone, P. Choi, H. Chacqui, Vladimir Gribkov, J. Herrera, K. Hirano, A. Krejci, S. Lee, Ch. Luo, F. Mezzetti, M.J. Sadowski, H. Schmidt, K. Ware, Ch. S. Wong, and V. Zoita. Scientific status of plasma focus research. *Moscow University Physics Bulletin*, 8:93–170, JAN 1998.

[133] D. Klir, J. Kravarik, P. Kubes, K. Rezac, S. S. Anan'ev, Yu. L. Bakshaev, P. I. Blinov, A. S. Chernenko, E. D. Kazakov, V. D. Korolev, B. R. Meshcherov, G. I. Ustroev, L. Juha, J. Krasa, and A. Velyhan. Neutron emission generated during wire array z-pinch implosion onto deuterated fiber. *Physics of Plasmas*, 15(3):032701, 2008.

[134] O. Zucker, W. Bostick, J. Long, J. Luce, and H. Sahlin. The plasma focus as a large fluence neutron source. *Nuclear Instruments and Methods*, 145(1):185 – 190, 1977.

[135] T. Darling, E. McKee, A. Covington, V. Ivanov, F. Wessel, H. Rahman. Gas puff z-pinches with deuterium-krypton gas mixtures. 57th Annual Meeting of the APS Division of Plasma Physics Volume 60, Number 19, Monday–Friday, November 16–20, 2015; Savannah, Georgia `http://meetings.aps.org/Meeting/DPP15/Session/YO4.7`, November 2015.

[136] S. Lee. Neutron yield saturation in plasma focus: A fundamental cause. *Applied Physics Letters*, 95(151503), 2009.

[137] T. C. Rust, E. V. R. DiBella, C. J. McGann, P. E. Christian, J. M. Hoffman, and D. J. Kadrmas. Rapid dual-injection single-scan ^{13}n-ammonia pet for quantification of rest and stress myocardial blood flows. *Physics in Medicine & Biology*, 51(20):5347, 2006.

[138] M. Roth, D. Jung, K. Falk, N. Guler, O. Deppert, M. Devlin, A. Favalli, J. Fernandez, D. Gautier, M. Geissel, R. Haight, C. E. Hamilton, B. M. Hegelich, R. P. Johnson, F. Merrill, G. Schaumann, K. Schoenberg, M. Schollmeier, T. Shimada, T. Taddeucci, J. L. Tybo, F. Wagner, S. A. Wender, C. H. Wilde, and G. A. Wurden. Bright laser-driven neutron source based on the relativistic transparency of solids. *Phys. Rev. Lett.*, 110:044802, Jan 2013.

[139] G. P. Grim, G. L. Morgan, M. D. Wilke, P. L. Gobby, C. R. Christensen, and D. C. Wilson. Progress on neutron pinhole imaging for inertial confinement fusion experiments. *Review of Scientific Instruments*, 75(10):3572–3574, 2004.